High-Frequency Dimensional Effects in Ferrite-Core Magnetic Devices

Glenn R. Skutt

Dissertation submitted to the Faculty of the Virginia Polytechnic Institute and State University in partial fulfillment of the requirements for the degree of

Doctor of Philosophy
in
Electrical Engineering

Fred C. Lee, Chair
Ioannis Besieris
Dušan Borojević
Dan Chen
Werner Kohler

October 4, 1996
Blacksburg, Virginia

Keywords: Ferrites, Dimensional Resonance, Eddy Currents, Transformers, Inductors

High-Frequency Dimensional Effects in Ferrite-Core Magnetic Devices

Glenn R. Skutt

(ABSTRACT)

MnZn ferrites are widely used in power electronics applications where the switching frequency is in the range of several tens of kilohertz to a megahertz. In this range of frequencies the combination of relatively high permeability and relatively low conductivity found in MnZn ferrite helps to minimize the size of magnetic devices while maintaining high efficiency. The continuing improvement in semiconductor switches and circuit topologies has led to use of high-frequency switching circuits at ever increasing power levels. The magnetic devices for these high-power, high-frequency circuits require magnetic CORES that are significantly larger than standard ferrite-core devices used at lower power levels. Often such large ferrite cores must be custom designed, and at present this custom design is based on available material information without regard for the physical size of the structure.

This thesis examines the issues encountered in the use of larger MnZn ferrite cores for high-frequency, high-power applications. The two main issues of concern are the increased power dissipation due to induced currents in the structure and the change in inductance that results as the flux within the core is redistributed at higher frequencies. In order to model these problems using either numerical or analytical methods requires a reliable and complete set of material information. A significant portion of this work is devoted to methods for acquiring such material information since such information is not generally available from the manufacturers. Once the material constants required for the analysis are determined, they are used in both closed-form and numerical model to illustrate that large ferrite cores suffer significant increases in loss and significant decreases in inductance for frequencies as low as several hundred kilohertz. The separate impacts of the electrical and magnetic losses in the core are illustrated through the use of linear finite element analyses of several example core structures. The device impedances calculated using the FEA tools show fair agreement with measurement. An analysis of gapped structures and segmented cross-sections shows that these design options can reduce the severity of the dimensional problems for some designs.

Acknowledgments

I would like to express my sincere appreciation to my advisor, Dr. Fred C. Lee, for the support and encouragement he provided throughout the course of this research. His extensive experience in the power electronics field has been a tremendous aid in focusing this work on the practical issues that face designers. I would also like to thank Dr. Ioannis Besieris for the interest he showed in this particular work and for the insight he provided into other similar applications in other fields. I am grateful to Dr. Dan Chen for his comments and suggestions on the topic and for his continued interest in magnetics and magnetics education. I would also like to thank Dr. Werner Kohler for his participation as part of my committee and for his comments and suggestions. I would like to thank Dr. Dušan Borjević not only for serving as part of my committee but also for the many discussions of power electronics, university teaching, and life in general that we shared over the past years.

I would like to extend my appreciation to the many students of the Virginia Power Electronics Center. In particular, I'd like to thank Dr. Ashraf Lotfi for the many discussions we have had both during our time together at VPEC and in the years since. Thanks are also due to my fellow VPEC students: Mr. Robert Watson, Mr. Michael Zhang, Mr. Stephen Dubovsky, Dr. Qing Chen, Dr. Ning Dai, Ms. Ping Han, Mr. Ju Zhang, and Mr. Liming Ye (among many others).

The staff of VPEC have the difficult task of keeping up with some sixty graduate students and all of their assorted problems, and I'd like to thank both the current and past members of the staff for all the work they do. In addition, I'd like to thank the VPEC sponsors. Specifically, Mr. Jim Florence from Ceramic Magnetics Inc., as well as Mr. John Gilmore and Mr. Adrian Perregaux at Ansoft Corporation.

Thanks also to: Dr. Gary Brown for his helpful advice and for the encouragement to keep asking questions; my Master's thesis advisor Dr. Thomas G. Wilson for starting me down this road in the first place; Mr. P. S. Venkatraman for mentoring me in the ways of practical magnetics design; Dr. Raymond B. Ridley for letting me share in the "real story" behind everything; Mr. Rudy Severns for reminding me of how much we've forgotten and keeping me stocked with reading material; Dr. Dan Sable and Dr. Guichao Hua for providing me with interesting things to do now that this is behind me.

I offer my deepest gratitude to my family and particularly to my parents, Dick and Mary Skutt, for their love and support and for their confidence in me. Finally, this dissertation is dedicatated to my wife Lesley Howard for her understanding, love and encouragement throughout this entire process.

This work was supported by the University-Industry Partnership.

Contents

List of Figures

List of Tables

Chapter 1

Introduction

1.1 Scope

This research examines potential problems with the use of ferrite-core magnetic devices for high-power applications that switch at high-frequencies. In particular, this work concentrates on the aspects of transformer and inductor design related to high-frequency effects in the core material itself. The frequency range of interest is chosen based on the upper end of the high-power conversion spectrum; it roughly covers the decade of frequencies from 100 kHz to one megahertz. MnZn ferrites are the primary material considered since this is the most common material in use for these frequencies.

1.2 Problem Statement

In recent years, the use of power conversion technologies at higher and higher power levels has emerged as a significant new design challenge for power electronics engineers. Manufacturers of high-power welding equipment, electric vehicle drives and charging systems, power inverters and line conditioning equipment have all found that the size reduction and performance improvements of high-frequency switching power conversion are as beneficial at high power levels as they have proven to be in lower power applications. These new high-power, high-frequency power conversion circuits often require not only energy storage inductors but electrical isolation as well. This need for high power magnetic devices operating under high frequency excitation introduces several new design issues which push the limits of standard design equations.

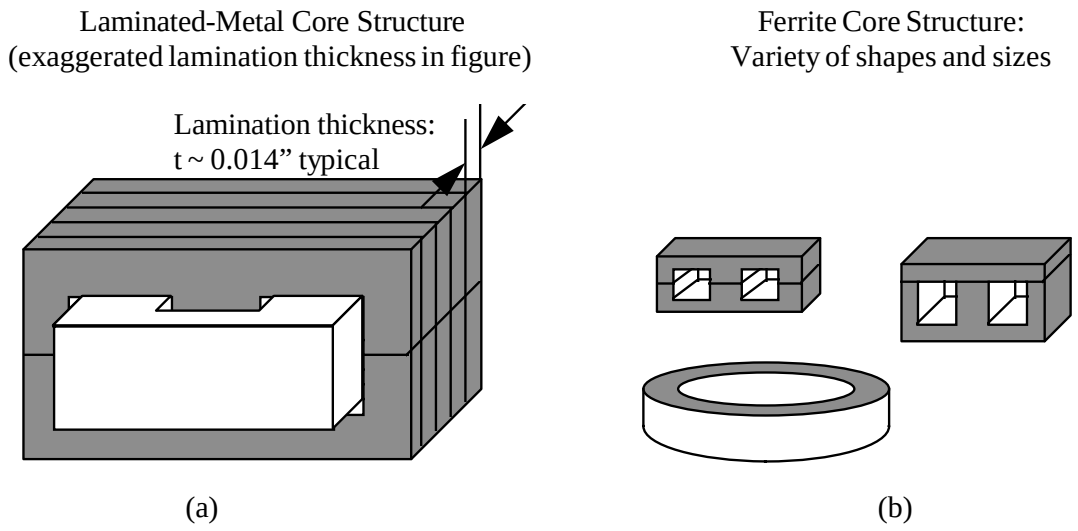

Figure 1.1: Low-Frequency and high-frequency core structures. (a) laminated core structure. (b) ferrite core transformer.

Traditional high-power magnetics are designed for excitation frequencies in the range of 50 hertz to several kilohertz. These transformers and inductors are constructed almost exclusively using laminated-iron structures such as shown in Figure 1.1(a). Lower power devices operated in the range of tens to hundreds of kilohertz, on the other hand, are usually wound on low-loss ferrite cores such as those illustrated in Figure 1.1(b). This dissertation focuses on what happens to standard design rules for ferrite core devices as the power level increases. These high-power devices require cores that are significantly larger than standard ferrite structures. Such large cores may be subject to significant losses due to high-frequency eddy current and flux shielding effects that are not present in smaller ferrite cores at these frequencies. Moreover, the information available in the design literature does not provide adequate guidance for how such size-dependent losses should be calculated or avoided. The significance of these dimensional effects are illustrated in Figure 1.2 where the differences in normalized inductance and loss density in two different devices of different sizes are plotted against frequency.

The changes in inductance and core losses illustrated in Figure 1.2 are of particular concern in high-power designs, but they are also relevant to many other areas of power electronics. Since the fundamental issues that cause problems in the high-power, high-frequency design space—namely skin effects and dimensional resonance—exist in all cores to some extent, they must be evaluated for any design that moves beyond standard practice. This dissertation illustrates that it is not always adequate to take well-known design equations in use

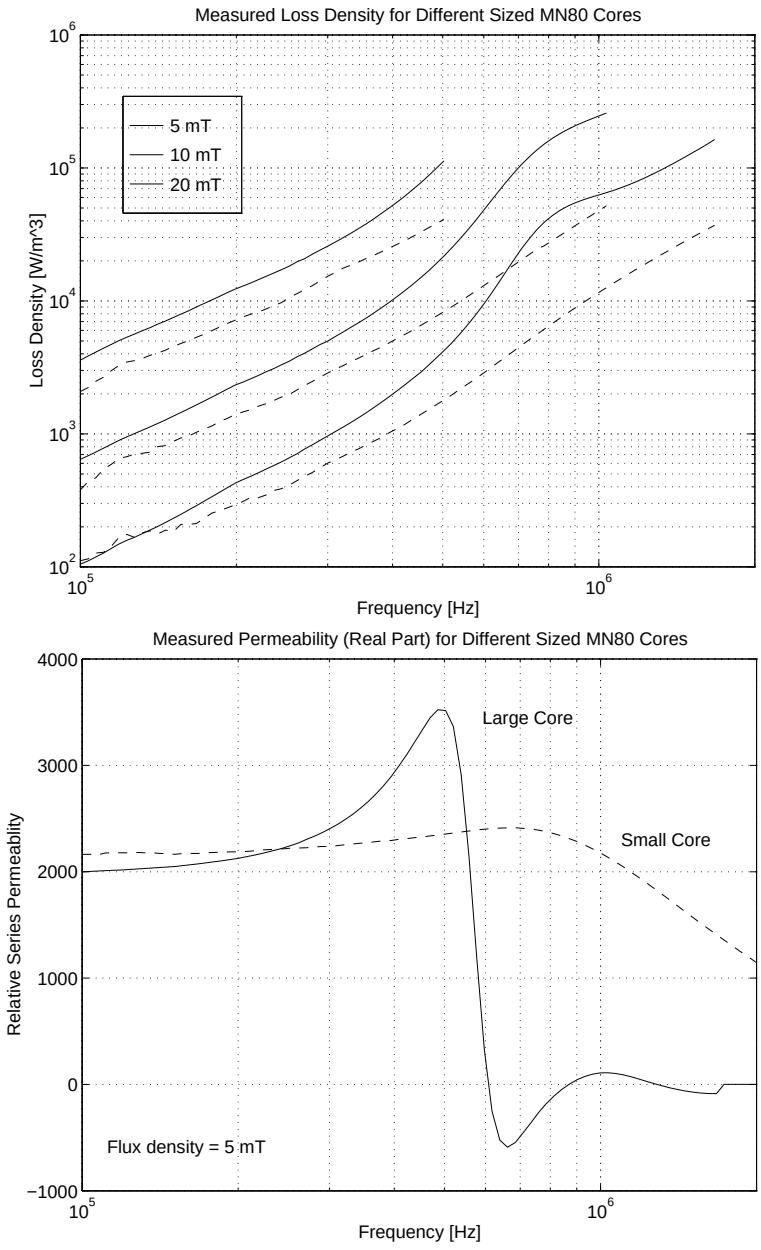

Figure 1.2: Power loss density and normalized inductance vs. frequency plotted for two cores of different sizes.

in one design space and apply them without modification to the designs of a completely different nature.

1.2.1 An Example Application

One high-power application that has been the focus of significant interest and research effort in recent years is the use of inductively-coupled battery charging for electric vehicles [1]. This application provides one example where the need to process a large amount of power in a relatively small space challenges standard design assumptions regarding core size and shape. In an inductively-coupled charger such as that shown in Figure 1.3[1], the energy to recharge the vehicle's batteries is coupled from a charging station to the batteries through a transformer with a removable primary winding. The majority of the transformer core as well as the secondary winding and the diode rectifier circuits are located on the vehicle; the primary winding is contained in the paddle that the user inserts into the transformer during the charging process. This strategy has certain advantages—primarily related to user safety—and has the possibility of becoming the standard charging approach used for commercial electric vehicles.

Figure 1.4 shows the ferrite core used in the existing charging system. It is designed to couple up to 120 kW of charging power during peak recharge operation. While the charger core is large by ferrite standards, the high operating frequencies (in the range of 50 kHz to 300 kHz) make it quite compact in comparison to an equivalent low-frequency transformer of the same power rating. Nonetheless, the transformer core in Figure 1.4 poses several interesting design questions, one of which is whether the large size of the core increases the effects of dimensional resonance and eddy currents in the core.

1.2.2 High-Frequency Dimensional Effects

Skin Effect

The skin effect is a well known problem with respect to the current distribution in the windings of magnetic devices, yet it is often considered insignificant in the ferrite cores used in conventional designs[2, p.146]. This assumption is usually acceptable for small cores, but is less valid as the size of the core cross-section increases. This distinction of skin effect as a problem related to the *relative* values of conductor or core size and the skin

[1]The figures included here are provided by GM/Hughes.

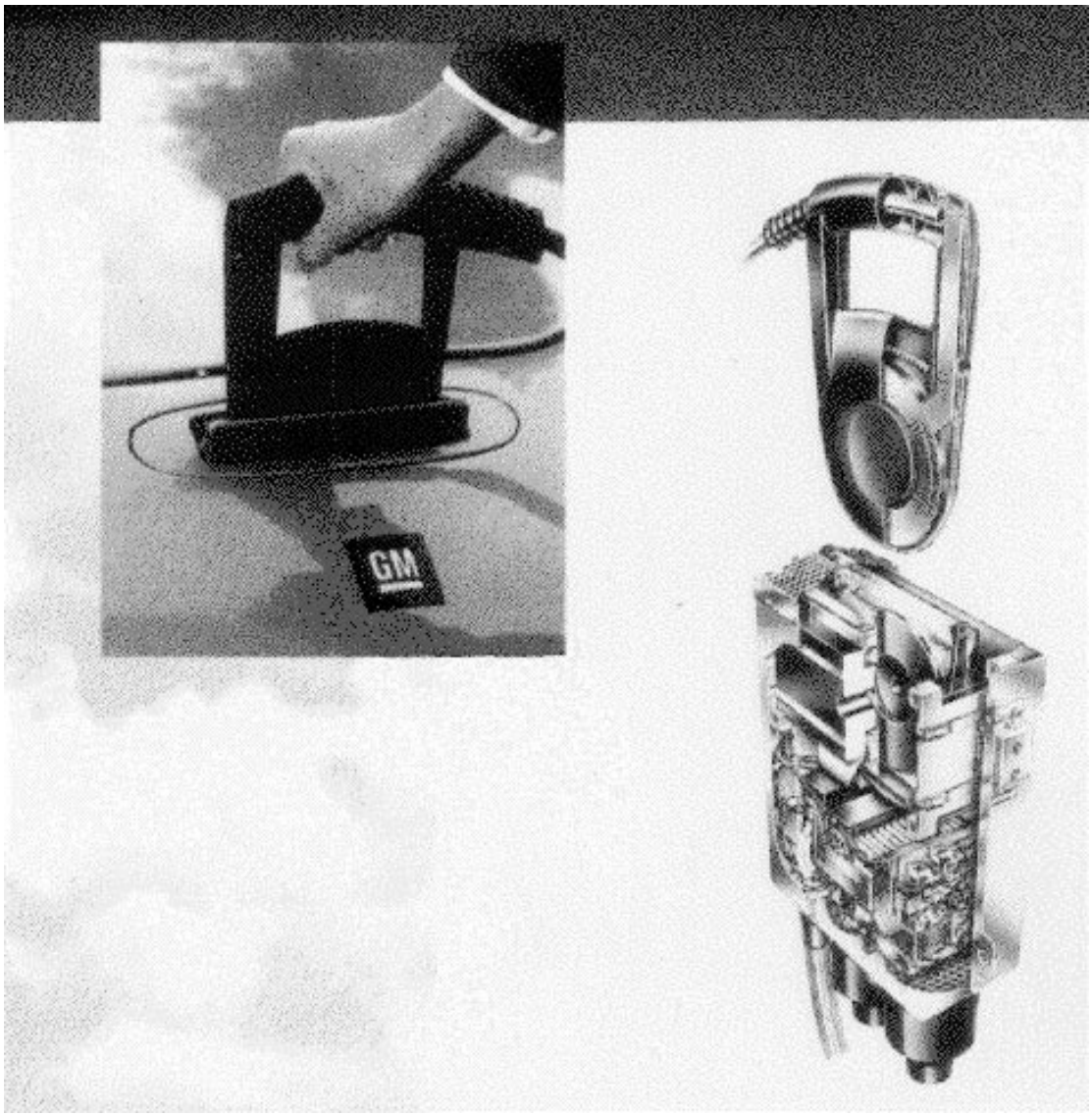

Figure 1.3: Inductively coupled electric vehicle charger.[Courtesy of GM/Hughes]

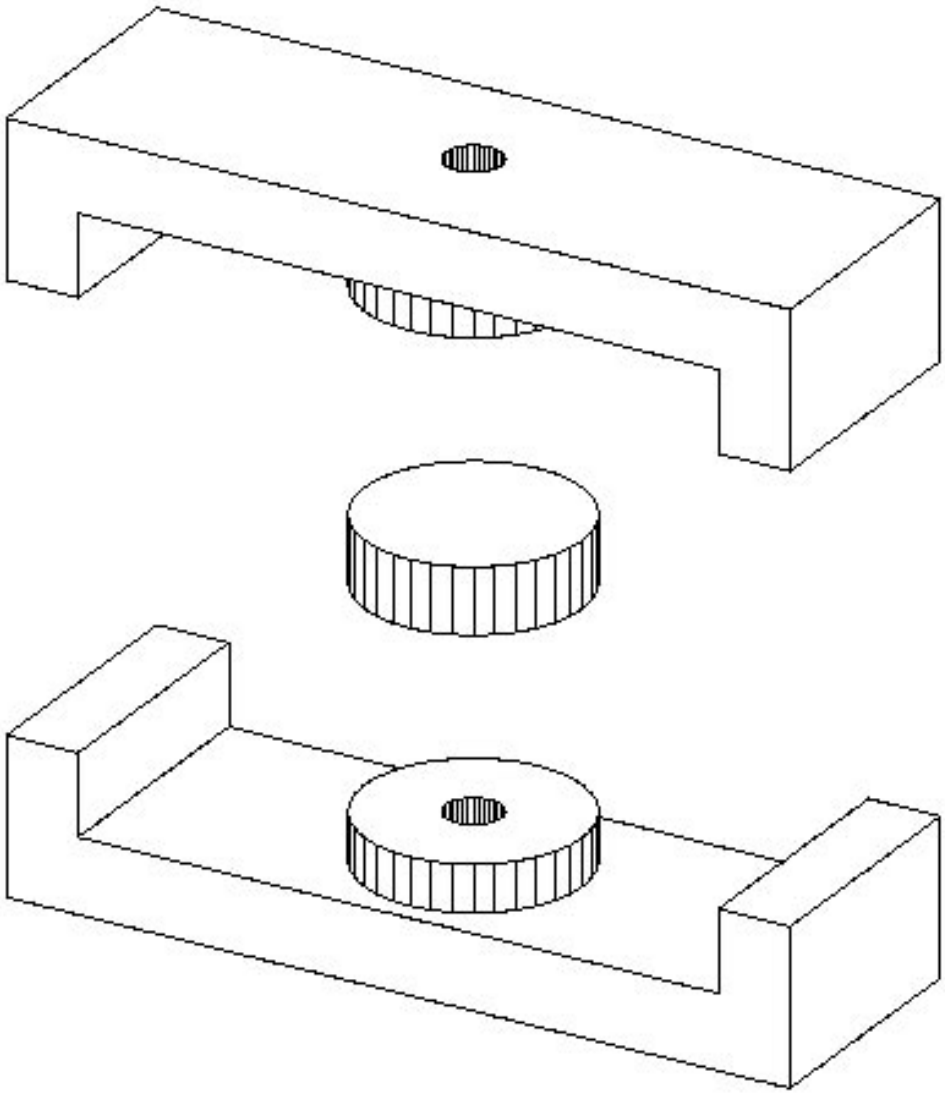

Figure 1.4: Inductive charger core geometry.

depth of the material is illustrated in the following brief review of skin effects in electrical and magnetic conductors.

Materials immersed in a time varying electromagnetic field have reaction currents induced within them, and these induced currents are a function of the time rate of change of the fields and the material's conductive and dielectric properties. The induced currents act to oppose the changing fields by generating reaction fields of opposite sense to the time rate of change of the source field. In the case of a sinusoidally varying excitation source and linear media, the superposition of the source field and the reaction field result in a new steady state field distribution that tends to shield the interior of the material from the time varying source field. This is the well-known skin effect, and it is illustrated for two different cases in Figure 1.5. The familiar case of a winding carrying a net current, I, is illustrated in Figure 1.5(a). For sufficiently high frequencies—or equivalently, in large enough conductors—the superposition of the source field, J_{source}, and the reaction currents, J_{eddy}, results in an increased current density near the conductor surface and negligible current density in the center of the material. An essentially dual situation occurs in a flux carrying region such as shown in Figure 1.5(b). Here the net flux, ϕ, is assumed constant, but the superposition of the source flux, ϕ_{source}, and the reaction flux, ϕ_{eddy}, results in a shielding of the flux from the interior of the material.

Table 1.1 lists typical conductivity and permeability values for various materials and gives the skin depth in these materials at low and high frequencies. For simplicity, the material constants are assumed to be constant for each material over the frequency range; while this is generally not true, such a comparison illustrates several important characteristics. First, the magnetic metals such as silicon steel have much lower skin depths than non-magnetic metals such as copper and aluminum. This is why it is so important to use finely laminated structures for iron-core devices even at line frequencies. Second, since ferrite is a fairly poor conductor it has a large skin depth at low frequencies. As the frequency increases, the skin depth comes into the range of a few centimeters, and therefore it is important that we consider skin effects in the core for relatively large ferrite structures.

The skin effects in ferrite are illustrated in Figure 1.6 for a cylindrical core section of diameter $a = 50$ mm. The excitation field is assumed to be provided by uniformly-wound turns of wire. In these plots, the field distribution is shown for the point in time when the excitation current is at the peak of its sinusoidal variation. Figure 1.6(a) shows that for low frequencies the field within the core is uniform and in phase with the exciting field. This is the usual quasi-static field assumption. As the frequency increases to the point where $a/\delta = 2.27$, the field becomes as shown in Figure 1.6(b). At higher frequencies, the flux density within the core becomes more and more concentrated on the surface of the core as shown in Figure 1.6(c) where $a/\sigma = 3.215$ and Figure 1.6(d) where $a/\sigma = 3.93$.

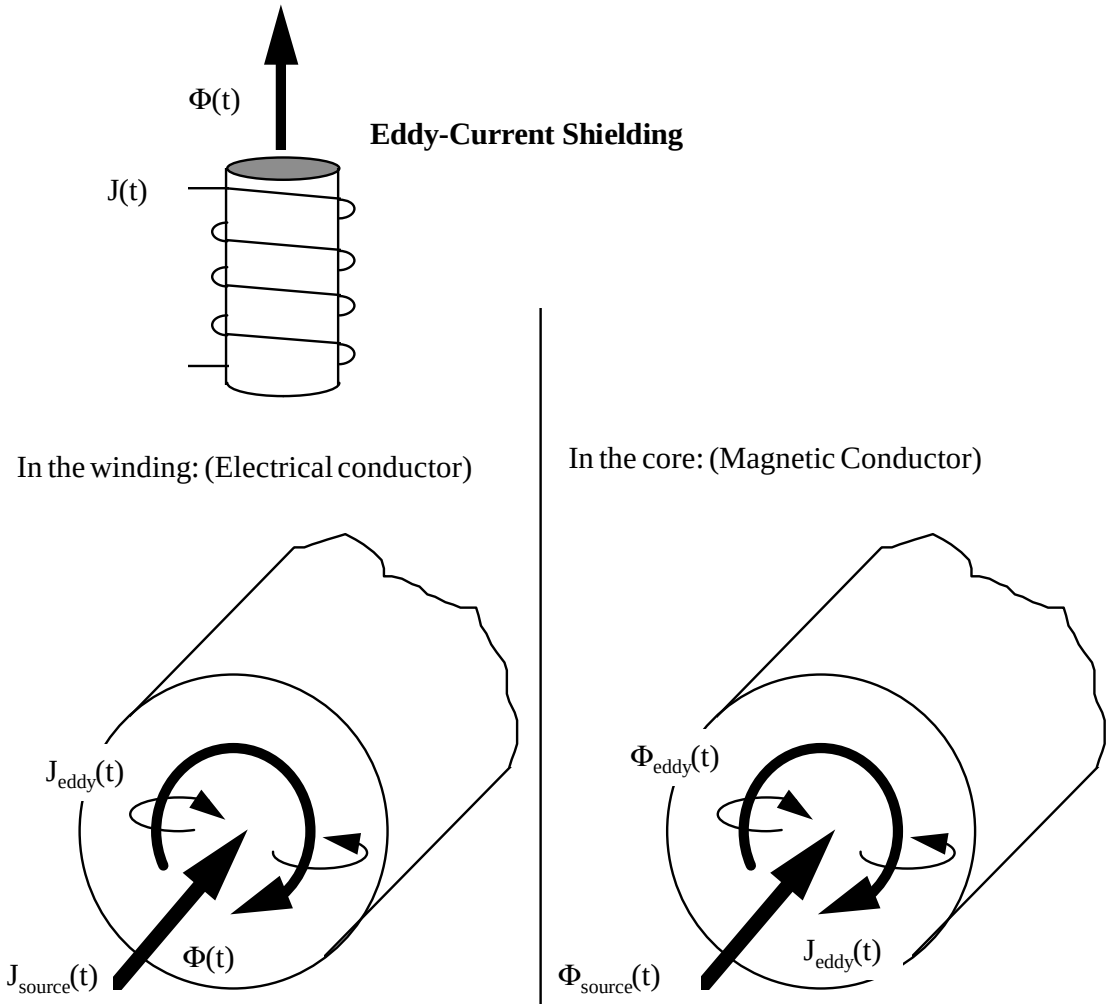

- The current and flux concentrate on the conductor surface at high frequencies
- Rule of thumb: winding or core should be approximately two skin depths wide

Figure 1.5: Skin effect in (a) a current carrying conductor and (b) a flux carrying conductor.

Table 1.1: Skin Depths in Various Materials

Material	Permeability	Conductivity		Skin Depth [m]	
	μ_r	σ [S/m]	60 Hz	100 kHz	1 MHz
Copper	1	5.8e7	8.534e-3	2.090e-4	6.610e-5
Aluminum	1	3.57e7	1.088e-2	2.664e-4	8.426e-5
Silicon Steel	5e4	2e6	2.055e-4	5.034e-6	1.592e-6
MnZn Ferrite	3e3	0.5	1.678	4.110e-2	1.300e-2
NiZn Ferrite	100	0.01	64.99	1.592	5.034e-1

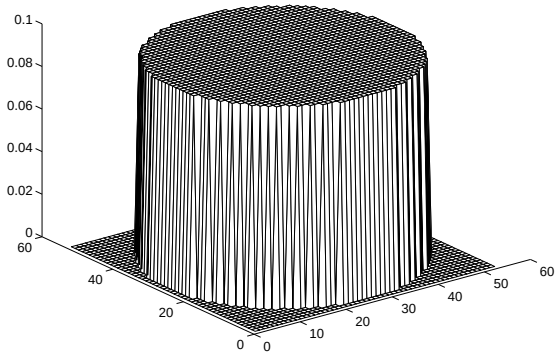

(a) 60 Hz

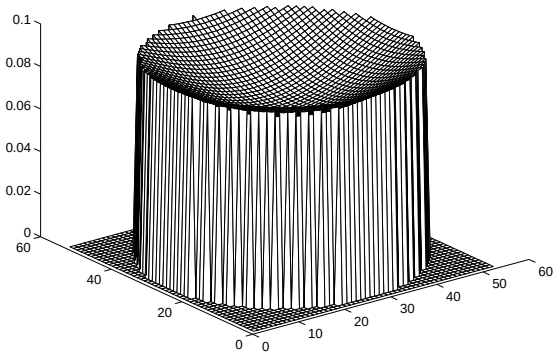

(b) $a/\delta = 2.27$ ($f = 173$ kHz)

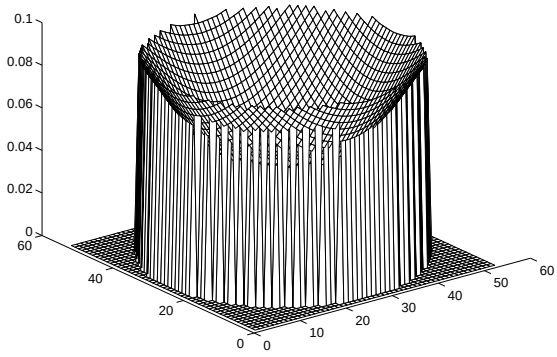

(c)$a/\delta = 3.215$ ($f = 346$ kHz)

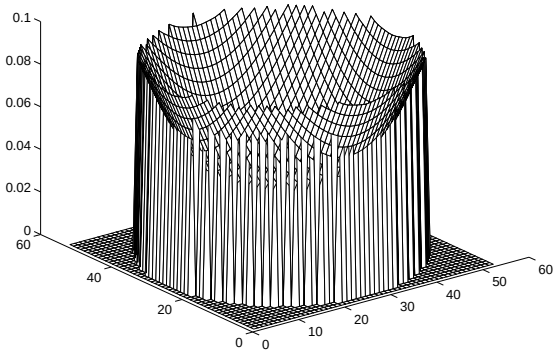

(d) $a/\delta = 3.93$ ($f = 520$ kHz)

Figure 1.6: Skin effect in a cylindrical ferrite core.

Dimensional Resonance

The shielding effects shown in Figure 1.5 are fundamental results for conductive materials such as device windings and core laminations. In both cases, well known design rules guide the magnetics designer to minimize these effects through the use of thin laminations in the core and small-diameter wires in the windings. In the case of ferrite materials, however, one must also consider the role that displacement currents—induced through the same time-varying fields—play in the final field distribution.

If the flux-carrying conductor of Figure 1.5(b) is modeled to include the dielectric nature of the material only (conductivity set arbitrarily to zero) then there are no reaction currents induced to cause the shielding effect described above. Since the ferrite is also highly magnetic, however, the source field will propagate into the core at a different velocity. That is, because ferrite has both high dielectric constant and high permeability, waves propagate slower in the ferrite than they do in free space. Ignoring for the moment the losses in the core, we can write the propagation velocity as,

$$v = \frac{1}{\sqrt{\mu\epsilon}} = \frac{c}{\sqrt{\mu_r \epsilon_r}} \tag{1.1}$$

where c is the speed of light in vacuum and μ_r and ϵ_r are the relative permeability and the relative permittivity respectively.

The propagation velocity is also given as the product of the wavelength, λ, and the frequency, f, and therefore the wavelength within the core is shorter than it is in free space. For high frequencies—or for large devices at lower frequencies—the short wavelength within the core means that the fundamental assumption of quasi-static fields is no longer valid. In this case, the fields within the core are out of phase with the surface fields and, in the case of the magnetic field, the net flux linking the windings is no longer a simple function of the core cross sectional area. It is possible to establish an electromagnetic resonance condition that results in equal amounts of flux in the positive and negative directions. This dimensional resonance condition results in a zero apparent inductance in the core since there is no net flux linkage of the winding turns when resonance occurs.

The effects of dimensional resonance are illustrated in Figure 1.7 for the cylindrical core of Fig. 1.6. Here the core is modeled without losses but with a dielectric constant of 150,000. The field distribution is again shown for the point where the excitation current is at the peak of its sinusoidal variation. Figure 1.7(a) shows that for low frequencies the field within the core is uniform and in phase with the exciting field as expected. As the frequency increases to the point where $a = \lambda_{core}/2$, the field becomes as shown in Figure 1.7(b). At higher frequencies, the flux density within this lossless core is as shown in Figure 1.7(c) where $a = \lambda_{core}$ and Figure 1.7(d) where $a = 3\lambda_{core}/2$.

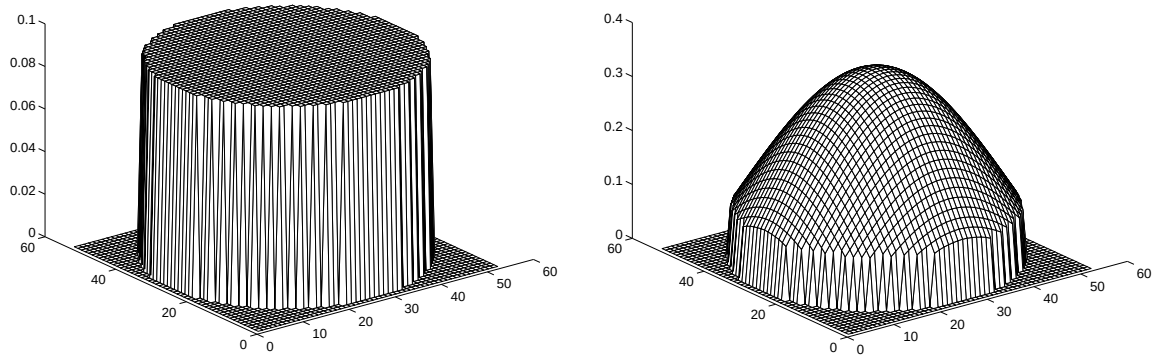

(a) 60 Hz

(b) a=$\lambda/2$ ($f = 173$ kHz)

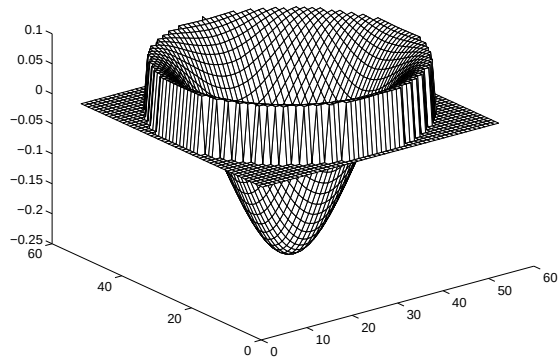

(c)a=λ ($f = 346$ kHz)

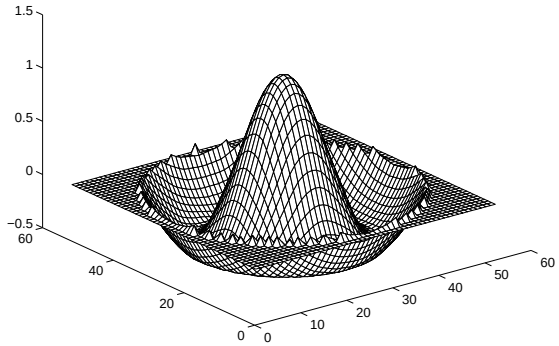

(d) a=$3\lambda/2$ ($f = 520$ kHz)

Figure 1.7: Dimensional resonance in a lossless cylindrical ferrite core.

Dimensional resonance—like the skin effect—is dependent on the size and shape of the core as well as the time rate of change in the source field. However, unlike the skin-effect shielding problem, there is little in the design literature that can help a designer minimize or even to recognize the effects of this resonance.

Combined Geometrical Effects

In the previous examples, we have looked at the skin effects due to eddy current shielding and the dimensional resonance effects due to wave propagation as separate phenomena. In reality, both of these effects occur together and interact to give a total response in the core. Figure 1.8 shows the flux density distribution in the cylindrical core cross-section of Figures 1.6 and 1.7 when the skin effect and the dimensional resonance effects are combined. The resulting flux distribution is dominated at higher frequencies by the skin effects, but the dimensional resonance effects are clearly evident as well.

Dimensional effects in the battery charger example

The lines A-A′ and B-B′ in Figure 1.4 show two different cross-sections of the core that correspond to the cross-sectional lines of Figure 1.5. These dimensions—which are 17 mm and 50 mm respectively—serve as examples throughout this dissertation as the various dimension-dependent losses are discussed, modeled and evaluated.

When these cross-sectional dimensions of the charger core are large enough to make skin-effect and/or dimensional resonance effects a concern, then one proposal for solving this problem is to use a laminated structure similar to standard low-frequency transformers. As we have seen, such laminated cores are necessary for low-frequency steel-cored devices because of the high conductivity and small skin depth that exists in such cores even at line frequencies. The question then is whether such a lamination strategy is required—or effective—for large ferrite cores under high-frequencies excitation.

Finally, if dimensional resonance exists within the core in Figure 1.4 (particularly within the circular center post and puck regions), then the flux distribution in the core will be highly non-uniform. This non-uniform flux distribution can place additional limitations on the use of such large structures for high-power, high-frequency designs. Figure 1.9 shows an example of such a non-uniform flux distribution for the 2D representation of the charger core structure. The high-frequency flux distribution (Figure 1.9(b)) that occurs when the the conditions for dimensional resonance are met is quite different from the low-frequency excitation shown in Figure 1.9(a). When dimensional resonance such as this occurs, the

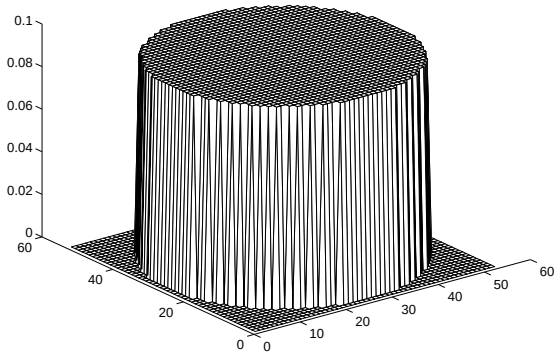

(a) 60 Hz

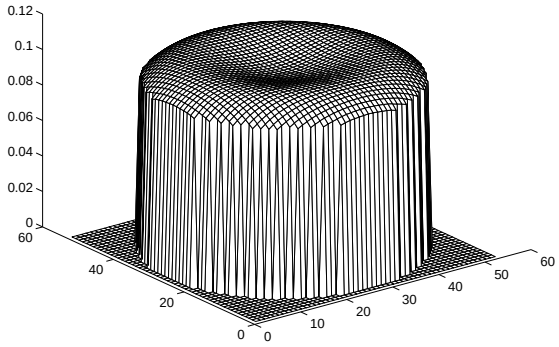

(b) a=$\lambda/2$ ($f = 173$ kHz)

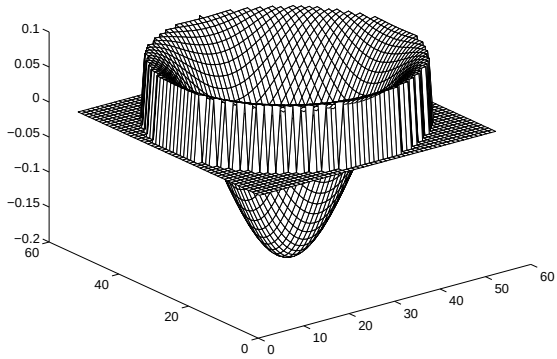

(c)a=λ ($f = 346$ kHz)

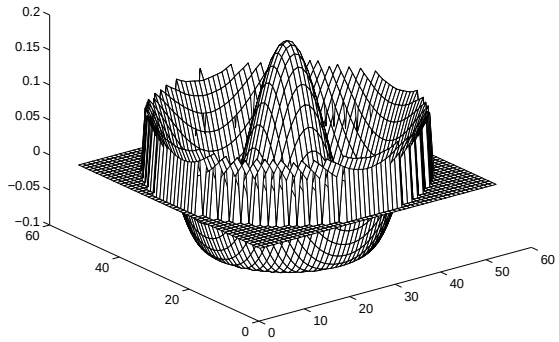

(d) a=$3\lambda/2$ ($f = 520$ kHz)

Figure 1.8: Flux distribution in a cylindrical ferrite core with both eddy currents (conductivity) and wave propagation (dielectric constant) included in the model.

losses in the core increase substantially and the inductance—which is related to the net flux linkage in the core per ampere of excitation current—decreases.

1.2.3 Research Scope and Approach

This thesis takes the characterization of ferrites as its starting point and examines the effects that core size and geometry have on the performance of magnetic devices used in high-power applications such as the inductive charger. The emergence of such large ferrite structures means that designers must now concern themselves not only with the design implications of different wire types and winding arrangements, but they must also consider the design implications of the core's geometry as well.

1.3 Outline

The present chapter provides an overview of the problems associated with large ferrite structures and indicates the specific focus of this work. The necessary background material on which later modeling efforts are based is presented in Chapter 2. The magnetics design issues and measurement techniques are reviewed with a focus on the ways ferrites are characterized for large amplitude excitation at frequencies up to a megahertz. Chapter 2 also presents a review of the literature related to high-frequency magnetics winding design in order to illustrate parallels between high-frequency models for winding loss and leakage inductance on one hand and high-frequency core characterization models on the other.

The background material of Chapter 2 is followed in Chapter 3 by a review of basic field equations and their application for calculating power dissipation and energy storage in ferrites. These field equations are used to establish appropriate methods for extracting ferrite material characteristics from laboratory tests, and these methods are then used to collect measured material data on representative MnZn ferrite materials. The measured material constants form the input for the numerical modeling efforts presented in Chapter 5. The final sections of Chapter 3 present laboratory measurements of the performance of several large ferrite core structures. This measurement study illustrates the decrease in high-frequency inductance and increase in losses that occur large ferrite structures.

While the primary analytical tool used in this thesis is finite-element based numerical field analysis, the closed-form analytical solution for the field distribution in a simple, ideal geometry provides certain valuable insights into the high-frequency processes in ferrites; Chapter 4 presents such a solution and uses it to illustrate the size limitations that exist

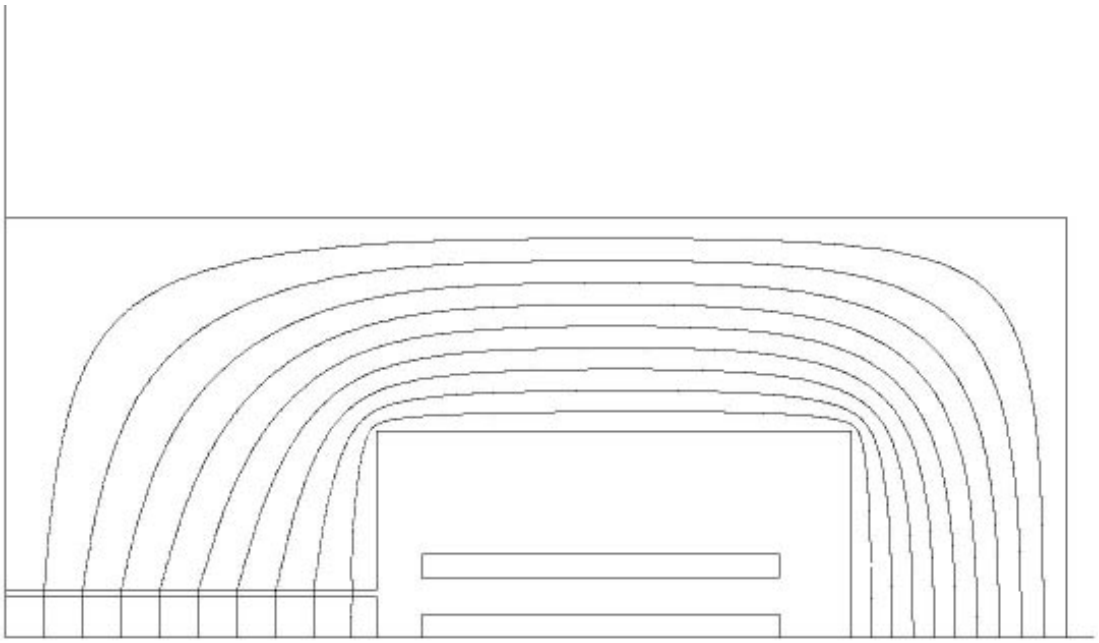

(a) Excitation frequency = 1 Hz

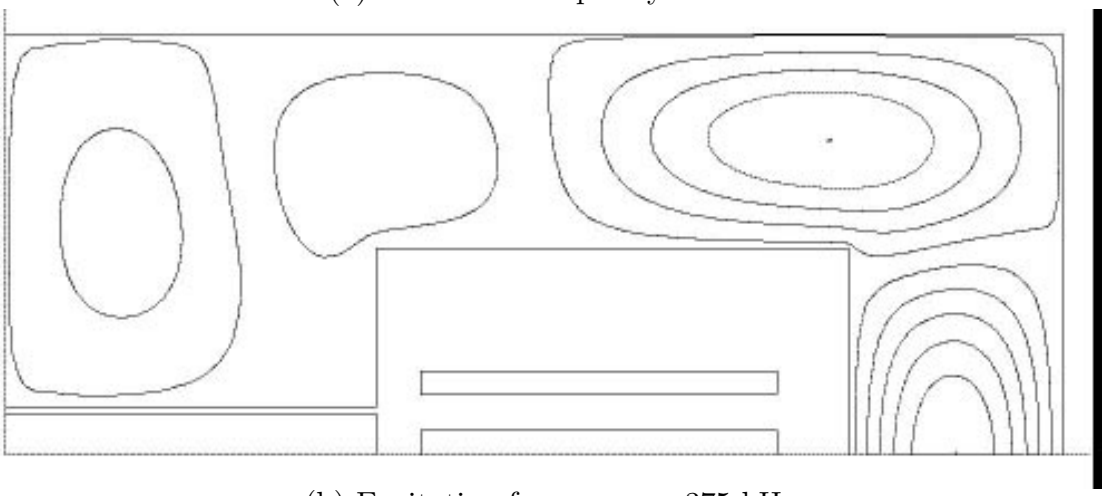

(b) Excitation frequency = 375 kHz

Figure 1.9: Flux in the charger core at low frequencies and under dimensional resonance conditions.

for a given set of material characteristics in a given range of frequencies. This analysis of the closed-form solution helps establish a design intuition that is useful in evaluating more complicated designs.

Chapter 5 takes the material characteristics measured in Chapter 3 and uses them to evaluate ferrite cores of various shapes and sizes using commercial numerical analysis tools. This numerical modeling effort begins with several baseline cases that mirror the one-dimensional analytical modeling of Chapter 4. Once the one-dimensional solution is verified, more complicated two-dimensional are considered. In particular, the set of cores measured in Chapter 3 are simulated in order to compare the numerically modeled frequency responses for inductance and loss with the measured results.

With the material characterization, analytical modeling and numerical analysis methods established, Chapter 6 returns to the electric vehicle charger core presented in Figure 1.4. This charger represents one example of a high-power, high-frequency application where the use of a large ferrite core may be problematic. Chapter 6 examines the flux distribution, loss and inductance of this structure with particular focus on the cylindrical disk that forms the middle section of the core center post. The analysis in Chapters 4-5 indicates that this region of the core is the most likely to suffer from eddy-current and dimensional problems. Chapter 6 presents several design options—including the lamination of the puck material—that reduce these high frequency effects.

1.4 Notational Conventions

Since the thesis deals with effects in ferrite devices that depend on the relative size of the core with respect to the skin depth and wavelength in the material it is important to establish clearly the intended meaning of terms such as *high frequency* and *high power* as used here.

1.4.1 Definition of High-Frequency and High-Power

The terms high-power and high-frequency are clearly arbitrary. For this discussion, however, *high power* is generally understood to refer to power levels in the range of several kilowatts and above. The inductive charger application mentioned above, for example, processes over 100 kilowatts, but similar sized cores may be used for lower power applications (in the range of kilowatts) especially when the inductive energy storage requirements demand ferrite cores with dimensions on the order of several centimeters. The term *high*

frequency is likewise arbitrary. In this document it refers to switching operation in the decade between 100 kHz and one megahertz.

1.4.2 Types of Materials Considered

This discussion focuses on MnZn ferrites; the other popular ferrite material for power electronics applications is the family of NiZn materials. While NiZn has definite advantages for frequencies above 1 MHz, MnZn is usually preferred for applications below 1 MHz. The differences between these two ferrite materials is discussed in depth in [2, 3].

1.4.3 Notation

This dissertation uses a set of symbolic notation that is uniform and self-consistent, but that may vary in some respects with other notational conventions[2]. In all cases, the use of SI units can be assumed unless specific notice is given within the text. The Glossary of Symbols provided in front of this document lists the various symbols used within the document, but as mentioned there, the same symbols may often appear with different type faces or subscript notation. This section describes the conventions used throughout this text in order to distinguish the various properties of symbols and variables.

Time varying quantities are generally represented by lower-case variables where an explicit time argument, "(t)", is sometimes included. When a quantity is constant with respect to time or represents an rms value, the symbol is usually given in upper-case. One exception to this rule is the representation of time-average values of density functions such as the power dissipation density, $p_d(t)$. In this case, even though time average power dissipation density is not time-varying, it is represented in lower-case with angle brackets placed around the dissipation density variable to indicate the time average, e.g., $\langle p_d(t) \rangle$. The lower-case notation for a constant value is used so that the upper-case symbol can be used for the *volume integrated* value of the time averaged density function. That is, when the time-average loss density is integrated over the volume of a given core for example, the total loss is designated as $\langle P_{core} \rangle$.

It is often convenient to represent quantities that vary sinusoidally in time using phasor notation. In this document, the magnitude of the phasor represents the *peak* value of the sinusoidally varying quantity. This is in accordance with the convention in use in much of the electromagnetic fields literature, but it should be noted that it is more common in

[2]Much of this section is taken with permission directly from [4].

power applications to use the *rms* value of the sinusoid as the magnitude of the phasor. All complex quantities—including phasors—are underlined. For example, a current $\underline{I} = I\angle\theta$ has a peak value of I, and rms value $I/\sqrt{2}$ or $|I|/\sqrt{2}$, and a phase angle θ. In detail, this is given as,

$$\begin{aligned} i(t) &= \Re(\underline{I}e^{j\omega t}) \\ &= \Re(Ie^{j\theta}e^{j\omega t}) \\ &= I\cos(\omega t + \theta) \end{aligned} \tag{1.2}$$

Vector quantities are designated using boldface characters. For example, the instantaneous value of a time varying magnetic field at a given point in space is written as $\mathbf{H}(x, y, x, t)$. If this field is varying sinusoidally in time, then it can be represented as a time-independent *vector phasor* $\underline{\mathbf{H}}(x, y, z)$.

$$\mathbf{H}(x, y, x, t) = \Re(\underline{\mathbf{H}}(x, y, z)e^{j\omega t}) \tag{1.3}$$

The three spatial components of the vector phasor are in turn represented by three component phasors,

$$\underline{\mathbf{H}}(x, y, z) = \underline{H}_x\hat{\mathbf{a}}_\mathbf{x} + \underline{H}_y\hat{\mathbf{a}}_\mathbf{y} + \underline{H}_z\hat{\mathbf{a}}_\mathbf{z} \tag{1.4}$$

When the spatial dependence of various quantities are clear, the explicit variable dependency such as "(x, y, z)" is often dropped.

Vector phasors such as the magnetic field in (1.3) above can be represented in many different ways in the text depending on the context. Recalling that an underline always indicates a complex quantity and boldface indicates a vector quantity, the following are all valid representation of the magnetic field, $\underline{\mathbf{H}}$:

$\underline{\mathbf{H}}$ magnetic-field-intensity vector phasor consisting of three phasors (complex numbers), one for each spatial dimension;

$\underline{H}_y$ (complex) phasor representing the y-directed component of the magnetic field vector phasor;

$\mathbf{H}$ magnetic field vector at some instant in time that can be represented by three time-varying quantities, one for each of the three spatial dimensions;

H_y (real) y-directed component of the magnetic field vector at a given instant in time;

$|\underline{H}_y(x)|$ (real) peak magnitude of the phasor representing the y-directed component of the magnetic field vector phasor, expressed as a function of x;

$\Re(\underline{H}_y)$ (real) real part of the y-directed phasor of the magnetic field.

Citation Numbers References cited in this document are listed in the bibliography in the order in which they are encountered in the text. This is in keeping with IEEE style guidelines. In addition, as the references are introduced in the text, the primary author's last name is used to identify key references; this should help the reader familiar with the field follow the discussion without having to refer to the bibliography.

Chapter 2

Background Information

2.1 High-Frequency, High-Power Design Issues

Power conversion circuits that function at high frequencies and high power levels require magnetic components—both inductors and transformers—beyond the current state of the art. In high-power, low-frequency applications the magnetic core is assembled from a set of thin laminations of suitable metallic alloy with the lamination thickness determined by the conductivity of the alloy and the operating frequency. Such laminated structures reduce the eddy-current effects in the core by breaking the conduction path into many high-resistance paths; such designs are limited on the upper end of the frequency range by the practical minimum thickness of the laminations.

High-frequency magnetic devices, on the other hand, are typically designed using ferrite core materials with inherently low conductivity[5, 6, 7]. Due to the low conductivity it is possible to use relatively large blocks of ferrite while maintaining low eddy-current losses. The low saturation flux density of ferrite, however, means that a high-power core must be relatively large, and this requirement for large core size means that several of the assumptions made in the design of high-frequency devices may no longer hold true. In particular, the design of most ferrite-core devices assumes that the flux in the core is distributed relatively uniformly throughout the core cross-section and that the losses in the core are therefore relatively uniform. Also, the assumption that the eddy-current losses in the ferrite are small requires the core to be small relative to the skin depth of the material. Both these assumptions—uniform flux distribution and low eddy current loss—are challenged by the use of the large ferrite cores required in order to handle large amounts of power.

2.2 Ferrite Material Data: Datasheets and Applications

Much has been written on ferrites and their various material characteristics since they were first introduced in the middle of the century (see [2] for a thorough review of the subject). In the power electronics area alone, their loss properties have been studied extensively under different conditions of frequency, flux density, DC bias and wave shape[8, 9, 10, 11, 12, 13, 14, 15, 16, 17, 18]. Through the past decades experimenters have developed several generally accepted testing methods for characterizing ferrites[19, 20] for a variety of applications including recording media for information storage, microwave filter elements for high-frequency communications, as well as energy storage inductors and isolation transformers for switch-mode power supplies. These testing methods are detailed in international standards[21] and are used extensively by ferrite manufacturers for the creation of general use data sheets [22].

The data available in the manufacturers' catalogs are designed to help ferrite users in various design environments compare the performance of different materials when used in common applications. However, since these datasheets represent average characteristics of a given material, they are often of limited use for detailed design analysis. The designer—and sometimes the end user as well—often must perform additional measurements to augment those provided by the manufacturer. Such shortcomings of the available data on ferrites forms the basis for lively debate and disagreements between manufacturers and customers as to what data is actually needed and what the proper methods are for collecting and reporting the additional information.

One limitation of the existing ferrite core information springs from the fact that most of the available data are measured on relatively small toroidal cores[23, 24, 25, 26, 27]. This practice has all the advantages that usually accompany a *de facto* standard: it establishes a uniform base for comparisons under normal operating conditions; it provides a good means of checking for process variations from lot to lot; and it is simple to implement on a routine basis. All of these are advantages for the manufacturer and large-volume customers, but it is not clear that having all data reported from a single core size is appropriate for all applications.

There is little mention in the published data of the effects that core size and shape can have on the performance of the magnetic device. Larger cores can experience deviations in loss characteristics from those expected based on the databook information. In some cases the discrepancy is within the expected variation of losses to which all magnetics designers are accustomed, but it is also possible for some devices to have significantly higher losses

than those predicted based on the small-core measurements[18, 28].

If the manufacturers' databooks do not provide enough detailed information to predict the performance of cores that are significantly different from the standard cores on which the data are measured, then designers who are considering the use of ferrite for unusual applications have little to go on in assuring an acceptable design. Still, since so many variables influence the core losses—from temperature, flux density and frequency to such non-environmental effects as batch-to-batch material variations, surface grinding effects, geometry variations and even mechanical stresses—it is generally not possible for manufacturers to anticipate all of the required information needed to obtain reliable data that can be used for all conceivable device structures. This is particularly true for custom core shapes where the manufacturer has no way of predicting the shape or size of any given core. This situation would be greatly improved if manufacturers would provide actual measured characteristics for *all* of their standard cores. But even if this information were available, designers of custom cores would still face the same problems predicting device performance without actually building and testing the component.

It would be useful, therefore, to establish methods that designers could use to evaluate any core shape—be it custom or standard—with regards to dimensional effects. The three main causes of significant losses in a core that are related to the geometry are eddy currents in the core, flux crowding in non-uniform cross sections and near sharp interior corners, and dimensional resonances. These three issues are addressed in the literature as difficulties that must be avoided, but little discussion has focused on what to do when design requirements dictate the use of structures susceptible to them. There is a need then for basic engineering evaluations of how geometry, frequency, and material constants interact to change the effective values of permeability, core loss density and inductance.

Material Information vs. Design Information

Before considering the specifics of the three geometrical effects listed above, it is useful to pause and consider in a little more detail the relationship between magnetic device designers and the manufacturers of the magnetic cores and core material (which are not always the same). The introduction above focuses on what the core manufacturers do and do not supply to the magnetics designer; there is an implication in that discussion—one often stated explicitly by designers—that the manufacturers do not provide enough of or the right kind of information to the end user. This complaint places the responsibility for alerting designers of possible design problems squarely on the manufacturers' backs. There is, however, good reason to argue that the manufacturers cannot, ultimately, be held responsible for the inappropriate application of their materials.

It is impossible for manufacturers to anticipate all of the uses that their customers will find for their material, and therefore they must find a reasonable compromise in the information they present to the user. The material data reported by ferrite manufacturers provides the basic starting point for a viable design, but any problems related to the use of these materials in specific applications must be addressed by the designer as part of a careful analysis of the device.

Such a separation of material characteristics from device characteristics is very familiar in the power electronics design community in regards to many other design decisions. Take as one example the calculation of resistance in the windings of an inductor or transformer. In that case, wire manufacturers supply basic material data and wires in various gauges, but the application of the raw material to a given design is solely the responsibility of the designer. The parallel between the development of the design rules for such copper loss formulations on the one hand and the current topic of geometrical effects in cores on the other is considered in detail in the following section.

2.3 High-Frequency Effects in Windings

The push for higher and higher switching frequencies and power densities that occurred in the early 1980's revealed a troublesome issue in the design of magnetic components: as the switching frequency increased the actual resistance seen in transformers and inductors was much higher than predicted by simple resistance formulas for the conductor material. This increase in resistance was well known [29] to come from skin and proximity effects in the coils. Still, it took several years of effort—and the reevaluation of some fundamental work performed in previous decades—before a set of design rules were established that could help component engineers design efficient high-frequency power devices [30, 31, 32, 33, 3, 34, 35, 36, 37, 38].

Most of the tools developed in recent years for winding loss analysis use a one-dimensional field approximations to the actual three-dimensional magnetic fields in the winding space of the device. These tools allow designers to consider the effects that the arrangement of windings and the size of the conductors have on the losses in the device. Through such analyses, the frequency dependencies of the terminal resistance and leakage inductance have been well documented; it is becoming common practice for power supply designers to calculate these critical performance characteristics with acceptable accuracy.

Where the one-dimensional approximations for the field distributions in a given device break down, the use of numerical models such as finite element analysis is often useful for

design analysis. Both two-dimensional and three-dimensional models for various structures [39, 40, 41, 42, 43, 44] have proven useful for the analysis of high-frequency winding losses.

While the gains that have been made in the calculation of winding losses and inductance are quite useful, it should be noted that the determination of the conductor resistance itself is the simplest part of the derivation of these results. The resistivity of copper or aluminum is well known and its only significant variation from a design perspective is its dependence on temperature. What makes the calculation of the overall resistance of a winding difficult is not the determination of the material constants of the conductors but rather the way that the geometry of the actual transformer or inductor affects the measured resistance.

2.4 High-Frequency Effects in the Core

If we now return to looking at ferrites and consider the state of research into their use, we see that most of the effort has been aimed at characterizing the material properties themselves. Little has been said about how the design of the core affects the resulting performance. This lack of attention in the design community is understandable since there is usually little that the individual designer can do to change the shape or construction of the magnetic cores available for a design; this is traditionally the province of the core manufacturers alone.

Furthermore, the research community's strong focus on the measurement of basic material characterization reflects the underlying complexity of the ferrites themselves. Since magnetic ferrites are not simple materials, it takes considerable effort just to agree on what the standard test conditions for the material should be and how the results of such tests should be interpreted [45]. The fact that ferrites have a nonlinear B vs. H characteristic and that most of their material values are dependent on temperature, frequency, flux density and past history makes the measurement of the the material values alone a significant problem [46, 9, 47, 48, 49].

The ferrite user community then is faced with a situation where the evolution of new applications requires devices with performance characteristics well beyond those traditionally encountered, but neither the manufacturers nor the users have the information they need to analyze such devices. In particular, designers of magnetic devices for new applications often find that there is no commercially available core that suits their needs, and so they design a custom core based on assumptions that may or may not hold true. The manufacturers of these custom cores, on the other hand, may have no experience with (or may not even be informed about) the application these cores are intended to serve. In such a situation

the lack of useful and well tested design information can cost all involved significant time and money. If the magnetic device does not perform as expected there is little to inform the designer as to how the situation can be improved.

In order to improve this situation it is necessary to have a clear picture of what information exists concerning ferrite materials and the methods of testing them. It is also critical to understand the various loss mechanisms that are present in any ferrite structure and how core size or shape can influence these characteristics. Finally, previous efforts at modeling these dimensional losses either analytically or numerically must be reviewed to see where they apply in high-power high-frequency applications. This historical background is summarized in the following research review.

2.5 Review of Previous Research

2.5.1 Characterization of Ferrites

The literature concerning the application of magnetic ferrites includes both the theoretical modeling of the material as well as the actual measurement methods used to validate such models[1]. These efforts can be broken down roughly into characterizing:

- magnetic characteristics (permeability)
- loss performance (hysteresis models, conductivity, eddy-current models)
- electrical performance (dielectric constant, capacitance models)

Permeability and B-H Characterization Initial measurements of magnetic material properties in the later part of the last century and early part of this century[50, 51, 52, 53] characterized the B-H relationship for low amplitude excitations and relatively low frequencies. Later, the use of ferrites for radio frequency applications resulted in a variety of methods for measuring high-frequency material performance[54, 55, 56, 57, 58, 59, 60, 61, 62]. Finally, different studies have examined the various aspects of ferrite's large-amplitude, non-linear B-H loops from low frequency to high frequency[63, 64, 65, 66, 67, 8, 68, 69]. In all of the above studies, the determination of the fundamental material characteristics is the

[1] Often, of course, the measured effects are not completely predicted by the theoretical models. This is the origin, for example, of the term *residual loss*; it originally accounted for the measured losses left over after all the theoretical loss mechanisms were included.

main focus. Therefore, these researchers take considerable care to minimize or eliminate any possible geometrical effects that might confound the measurements. This material characterization work is well examined from the power electronics perspective in Gradzski's work [9]. Issues related to the effects that core size have on the loss characteristics are much more limited and more recent [70, 67, 28, 71].

Loss Characterization Another trail of research concentrates on techniques for measuring core losses under various excitation conditions. There are a variety of linear, impedance-based measurements for core loss, from the Wien bridge[52] and resonant method[54] to sophisticated network analyzer-based measurements such as presented by Gradzski[9]. For linear operating conditions, losses are measured with excitations that minimize the nonlinear core effects. The loss density values that result from such linear-operation (sinusoidal) loss measurements can be represented either as equivalent circuit elements or normalized impedances of various sorts. Therefore, these linear-model test results form the basis for most transformer and inductor design equations relating to core losses. As in the characterization of the B-H loop, the impedance tests require that the results are not a function of the core geometry but are rather applicable to all cores of a given material. In practice this means that the losses are generally measured on a small toroid where eddy-current losses are assumed to be negligible.

Since ferrites are nonlinear materials, significant effort has gone into modeling hysteretic phenomena. Jiles and Atherton's model [72] for the B-H loop response of ferrite has become somewhat of a standard in the field due to its apparent simplicity and its acceptance into a variety of SPICE modeling tools. While the Jiles-Atherton model can describe the hysteresis loop with only a small number of constants, actually deriving these constant from core loss measurements proves to be a relatively delicate task[73, 74]. Finally, the original Jiles-Atherton model is limited to static loops, and significant work has appeared to extend this model to dynamic excitation conditions as well[75, 76, 77, 78, 79, 80, 81]. Takach and Lauritzen provide a good summary of the various models for different magnetic materials and the range of applicability for each in [82].

In power electronics applications the excitation waveforms are seldom pure sinusoids, and so it is useful to measure core losses for other waveforms as well[18, 12, 83]. In such cases where the nonlinearities of ferrite are evident, the total core loss is measured without regard to modeling the material through an equivalent circuit impedance. When only the effective loss characteristics of the material are of interest, there are a number of curve-fit approximations that are useful in deriving empirical loss equations[84, 85, 86, 87, 88]. Finally, the losses of in a given core can be measured indirectly through a calorimetric measurement[89]. This method has the advantage that it does not depend on the accurate

measurement of voltage or current, but it suffers from problems of repeatability and it is difficult to separate one particular loss mechanism from the measured total loss.

Network Analyzer Core Testing Approach The measurement approach used in this dissertation is that used by Gradzski in [9]. This test set-up is based on the use of an impedance analyzer along with separate linear amplifiers and attenuators. It permits the rapid and accurate determination of the complex impedance of a given device under large signal sinusoidal excitation. Recent work by Zhang[17] has expanded on Gradzski's original set-up by improving the low-frequency and low-permeability performance of the test set-up.

The impedance analyzer core loss measurement approach requires a significant investment in equipment, but it allows for the accurate and rapid collection of measurement data for test samples. However, like all impedance-based measurement systems the impedance analyzer method is limited to linear models of the losses and inductance in the device under test. That is, since the device is characterized by a simple R-L linear circuit, there is no simple way to represent the nonlinearities of the device. A further drawback of the measurement is characteristic of all lumped-parameter measurement strategies: there is no direct way to separate the measured resistance into components related to the various types of losses that occur in ferrite. Specifically, when measuring a given core, all losses—hysteresis, eddy-current, residual, etc. —are included in the single measured resistance term.

The fact that all losses are lumped together in the laboratory measurement is usually addressed by designing the device under test such that only one loss mechanism dominates in any given test. The eddy current loss can be screened out by using cores that are small enough to essentially eliminate the eddy currents themselves. This is the usual approach, and most manufactures' data is reported from measurements on relatively small cores under the assumption that eddy current loss is small for those cores[2]. Such small cores also minimize the dimensional resonance effects in the core. Once these loss mechanisms are eliminated, the measured loss is the combination of hysteresis and residual losses; the combination of these two loss terms is often referred to simply as the *magnetic loss*.

2.5.2 Eddy-Current Losses

Ferrite magnetic material are characterized as having relatively high magnetic permeability (in the range of 2000 to 10,000 times that of free space), and medium levels of saturation flux density (on the order of 20% that of iron). While these magnetic characteristics of ferrite cannot compare with the much higher values found in magnetic metals, ferrites have

many advantages over metallic-core devices in high-frequency applications. Chief among these advantages is ferrite's low core losses, which result from the material's high electrical resistivity.

For small cores that are not significantly effected by eddy-current losses, the permeability bandwidth of the wound component approaches that of the permeability-bandwidth of the material. Figure 2.1 shows typical permeability curves for commercial MnZn ferrites; it illustrates that the intrinsic permeability bandwidth of most materials is on the order of several megahertz. This cutoff frequency is well above the operating frequencies presently common for high-power conversion circuits, and therefore the ferrite material itself has suitable bandwidth and core losses required in such circuits.

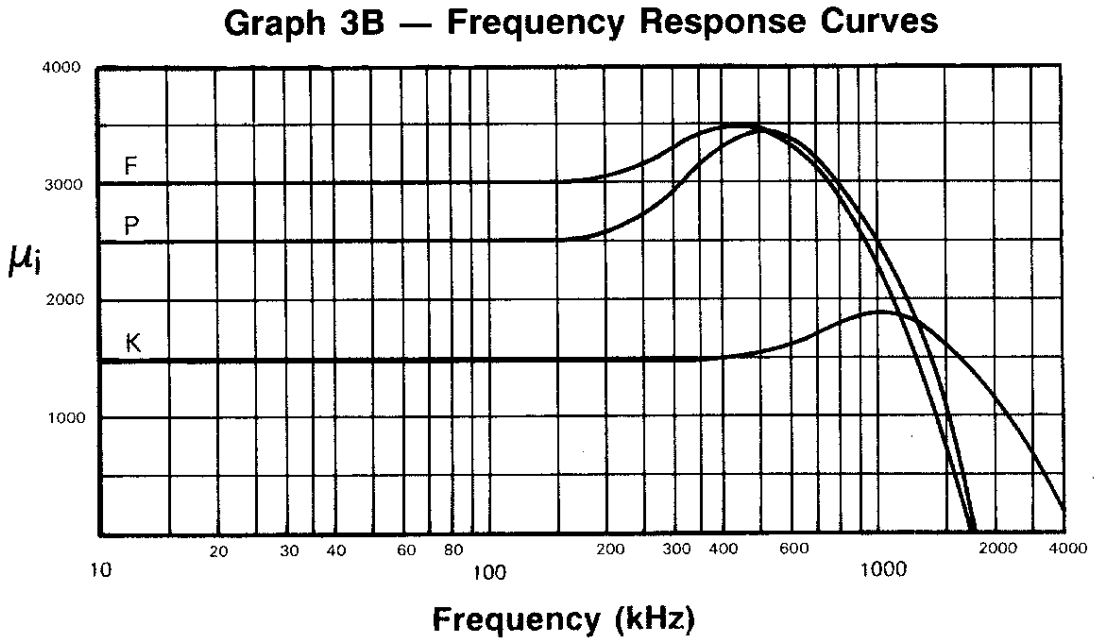

check

Figure 2.1: Typical permeability vs. frequency curves for MnZn ferrites. [Magnetics Inc. Catalog]

Since the conductivity of ferrite is usually assumed to be high enough to limit the flow of significant eddy currents in the core, standard formulas for eddy current losses assume the flux density in the core is essentially unchanged by the existence of eddy-currents[2, Eq. 2.46]. This is valid when the skin depth of the material is much greater than the cross-sectional dimension through which the core flux flows. The calculation of eddy current losses when this uniform flux density assumption is not valid requires the full solution of resultant field within the core. Such a solution is presented by Lammeraner and Štafl[90]

for conductive magnetic materials such as iron laminations and inductive heating targets; other modeling efforts such as those in [91, 92, 10] concentrate on eddy current losses in various soft magnetic materials. In general, however, the reaction flux generated by the induced eddy currents in ferrites is assumed to be so small that the overall flux in the core is not disturbed. Under such conditions, the standard formula for eddy-current loss is given in terms of the inducing flux, $\underline{B}$, the dimension of the core,d, the excitation frequency, f, and the material conductivity, σ, as,

$$p_{eddy} = \frac{(\pi \underline{B} f d)^2 \sigma}{\beta} \tag{2.1}$$

where the constant β accounts for the shape of the core cross-section. Standard values of β are:

- $\beta = 6$ for a thin lamination
- $\beta = 16$ for a cylinder
- $\beta = 20$ for a sphere

The dimension d in (2.1) is the lamination thickness in the lamination case; for the cylindrical and spherical cases, d is the diameter of the structure. Since eddy current losses are usually not a significant portion of the overall core loss, the effective cross-sectional area of the core is often used in (2.1). For a cylindrical cross-section, the area is given as $A_{cyl} = \pi d^2/4$. Rewriting (2.1) in terms of this cross-sectional area, we can then substitute the effective core cross-sectional area for the cylindrical area and use $\beta = 16$ to yield

$$\begin{aligned} p_{eddy} &= \frac{\sigma \pi \underline{B}^2 f^2 4 (\frac{\pi d^2}{4})}{\beta} \\ &= \frac{\sigma \pi \underline{B}^2 f^2 A}{4} \qquad (2.2) \\ A &= \begin{cases} A_{cyl} & \text{for cylinder} \\ A_e & \text{for other cores (E cores, etc.)} \end{cases} \qquad (2.3) \end{aligned}$$

The values of loss density predicted for cores of various sizes using the standard eddy-current loss formula of (2.1) are plotted in Figure 2.2. The plots in Figure 2.2 show first that the eddy current loss density for small cores is well below the overall loss density for the material given in the data book. However, as the size of the core increases, the eddy current loss density can become a significant fraction of the predicted loss density.

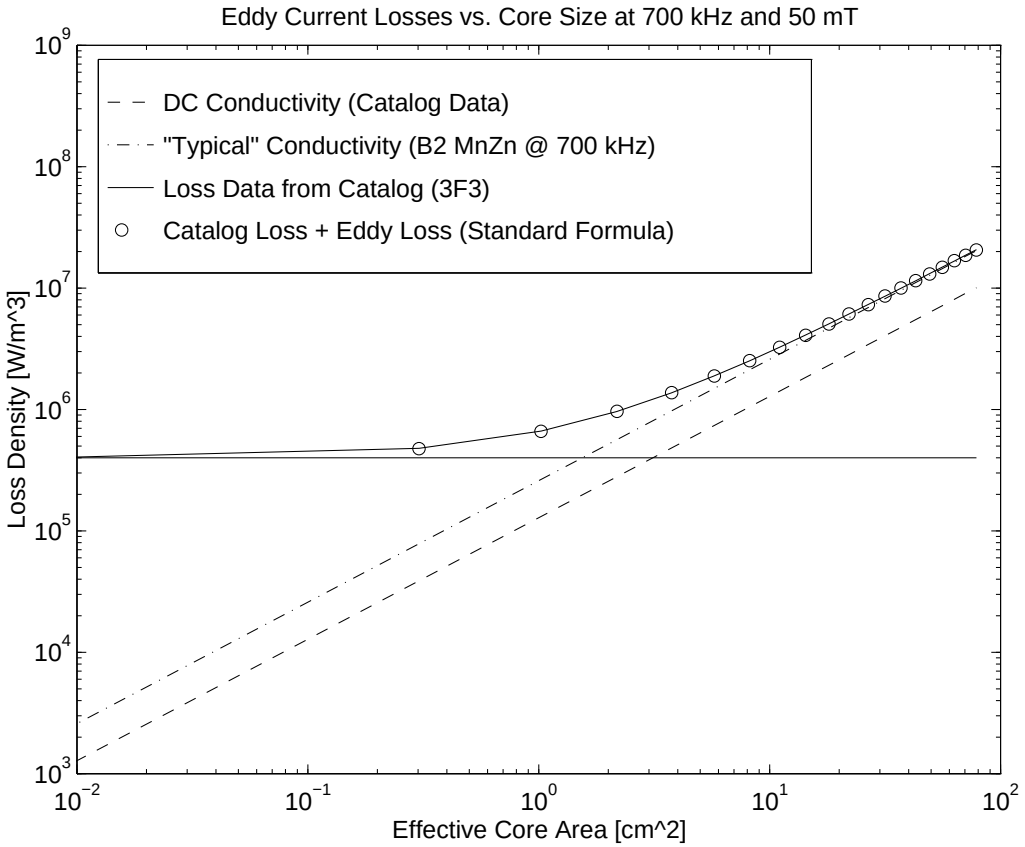

Figure 2.2: Eddy current loss density vs. core cross-sectional area based on (2.3) for several values of core conductivity. The flux density and frequency are 0.1 T and 500 kHz respectively.

While the above discussion of eddy current losses starts from the assumption that the overall flux distribution within the core is not changed by the existence of the eddy currents, it is of use only for relatively small cores at relatively low frequencies. The use of cores in higher frequencies ranges—where the flux distribution is significantly effected by the eddy currents—is generally assumed to be unwise, and therefore the examination of such effects in ferrites has received little attention in the literature. What measurements have been presented focus on characterizing the material resistivity[93, 94], the relative importance of macroscopic and microscopic eddy currents[28] or on the relative importance of the electrical losses due to eddy currents and the dielectric losses due to the high dielectric constant[95]. This later issue is examined in more detail in the following discussion of dimensional resonance losses.

2.5.3 Dimensional Resonance Losses

As illustrated above, the high resistivity of ferrite cores is extremely beneficial from an eddy current perspective since it can often allow for the use of relatively high frequency excitation without significant induced currents. However, the same grain structure that makes ferrite highly resistive also results in an extremely high value of effective permittivity or dielectric constant. This combination of high dielectric constant, high permeability, and finite resistivity in ferrite gives rise to the concern over geometrical—or dimensional—resonances. In such a material, the electromagnetic wavelength is shortened considerably; for ferrites, the wavelength at 500 kHz can be as low as a few centimeters. This short electromagnetic wavelength means that it is possible to establish standing waves within the ferrite material, and these resonant electromagnetic waves make the device ineffective as a transformer or inductor.

This issue is one that has been mentioned often[2, 18, 1, 96] and investigated in detail only rarely. The most complete examination of dimensional resonance appeared soon after the introduction of commercially viable ferrites in the late 1940's in a paper by Brockman, Dowling and Steneck published in 1950[97]. In [97], Brockman, et al. present a thorough analysis of the dimensional resonance problem in an infinite slab of material based only on the assumption of a simple medium and sinusoidal excitation. The results they obtain form the basis for all other extant information on the subject, and their conclusions, likewise, have informed most of the subsequent work. Specifically, Brockman, et al. concluded that MnZn ferrites are problematic for large-core applications in the low MHz range. Almost 40 years later, Snelling restated this conclusion[2, p. 146]:

> Although dimensional resonance could have a serious effect on transformer and inductor performance, in practice it rarely does so. At higher frequencies

> smaller cores are normally used and at frequencies above a few MHz it may be preferable to change over to nickel zinc ferrite cores to avoid the ferromagnetic resonance dispersion that occurs in manganese zinc ferrites at these frequencies. These two reasons tend to make the avoidance of dimensional resonance automatic. *Therefore it is in the design of devices requiring large manganese zinc ferrite cores at frequencies between 100 kHz and 5 MHz that the possibility of dimensional resonance should be checked.*[2]

The large MnZn-cored structures described by Snelling are becoming realistic design options for some high-power applications as illustrated above by the example of the inductively coupled battery charger. The continued improvement in semiconductor devices, the development of new topologies for high-power conversion circuits, and the continuing need to reduce the size of power processing equipment has pushed switching frequencies up while at the same time requiring large devices to handle the additional power. In other words, the assumption that high-frequency effects such as dimensional resonance and skin effect are not significant in ferrite devices is called into question as the size of high-frequency magnetics continues to grow. Tung, et al. in [95] state that dielectric losses dominate for freqencies between 1.1 and 3 MHz while losses due to eddy currents dominate for frequencies from three to ten megahertz. This interaction between different loss mechanisms with different mechanisms being dominant in different frequency ranges is further complicated by the overall size of the core as is demonstrated in Chapters 4 and 5.

2.5.4 Finite Element Modeling

As mentioned above, the use of finite element numerical models has become relatively routine in the analysis winding losses in high-frequency devices. The same cannot be said, however, of efforts to model the losses in the ferrite cores themselves. Research efforts in core loss simulation have concentrated on mapping the flux distribution within the core [98, 99], various methods of combining analytical and numerical techniques [100, 101, 102, 103], or on the combination of magnetic and thermal effects within the core [104, 105, 106]. In addition, since a key benefit of the numerical modeling process is the insight it provides to the way that flux and loss densities distribute within the device, there has been a significant amount of work presented related to the visualization and data exchange issues [107, 108, 109, 110, 111, 112]. While the FEA tools used in this dissertation use linear models for sinusoidal excitations, significant research has also been presented on the use of nonlinear hysteretic models and/or transient solution techniques [113, 114, 115, 116]. Finally, Logcais, et al. [117] present a comparison between the use of 2D and 3D field

[2] Emphasis added

solvers as one example of the tradeoffs that must be considered in modeling a particular structure.

Chapter 3

Characterization of Ferrite Materials

In Chapter 5 we use commercially available numerical field modeling software to examine the effects of core geometry on the losses and magnetic performance of various structures. Before proceeding with that analysis, however, it is important to establish clearly the mathematical and material bases for such solutions. This chapter reviews the various loss mechanisms in ferrites and simple methods for modeling them analytically. Since we use linear solvers in the numerical modeling process, the review of loss mechanisms is followed in Section 3.4 by a discussion of the field equations evaluated in the numerical solvers and a review of basic field relations for simple media.

3.1 Description of Loss Mechanisms in Ferrites

Core losses in ferrites are generally divided into hysteresis losses, eddy current losses and residual losses. For power electronics applications which are under large-amplitude and high-frequency operating conditions, the hysteresis loss is mainly caused by the irreversible rotation of magnetization [72] and depends only on the chemical composition, microscopic structure, and internal stresses of the core material. The eddy current loss is due to the current induced in the core under the influence of a time varying magnetic flux. It is determined by the conductivity of the core material and the geometry of the cross-section through which the flux flows. The residual loss is generated by the power dissipation resulting from the reversible domain wall damping[118] and the reversible rotation of domains[119].

In addition to these losses, there is the additional loss introduced by dimensional resonance, which is often neglected. However, as illustrated above, dimensional resonance loss—like

eddy current loss—must at least be evaluated for large cores. The losses associated with dimensional resonance arise due to an increase in the induced eddy currents as well as from an increase in magnetic losses; both of these are due to the non-uniform flux distribution established as the core approaches resonance. This combination of loss mechanisms in the resonant condition makes the independent evaluation of dimensional resonance losses and eddy current losses difficult.

The various loss components listed above can be grouped into two primary groups: losses due to magnetic processes in the material and losses due to electrical processes. The hysteresis losses and residual losses are essentially magnetic material properties, and therefore are often lumped together into a single *magnetic loss* term. The eddy current losses are electrical in nature and are included in the *electrical loss* term. The dimensional resonance effects manifest themselves in a rather more complicated fashion. The large-amplitude flux that can occur under resonant conditions results in increased magnetic losses in the core. In addition, these same high flux levels induce additional eddy currents in the core and thereby result in increased electrical losses as well. Dimensional resonance,therefore, results in changes in the magnetic and electrical losses in the core. Like the eddy current losses, the dimensional resonance effects are dependent on the size of the core, and therefore when the core size is large the total losses in the core are greater than the losses predicted based solely on the material characteristics. The following sections discuss the magnetic and electrical loss mechanisms and methods used for measuring the material characteristics of two sample ferrites.

3.2 Magnetic Losses

The characteristic relationship between the magnetic field, H, and the magnetic flux density, B, in a ferromagnetic material such as ferrite has been explored in great depth in previous work. Figure 3.1 shows a standard representation of the B–H hysteresis loop. This loop is characterized by an initial magnetization curve leading from the origin to saturation and by the upper and lower paths traced out by the B–H relationship as the excitation is varied in a cyclic manner. For our purposes here the most important aspects of this loop to consider are the differences between the initial permeability, μ_i, and the amplitude permeability, μ_a. The former corresponds to the slope of a minor loop around the origin when the excitation is small and the latter corresponds to the slope of a larger minor loop that exists for larger excitation levels. The slopes of these loops are taken as the slope of a line connecting the extreme tips of the loops.

For power applications we are usually concerned with the amplitude permeability rather

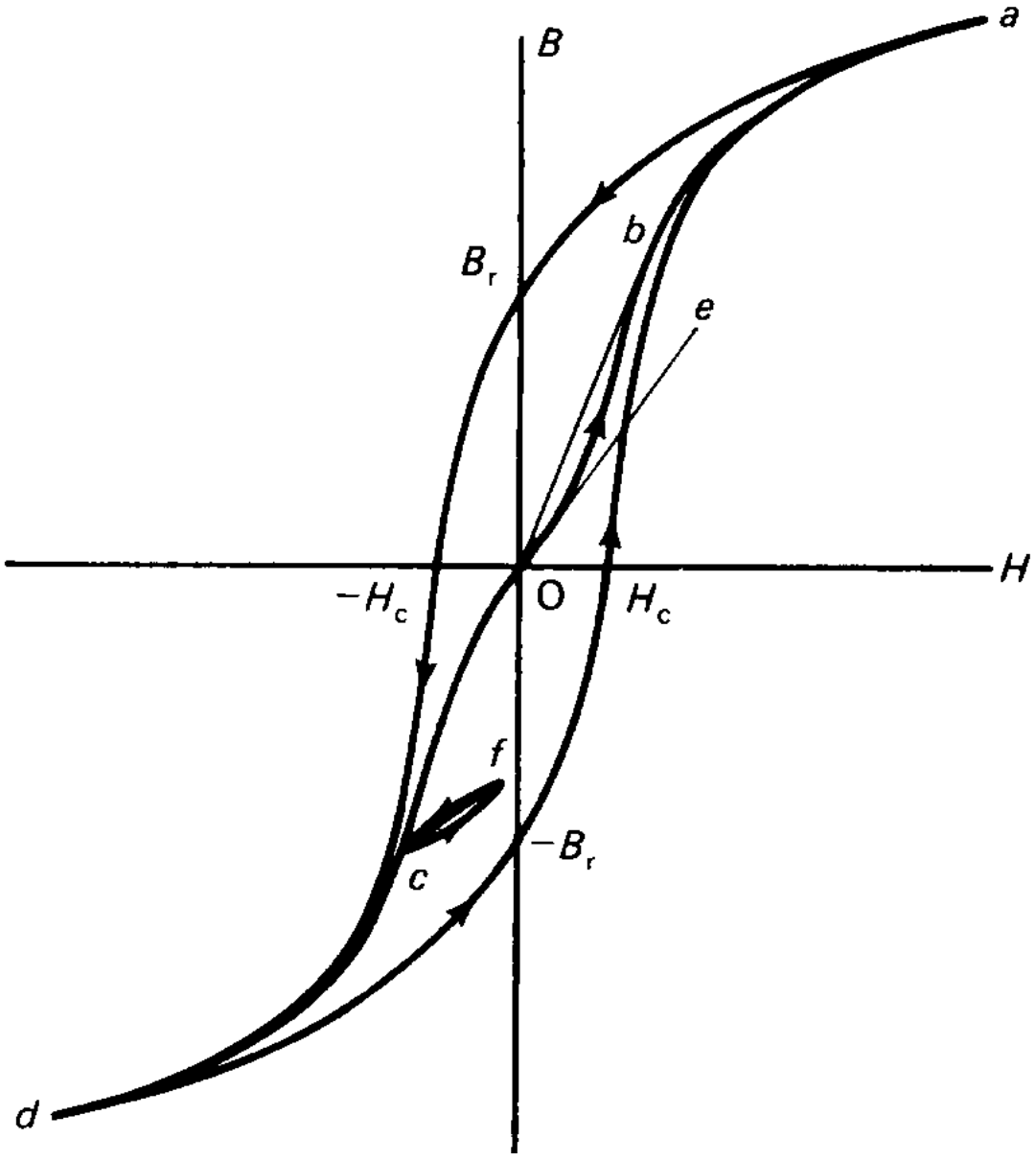

Figure 3.1: Standard B-H Loop for ferrite [22, MMPA]

than the initial permeability, while most manufacturer's data reports mainly the initial permeability characteristics. Typically, the amplitude permeability is reported at one given frequency and temperature such as shown in Figure 3.2. Here we see that the permeability

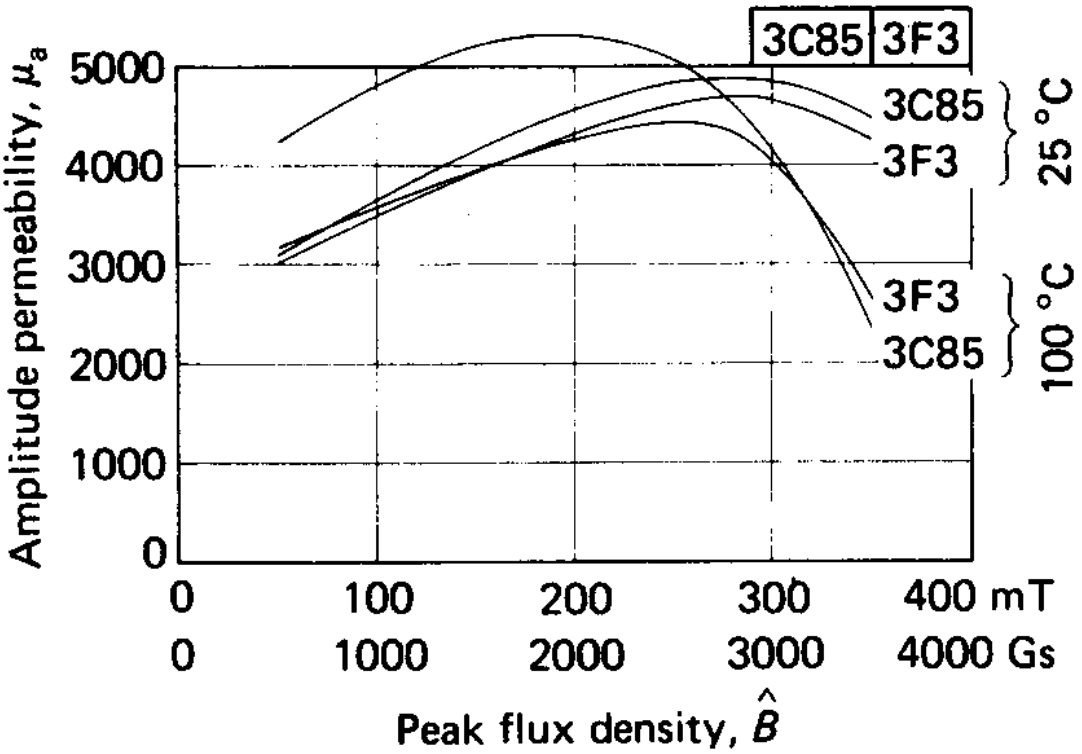

Figure 3.2: Plot of the amplitude permeability from a data book.[2, Snelling]

increases from its initial value and reaches a peak before decreasing to a low value as the core material saturates.

3.2.1 Representing Magnetic Losses Using Complex Permeability

The calculation of core losses using the numerical solvers discussed in Chapter 5 is based on an assumption that the material can be modeled using a complex permeability, $\underline{\mu} = \mu' - j\mu''$, that represents both the energy storage and dissipation aspects of the core. This concept of complex permeability assumes that the field strength, flux, and e.m.f. in the core are all sinusoidal. In other words, the use of complex permeability models immediately assumes the core material is linear. This assumption and its implications are discussed further in

Chapter 5; it is sufficient at this point to describe how this complex permeability relates to the familiar B–H hysteresis loop.

Starting from the assumption that the ferrite material can be considered linear for a given excitation level, the hysteresis loop may be approximated by an ellipse in the B–H plane as shown in Figure 3.3. Clearly the assumption that the ferrite is linear means that this approximation cannot predict or accommodate the saturation of the core, but it is often useful for predicting losses for power applications. The elliptical representation of the hysteresis loop is based on the fact that the losses in the core can be represented as a resistive element in combination with an energy storage inductive element. That is, an ideal inductive element with no loss has an inductance, L, defined in terms of the flux linkage per ampere of current, I,

$$L = \frac{N\Phi}{I} \tag{3.1}$$

where Φ is the flux in the core and N is the number of turns.

For a simple toroidal core of cross-section, A_e, and path length,ℓ_e, this can be written as,

$$L = \frac{\mu_o \mu_{r_s} N^2 A_e}{\ell_e} = L_o \mu_{r_s} \tag{3.2}$$

$$L_o = \frac{\mu_o N^2 A_e}{\ell_e} \tag{3.3}$$

where L_o is the "air core" inductance and μ_{r_s} is the relative series permeability of the core. Since any actual inductor under sinusoidal excitation is subject to some losses, it will not present a pure reactance in the circuit; there will be a resistive element included as well. If this resistive element is assumed to be in series with the reactance then the impedance of the device is given by the series combination of a resistance R_s and and an inductance L_s as,

$$\underline{Z} = j\omega L_s + R_s = j\omega L_o(\mu'_{r_s} - j\mu''_{r_s}) \tag{3.4}$$

In the above equation, μ'_{r_s} is the real part of a series complex relative permeability and represents the energy storage term; μ''_{r_s} is the imaginary part of the complex relative permeability and represents the losses in the component. In terms of the measured inductance and resistance values they are given by,

$$\mu'_{r_s} = \frac{L_s}{L_o} = \frac{L_s \ell_e}{\mu_o N^2 A_e} \tag{3.5}$$

$$\mu''_{r_s} = \frac{R_s}{\omega L_o} = \frac{R_s \ell_e}{\omega \mu_o N^2 A_e} \tag{3.6}$$

Since the complex permeability contains a term for the magnetic losses as well as the energy storage in the material, it is often useful to consider the ratio between these two terms as a

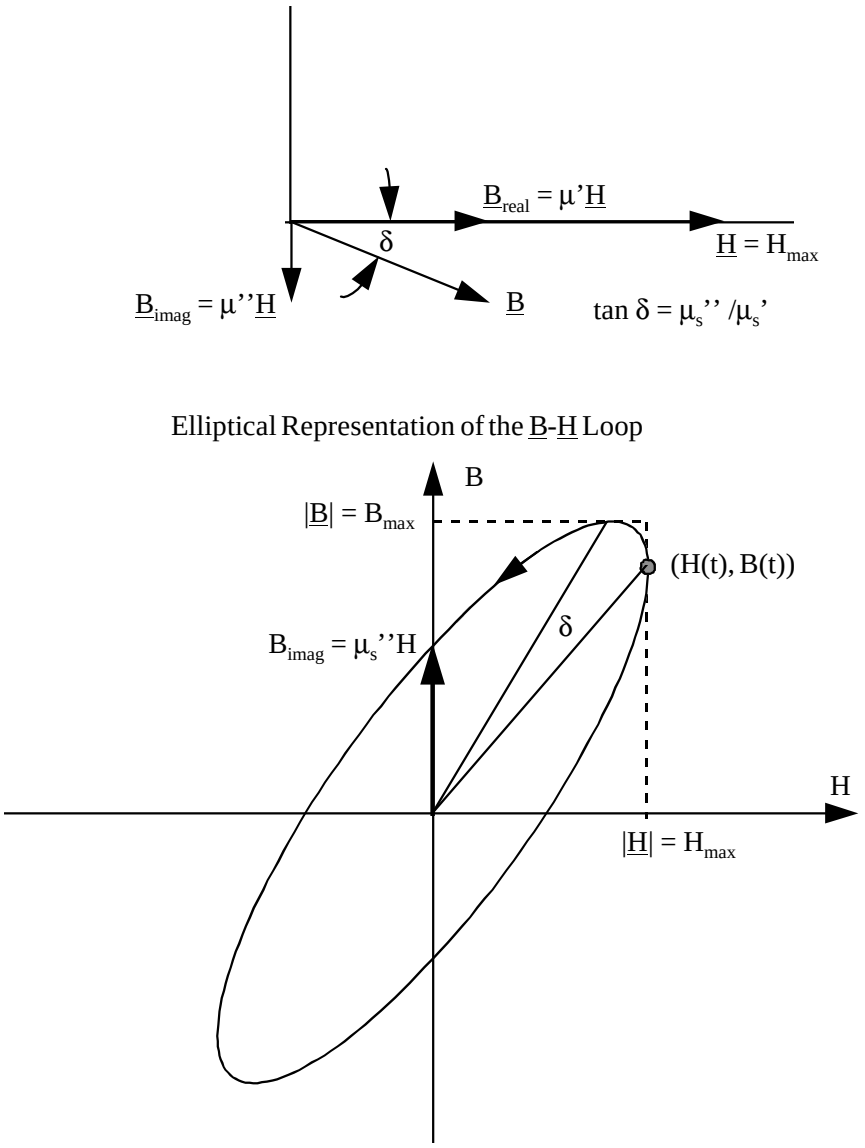

Figure 3.3: Elliptical B–H Loop. (a) Phasor relationship between B and H for a complex permeability material. (b) Elliptical representation of the B vs. H relationship.

measure of the quality of the material. Figure 3.3(a) shows the phasor relationship between the $\underline{H}$ field and the two components of the $\underline{B}$ field that result for a given lossy magnetic material. Here the in-phase B-field, $\underline{B}_{real} = \mu'_s \underline{H}$, represents the inductive energy storage field. The lossy component of the B-field, $\underline{B}_{imag}$, is directed in the same direction in space, but is delayed by a phase angle of 90 deg. The resulting B-field phasor forms an angle δ with the H-field phasor, and this angle is usually referred to as the loss angle of the material. The loss angle is given by[1]

$$\delta_m = \tan^{-1} \frac{\mu''_s}{\mu'_s} = \tan^{-1} \frac{\mu''_{r_s}}{\mu'_{r_s}} \tag{3.7}$$

Similarly, a measure of the losses in the material is given by the value of this angle which is usually referred to in terms of its tangent[2],

$$\tan \delta_m = \frac{\mu''_{r_s}}{\mu'_{r_s}} \tag{3.8}$$

3.2.2 Characteristics of the Elliptical Model of the B-H loop

Returning now to the elliptical representation of the hysteresis loop, we can relate the real and imaginary parts of the complex permeability to various characteristics of the ellipse. First, since the flux density phasor, $\underline{B}$, is given in terms of a component in phase with the exciting field, $\underline{B}_{real}$, as well as a component that lags the exciting field by 90 degrees, $\underline{B}_{imag}$, the value of B at the point when H is zero must correspond to the magnitude of $\underline{B}_{imag}$. Therefore, the imaginary component of the permeability is given as the ratio of the value of B at $H = 0$ to the value of the excitation field phasor, $\underline{H} = H_m$:

$$\begin{aligned} \mu''_s &= \frac{B_{H=0}}{H_m} \\ &= \underline{B}_{imag}/\underline{H} \end{aligned} \tag{3.9}$$

[1]The permeability and permittivity of a material is usually given in terms or its value relative to that of free space. Unless otherwise noted, the use of the terms permeability and permittivity in this document refer to the *relative* values of these constants. In particular, when the free space constants μ_o and ϵ_o are understood then the r subscript on the dielectric and magnetic constants will often be suppressed.

[2]This is in keeping with the terminology for computing losses in reactive components in general where the loss tangent is related directly to the Q of the element. An advantage of using the loss tangent is that the total losses in a device can be obtained by simply adding the loss tangents due to various loss mechanisms. See [2, Section 5.7.6] for a good example of how to combine different loss tangents for a given device.

Furthermore[3], the real component of $\underline{B}$ can be written in terms of the $\underline{H}$ field phasor,

$$\begin{aligned} \underline{B}_{real} &= \mu' \underline{H} \\ &= \sqrt{\underline{B}^2 - \underline{B}_{imag}^2} \end{aligned}$$

If the complex permeability is taken as a material characteristic—as opposed to a core characteristic—then the above relationships are true at every point within a given device. The exact values of the complex permeability at these various locations within the core, however, are a function of the local value of H. Therefore the flux density amplitude and phase angle will vary within the core to the extent that the H-field varies. The total flux that links a given cross-section of the core at any given time, then, is the integral of the flux density at each point in the core cross-section. As shown in Chapter 5, the interior of a large ferrite core is often shielded from the exciting H field due to eddy-currents, and this shielding effect reduces the total flux linkage in the core. In addition, the interior H field can be increased in cases of dimensional resonance and this changes the net flux in the core as well.

In the discussion of core losses in ferrites there are many different physical mechanisms to consider, however the microscopic detail of these loss mechanisms are usually not of interest in practical designs. For the present discussion, we make the following assumptions concerning the behavior of ferrites from a bulk-material perspective:

1. the *hysteresis loss* component is linearly dependent on frequency.
2. any increase in loss above the predicted linear frequency dependence is attributed to *residual loss* provided the core is small enough to minimize any geometric losses (eddy currents and dimensional resonance).
3. losses caused by eddy-currents and dimensional resonance effects cannot be separated in the laboratory; the ratio of the measured losses for a given core to the losses predicted based on material constants alone is represented through a single *geometric loss constant*.

The sum total of the hysteresis loss and residual losses is often termed the *magnetic loss*—to

[3]Note that while the elliptical representation of the B-H relationship is similar in many respects to the actual hysteresis loop, the axis intercepts have nothing to do with the more familiar axis intercepts identified with the B-H loop. For example, the B-axis intercept is not the same as the remnant flux in the material and the H-axis intercept is not the material coercivity. The ellipse is meant to represent the losses for any given excitation level whereas the coercivity and remnant flux are characteristics of the overall material saturation B-H characteristic.

distinguish it from the conduction losses caused by eddy-currents and dielectric effects—and we shall use that terminology here as well.

3.3 Electrical Losses

The previous section presented concepts of complex permeability as they are often used in modeling ferrite core losses. This section presents a completely analogous exercise for the electrical losses in the core based on the complex permittivity.

3.3.1 Representing Dielectric Losses Using Complex Permittivity

As mentioned above, ferrites have an extremely high relative dielectric constant below approximately 1 MHz and a conductivity that is small relative to metals but much larger than that of a good insulator. We can model such a dielectric material at any given frequency as a simple lossy capacitor. However, since ferrite is composed of highly conductive grains separated from each other by low conductivity grain boundaries, the apparent dielectric constant and conductivity of ferrite have a relaxation characteristic as a function of frequency. In this case, a single lossy capacitor model can be replaced with a series combination of two parallel $R-C$ stages such as that shown in the top part of Fig. 3.4[48]. This combination of $R-C$ stages models the grain and the grain boundary of the ferrite using frequency independent circuit elements. The dielectric constant in both the grain and the grain boundary are essentially equal, however the respective capacitances, C_g and C_b are significantly different due to the short length of the grain boundary. The conductivities of the grain and grain boundary are different by many orders of magnitude.

The combination of the two R-C stages in Figure 3.4 is useful for curve-fitting a measured frequency response to a set of frequency independent resistance and capacitance values. However, once the frequency response of the apparent conductivity and dielectric constant of the material is known, it is often convenient to represent the measured impedance of the device using a simple $R-C$ circuit with frequency dependent resistance and capacitance values as shown in the lower portion of Figure 3.4. This frequency-dependent-element circuit corresponds directly to the measured impedance values for a given piece of material as it is measured in the lab. From ideal parallel plate capacitor equations we can write the capacitance and admittance in terms of the sample cross-sectional area, A_c, and the

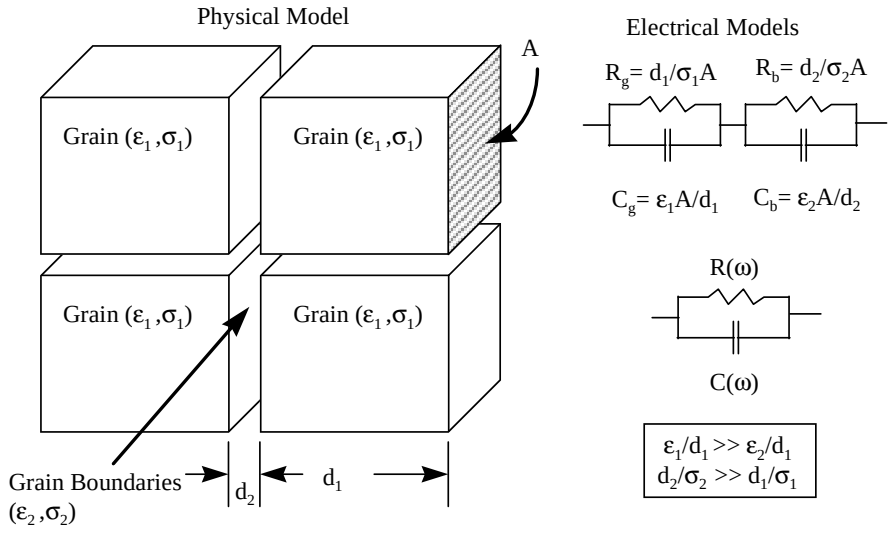

Figure 3.4: Models of the capacitive nature of ferrite materials. (a) the simplified grain structure of the ferrite, (b) a two-stage R–C circuit that models the frequency relaxation of the permittivity and conductivity as well as a frequency-dependent-element R–C network that corresponds to the measured admittance values.

thickness, d_c, as

$$C = \frac{\epsilon A_c}{d_c} \tag{3.10}$$

$$G = \frac{\sigma A_c}{d_c} \tag{3.11}$$

As in the inductor case, we can combine the reactive and resistive elements into a single complex element.

$$\underline{Y} = j\omega C_p + G_p = j\omega C_o(\epsilon'_{r_p} - j\epsilon''_{r_p}) \tag{3.12}$$

$$C_o = \frac{\epsilon_o A_c}{d_c} \tag{3.13}$$

where $\underline{Y}$ is the admittance of the capacitor and $\underline{\epsilon}_r = \epsilon'_{r_p} - j\epsilon''_{r_p}$ is the complex relative dielectric constant, the components of which are given as

$$\epsilon'_{r_p} = \frac{C_p}{C_o} = \frac{C_p d_c}{\epsilon_o A_c} \tag{3.14}$$

$$\epsilon''_{r_p} = \frac{G_p}{\omega C_o} = \frac{G_p d_c}{\omega \epsilon_o A_c} = \frac{\sigma}{\omega \epsilon_o} \tag{3.15}$$

The complex permittivity describes a relationship between the electric field, E, and the electric flux density, D, that is analogous to the elliptical B-H loop shown in Figure 3.3. Figure 3.5 shows the electrical characteristics of a lossy material as an equivalent D–E loop. The real part of the complex permittivity, ϵ'_{r_p}, represents the electrical energy storage in the dielectric material and the imaginary part, ϵ''_{r_p}, represents the conduction losses. This complex permittivity notation is standard for lossy dielectrics of all sorts. As in the lossy magnetic material case, the loss tangent is defined based on the ratio of the loss component to the energy storage component,

$$\tan\delta_e = \frac{\epsilon''_p}{\epsilon'_p} = \frac{\sigma}{\omega \epsilon'_p \epsilon_o} \tag{3.16}$$

Figure 3.5 also shows the phasor relationship between the electric field and the current density, $\underline{J}$. The imaginary portion of the complex permittivity adds in phase with the static conduction current; the fact that the conduction current is composed of both a static and dynamic component leads to the definition of an effective ac-conductivity that accounts for both loss components. This relationship between the electrical conductivity and the loss component of the complex dielectric constant is explored in greater detail in Section 3.4.2 below.

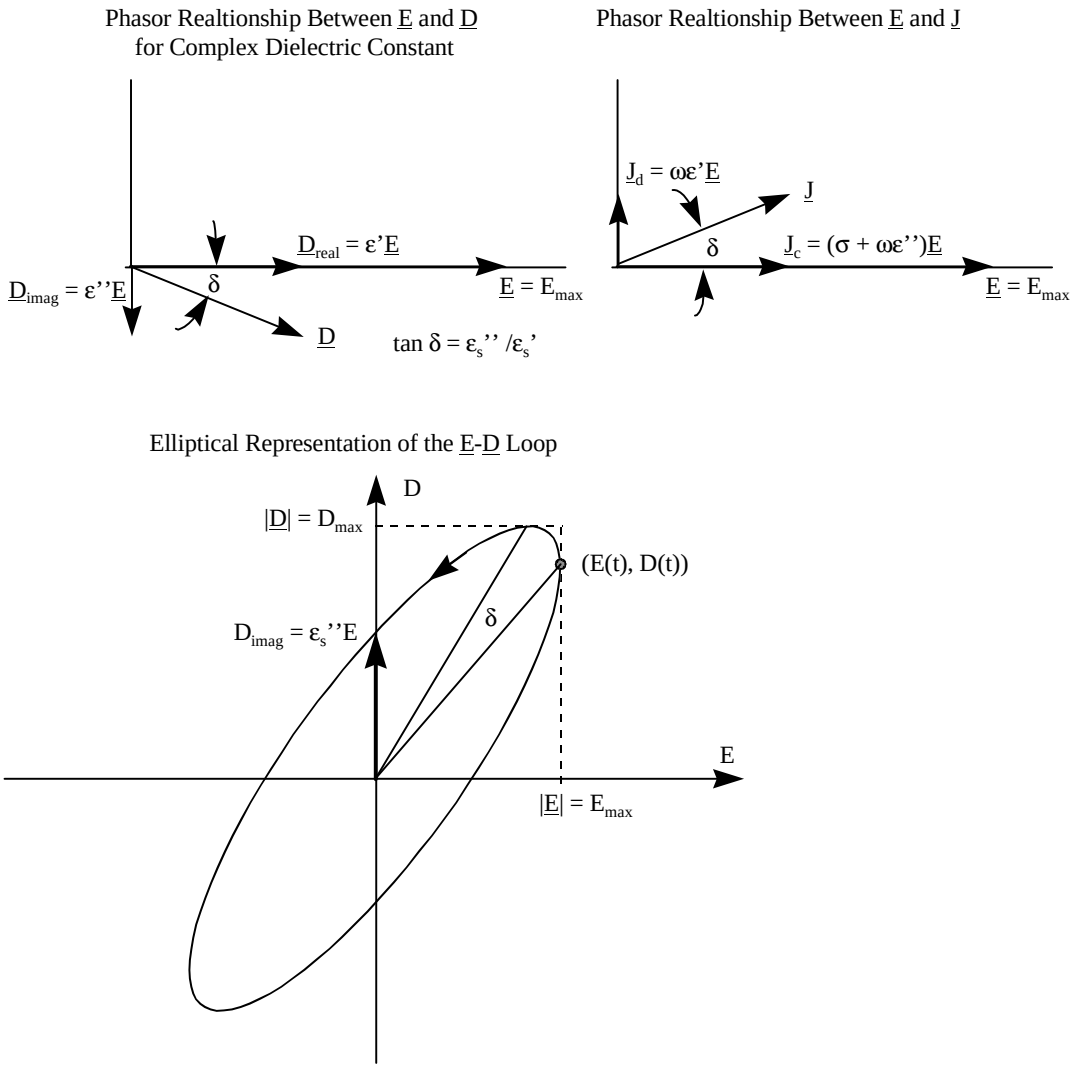

Figure 3.5: Elliptical D–E Loop. (a) Phasor relationship between D and E for a complex permittivity material. (b) Phasor relationship between the E and J vectors, (c) Elliptical representation of the D vs. E relationship.

3.4 Field Equations in Ferrite Materials

The previous sections describe the use of complex material characteristics to represent the losses in magnetic and dielectric materials from a circuit-element perspective. This section reviews the fundamental field relationships that can be used to model ferrite as a linear material. The goal in this discussion is to arrive at field relationships for the various loss mechanisms in the material in terms of the complex material values. Such loss relationships are necessary in order to calculate the apparent resistance or inductance of a device based on the solution for the field distribution within the geometry as provided by either a closed-form analytical solution or a numerical solver. This discussion presents relevant excerpts of the the development usually presented in fields textbooks [120, 121, 122, 123, 124]. The particular focus here however is the inclusion both complex permittivity and complex permeability in the energy and loss equations which is a detail that is often left out of standard field relationships.

3.4.1 General Loss Equations in Simple Media

Maxwell's equations relating the electric and magnetic fields at any point in a given medium are written in their most general forms as,

$$\nabla \times \mathbf{E} = -\frac{\partial \mathbf{B}}{\partial t} \tag{3.17}$$

$$\nabla \times \mathbf{H} = \mathbf{J}_c + \frac{\partial \mathbf{D}}{\partial t} = \mathbf{J}_c + \mathbf{J}_d = \mathbf{J}_{total} \tag{3.18}$$

$$\nabla \cdot \mathbf{B} = 0 \tag{3.19}$$

$$\nabla \cdot \mathbf{D} = \rho \tag{3.20}$$

While these relations can in theory be solved directly using a time-transient field solution that computes the time derivatives at each point in the simulation, such a solution is usually too cumbersome and resource intensive for general use. In addition, such general solvers do not easily allow for the accurate calculation of hysteretic magnetic losses. For these reasons we concentrate on solvers that apply to a more restrictive set of problems.

Since the field solvers used in this work are based on sinusoidal excitation conditions, we can replace the time derivatives $j\omega$ terms and write the field relationships as,

$$\nabla \times \underline{\mathbf{E}} = -j\omega\mu\underline{\mathbf{H}} \tag{3.21}$$

$$\nabla \times \underline{\mathbf{H}} = \sigma\underline{\mathbf{E}} + j\omega\epsilon\underline{\mathbf{E}} \tag{3.22}$$

$$\nabla \cdot \underline{\mathbf{H}} = 0 \tag{3.23}$$

$$\nabla \cdot \underline{\mathbf{E}} = 0 \tag{3.24}$$

where σ, $\underline{\mu}$, and $\underline{\epsilon}$ represent the material constants of the medium. For ferrites, these material constants are generally functions of frequency and temperature as well as field amplitude and/or direction.

While the FEA simulator used here can accommodate simple materials or linear materials with anisotropy, we neglect the anisotropy of the ferrite and restrict the material constants in (3.22)–(3.24) to linear, isotropic media. As mentioned in Chapter 1, a chief drawback of using this linear material assumption is that we must always check the results of such simulations to be certain that the nonlinear and inhomogeneous nature of ferrite—which is not modeled—does not have a significant impact on the results. Making such a verification is not always a simple or straightforward task. In most cases, it is a simple matter to check that the flux density levels are below the saturation flux level, but evaluating the effects of inhomogeneous core permeability is more difficult.

In modeling transformers and inductors, both the energy storage characteristics of the device as well as the overall losses that exist in the structure are of concern. These different aspects are considered separately in the following section.

3.4.2 Energy Storage and Power Loss Equations

In order to examine the energy stored and dissipated in a region of ferrite material, we start with the statement of Poynting's theorem for power flow through a closed surface, S, that surrounds a given volume, V,

$$-\oint_S (\mathbf{E} \times \mathbf{H}) \cdot d\mathbf{S} = \int_V \left(\mathbf{E} \cdot \mathbf{J} + \mathbf{E} \cdot \frac{\partial \mathbf{D}}{\partial t} + \mathbf{H} \cdot \frac{\partial \mathbf{B}}{\partial t} \right) dV \tag{3.25}$$

While (3.25) is general and applies to any medium, it can be recast for use in linear, time-invariant materials as,

$$-\oint_S (\mathbf{E} \times \mathbf{H}) \cdot d\mathbf{S} = \int_V \left\{ \mathbf{E} \cdot \mathbf{J} + \frac{\epsilon}{2} \frac{\partial}{\partial t} (\mathbf{E} \cdot \mathbf{E}) + \frac{\mu}{2} \frac{\partial}{\partial t} (\mathbf{H} \cdot \mathbf{H}) \right\} dV \tag{3.26}$$

The left hand side of the equation represents the complex power flowing out of the volume bounded by S while the three integrands on the right hand side of (3.26) represent the ohmic loss in the medium, the rate of change of energy stored in the electric field, and the

rate of change of energy stored in the magnetic field respectively. This is simply a statement of the conservation of energy. A similar expression to (3.26) can be derived for sinusoidal excitation with the field quantities represented by their phasor magnitudes directly from Maxwell's equations [120]

$$-\oint_S \frac{1}{2}(\underline{E} \times \underline{H}^*) \cdot dS = \frac{1}{2}\int_V \sigma |\underline{E}|^2 dV + j2\omega \int_V \left[\frac{1}{4}\underline{\mu}|\underline{H}|^2 - \frac{1}{4}\underline{\epsilon}^*|\underline{E}|^2\right] dV \tag{3.27}$$

In this equation, the material constants, $\underline{\mu}$ and $\underline{\epsilon}$ are shown as complex numbers to allow for the use of complex permeability and complex permittivity in the model. Substituting the real and imaginary parts of the complex material constants into (3.27) and simplifying gives

$$\begin{aligned} -\oint_S \frac{1}{2}(\underline{E} \times \underline{H}^*) \cdot dS &= \frac{1}{2}\int_V (\sigma|\underline{E}|^2 + \omega\mu''|\underline{H}|^2 + \omega\epsilon''|\underline{E}|^2) dV \\ &\quad + j2\omega \int_V \left[\frac{1}{4}\mu'|\underline{H}|^2 - \frac{1}{4}\epsilon'|\underline{E}|^2\right] dV \end{aligned} \tag{3.28}$$

We can rewrite (3.28) in terms of the complex power exiting the volume, P_e, the average dissipated power, $\langle P_d \rangle$, the time-average magnetic energy density, $\langle W_m \rangle$, and the time-average electric energy, $\langle W_e \rangle$ as

$$-\underline{P_e} = \langle P_d \rangle + j2\omega(\langle W_m \rangle - \langle W_e \rangle) \tag{3.29}$$

where,

$$\underline{P_e} = \oint_S \frac{1}{2}(\underline{E} \times \underline{H}^*) \cdot dS \tag{3.30}$$

$$\langle P_d \rangle = \frac{1}{2}\int_V (\sigma|\underline{E}|^2 + \omega\mu''|\underline{H}|^2 + \omega\epsilon''|\underline{E}|^2) dV \tag{3.31}$$

$$\langle W_m \rangle = \int_V \left[\frac{1}{4}\mu'|\underline{H}|^2\right] dV \tag{3.32}$$

$$\langle W_e \rangle = \int_V \left[\frac{1}{4}\epsilon'|\underline{E}|^2\right] dV \tag{3.33}$$

Since the time average power loss density at a given point in space is given in general by $\langle p_d \rangle = \frac{1}{2}\left[(\sigma + \omega\epsilon'')|\underline{E}|^2 + \omega''|\underline{H}|^2\right]$, we can write,

$$\langle p_d \rangle = \frac{1}{2}\Re(\underline{E} \times \underline{H}^*) \tag{3.34}$$

Therefore the total power dissipated in a given volume is simply given as the integral,

$$\langle P_d \rangle = \int_V \frac{1}{2}\Re(\underline{E} \times \underline{H}^*) dV \tag{3.35}$$

which agrees with the form given in (3.31).

The relationships in (3.31)–(3.33) form the basis for all of the calculations of power loss and inductance in the devices studied here. We examine the loss components and the energy storage components separately in the following sections.

Power Loss Density Equations

The calculation of the power dissipated in a given region through the use of (3.31) is relatively straight-forward for a numerical solution provided that we have knowledge of the E-field, and the H-field as well as the material constants σ, μ'', and ϵ''. The imaginary part of the complex permeability is used to calculate the magnetic loss, and the conductivity and lossy portion of the dielectric constant are used to calculate electric losses.

Assuming that all of the magnetic losses are adequately modeled through the use of a complex permeability, the total magnetic loss is given as,

$$\langle P_{d_m} \rangle = \frac{1}{2} \int_V (\omega \mu'' |\underline{H}|^2) dV \tag{3.36}$$

It is important to reiterate that while (3.36) is in general applicable to non-homogeneous materials where the permeability is a function of location within the core material, in practice the permeability is assumed constant throughout the core. This assumption may have significant effects on the accuracy of the calculated magnetic losses when the flux density is non-uniformly distributed throughout the core.

The electrical losses in a given volume of material are given by the integration of the first and third terms under the integral on the right hand side of (3.31). However, the form of (3.31) is not the way the power dissipation is usually encountered in the literature and is not in a form that is compatible with the particular Ansoft FEA solver used in the majority of this work. The Ansoft product requires that the dielectric constant of a material be a real constant, i.e. the solver does not model complex dielectric constants. Rather, the solver computes all electrical losses based solely on the material's conductivity. In addition, the field quantities directly available for calculations in the post processing phases of the FEA modeling are the H-field and the J-field. The following manipulations and definitions remedy this situation by putting the electrical loss equation in a form more useful to our use.

Since both the first and third terms of (3.31) multiply the E-field, they can be combined into a single "electrical-loss" term, $\langle P_{d_e} \rangle$, by defining an effective material that combines the conductivity losses due to the σ term with the *lossy dielectric* dissipation of the ϵ'' term.

However, these two terms can be combined into either an effective conductivity, σ_{eff}, or an effective lossy dielectric constant, ϵ''_{eff}. Each of these options have advantages for certain applications, and the resulting loss, of course, is the same no matter which is used, which can be shown as follows.

If (3.31) is rewritten in terms of an effective lossy dielectric constant, ϵ''_{eff}, we have

$$\begin{aligned} \langle P_{d_e} \rangle &= \frac{1}{2}\int_V (\sigma|\underline{E}|^2 + \omega\epsilon''|\underline{E}|^2)dV \\ &= \frac{1}{2}\int_V (\omega\epsilon''_{eff}|\underline{E}|^2)dV \end{aligned} \tag{3.37}$$

where the effective dielectric constant is given by,

$$\epsilon_{eff} = \epsilon'' + \frac{\sigma}{\omega} \tag{3.38}$$

Alternatively the electric field terms of (3.31) can be combined using an effective conductivity, σ_{eff}.

$$\begin{aligned} \langle P_{d_e} \rangle &= \frac{1}{2}\int_V (\sigma|\underline{E}|^2 + \omega\epsilon''|\underline{E}|^2)dV \\ &= \frac{1}{2}\int_V (\sigma_{eff}|\underline{E}|^2)dV \end{aligned} \tag{3.39}$$

where the effective conductivity is given by,

$$\sigma_{eff} = \sigma + \omega\epsilon'' \tag{3.40}$$

The relationship in (3.39) can be further manipulated through the use of the constitutive relationship, $\underline{J_c} = \sigma_{eff}\underline{E}$ to compute the electrical losses in terms of the current density in the volume as,

$$\begin{aligned} \langle P_{d_e} \rangle &= \frac{1}{2}\int_V (\sigma_{eff}|\underline{E}|^2)dV \\ &= \frac{1}{2}\int_V \left(\sigma_{eff}\frac{|\underline{J_c}|^2}{\sigma_{eff}^2}\right)dV \\ &= \frac{1}{2}\int_V \left(\frac{|\underline{J_c}|^2}{\sigma_{eff}}\right)dV \end{aligned} \tag{3.41}$$

This equation matches the requirements of the FEA solver, and therefore is the form of the electrical loss equation used in throughout the rest of this document for calculating the electrical losses in any given material.

Relationship Between Conductivity and Complex Permittivity

Some additional comments should be made at this point considering the various ways that conductivity and dielectric loss are included in the calculation of electrical losses. In the literature, it is not always clearly stated that the conductivity term in (3.31) is the static conductivity. In (3.19) the total current, $\mathbf{J}_{total}$, is given as the sum of the conduction current and the displacement current. In terms of effective conductivity, this is given as

$$\begin{aligned} \mathbf{J}_{total} &= \mathbf{J}_c + \mathbf{J}_d \\ &= \sigma_s \mathbf{E} + j\omega(\epsilon' - j\epsilon'')\mathbf{E} \\ &= (\sigma_s + \omega\epsilon'')\mathbf{E} + j\omega\epsilon'\mathbf{E} = (\sigma_s + \sigma_{ac})\mathbf{E} + j\omega\epsilon'\mathbf{E} \\ &= \sigma_{eff}\mathbf{E} + j\omega\epsilon'\mathbf{E} \end{aligned} \tag{3.42}$$

where the effective conductivity, σ_{eff}, is the same effective conductivity given above in (3.40), σ_{ac} is the alternating field conductivity and σ_s is the static or DC conductivity. In particular, these are given as

$$\sigma_{eff} = \sigma_s + \omega\epsilon'' = \sigma_s + \sigma_{ac} \tag{3.43}$$

$$\sigma_{ac} = \omega\epsilon'' \tag{3.44}$$

The conductivity of a material as a function of frequency measured in the laboratory is the effective conductivity σ_{eff} whereas the conductivity for most ferrites is specified by the manufacturers only at DC. For dielectric materials, the frequency dependent losses are generally presented in term of the loss tangent of the material. While in reality this loss tangent is the summation of a DC loss tangent and frequency dependent loss tangent this is rarely stated explicitly since for these dielectric materials the DC losses are extremely small. This distinction between DC conductivity, AC conductivity and dielectric loss, while not difficult to incorporate into the fundamental loss equations, is particularly important when dealing with semiconductive materials such as ferrites.

Use of material values in simulation

The field solutions described above are generally those used in the commercial FEA solvers used here. In order to use the solvers, therefore, we need reliable and complete information on the material constants μ, ϵ, and σ. In the simulations presented in Chapter 5, we use measured values of complex permeability, permittivity and conductivity directly and thereby include all three of the loss terms on the right hand side of (3.31). The details of the measurement strategy and a collection of the measured results for a given set of ferrite samples is given in Section 3.5.

3.4.3 Relationship Between Field Equations and Device Characteristics

Equations (3.31)–(3.33) are useful for computing the losses and energy storage for a given model of a device based on a known field distribution. In order to be useful, however, these equations must be related to quantities of interest such as the effective resistance or inductance of a structure. Sections 3.2.1 and 3.3.1 show how such circuit elements are related to the geometry and material characteristics of ideal structures. What is left to establish is how the loss calculations relate to the measured lumped element resistance and inductance presented by a device in a circuit.

Effective Resistance

The losses in a given device can always be related to the losses in an appropriate resistance in a lumped element impedance representation of the device. In particular, the electrical power dissipation from (3.39) can be represented by the loss generated by a reference current, $\underline{I}$, in a *electrical-loss resistance*, R_σ, in terms of the loss density as follows:

$$\begin{aligned} P_{d_e} &= P_{R_\sigma} \\ &= (\underline{I}/\sqrt{2})^2 R_\sigma \\ &= \frac{1}{2}\underline{I}^2 R_\sigma \qquad (3.45) \\ R_\sigma &= \frac{2P_{d_e}}{\underline{I}^2} \qquad (3.46) \end{aligned}$$

where R_σ represents only the loss in the device due to the effective conductivity of the material. The magnetic loss term can be similarly related to a magnetic resistance, R_μ. This hysteresis resistance is computed from the contribution of μ'' as given in (3.36); it is converted to a resistance referenced to the excitation current as

$$\begin{aligned} P_{d_m} &= P_{R_\mu} \\ &= (\underline{I}/\sqrt{2})^2 R_\mu \\ &= \frac{1}{2}\underline{I}^2 R_\mu \qquad (3.47) \\ R_\mu &= \frac{2P_{d_m}}{\underline{I}^2} \qquad (3.48) \end{aligned}$$

Therefore, in order to use a field solution to calculate the apparent resistance presented by a given device, we need to evaluate the integral given in (3.39) and compute the resistances

using (3.46) and (3.48). Both of these equations for effective resistance are based on a current reference for the losses and therefore assume a series model for the equivalent impedance of the device. Similar relationships can be written in terms of the excitation voltage, and these expressions fit a parallel model of the device. The choice of a series model here is based once again on compatibility issues related to the FEA solver; most such tools are based on current excitations and therefore the series-element circuit model is more easily related to the field solutions. In any case, standard series-parallel transformations of the impedance models can be used to transform one result to the other.

Effective Inductance

In a similar fashion, the inductance of a device is calculated based on the energy integrals by equating the time-average energy integral, $\langle W_m \rangle$, given in (3.32) to the average energy stored in an "ideal" inductance,

$$\langle W_m \rangle = \frac{1}{2} L \left(\frac{\underline{I}^2}{\sqrt{2}}\right) = \frac{1}{4} L \underline{I}^2 \tag{3.49}$$

For most field simulation software packages the field solution from which the energy integral of (3.32) is derived results from a source current excitation, $\underline{I}_{source}$, given in terms of a peak value of the sinusoid. In that case, the equivalent inductance of the given problem can be written as

$$\begin{aligned} L_{eq} &= \frac{4\langle W_m \rangle}{I_{source}^2} && (3.50) \\ &= \frac{4}{\underline{I}_{source}^2} \frac{1}{4} \int_{vol} (\mu' \underline{H} \cdot \underline{H}^*) dv \\ &= \frac{\int_{vol} (\mu' \underline{H} \cdot \underline{H}^*) dv}{\underline{I}_{source}^2} && (3.51) \end{aligned}$$

Since this equivalent inductance is referred to a particular excitation condition it can represent either the magnetizing inductance of a transformer or inductor or the leakage inductance of a transformer. That is, when the model being considered represents the open-circuit excitation of a transformer for example, the energy stored and the current flowing in the device windings are related to the magnetizing inductance. Likewise when the excitation models a short-circuit excitation (through the use of equal and opposite ampere-turns on the primary and secondary windings), the energy and excitation current are related to the leakage inductance only. This means that for a typical transformer, the

impedances of the series branch of the standard T-model of the transformer—which represent the leakage inductance and winding resistance—and the impedances of the parallel branch are determined through two separate simulations.

The successful use of any simulation techniques, however, is always reliant on the availability of accurate and appropriate material data for the simulation. With the loss and energy equations as background, we now turn our attention to the issues involved in the acquisition on such data for ferrites.

3.5 Measurement of Material Characteristics

The loss and energy equations given above are given in terms of the field distribution and material constants of a particular device. In order to use these field equations—whether in analytical or numerical forms—it is important to have reliable values for these material constants. In general, the required values for the conductivity, permeability and permittivity are available in the reference literature for most materials over a range of excitation conditions. Ferrite materials are no different; the fundamental material constants have been widely reported as each of the different ferrites have been introduced. Nonetheless, for some power electronics applications, complete material information is not available, and magnetic designers often must perform measurements themselves to fill in the missing data.

Since the dimensional effects described in this thesis are not routinely evaluated in standard magnetics designs, manufacturers typically do not report the information needed to fully investigate these effects. Specifically, the evaluation of dimensional effects encountered in larger cores requires complete information on the high-amplitude complex permeability of the core material as a function of frequency and flux density level; the frequency variation of the electrical conductivity and dielectric constant—or permittivity—of the material is also required.

In order to extract these data in the laboratory, we use two different test set-ups as illustrated in Figure 3.6. The complex permeability and magnetic loss density values for various flux density levels and excitation frequencies are extracted from measurements of the inductive impedance of a thin toroidal core as shown in Fig. 3.6(a). The electrical characteristics—dielectric constant, ϵ, and conductivity, σ—are derived from capacitive measurements on thin plates such as shown in Fig. 3.6(b).

In preparing the ferrite samples for these measurements there are several important issues to consider in order to ensure the most accurate measurements possible. These are discussed separately for the magnetic and electric measurements in the following sections.

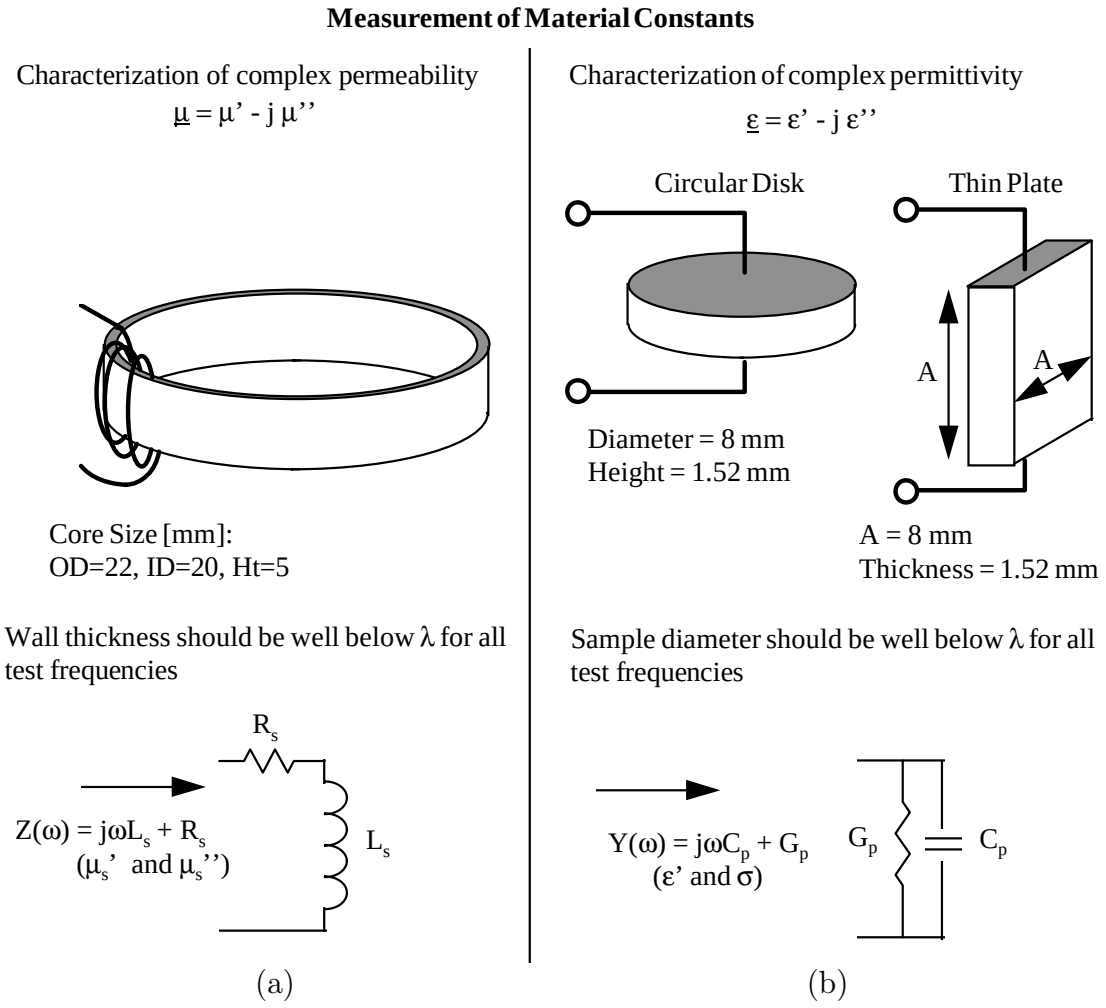

Figure 3.6: Core samples of B2 ferrite used to measure magnetic and electric characteristics of the material. (a) a thin-walled toroid ensures a uniform flux density, low thermal gradients and low eddy-current effects. (b) plated contacts ensure ohmic contacts and low fringing effects. The thin plate of material ensures that the electric flux density is uniform within the sample.

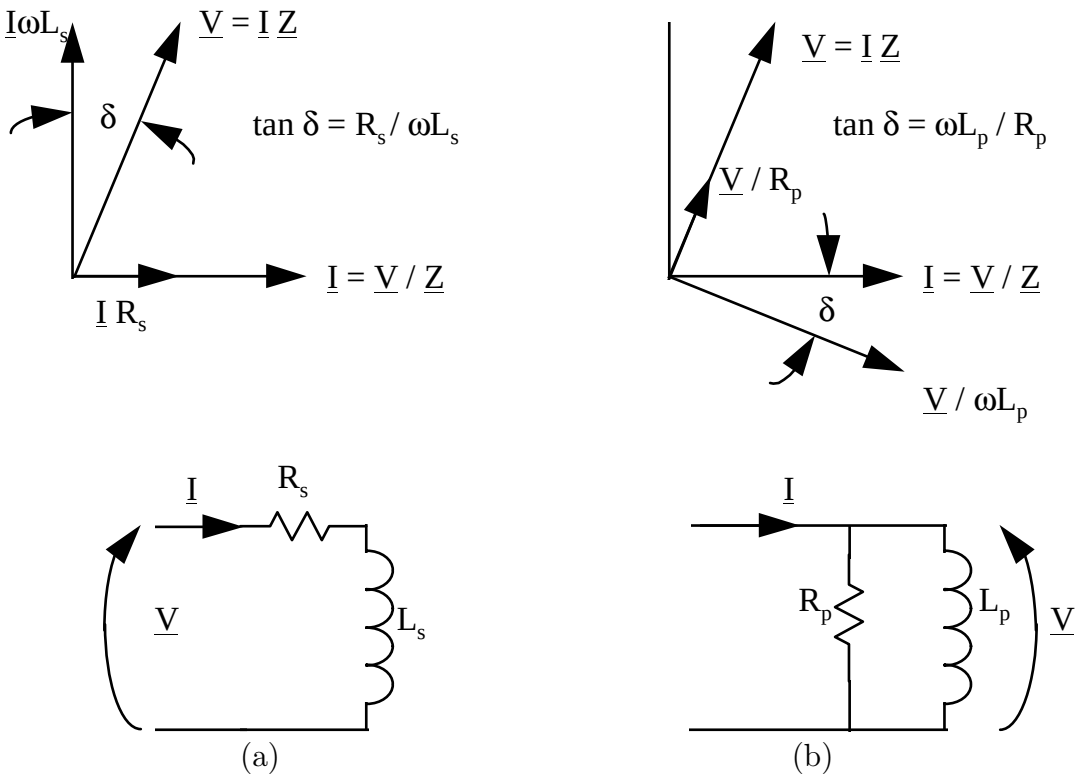

Figure 3.7: Lumped element equivalent circuits for thin toroid used to measure complex permeability. (a) a series RL circuit, (b) a parallel RL circuit. The phase relationships between current and voltage are as shown above the respective circuits.

3.5.1 Magnetic Material Characteristics

Testing Setup

The impedance measurement approach based on [9] is used in the measurements of ferrite magnetic characteristics presented below. This high-amplitude impedance test strategy is described in both [125] and [9]; we include the following description here for completeness.

For the relatively low frequencies considered here, the lumped element model of any given inductor can be simplified to either the series R-L circuit of Fig. 3.7(a) or the parallel R-L combination of Fig. 3.7(b). In these equivalent circuit representations all of the losses in the device are combined into a single resistive element; all of the inductance—both the inductance associated with the flux in the core itself as well as the inductance of the air flux—is represented by the single inductive element. Since the losses and energy storage

characteristics of the device are functions of the excitation frequency[4], these lumped element circuit components are generally function of ω as noted in Fig. 3.7.

The impedance value measured on an N-turn inductor such as that shown in Figure 3.6 is used to compute the complex permeability. From (3.4) we know that the measured impedance of the core can be represented at any given frequency by the series combination of a resistance, R_s, and an reactance, $j\omega L_s$. Rewriting the complex permeability equation (3.6) and solving for the resistance gives,

$$R_s = \frac{\omega N^2 A_e}{\ell_e}\mu''_{s_r}\mu_o \tag{3.52}$$

$$= \omega L_o \mu''_{r_s} \tag{3.53}$$

The series inductance is that given in (3.3) which is repeated here for convenience:

$$L_s = \frac{\mu_o \mu_{r'_s} N^2 A_e}{\ell_e}$$

$$= L_o \mu_{r'_s}$$

The software that runs the impedance measurement system models the impedance of the device under test is using the parallel circuit shown in Figure 3.7(b). This parallel circuit is more appropriate for determining the excitation conditions of the core since the test voltage generated in the testing procedure corresponds directly to the flux value in the device under test (DUT). That is, the flux density in the core and the voltage across the parallel $R_p - L_p$ combination are directly related by the transformer equation,

$$\frac{\underline{V}}{\sqrt{2}} = 4.44 N A_e \underline{B} f \tag{3.54}$$

Since the voltage across the inductor in the series model is determined by the voltage divider between the resistive and reactive element, the flux density in the core is not directly related to the excitation voltage.

The parallel R-L circuit impedance is,

$$\underline{Z}_p(\omega) = \frac{1}{\frac{1}{R_p} + \frac{1}{j\omega L_p}} \tag{3.55}$$

[4] An alternate approach to modeling the frequency dependence is to use a combination of several stages of constant-valued circuit elements in series/parallel combination to yield the correct frequency dependence. This method has advantages for circuit simulation since the use of frequency dependent elements is avoided; the disadvantage of this approach is the rather limited frequency over which the impedance match is satisfactory. Niemela et. al present a discussion of the use of frequency-independent-element models with relation to winding characteristics in [36].

where R_p and L_p represent the measured values of parallel resistance and inductance for any frequency. These circuit elements can be represented in terms of a parallel complex permeability as

$$R_p = \frac{\omega \mu_o \mu''_{p_r} N^2 A_e}{\ell_e} \tag{3.56}$$

$$= \omega L_o \mu''_{p_r} \tag{3.57}$$

$$L_p = \frac{\mu_o \mu'_{p_r} N^2 A_e}{\ell_e} \tag{3.58}$$

$$= L_o \mu'_{p_r} \tag{3.59}$$

The parallel complex permeability values can be determined by rearrangement of (3.57) and (3.59). However, the FEA software requires the series complex permeability as the input material characteristic, and therefore the parallel complex permeability components must be transformed to their series equivalents using the relationship,

$$\frac{1}{\mu'_s - j\mu''_s} = \frac{1}{\mu'_p} - \frac{1}{j\mu''_p} \tag{3.60}$$

This yields,

$$\mu'_s = \frac{\mu'_p}{1 + (\frac{\mu'_p}{\mu''_p})^2} \tag{3.61}$$

$$\mu''_s = \frac{\mu''_p}{1 + (\frac{\mu''_p}{\mu'_p})^2} \tag{3.62}$$

Description of Test Equipment

The equipment configuration is shown in Figure 3.8. It uses an HP4194A Impedance/Gain-Phase analyzer controlled by a personal computer through a GPIB bus. The small-signal output of the impedance analyzer is amplified to a large signal from its maximum output of 1.2 V_{ac} through the use of the wide band amplifier shown. Two different amplifiers are available for use depending on the testing requirements: an Audio Research model 10A250 amplifier with an output power of 10 watts and a bandwidth of 250 MHz is used for low-power, high-frequency tests; an Audio Research model 700A1 with a maximum output power of 700 watts and a bandwidth of 1 MHz is used for high-power tests or test that require relatively low bandwidth.

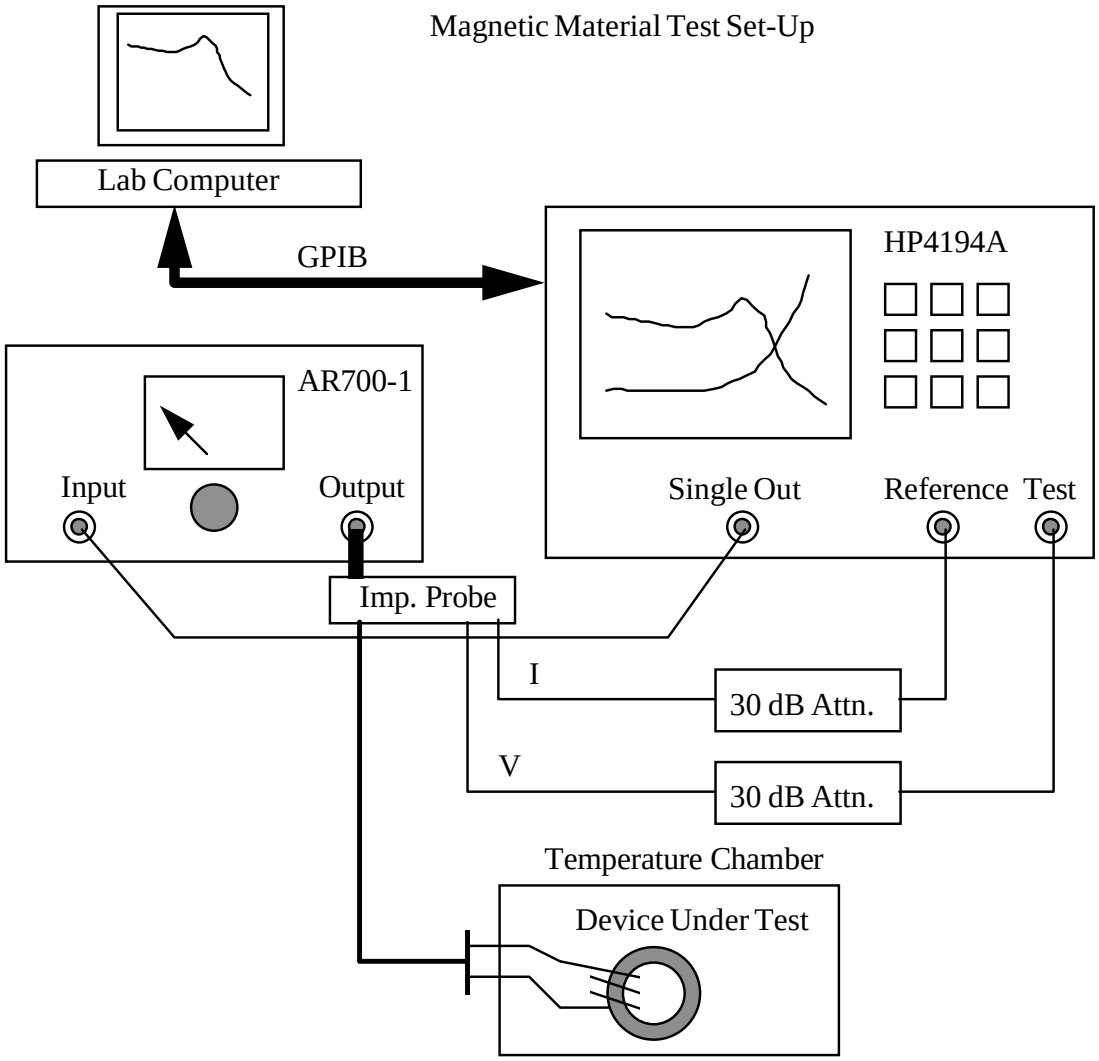

Figure 3.8: Impedance-analyzer based magnetic loss measurement system set-up.

The output of the power amplifier is applied to the DUT through the HP4194A impedance probe shown schematically in Figure 3.9. The impedance probe generates signals proportional to the voltage applied across the terminals of the DUT and the current into the DUT terminals and feeds these signals back to the impedance analyzer test and reference channel inputs respectively. The maximum voltage the probe can withstand is 150 V_{ac}, and the maximum DC bias current is 0.5 amps. Before the measured signals are input to the impedance analyzer, they must be attenuated to below the maximum input voltage of 1.0 V_{ac}. This is accomplished using 30-dB attenuators—Pasternack model PE7010-30—in series with each of the measured signals. Since the maximum input voltage is limited to one V_{ac} after the 30 dB attenuators, the maximum voltage that can be applied to the DUT is 30 dBV or 31.62 V_{ac}.

Test Setup Calibration

The impedance analyzer software is designed to test a given DUT using either a constant flux density at a variety of test frequencies or a set frequency for a range of flux density values. Whichever test is chosen, the equipment must be calibrated with respect to the DUT, and this can be done in one of several ways. First, the HP4194A itself should be calibrated through the standard impedance probe calibration procedure. In this calibration step, the open circuit (0 siemens), short circuit (0 ohms) and reference impedance (50 ohms) fixtures are used to calibrate the *probe-plus-amplifier* configuration. Second, the winding resistance and stray inductance of the core can be compensated for by performing an open-circuit and short-circuit calibration in place of the DUT. The short-circuit calibration uses a winding similar to that used on the DUT but wound on a non-magnetic structure[5].

The calibration for the winding resistance and stray inductance is often inconsequential for the measurement of the ferrite toroids considered here since the high permeability and relatively low core losses result in parasitic elements that are only a small fraction of the measured impedances. This is illustrated in Figure 3.10(a) which shows the measured values of core loss density of a given core with and without calibration of the excitation winding. The close agreement of the measured losses is further illustrated in Figure 3.10(b) as a percentage difference between the given core impedance measured with and without the winding calibration procedure. The measurement difference between the two tests is in all cases below five percent and is below one percent for the frequencies of interest below one megahertz.

[5]It is possible to include the short-circuit calibration in a different way as well. A reference measurement is made on the non-magnetic equivalent structure and then the winding impedance can be compensated during post-processing.

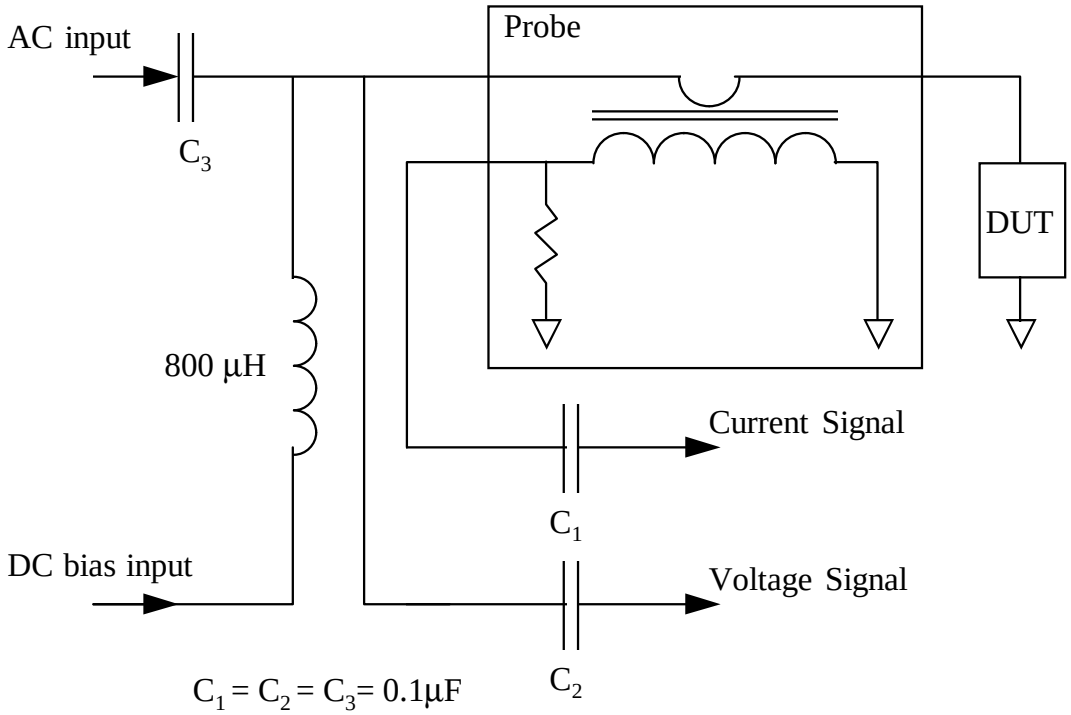

Figure 3.9: Schematic diagram of the impedance probe circuit. The voltage drop across capacitors C1 and C2 below 100 kHz and prevent direct sensing of the core excitation current and voltage.

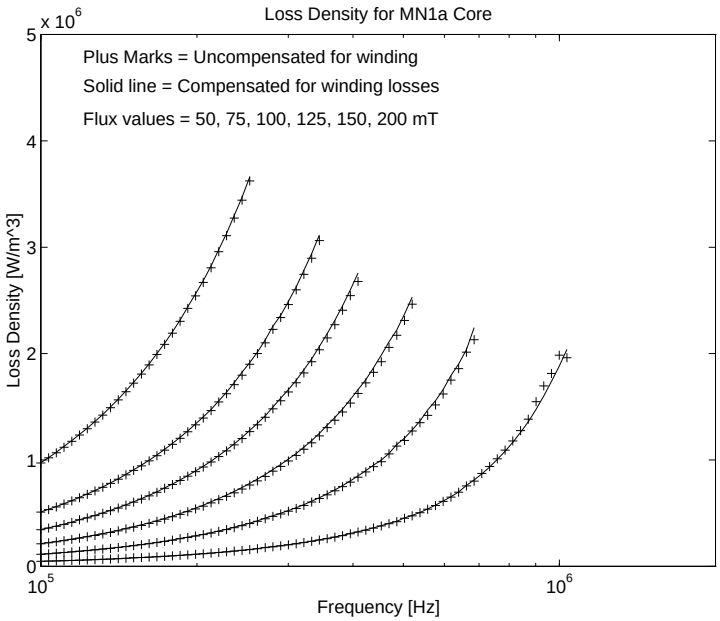

(a)

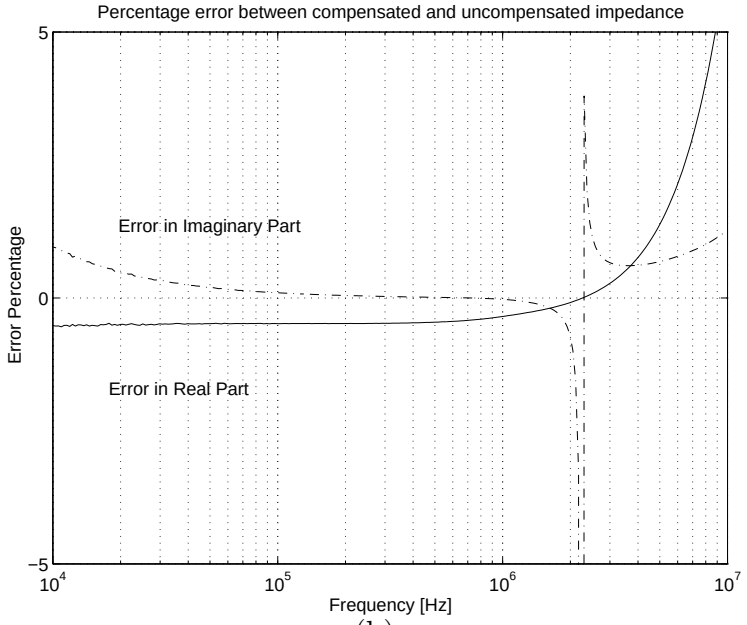

(b)

Figure 3.10: (a) Plot of measured loss density of core #3b from Table 3.5.1 below with and without compensating for the winding impedance, (b) measurement error vs. frequency for the real and imaginary parts of the impedance.

Specifications of Toroid Sample

The geometry of the sample toroid is very important to the accuracy of the complex permeability values derived from the measurement. In performing such measurements of the *material* characteristics, it is important to minimize the effects that can change the losses in the core: eddy-currents, thermal gradients through the core, and flux density variations.

Commercial ferrite toroidal cores typically have a ratio of outside diameter to inside diameter in the range of 1.5 to 2.0. This means that the flux density—which varies as $1/r$ through the core cross-section—can be significantly higher on the inner edge of the core than on the outer portion of the toroid. This variation of flux density is compensated in the inductance calculations through the use of *effective* core geometries A_e, ℓ_e and V_e. These effective parameters are given[126] in terms of the core constants C_1 and C_2 as,

$$A_e = \frac{C_1}{C_2} \tag{3.63}$$

$$l_e = \frac{C_1^2}{C_2} \tag{3.64}$$

$$V_e = A_e \ell_e \tag{3.65}$$

where the core constants are computed for toroidal cores in terms of the inner and outer radii of the core, r_o and r_i, as,

$$C_1 = \frac{2\pi}{h \ln(r_o/r_i)} \tag{3.66}$$

$$C_2 = \frac{2\pi(1/r_i - 1/r_o)}{h^2 \ln^3(r_o/r_i)} \tag{3.67}$$

The above equations for the effective core geometry constants are derived[2] based on the assumption that the B and H fields obey the Rayleigh or Peterson relation given as,

$$\frac{B}{\mu_o} = (\mu_i + \nu H_m)H \pm \frac{\nu}{2}(H_m^2 - H^2) \tag{3.68}$$

where B and H are the instantaneous values of the fields, H_m is the peak value of the magnetic field and ν is the Rayleigh hysteresis coefficient. This relationship is generally true only for small amplitude excitations; however, the effective core constants based on this relation are used routinely with satisfactory results in power electronics applications which use much larger excitation levels. In order to minimize any adverse effects that variations in flux density within the core have on the measurement of the material constants, however, it is helpful to use very thin cores that minimize the ratio of the outer diameter to the inner diameter.

Single-Port vs. Dual-Port Measurements

The single port impedance probe measurement setup and calibration procedures outlined above are generally adequate for small cores without air gaps. For such devices the magnetizing current and leakage inductance are kept relatively small. However, at low frequencies where the blocking capacitors of the impedance probe (C_1 and C_2 of Fig. 3.9) present significant series impedance, an alternative test strategy that uses two separate windings such as shown in Figure 3.11 is useful. This two-winding test approach [12] uses one winding to excite the core and a separate winding to sense the flux induced in the core.

There are several advantages to using separate excitation and sensing windings including the elimination of voltage drops due to winding resistance and the ability to sense the flux in several regions of the core through the use of additional voltage pick-up windings. However, error in the pickup winding, phase errors between the different probe channels and errors introduced in processing the measured data can limit the accuracy of such measurements to frequencies below the megahertz range [9]. The setup shown in Figure 3.11 eliminates some of these problems by using the impedance analyzer in its gain/phase mode to derive the impedance of the DUT. This setup is limited by the maximum input voltage of 1.2 V_{ac} of the impedance analyzer test and reference channels[6]; only relatively small voltages can be sensed with such a setup, but this is not a significant restriction for measuring the small core samples of Table 3.5.1 at frequencies of approximately 10 kHz.

Thermal Gradients

An additional issue that must be considered when measuring material characteristics is the presence of thermal gradients in the core. This is critical in ferrites since the core loss and permeability is dependent on temperature. If all sections of the core are not at the same temperature then the measurement results can be unreliable. We address this issue in two ways: (1) the use of thin cores with small values of OD/ID prevents the buildup of thermal gradients between different portions of the core; (2) the use of the impedance analyzer to excite the core for short duration at each measurement point prevents significant self-heating of the core. Finally, when testing at elevated temperatures the core is allowed to soak at the test temperature for at least 20 minutes before testing to ensure the core is isothermal.

[6]The attenuators used in the single port measurement cannot be used in this case since they would place a 50 ohm load on the output of the DUT. This could be alleviated through the use of high-impedance probes or through the use of an impedance-matching transformer.

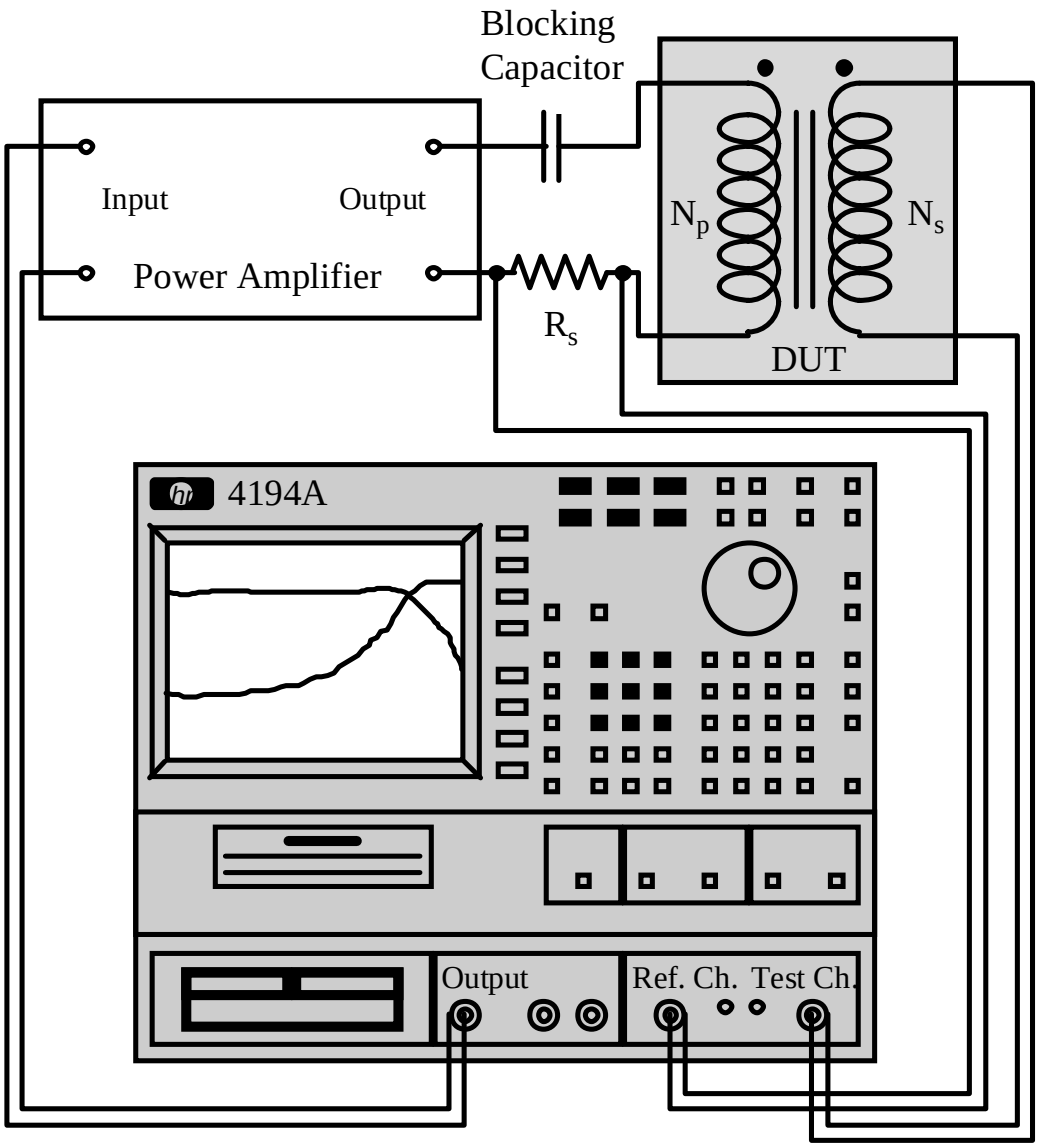

Figure 3.11: Two-port measurement system

Winding Arrangement

The windings on the sample cores should ideally wrap fully around the circumference of the toroid. This uniform winding reduces the amount of flux that leaves the core which provides for a more uniform flux density in the core. When the number of turns required to excite the core is limited due to the maximum voltage limits of the test setup, a multistranded winding with fewer turns can provide the same uniform winding with the smaller number of turns. These winding variations are illustrated in Figure 3.12. While the use of a fully-wound device—whether it be wound with only a small number of multi-stranded turns or with many single-strand turns—provides a more uniform flux density, it is not well documented what impact a "non-ideal" winding has on the measured characteristics of the material. For high-permeability ferrite cores, the difference in flux density in the core due to leakage is relatively small. This is illustrated in Figure 3.13(a) which shows the results of an FEA simulation of the flux in a thin toroidal core. The graphs in Figure 3.13 give the ratio of the net flux in the core at locations 2, 3, and 4 relative to the flux that links the excitation winding (point 1). The ratio $\beta = \Phi_2/\Phi_1 = \Phi_4/\Phi_1$ gives the percentage of the source flux that links points 2 and 4; the ratio $\zeta = \Phi_3/\Phi_1$ gives the percentage of the source flux that reaches the opposite side of the toroid (point 3). The flux that links all parts of the core is approximately 90% of the source flux for core permeability values above 1000. When the relative permeability is 3000, approximately 97% of the flux remains within the core. Fig. 3.13(b) shows that the loss density values measured using the multi-stranded six-turn winding correlate well with the fully-wound 25-turn winding; a six-turn winding that is localized in only a small section of the core, however, underestimates the loss in the core by approximately 20 percent. The results in Fig. 3.13(a) and (b) show that while the location of the winding may introduce only a small difference in flux density in the different parts of the core (on the order of 5–10%), this relatively small change in flux density can introduce a significant error in the measured losses since the loss density is a string function of the flux density; typically, the loss density in ferrite depends on the flux density to the power of 2.2 to 2.5 which means a 10% error in flux leads to a 20–25% error in loss.

Results

The core samples tested include MnZn ferrite toroidal cores of various sizes. All of the cores are manufactured by Ceramic Magnetics, Inc. (CMI) by machining toroidal shapes out of larger blocks of ferrite. The two materials considered here are B2 and MN80. B2 ferrite is made from a ferrite powder supplied to CMI by Thompson; CMI presses and fires the raw powder to produce bulk material from which the toroids are cut. CMI produces the MN80 material cores in a similar fashion from powder they produce themselves. Both

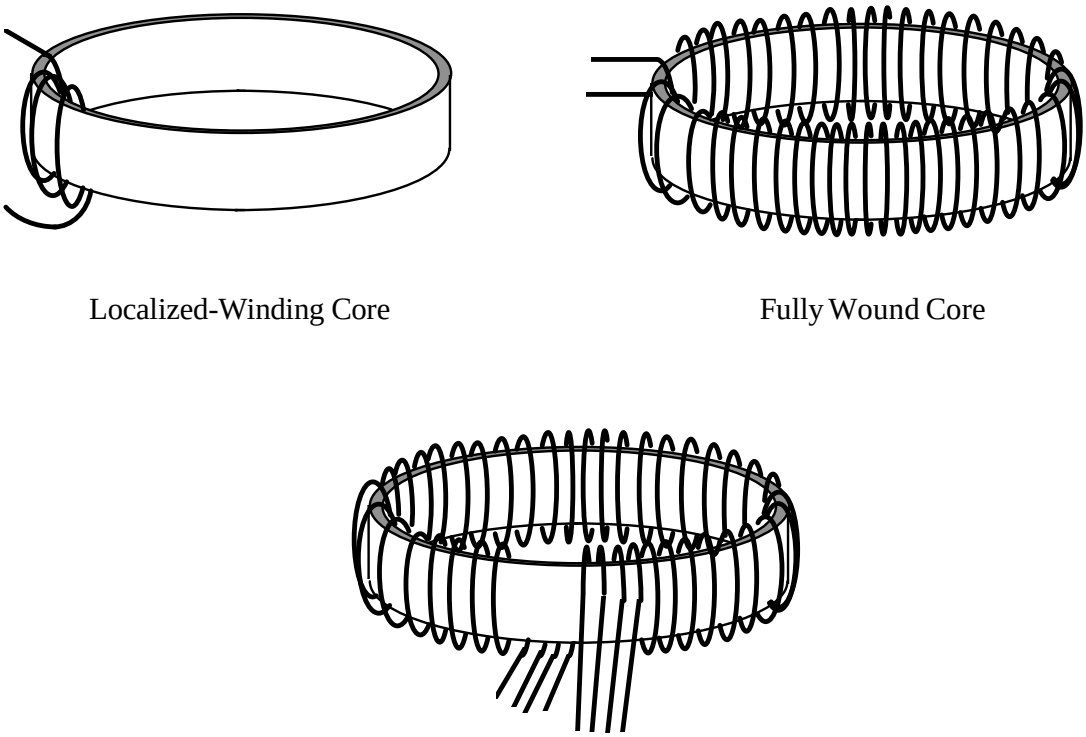

Figure 3.12: Winding arrangements for thin toroidal cores.

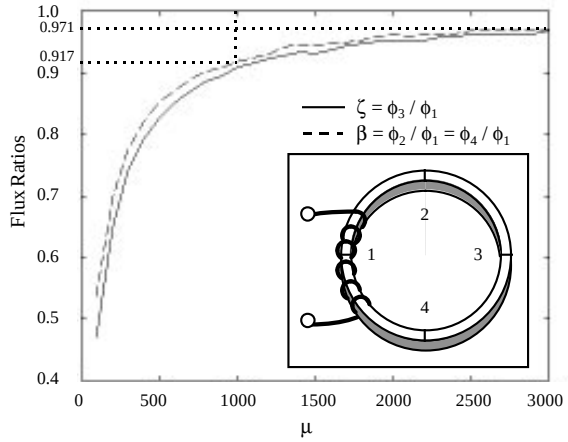

(a)

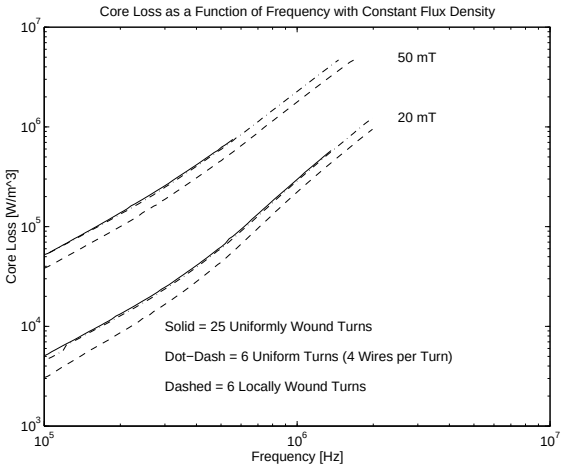

(b)

Figure 3.13: Comparison of flux density for different winding arrangements on toroid sample #1. (a) Ratio of flux density at different locations within the core as a function of the core permeability. (b) Measured loss density for six single-strand turns concentrated in one section of the core, six multi-strand turns that wrap around the entire circumference, and 25 single-strand turns that wrap around the circumference.

of these materials are suitable for power electronics applications in the frequency range of interest. The geometrical details of the thin toroidal core samples are listed in Table 3.5.1.

Figures 3.14 and 3.15 show the measured values of the real and imaginary components of μ for flux density levels of 10 mT and 100 mT for various excitation frequencies for the B2 and MN80 materials respectively. These curves are taken from tests on core #3a for the B2 material and core #3a for the MN80 material; the spread of the results from core to core was within 10%, and these cores were typical for the material.

3.5.2 Electric Material Characteristics

The measurement of magnetic material characteristics described in the previous section follows from the assumption that the thin toroidal core is a good inductor with uniform magnetic flux density. This section presents measurements of the electrical conductivity and dielectric constant of these ferrites based on the the assumption that thin plates of material are good capacitors with uniform electric flux density.

Testing Setup

The electrical measurements use the parallel-plate capacitor model shown in Figure 3.6(b). The capacitive admittance of each thin plate is measured using an HP4194A impedance analyzer with the HP16451B dielectric test fixture. The real part of the measured admittance is used to derive the frequency dependent conductivity of the core and the measured capacitive reactance gives the core permittivity spectrum. The calibration procedures used in this test procedure are those outlined in the HP16451B manual[127]. The key aspects of this calibration procedure as well as the sample preparation and size restrictions are the main issues of concern in measuring the ferrite electrical characteristics. These issues are discussed separately in the following paragraphs.

Test Electrodes and Ferrite Samples for Electrical Measurements

The HP16451B test fixture has four different electrodes that can be used for measuring different types of samples: one large and one small electrode for testing samples with thin-film electrodes attached to them and one large and one small electrode for testing samples without thinfilm electrodes. Each of the HP16451B's electrodes provides both a guarded

Table 3.1: Geometry details for the thin toroids used for testing

Core Name	Material	OD	ID	Height	A_e	ℓ_e	V_e
		[mm]	[mm]	[mm]	[m^2]	[m]	[m^3]
1a	MN80	44.53	40.25	5.04	1.08e-5	1.33e-1	1.44e-6
3a	MN80	22.46	19.56	5.05	7.31e-6	6.58e-2	4.81e-7
1a	B2	33.12	30.22	5.07	7.35e-6	9.94e-2	7.306e-7
1b	B2	33.07	30.03	5.02	7.62e-6	9.90e-2	7.544e-7
1c	B2	33.11	30.25	5.07	7.25e-6	9.94e-2	7.207e-7
1d	B2	33.13	30.25	5.07	7.30e-6	9.94e-2	7.256e-7
2a	B2	39.4	35.84	4.98	8.86e-6	1.18e-1	1.045e-6
2b	B2	39.39	35.65	5.06	9.45e-6	1.18e-1	1.115e-6
2c	B2	39.4	35.68	4.97	9.24e-6	1.18e-1	1.090e-6
2d	B2	39.38	35.5	5.08	9.85e-6	1.17e-1	1.152e-6
3a	B2	21.87	19.95	5.01	4.81e-6	6.56e-2	3.155e-7
3b	B2	21.88	19.86	5.01	5.06e-6	6.55e-2	3.314e-7
3c	B2	21.88	19.9	5.0	4.95e-6	6.55e-2	3.242e-7
3d	B2	21.87	19.79	5.01	5.21e-6	6.53e-2	3.402e-7
4a	B2	14.25	6.33	7.01	2.63e-5	2.90e-2	7.627e-7
4b	B2	14.21	6.25	7.01	2.64e-5	2.88e-2	7.603e-7
4c	B2	14.23	6.33	7.0	2.62e-5	2.90e-2	7.598e-7
4d	B2	14.2	6.28	7.01	2.63e-5	2.89e-2	7.601e-7

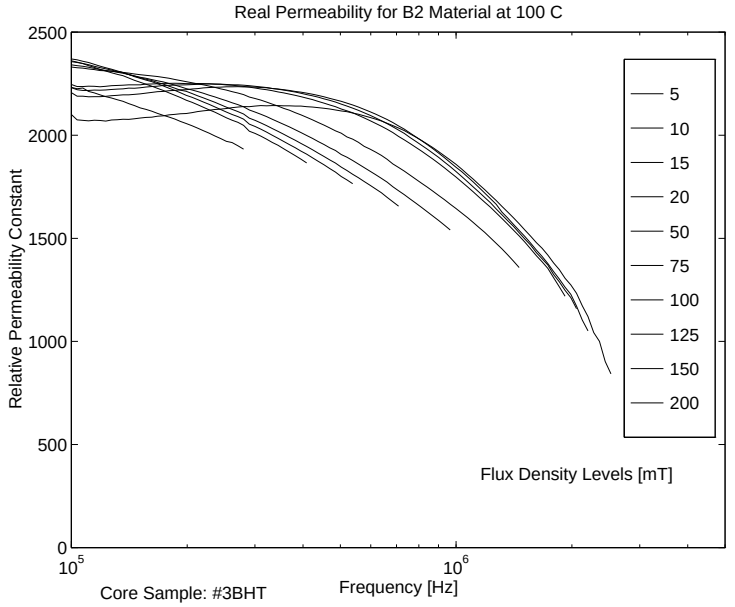

(a)

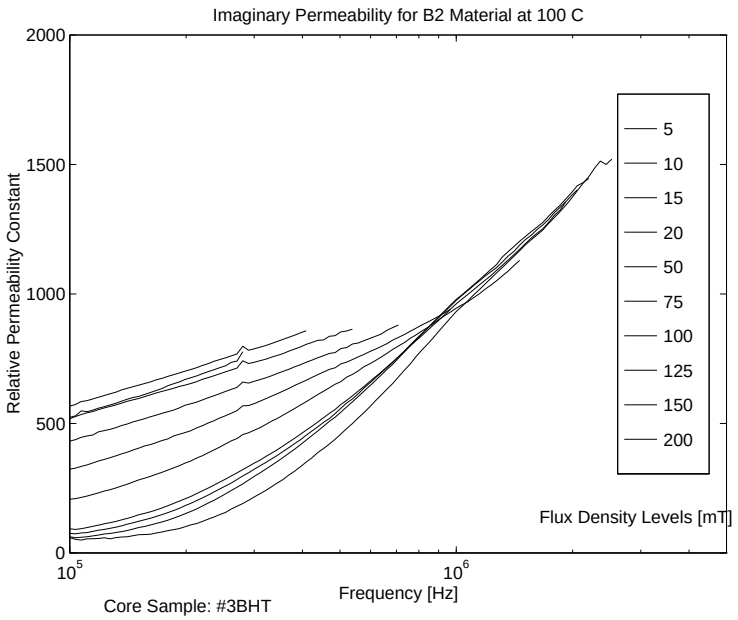

(b)

Figure 3.14: Magnetic characteristics of B2 MnZn ferrite material at 100 degrees celsius for flux density values from 5 mT to 200 mT. (a)μ': Real part of the complex permeability. (b)μ'': Imaginary part of the complex permeability.

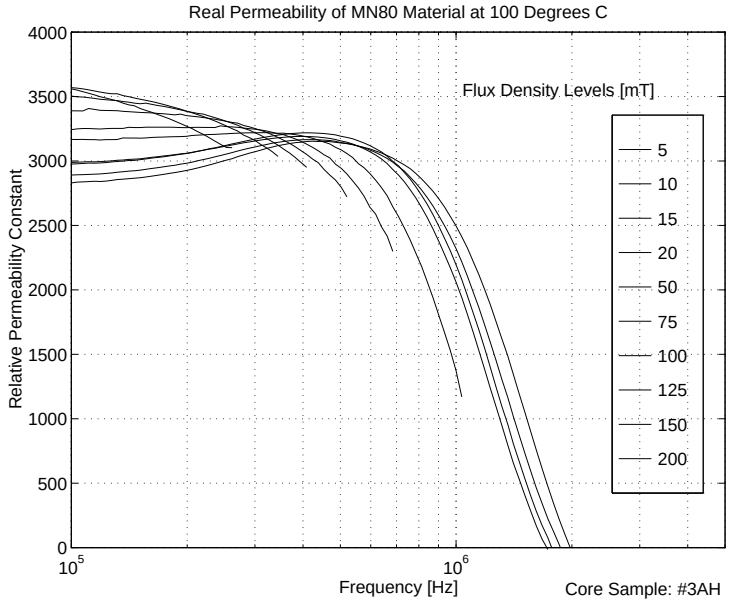

(a)

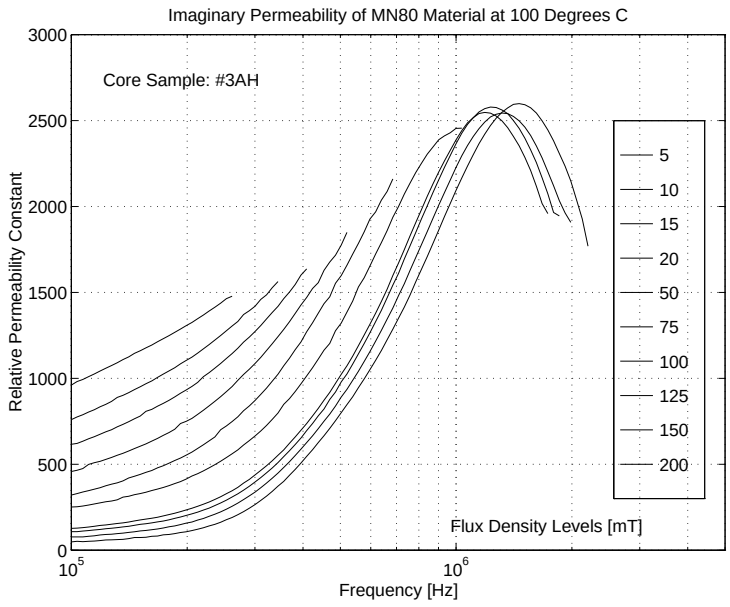

(b)

Figure 3.15: Magnetic characteristics of MN80 MnZn ferrite material at 100 degrees celsius for flux density values from 5 mT to 200 mT. (a)μ': Real part of the complex permeability. (b)μ'': Imaginary part of the complex permeability.

electrode and an unguarded electrode where the guard electrode is intended to minimize the effects of fringing near the edged of the guarded electrode. The sample dimensions and thin-film electrode dimensions applicable for the different test fixtures are listed in Table 3.2

Table 3.2: Applicable samples sizes for the electrodes of the HP16451B Dielectric Tester

Electrode Number	Type	Min. Sample Diam. [mm]	Max. Sample Diam. [mm]
A	Contact	40	56
B	Thin Film	10	56
C	Contact	56	–
D	Thin-Film	20	50

The tests results reported below are obtained using Electrode-B from Table 3.2 on two samples each of the two MnZn ferrite material as listed in Table 3.3.

Table 3.3: Geometrical details of the MnZn Ferrite Samples used for the Electrical Characterization Tests

Sample Number	Material	Type	Electrode Area [mm^2]	Sample Length [mm]
5B	B2	Thin Plate	12.16	8
6	B2	Disk	50.26	1.52
8B	MN80	Thin Plate	12.16	8
9B	MN80	Disk	50.26	1.52

Fringing Effects and Guard Electrodes The ferrite samples listed above do not meet the size restrictions listed in Table 3.2 since the plated contacts are smaller than the minimum sample dimensions recommended for any of the electrodes. However, the use of this equipment is justified based on the assumption that the high dielectric constant of MnZn ferrite materials makes the fringing of the electric field near the edges of the samples relatively unimportant. This assumption permits us to use ideal parallel-plate capacitance equations in deriving the material constants and is equivalent to the assumption of ideal flux distribution made in the derivation of the magnetic material characteristics.

Effect of Sample Size on Measured Characteristics

The calculation of capacitance based on the ideal parallel-plate capacitance equation assumes that the plates that bound the material under consideration are equipotential surfaces. This assumption is completely rigorous at DC since the conductive plates cannot support a voltage difference under static conditions. However, under AC excitation it is possible that the conductive plates are not equipotential. In such as case, the electric field is not uniform within the sample cross-section and the electric flux density is similarly non-uniform. The existence of such a non-uniform field is possible when the cross-sectional dimension of the sample being tested is a significant fraction of the electromagnetic wavelength at the excitation frequency. In other words, if the diameter of the sample used for testing the dielectric nature of the ferrite is large, then what is measured is not the inherent complex dielectric constant of the material but rather the *effective* dielectric constant. This is the dual situation of the dimensional resonance issue considered for the magnetic field to this point. In order to measure the true material constant, therefore, the sample should have a minimum cross-sectional dimension that is a small fraction of the wavelength over the entire frequency range of interest.

This electric-field dimensional effect is illustrated in the graphs of measured conductivity and real dielectric constant in Figure 3.18 below. In these plots, the measured values from samples with small cross-sectional dimensions (samples #5B and 8B) are compared to those measured on samples with relatively large diameters (samples #6 and 9B). The fact that the larger samples show a resonant behavior at relatively low frequencies indicates that the samples are not sufficiently thin to permit the measurement of the true material constants for these frequencies. The results in Figure 3.18 confirm the results presented by Brockman, et al. in [97] where the apparent dielectric constant for a 0.127 cm. thick MnZn ferrite sample is compared to a sample approximately ten times thicker. The samples that we take as giving the "true" result in Figure 3.18 are approximately the same thickness as those used in [97].

Surface Preparation and Plating

The tests of the ferrite's electrical characteristics minimize the contact resistance to the ferrite by first plating the samples with a thin layer of metal. It is possible to then solder leads to the metallization layers and test the samples as one would test any capacitor. However, the use of the dielectric test fixture on the impedance analyzer simplifies this process since there is no need to solder leads to the samples; all of the test results presented here use this ''leadless" testing approach.

In order to achieve a good contact for the plating material it is important to prepare the samples correctly. The test surfaces of the samples are first lightly wet-sanded to remove surface contamination and to provide a smooth surface for electrode plating. This is followed by ultrasonic cleaning in acetone and isopropyl alcohol to remove organic contaminants from the surface; this improves the attachment of the plating material. The samples are then taped so that only the surfaces that should have metal plating deposited on them are exposed, and finally metallic contacts are deposited through vacuum sputtering process. For the samples tested here the plating metal is platinum.

Results

Figure 3.16 shows the electrical conductivity for one sample of each of the two MnZn material considered. The data show that the conductivity varies approximately one order of magnitude as the frequency varies over the two decades from 10 kHz to 1 MHz with the majority of this variation occurring for frequencies above 100 kHz. This means that any estimates of the eddy current losses in the core that use the DC conductivity provided by the manufacturer will underestimate these losses by a similar amount. While this may not be a problem for small cores where eddy-current losses are only a couple percent of the total loss the same cannot be said for larger cores where the eddy-current losses are more significant.

The measured values of the real part of the relative dielectric constant are shown for the MN80 and B2 core samples in Figure 3.17. This graph shows that while the dielectric nature of both materials does in fact decrease as frequency increases, the relative dielectric constant is still greater than 50,000 even at one MHz. For frequencies in the range of 100 kHz to one MHz the dielectric constant is in the range of 60,000 to 125,000 which confirms the concern over dimensional effects in the large cores in this range of frequencies.

Figure 3.18 illustrates the dimensional effects mentioned above that are present in the tests of electrical material characteristics. The two lines in Figure 3.18(a) show the measured real dielectric constant for two samples of MN80 material: one is a circular disk of the type in the left-hand portion of Figure 3.6(b) with a diameter of 8 mm; the other sample is 8 mm x 8 mm x 1.52 mm slab with the electrodes plated onto opposite 8 mm x 1.52 mm faces. The difference in the measured dielectric constant for frequencies above approximately 300 kHz is the result of the dimensional resonance within the sample. This is seen in the measurement of conductivity for these samples as is illustrated in Figure 3.18(b). In this case the conductivity of the two samples is significantly different for frequencies above a megahertz. The differences in the measured electrical characteristics—dielectric constant and conductivity—for the different size samples in Figure 3.18 provides some validation of

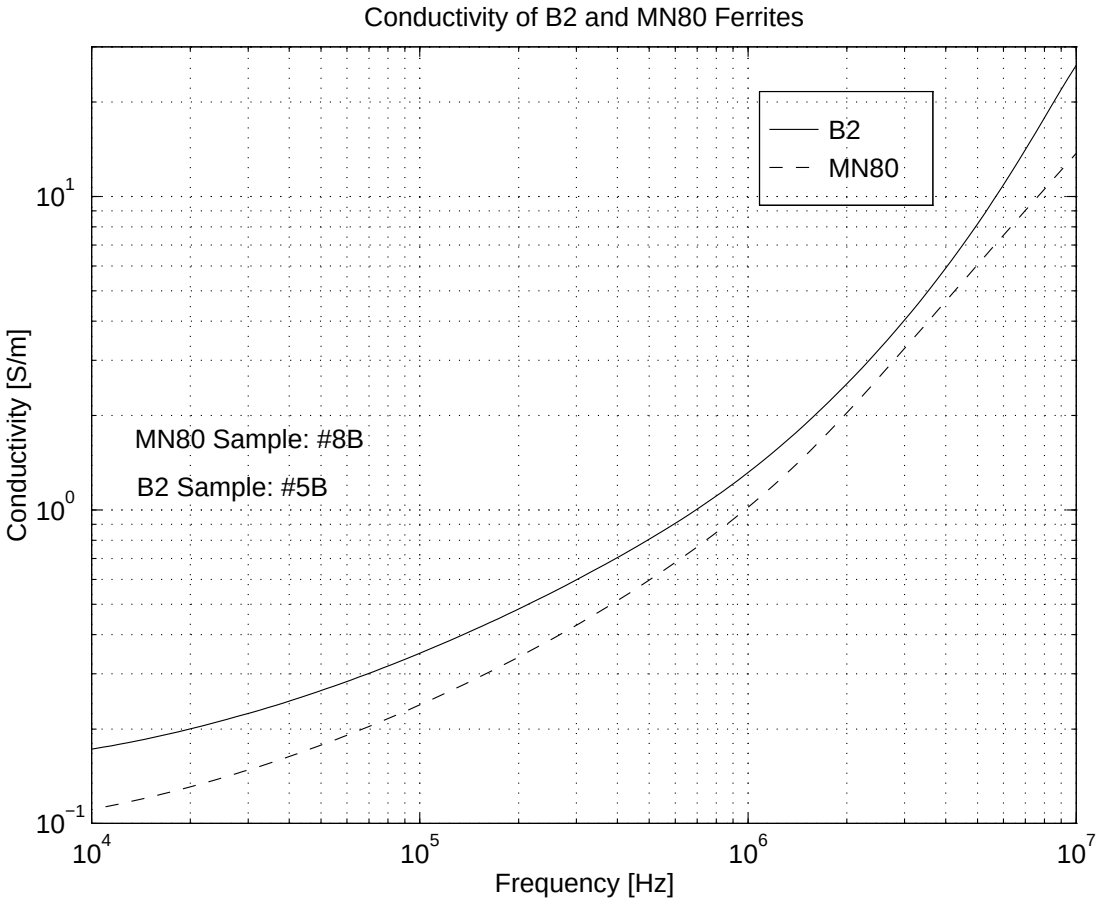

Figure 3.16: Electrical conductivity of B2 and MN80 MnZn ferrite materials vs. frequency.

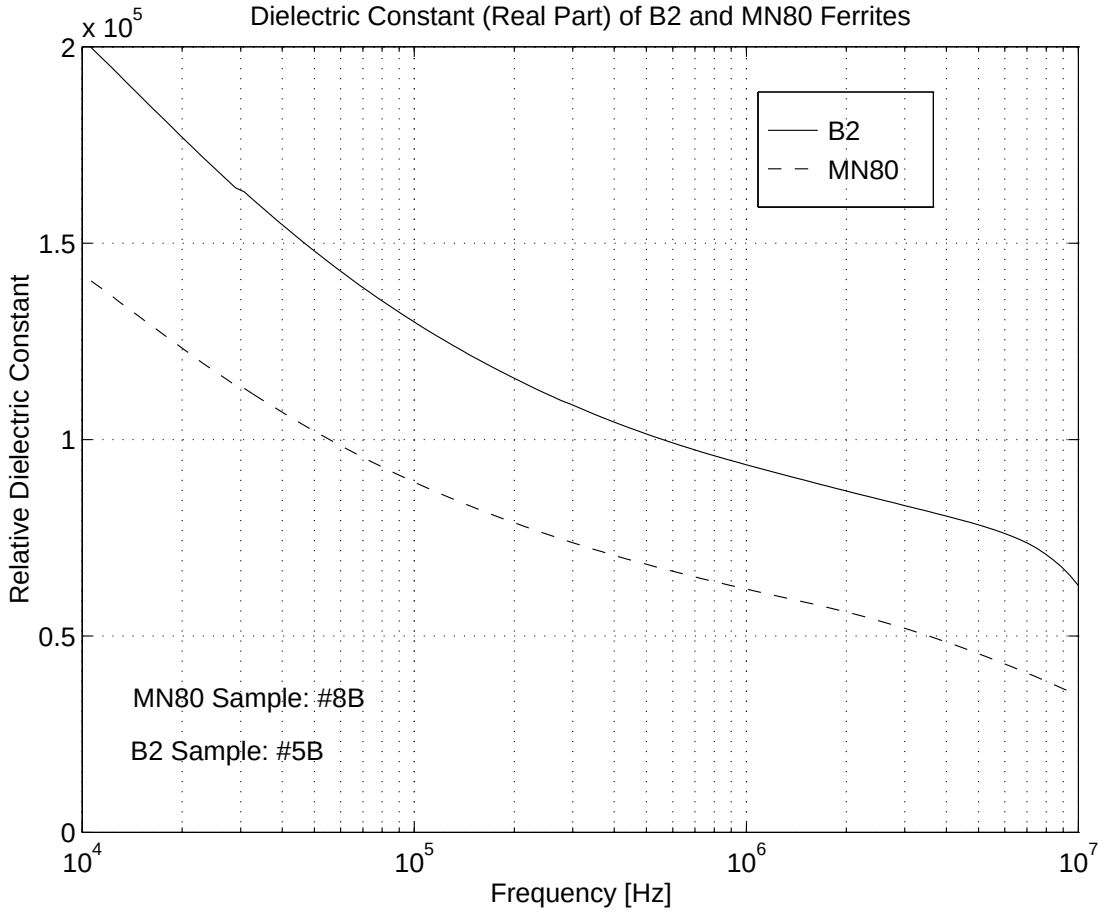

Figure 3.17: Real part of the dielectric constant for B2 and MN80 MnZn ferrite materials vs. frequency.

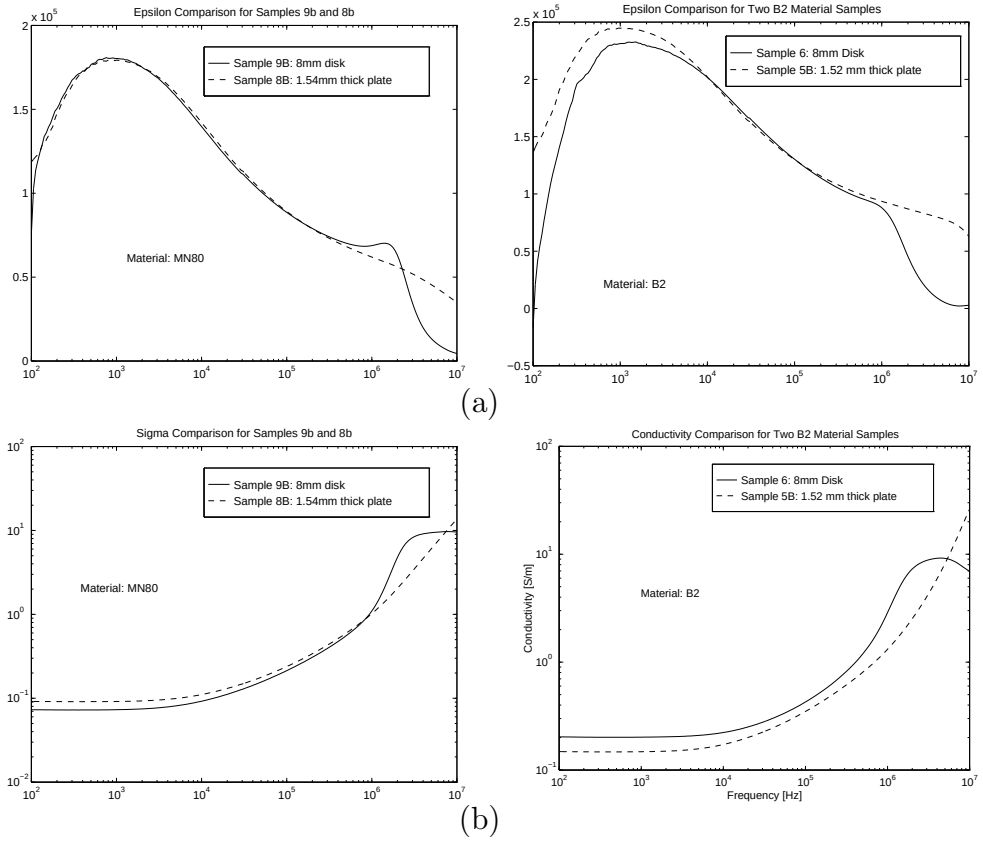

Figure 3.18: Illustration of the effect of sample size on the measurement of ϵ and σ. (a) real part of the dielectric constant for MN80 and B2 MnZn ferrite materials for two different sample sizes. (b) corresponding values of conductivity of MN80 and B2 ferrite.

the dimensional resonance effects predicted in the discussion in Chapter 1; Section 3.6 below provides a similar demonstration of such effects with respect to the magnetic performance devices of various sizes.

Machining effects on ferrite samples The ferrite samples used in the measurements above are machined from larger blocks of ferrite. Because of the physical stresses that result on the surfaces of these small parts, there is a concern over the effect that this machining has on the magnetic and electrical characteristics. In order to examine this issue, several of the core samples were processed through a post-machining heat treatment. This heat treatment is intended to provide a slight annealing of the part that may relieve the mechanical stress in the machined surfaces while leaving the ferrite crystal lattice relatively unaltered. Figure 3.19 shows a comparison of the measured dielectric constant and conductivity of the MN80 material samples with and without heat treatment. These plots show that while there is a slight difference between the treated and untreated samples this different is relatively small. To a first approximation, therefore, the material constants measured for the ferrite materials are used without regard to the application of heat treatment; in particular, the values of the B2 material constants are used without submitting the samples to heat treatment. The assumption here is that the variation due to machining is a second order effect that is on the order of the inherent variation in sample-to-sample characteristics typical of ferrites.

3.6 Demonstration of Dimensional Effects

The theoretical basis for dimensional effects in large ferrite cores is well established as detailed in Chapter 4. However, the fact that this issue remains of fringe interest in the literature indicates that it is not a recognized problem in practice. Therefore, before proceeding with the additional details of the field analysis for large ferrite cores, it is worthwhile to demonstrate the existence of such dimensional effects and to show how they manifest themselves in measurements of actual cores. This section presents measurements that illustrate the impact of dimensional resonance on a set of large toroidal and "block-core" structures. These tests replicate to some degree the measurements presented in [97], and are intended to establish that such effects should be expected to result in significant losses in more complicated structures—such as the inductive charger core example introduced in Chapter 1.

The dimensional effects in a given core can be evaluated by comparing the core's measured values of permeability and loss density to the response expected based on similar measure-

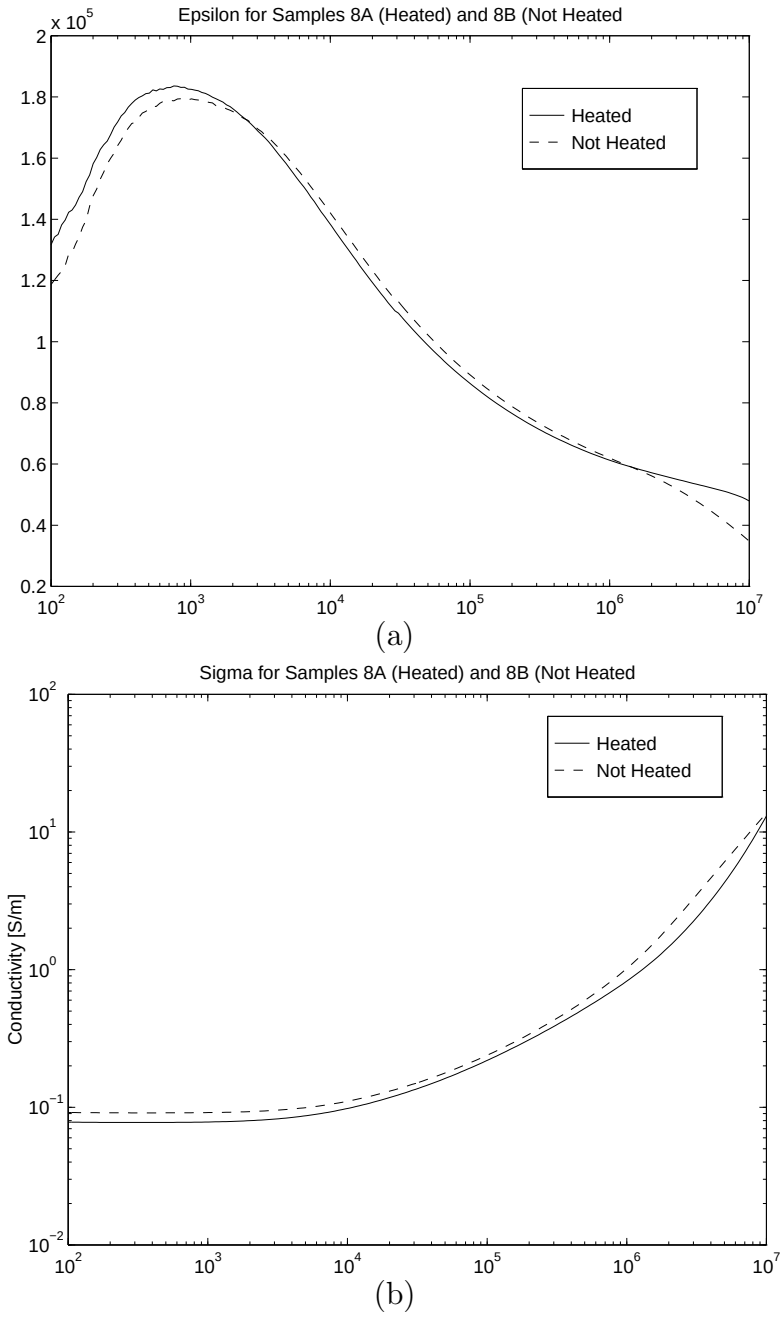

Figure 3.19: Effect of heat treatment on measured values of ϵ and σ: (a) dielectric constant for MN80 samples with and without heat treatment; (b) corresponding values of conductivity.

ments of the material characteristics alone. The following section shows the results of such measurements on a selection of large and small cores of the same material.

3.6.1 Sample Core Structures

Fig. 3.20 shows the physical dimensions of a set of test structures ranging in size from the thin-walled toroid used for a baseline measurement (Fig. 3.20(a)) to a large core constructed from six 2"x3"x4" blocks of material (Fig. 3.20(e)). The geometrical data for these cores are listed in Table 3.4. All of these sample cores are constructed of the same MnZn ferrite

Table 3.4: Geometrical data for the large toroidal and block-core devices.

Core Name	Material	Type	A_e [m^2]	ℓ_e [m]	V_e [m^3]	Wall Thickness [m]
#5	B2	toroid	4.55e-4	1.9e-1	8.645e-5	17.97
#6	B2	toroid	3.44e-4	2.78e-1	9.563e-5	13.49
#10	B2	block	7.26e-4	2.88e-1	2.09e-4	19.05
#9	B2	block	3.87e-3	5.66e-1	2.19e-3	50.8
#95-1a	MN80	toroid	7.15e-4	1.59e-1	1.14e-4	30.85
#99-1a	MN80	toroid	1.71e-4	1.59e-1	2.72e-5	11.28

materials (B2 and MN80) as tested in the previous section. The block cores are assembled with no intentional air gap between their component blocks in order to minimize any effects due to magnetizing current losses.

3.6.2 Measured Permeability

Figure 3.21 shows the measured series permeability (real part) as a function of frequency normalized to the low-frequency values of the inductance of each core for the different core structures. The flux density[7] in these tests is 5 mT. For all of the large cores, the bandwidth of the apparent permeability is much less than that of the thin toroid; the largest cores have the lowest roll-off frequency since they have the lowest resonant frequency.

[7]The large size of these core and the limited excitation voltage allowed by the impedance analyzer testing setup means that it is not possible to excite a large flux density in all of the cores.

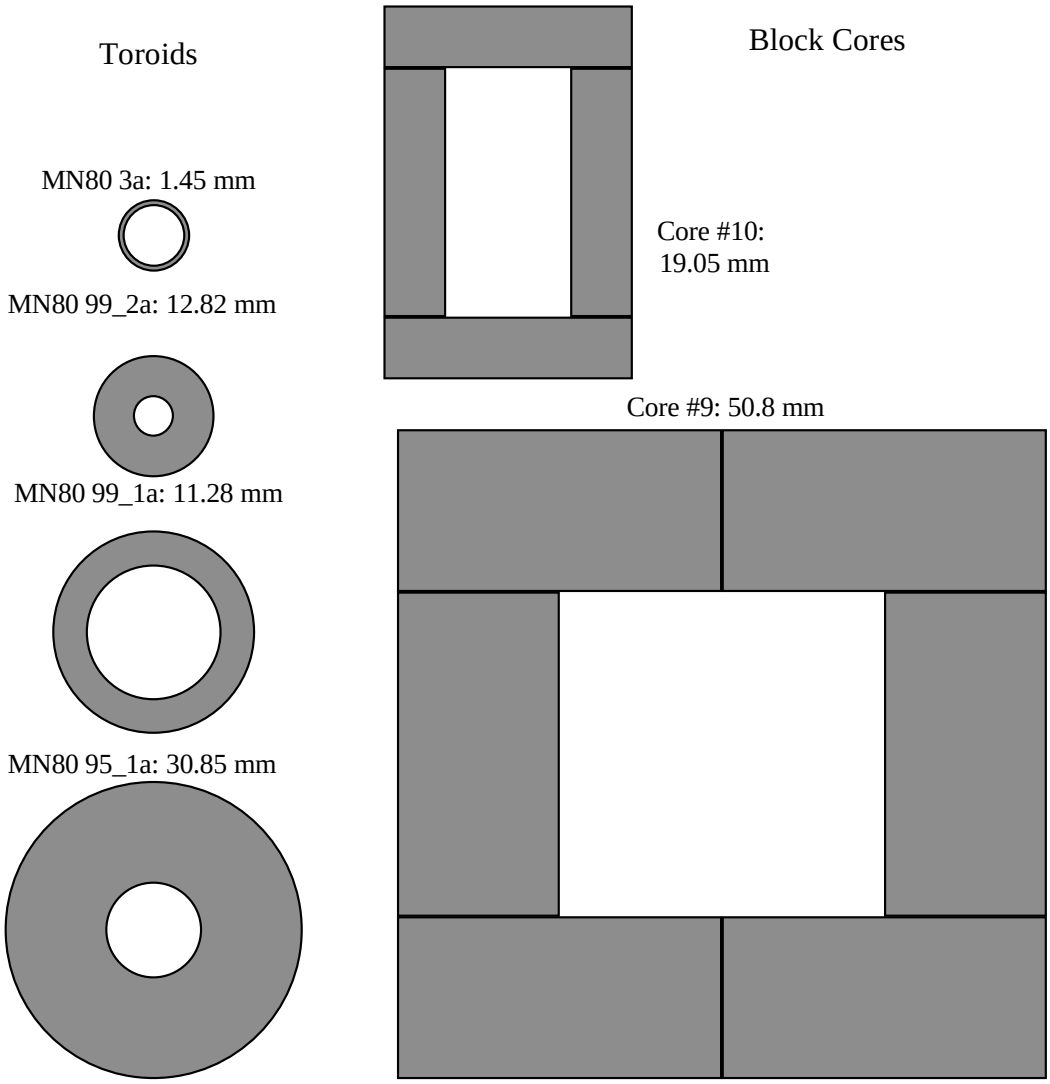

Figure 3.20: Various core geometries for measurement of dimensional resonance.

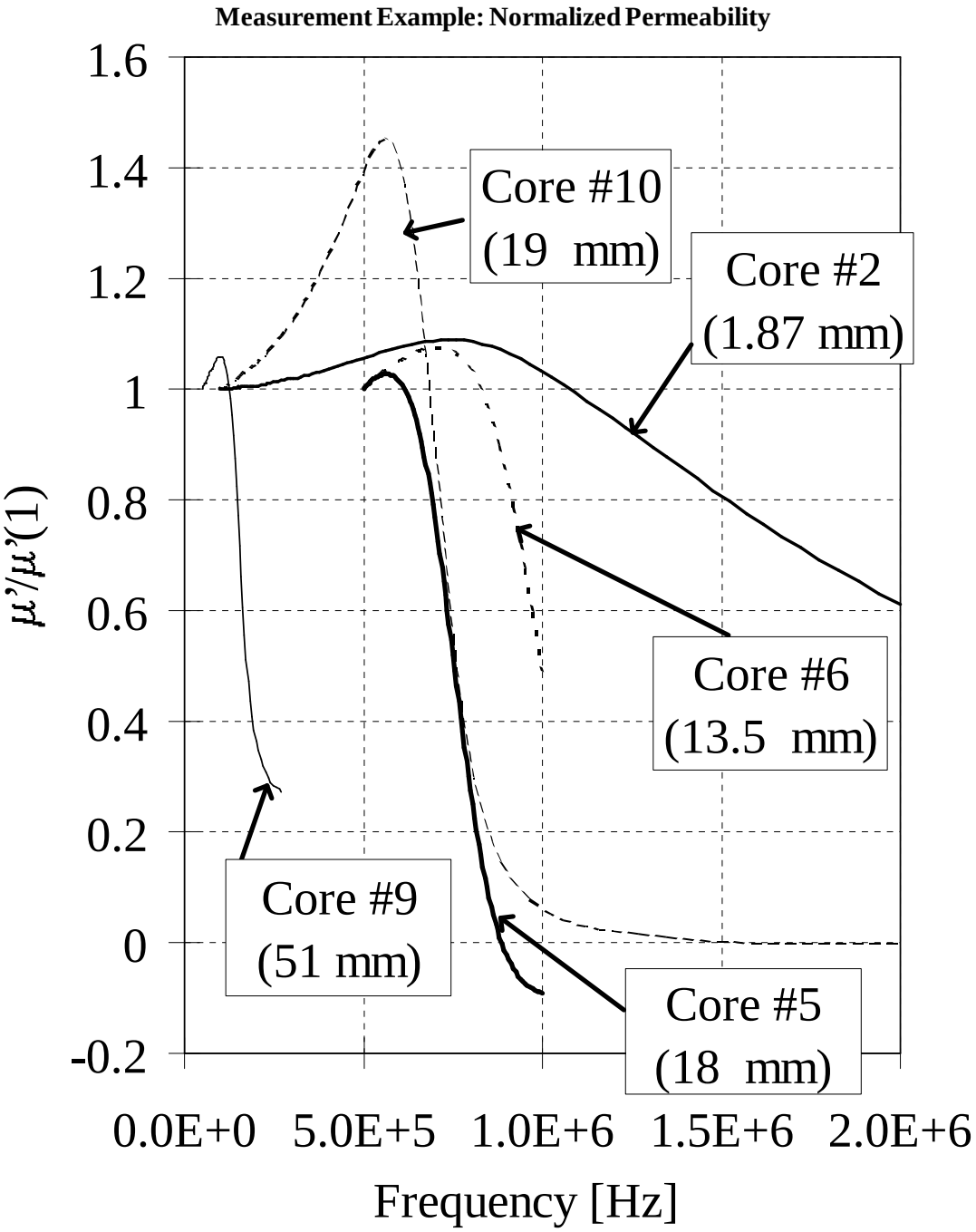

Figure 3.21: Normalized real permeability of the various core geometries in Figure 3.20.

3.6.3 Measured Core Loss Density

Figure 3.22 shows the differences in the core loss density measurements for the different size samples of B2 material. The loss density values are given simply by dividing the measured loss values by the effective volume of the core. While this approach assumes that the flux is distributed uniformly through out the core, it is the way that loss density is usually determined in practice. The graphs of Figure 3.22 show that in all cases the loss density increases with increasing core dimension and that loss is significantly higher than predicted by the published material data. This increase in loss density is shown in more detail in Figure 3.23 which compares the loss density for the small MN80 core (#1a) to that of the large toroidal core (#95-1a). These loss density curves show that the loss density values of these two cores are nearly equal at low frequencies but that there is a large increase in the loss density in the larger core as the frequency increases. At 1 MHz the loss density in the large core is approximately a factor of ten higher than that of the smaller core.

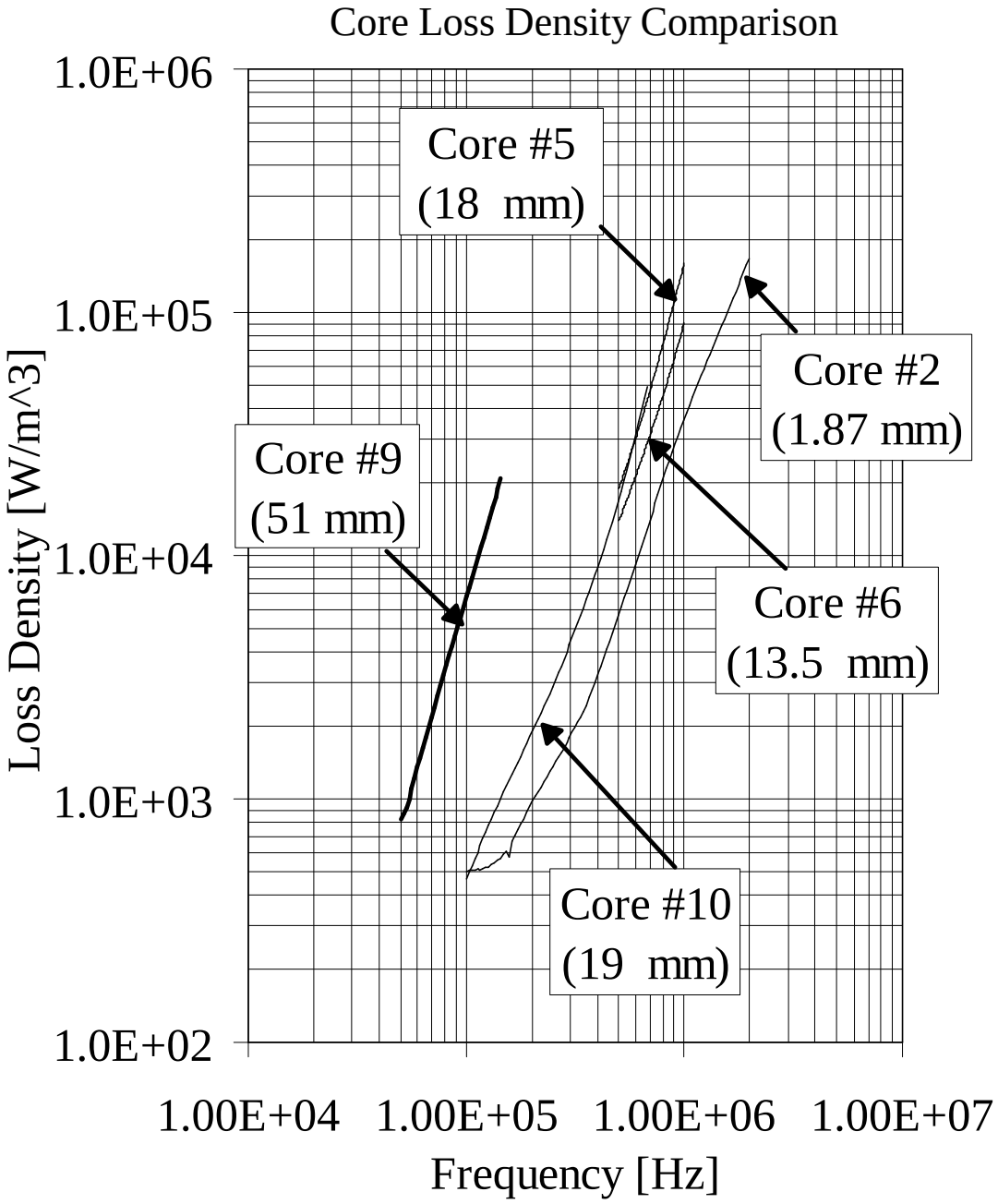

Figure 3.22: Core loss density in the cores of 3.20.

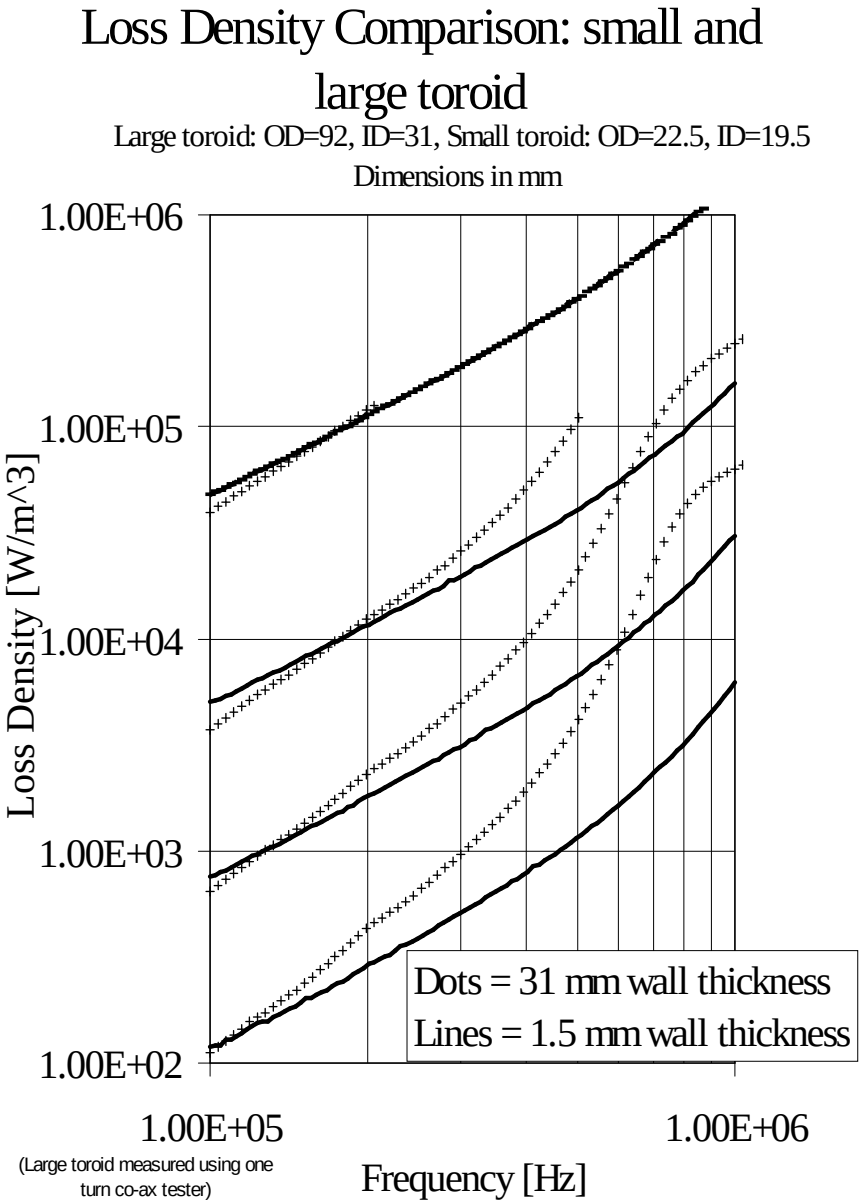

Figure 3.23: Comparison of loss density vs. frequency for various values of flux density in a small cross-section core (Solid lines) and a large cross-section core (+ symbols). Both cores are MN80 material.

Chapter 4

Analytical Modeling of Field Distribution in Ferrites

With the measurement data in Fig. 3.15 and the apparent shift in device performance based on core size illustrated in Fig. 3.21 as background, we now consider ways of modeling such effects analytically and numerically. In [97], Brockman, et al. present a thorough mathematical model of the dimensional resonance solution for a semi-infinite slab of a given thickness. That analysis is examined here—in a somewhat modified form—to illustrate how the physical geometry and material characteristics of the core interact in large structures.

4.1 Wave Propagation Constants in Ferrite

For time harmonic excitations and a known medium, solutions for the wave equation yield expressions for the electric and magnetic fields in terms of the complex wave number, $k = \omega\sqrt{\mu\epsilon}$ where μ and ϵ are the permeability and permittivity of the medium respectively. In general, both μ and ϵ are complex and therefore $\underline{k}$ can be written in its complex components as,

$$\underline{k} = \omega\sqrt{\underline{\mu}\underline{\epsilon}} = \omega\sqrt{(\mu' - j\mu'')(\epsilon' - j\epsilon'')} = k' - jk'' \tag{4.1}$$

The real and imaginary parts of $\underline{k}$ represent the phase constant and attenuation constant respectively. The wavelength λ is related to the phase constant k' as $\lambda = 2\pi/k'$, and therefore an expression for k' also provides an equation for the wavelength. In terms of the real and imaginary components of the complex permeability and permittivity, k' and k''

can be written as,

$$k' = \frac{\omega}{\sqrt{2}}\sqrt{|\mu||\epsilon| + (\mu'\epsilon' - \mu''\epsilon'')} \tag{4.2}$$

$$k'' = \frac{\omega}{\sqrt{2}}\sqrt{|\mu||\epsilon| - (\mu'\epsilon' - \mu''\epsilon'')} \tag{4.3}$$

4.2 Wavelength and Skin Depth Relations

Equations (4.2) and (4.3) are general equations that are valid for all simple media under sinusoidal excitation conditions. These relations are often presented in terms of a real dielectric constant, ϵ, and an explicit conductivity term, σ[1]. Additionally, the literature usually assumes that the magnetic material is lossless whereas (4.2) and (4.3) do not.

Retaining both the electric and magnetic loss terms in the formulation of the complex propagation constant allows us to write expressions for the material's wavelength and skin depth in a more general form.

$$\frac{\lambda}{2} = \frac{\sqrt{2}\pi}{\omega}\frac{1}{\sqrt{|\mu||\epsilon| + (\mu'\epsilon' - \mu''\epsilon'')}} \tag{4.4}$$

$$\delta = \frac{1}{k''} = \frac{\sqrt{2}}{\omega}\frac{1}{\sqrt{|\mu||\epsilon| - (\mu'\epsilon' - \mu''\epsilon'')}} \tag{4.5}$$

In [2], Snelling states that any given material cannot support standing waves due to dimensional resonance if certain conditions hold true for the dielectric and magnetic loss tangents. These loss tangents relate the real and complex parts of the complex permittivity and permeability respectively as defined in (3.8) and (3.16) which are repeated here.

$$\tan\delta_m = \frac{\mu''}{\mu'}$$

$$\tan\delta_e = \frac{\epsilon''}{\epsilon'} = \frac{\sigma}{\omega\epsilon'}$$

Substituting (3.8) and (3.16) in (4.2) and (4.3), the half-wavelength, $\lambda/2$, is [2],

$$\frac{\lambda}{2} = \frac{\sqrt{2}\pi}{\omega}\frac{1}{\sqrt{|\mu||\epsilon| + \mu'\epsilon'(1 - \tan\delta_m \tan\delta_e)}}$$

[1]Equations (4.2) and (4.3) can be converted to other forms by substituting σ/ω for ϵ'' and simplifying[1, 124] as given in detail in Section 3.4.2.

$$= \frac{\sqrt{2}\pi}{\omega} \frac{1}{\sqrt{\mu'\epsilon'\left(\sqrt{(1+\tan\delta_m^2)(1+\tan\delta_e^2)}+(1-\tan\delta_m\tan\delta_e)\right)}} \tag{4.6}$$

Similarly, the skin depth in terms of the wave attenuation constant, k'' and the loss tangents is,

$$\begin{aligned}\delta &= \frac{1}{k''} = \frac{\sqrt{2}}{\omega\sqrt{|\mu||\epsilon| - \mu'\epsilon'(1-\tan\delta_m\tan\delta_e)}} \\ &= \frac{\sqrt{2}}{\omega} \frac{1}{\sqrt{\mu'\epsilon'\left(\sqrt{(1+\tan\delta_m^2)(1+\tan\delta_e^2)}-(1-\tan\delta_m\tan\delta_e)\right)}}\end{aligned} \tag{4.7}$$

Equations (4.6) and (4.7) provide a general solution that is useful in modeling the complete response of a lossy material such as ferrite. These equations simplify to the standard values applicable for good conductors and good dielectrics when $\tan\delta_e \ll 1$ and $\tan\delta_e \gg 1$ respectively[2]. In the good conductor case, the attenuation in the material dominates the field penetration, and therefore the field is concentrated in a skin region near the surface. In the good dielectric case, the wave propagates relatively unattenuated into the material with an oscillation wavelength given by $\lambda \approx \sqrt{2}\pi/(\omega\sqrt{\mu'\epsilon'})$.

In MnZn ferrites and other semiconductor materials the field solution falls somewhere between the good conductor and good dielectric extremes. The skin depth (or penetration depth) and the wavelength is therefore a complex function of the magnetic, electric and dielectric nature of the material. This is illustrated in Figure 4.1 which plots the wavelength and skin depth respectively in B2 ferrite based on (4.6) and (4.7). In order to illustrate how the lossy nature of the ferrite affects these parameters, the wavelength and skin depth are plotted for four different cases: (a) a lossless case where μ and ϵ are purely real[3]; (b) a magnetic loss case where the permeability is complex but ϵ is real; (c) an electrical loss case where the permittivity is complex and μ is a real constant; (d) a combined loss case with both μ and ϵ complex. In all cases the material constants are the frequency dependent values taken from the measured data presented in Fig. 3.14.

Figure 4.1 shows that for frequencies in the range of a few hundred kilohertz the wavelength and the skin depth are comparable to each other and that they are both on the order of centimeters. The rough parity of the wavelength and skin depth at the frequencies of interest means that wave propagation and attenuation must be considered together; it is

[2]In the standard formulations of δ and λ, the magnetic loss tangent is usually assumed to be zero in all cases.

[3]The skin depth is not defined in this lossless case.

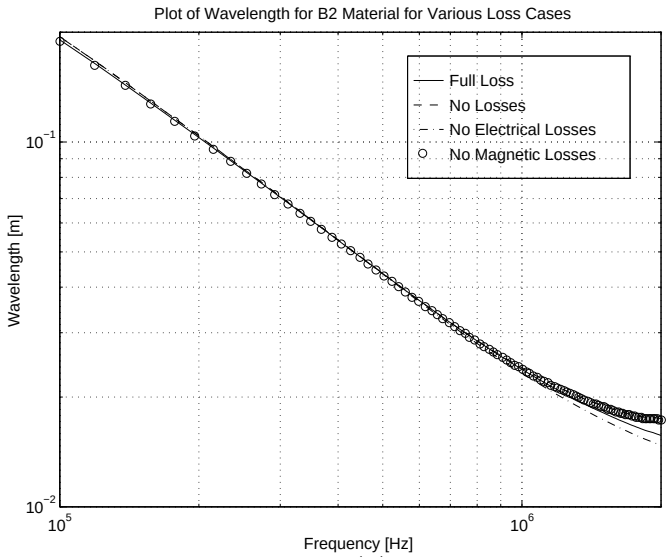

(a)

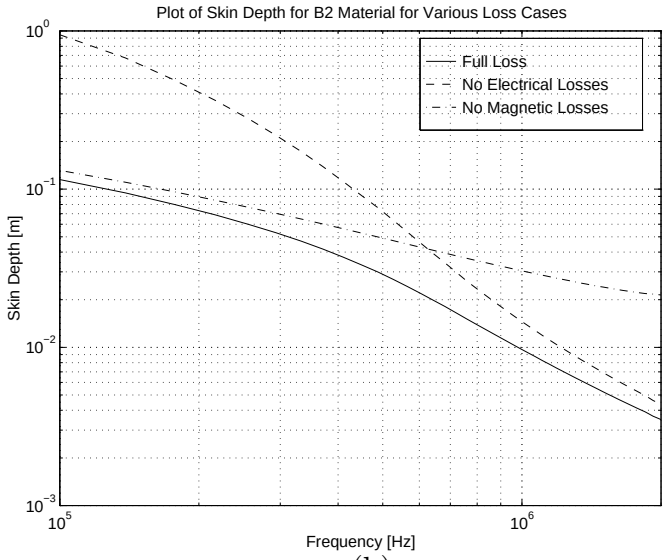

(b)

Figure 4.1: (a)Electromagnetic wavelength in ferrite vs. frequency for various combinations of loss mechanisms.(b) skin depth for the various combinations of loss mechanisms.

not adequate to examine only one aspect or the other through the use of simplified skin depth or wavelength relationships. This interdependence of propagation and attenuation is further demonstrated in Fig. 4.1 by the clear influence that the loss mechanisms play in determining δ and λ. The different curves in this figure show that the combination of magnetic losses and electrical losses results in more significant attenuation than is present for either mechanism acting alone. The wavelength, however, is not as significantly different for the various cases.

4.3 Field Solution in an Infinite Slab

The analytical model in [97] gives the solution for the magnetic field within an infinite slab such as that shown in Figure 4.2 in terms of the wave propagation constant, $\underline{k_b}$, the thickness of the slab, d, and the value of the magnetic field on the two infinite surfaces of the slab, $\underline{H}_{z_o}$, as

$$\underline{H}_z(x) = \underline{H}_{z_o} \frac{\cos(j\underline{k_b}x)}{\cos(j\underline{k_b}d/2)} \tag{4.8}$$

where k_b is the wave propagation constant used in [97], which is defined in terms of $\underline{\mu_r}$ and $\underline{\epsilon_r}$ and the propagation velocity in free space, c, as

$$\underline{k_b} = \frac{j\omega\sqrt{\underline{\mu_r}\underline{\epsilon_r}}}{c} = j\omega\sqrt{\underline{\mu\epsilon}} \tag{4.9}$$

This formulation differs from that used in (4.1) only in the inclusion of the phase constant, j, in k_b. In all of the discussion here the sinusoidal time variation is implied through the use of the phasor notation for the boundary field value, $\underline{H}_{z_o}$.

When the propagation constant notation of (4.1) is substituted for that used in [97], (4.8) is simplified somewhat as,

$$\underline{H}_z(x) = \underline{H}_{z_o} \frac{\cos(\underline{k}x)}{\cos(\underline{k}d/2)} \tag{4.10}$$

Based on the geometry of Figure 4.2, the electric field can be written by inspection from (4.10) in terms of the electric field phasor on the surface, $\underline{E}_{y_o}$ as,

$$\underline{E}_y(x) = \underline{E}_{y_o} \frac{\cos(\underline{k}x)}{\cos(\underline{k}d/2)} \tag{4.11}$$

This electric field solution, while not addressed in detail here, is related as a dual to the magnetic field solution.

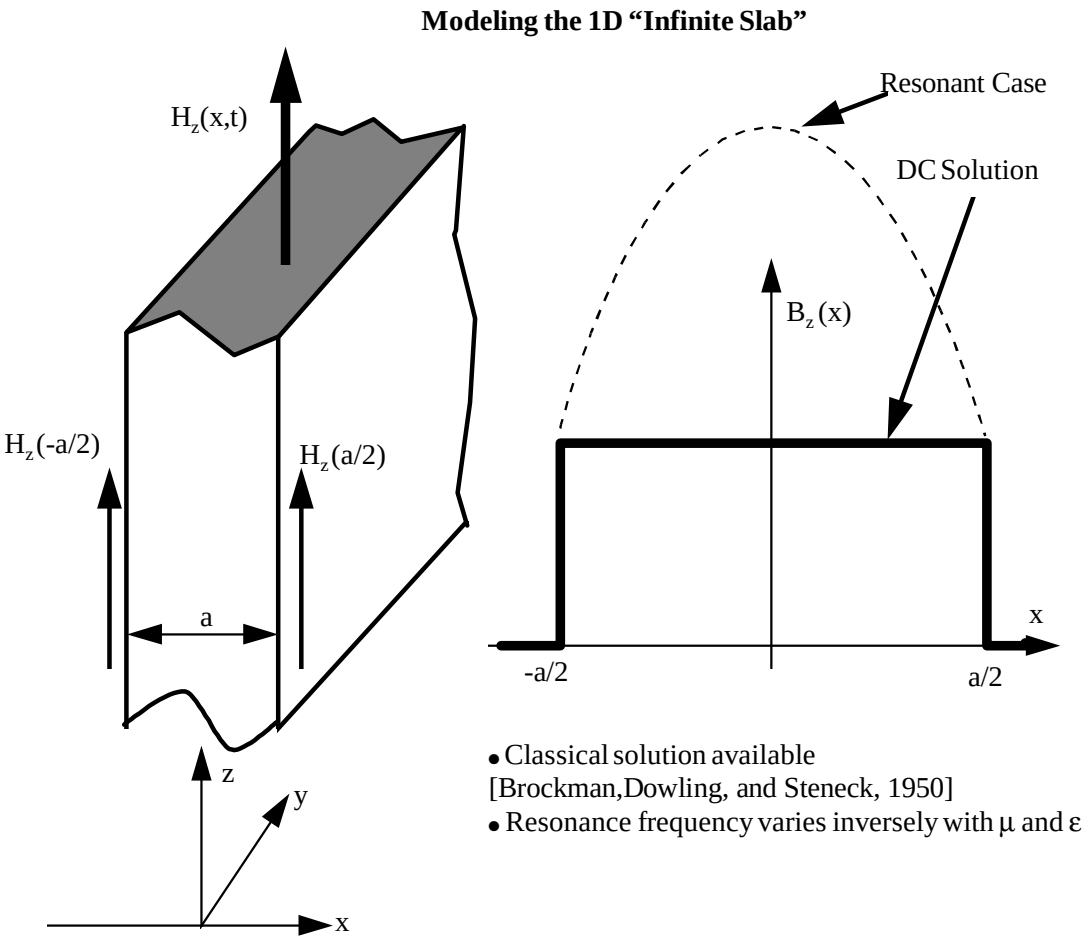

Figure 4.2: Infinite slab model for analytical solution of the flux distribution in the core.

4.3.1 Plots of Field Distribution for B2 material

Both (4.10) and (4.11) state that the distribution of the fields within the slab is dependent on the material through the propagation constant, $\underline{k}$, and on the size of the slab through the thickness, d. Since the propagation constant itself is frequency dependent as given in (4.1), the field distribution is also dependent on frequency. Figures 4.3–4.6 examine the magnetic field solution for a variety of slab thicknesses and excitation frequencies. For all of these plots, the field solution is plotted along a line that cuts horizontally through an infinite slab as shown by the line indicated by the dimension A in Figure 4.2.

In Figures 4.3 and 4.4, the magnetic field intensity as well as the magnetic flux density are plotted at a constant frequency of 500 kHz for slab thicknesses that vary from one millimeter to 50 millimeters. These plots show that when the thickness of the slab is small, the magnetic field and the resulting flux density are uniform and in phase with the boundary field phasor, $\underline{H}_{z_o} = 20$ [A/m]; As the thickness increases to approximately 2–3 mm, however, the slab reaches a significant fraction of the electromagnetic wavelength of the ferrite, and the field is significantly changed from the ideal uniform distribution. The fields first peak in the center of the core and then for larger cores the field distribution is highly non-uniform.

The flux density, $\underline{B}_z(x)$, in the core is related to the $\underline{H}_z(x)$ field by the permeability of the core. Since the hysteresis loss in the core is modeled through the use of a complex permeability, the flux density, is shifted in phase by an angle $\delta_\mu = \tan^{-1}(\mu''/\mu')$. The magnitude of the flux density at any point in the core is therefore the result of an in-phase real part, B_{real}, and an out-of-phase imaginary part, B_{imag}.

The real part of the B and H fields plotted in Figures 4.3 and 4.4 show that under the resonant condition the flux density in phase with the boundary source, $\underline{H}_{z_o}$, exhibits a full phase reversal in the central portion of the core. This means that the net flux that links the windings that excite such an idealized structure goes to zero for cores of a given size. Therefore, the apparent inductance of the device—given as the net flux linkage per ampere of exciting current—also goes to zero. This is the exact dimensional resonance phenomena discussed throughout this document and demonstrated in the measurement data of Section 3.6.

The slab of varying thickness in Figures 4.3 and Figure 4.4 are modeled with the material characteristics of the B2 ferrite at 500 kHz measured in Chapter 3. These plots indicate that under certain assumptions of core size and excitation frequency the establishment of dimensional resonance within the core can be modeled and predicted based on the idealized one-dimensional analytical model. In particular, the plots show that for B2 ferrite excited

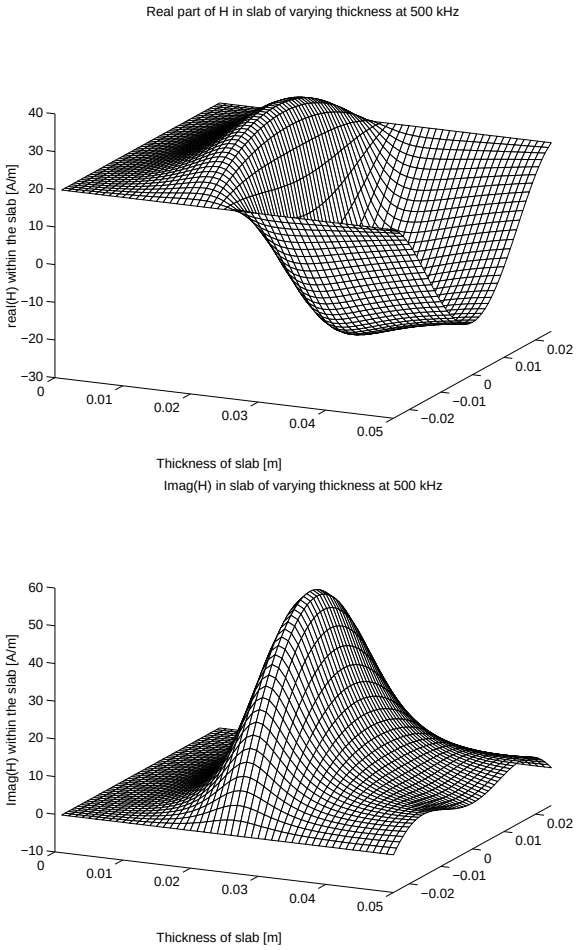

Figure 4.3: Real and imaginary components of the magnetic field within infinite slab of various thicknesses.

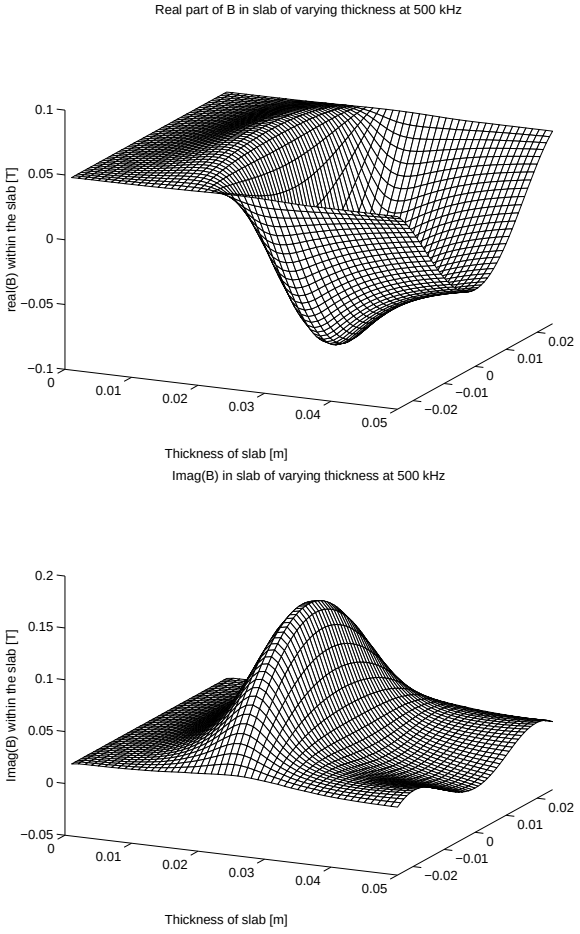

Figure 4.4: Real and imaginary components of the magnetic flux density within infinite slab of various thicknesses.

Table 4.1: Material Constants Used in Cases A–D

Case	Loss Mechanism	μ'	μ''	ϵ	σ [S/m]
A	None	3000	0	1e5	0
B	Magnetic	3000	-1000	1e5	0
C	Electric	3000	0	1e5	1
D	Combined	3000	-1000	1e5	1

at 500 kHz and with flux densities in the range of 50 to 100 mT, problems related to dimensional resonance can be expected for cores with cross-sectional dimensions of two to three centimeters.

Figures 4.5 and 4.6 present the results of a similar calculation; however in these figures the thickness of the slab is fixed at 20 millimeters and the frequency is allowed to vary from 100 kHz to 1000 kHz. These plots demonstrate the frequency response of a core of a fixed size to excitations of varying frequency much along the lines of the measurements of Section 3.6.

4.3.2 Field Distributions in Various Hypothetical Materials

The results plotted in the previous section show the distribution of the magnetic field within the infinite slab model based on the complete material characteristics measured for B2 ferrite as presented in Chapter 3. It is instructive, however, to also examine the calculated field distribution that results from various hypothetical models of the material characteristics. In this way, the relative importance of the lossy nature of the magnetic material as well as the conductivity and dielectric constant of the core can be determined. This follows much the same reasoning as the plots of electromagnetic wavelength and skin depth presented in Section 4.2. The specific material constants used in modeling each of the following cases are given in Table 4.1

Case A: Lossless Material

For this model, the core conductivity and the imaginary part of the permeability are both zero. The dielectric constant and relative magnetic permeability are 100,000 and 3000 respectively. For this lossless material, the 20 mm sample thickness will be equal to $\lambda/2$ at 433 kHz. Figure 4.7 shows the field solution for this case, and we see in that plot that the field peaks first in the range of 450 kHz and then has a large resonance at approximately

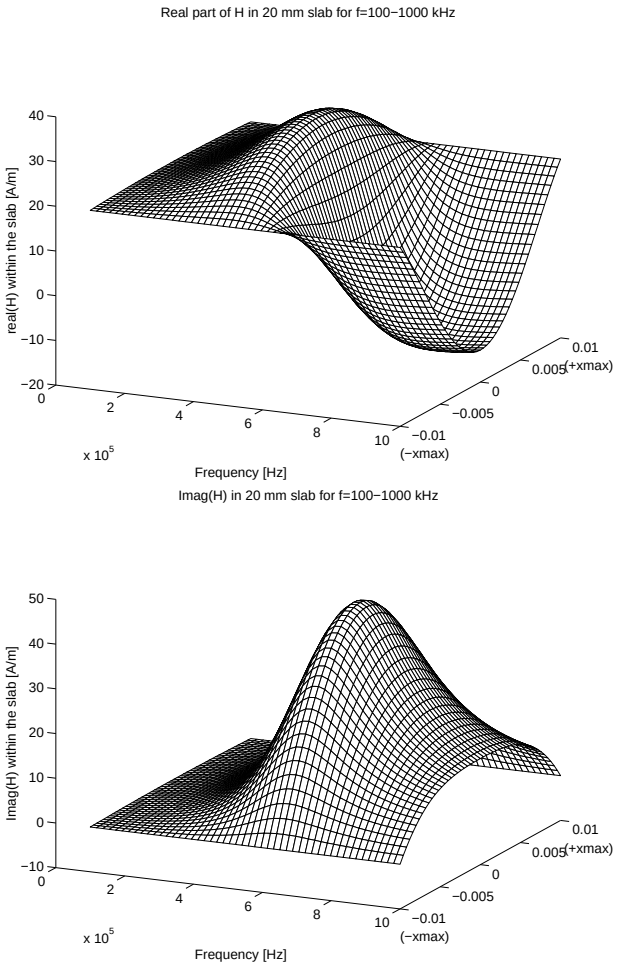

Figure 4.5: H Field components within a 20 mm thick infinite slab at frequencies from 100 kHz to 1 MHz.

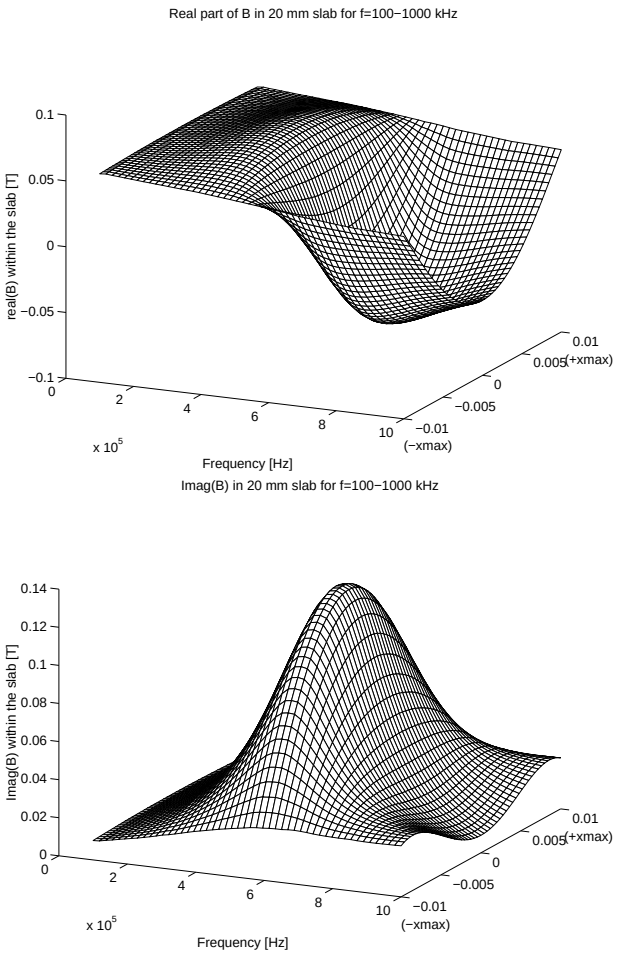

Figure 4.6: B Field components within a 20 mm thick infinite slab at frequencies from 100 kHz to 1 MHz.

1.3 MHz where $d = 3\lambda/2$.

Case B: Magnetic Loss Case

When the lossy nature of the magnetic material is included in the model, the wavelength shifts slightly, but more importantly, the material now attenuates the penetration of the field at high frequencies. This is seen in Figure 4.8.

Case C: Electrical Loss Case

For this model, the magnetic material is modeled as lossless (μ is real), but the core conductivity is included. The conductivity used here is 1 S/m, which is higher than the value typically specified for ferrite. However, as illustrated in the measurements of Chapter 3, the conductivity is a strong function of frequency. In addition, the conductivity is also strongly dependent on temperature—showing at least a two-to-one increase from room temperature to 100 degrees celsius—and therefore the use of 1 S/m for the conductivity is a rough compromise for illustrative purposes.

The plots of the field distribution for this electrical loss case are similar to those of Case B, however the attenuation due to the electric skin effect is not as pronounced as that due to the magnetic losses. For the material constants chosen here, the skin depth of the material at 500 kHz is 13 mm which makes the slab approximately one and on-half skin depths thick; at one megahertz, δ is 7.55 mm and the core is 2.7 skin depths thick.

Case D: Combined Loss Case

The individual loss mechanisms examined in the previous sections are now combined into a "combined-loss" case. This model is similar to that presented in the B2 example of Section 4.3.1; here, however, the material constants are simplified to those listed in Table 4.1 rather than the measured material constants. The field distribution for this case again shows the effect of the core resonance, but now the shielding effects of the attenuation due to the combined loss mechanisms is more pronounced. As illustrated in Figure 4.1, the skin depth when all losses are included is lower than it is when the electrical loss or magnetic loss is considered alone. This is born out in the field distribution for Case D shown in Figure 4.10.

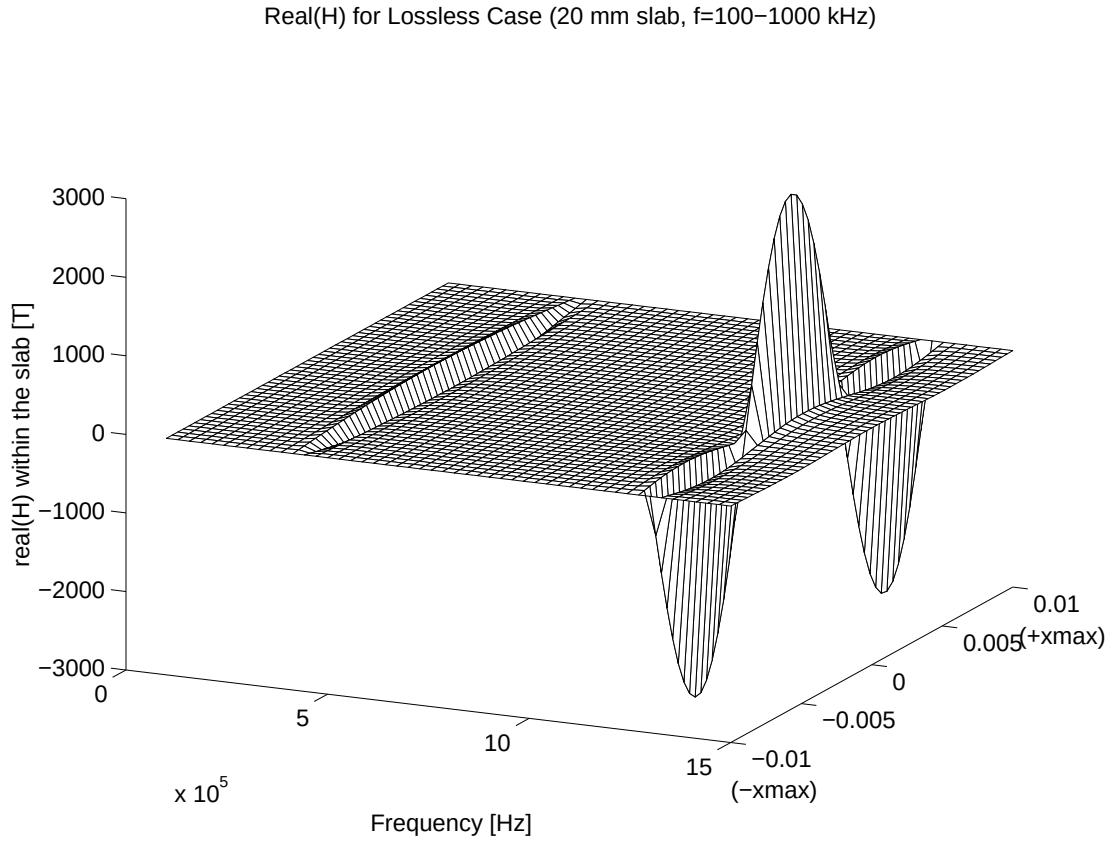

Figure 4.7: Case A: Lossless model. The one dimensional model of the field distribution within a infinite slab of thickness $d = 20$ mm. The H-field distribution within the ferrite is uniform and in phase with the exciting current at low frequencies. There is a peak in the center of the slab at approximately 450 kHz and a second resonance at the point where $d = 3\lambda/2$.

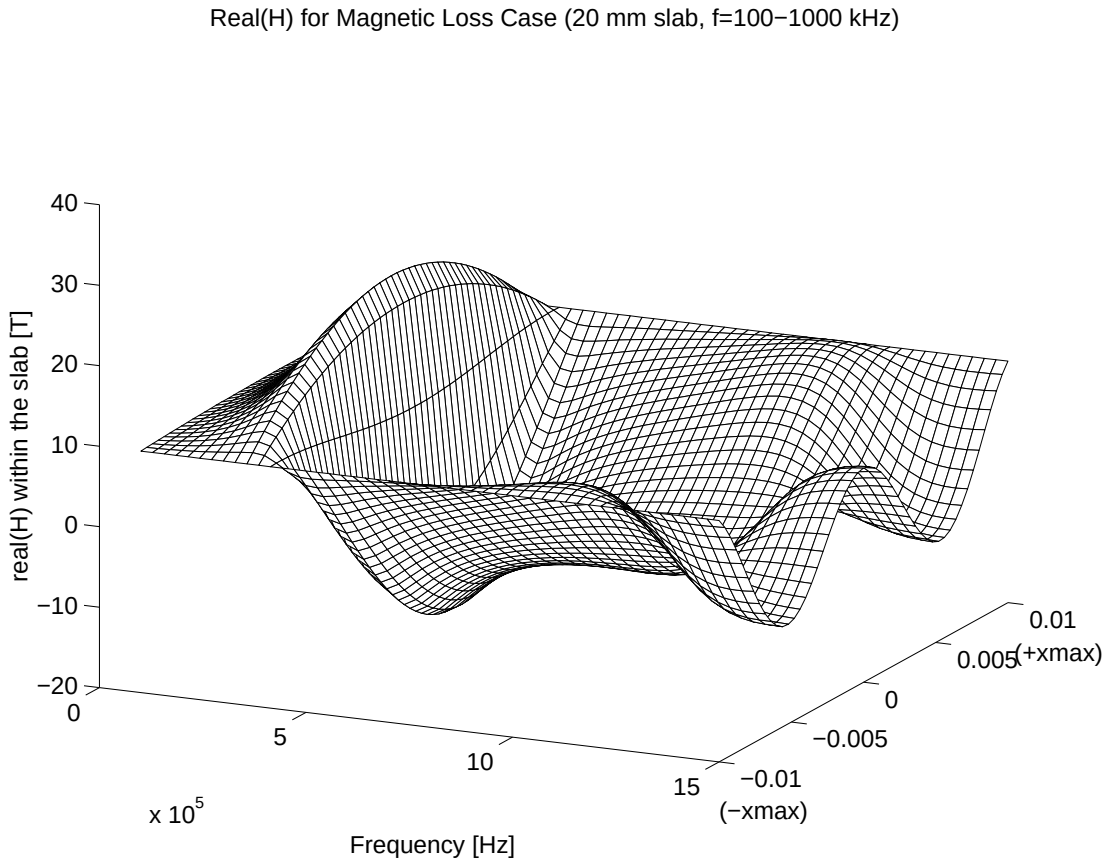

Figure 4.8: Case B: Magnetic loss model. The H-field distribution within the ferrite is uniform and in phase with the exciting current at low frequencies. The peak in the center of the slab at approximately 450 kHz is evident, but the slab is shielded from the exciting field as the frequency increases.

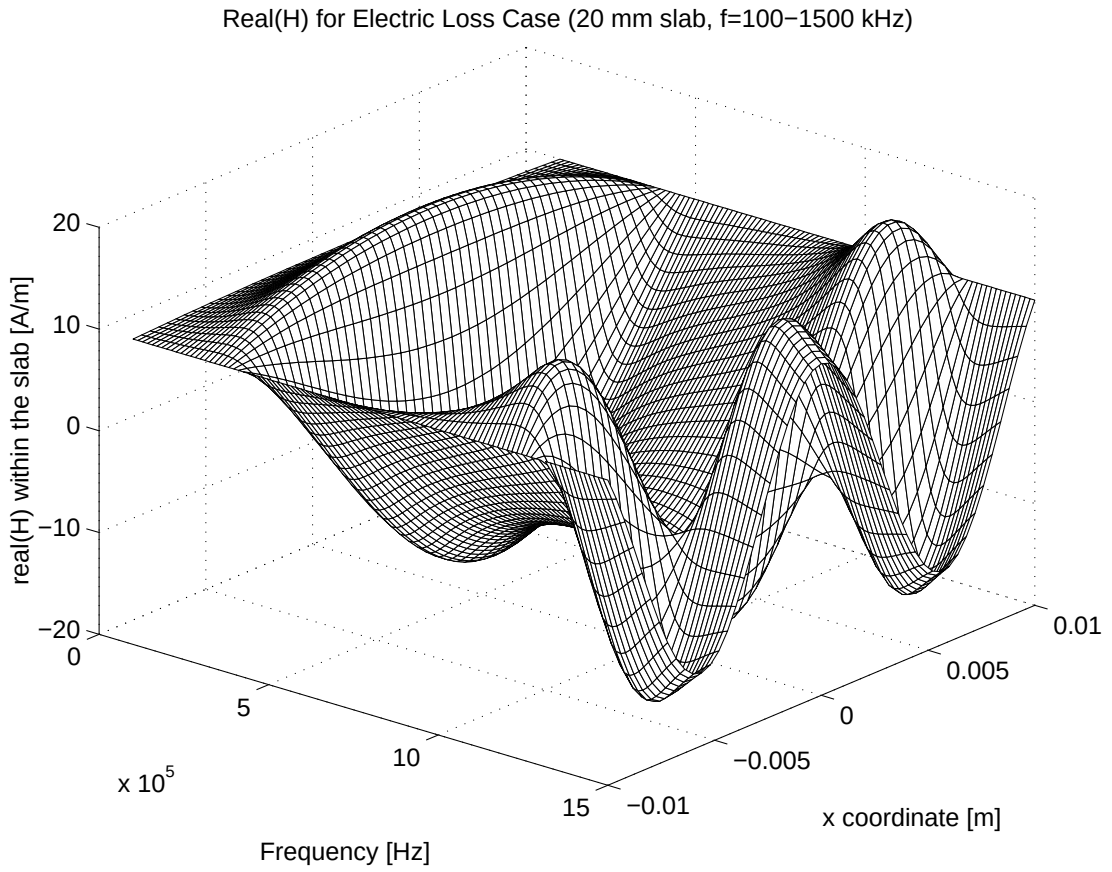

Figure 4.9: Case C: Electric loss model. The H-field is uniform and in phase with the exciting current at low frequencies. The peaks at both the half wavelength and at $d = 3\lambda/2$ are approximately the same amplitude.

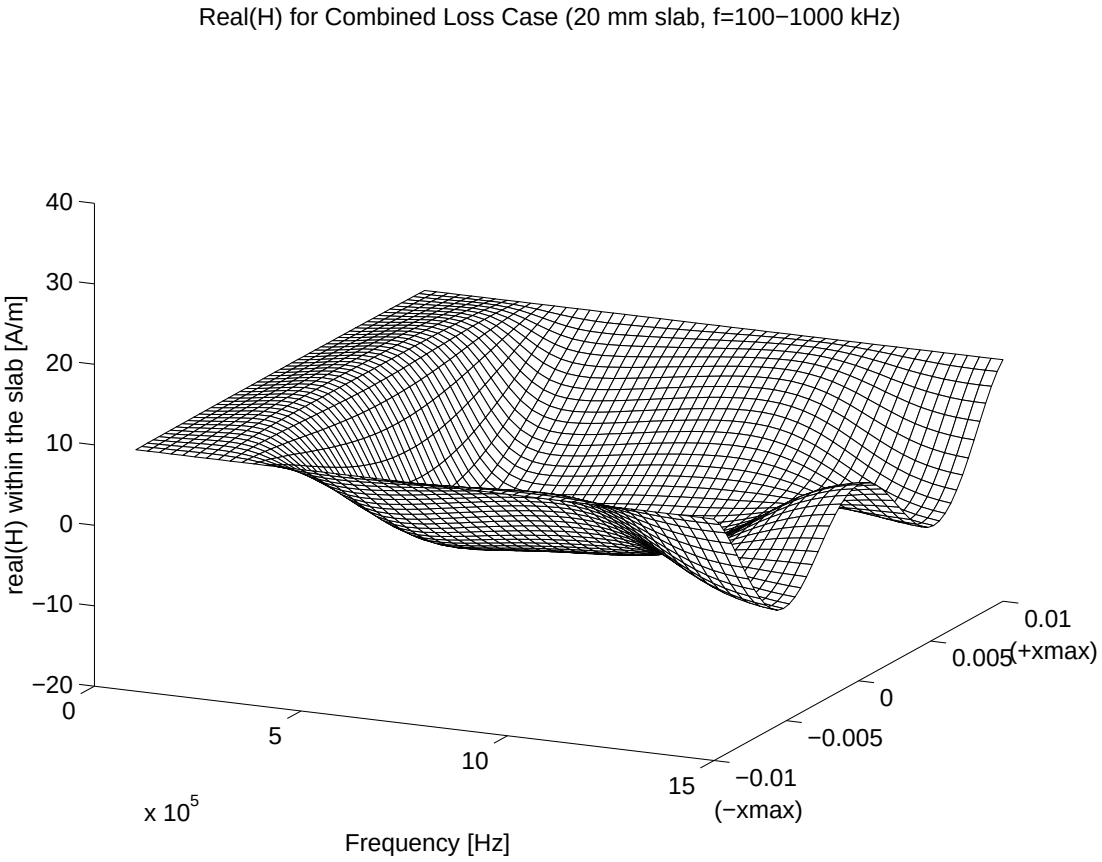

Figure 4.10: Case D: Combined Loss Model.

4.4 Relating the Field Solution to Device Characteristics

The field distribution plots in the previous section are helpful tools for understanding the way that the size of the core, the frequency and the material constants effect the overall performance of the device. However, in order to use this solution in practice, it is important to relate how changes in the field distribution effect the apparent impedance of a device built on such a core.

Equation (4.10) gives a solution for the $\underline{H}_z(x)$ field that can be used to compute the device impedance as follows: The impedance, $\underline{Z}$, is given by the ratio of the excitation voltage, $\underline{V}$, and the excitation current, $\underline{I}$. The voltage is related to the $\underline{H}_z(x)$ field through Faraday's Law. For a given core where the excitation winding has N turns and the core is characterized by geometrical constants ℓ_e for the effective magnetic path length and w for the width of the core, the induced voltage is,

$$\underline{V} = \frac{\partial \Lambda}{\partial t} = N\frac{\partial \Phi}{\partial t} \tag{4.12}$$

$$= Nw\int_{-d/2}^{d/2} \frac{\partial \underline{B}_z(x)}{\partial t}dx \tag{4.13}$$

If the permeability of the core is assumed constant throughout the core—which is a large assumption to make considering the variation of flux density that exists under resonant conditions—then the integral in (4.13) can be simplified to an integral of the known function for $\underline{H}_z(x)$. Carrying out this process gives,

$$\begin{aligned}
\underline{V} &= j\omega\underline{\mu}Nw\int_{-d/2}^{d/2}\underline{H}_z(x)dx \\
&= j\omega\underline{\mu}\underline{H}_{z_o}Nw\int_{-d/2}^{d/2}\frac{\cos(\underline{k}x)}{\cos(\underline{k}d/2)}dx \\
&= \frac{2j\omega\underline{\mu}Nw\underline{H}_{z_o}\sin(\underline{k}d/2)}{\underline{k}\cos(\underline{k}d/2)} \\
&= \frac{j\omega\mu Nw\underline{H}_{z_o}\tan(\underline{k}d/2)}{\underline{k}/2}
\end{aligned} \tag{4.14}$$

The excitation boundary field, $\underline{H}_{z_o}$, is given in terms of the excitation current as,

$$\underline{H}_{z_o} = \frac{N\underline{I}}{\ell_e} \tag{4.15}$$

Solving now for the impedance results in a closed-form expression that is useful for computing the performance of a given structure:

$$\underline{Z} = \frac{j\omega\underline{\mu}N^2 w}{\ell_e}\frac{\tan\underline{k}d/2}{\underline{k}/2} \tag{4.16}$$

$$= j\omega L_o\frac{\tan\underline{k}d/2}{\underline{k}/2} \tag{4.17}$$

where the L_o term represents the inductance of the structure independent of the dimensional effects in the core; the dimensional effects are represented by the terms involving the propagation constant and core dimension d.

The impedance expression in (4.17) shows the same alternation of inductive and capacitive nature characteristic of the impedance encountered at the input of a short-circuited transmission line [128]. This is illustrated in Figure 4.11 which plots the apparent impedance of a two lossless infinite slab of ferrite. The impact of the slab thickness is indicated by the shift in the location of the first resonant frequency for each of the geometries: the one millimeter slab resonates at 17 MHz while the 20 mm core resonates at approximately 866 kHz.

The responses of lossless geometries such as presented in Figure 4.11 form an outer envelope of the response of actual, lossy materials. Figure 4.12 shows how the various loss mechanisms present in ferrites effect the magnitude of the impedance spectrum. The losses in the core attenuate the extremum of the impedance spectrum, but the oscillatory nature of the response at multiples of the material wavelength are clearly evident. Both the eddy currents modeled through the conductivity and the magnetic losses modeled through the complex permeability act similarly, the combined-loss case shows the greatest degree of attenuation.

Figure 4.12 shows that the impedance of a lossy material approaches a flat, relatively constant—that is, a resistive value—for frequencies above the first resonance frequency. The net effect of this standing-wave phenomena, therefore, is a phase rotation in the material that places an upper limit on the impedance that a particular core can attain. In power electronics applications such as noise filters and energy storage inductors this is a significant limitation since a given design inductance is required. Figure 4.13 shows how the apparent inductance changes for a 20 mm thick slab of material as the excitation frequency changes; the material constants are the same as those used in Case A–Case D of the previous section. The apparent inductance is normalized to a value of unity at low frequencies, but as the excitation frequency approaches the first resonance, the inductance decreases and becomes negative for the lossless or low-loss models. For the combined-loss model, the inductance is essentially reduced to zero for frequencies above 400-500 kHz, which is less than have the bandwidth typical of MnZn ferrites.

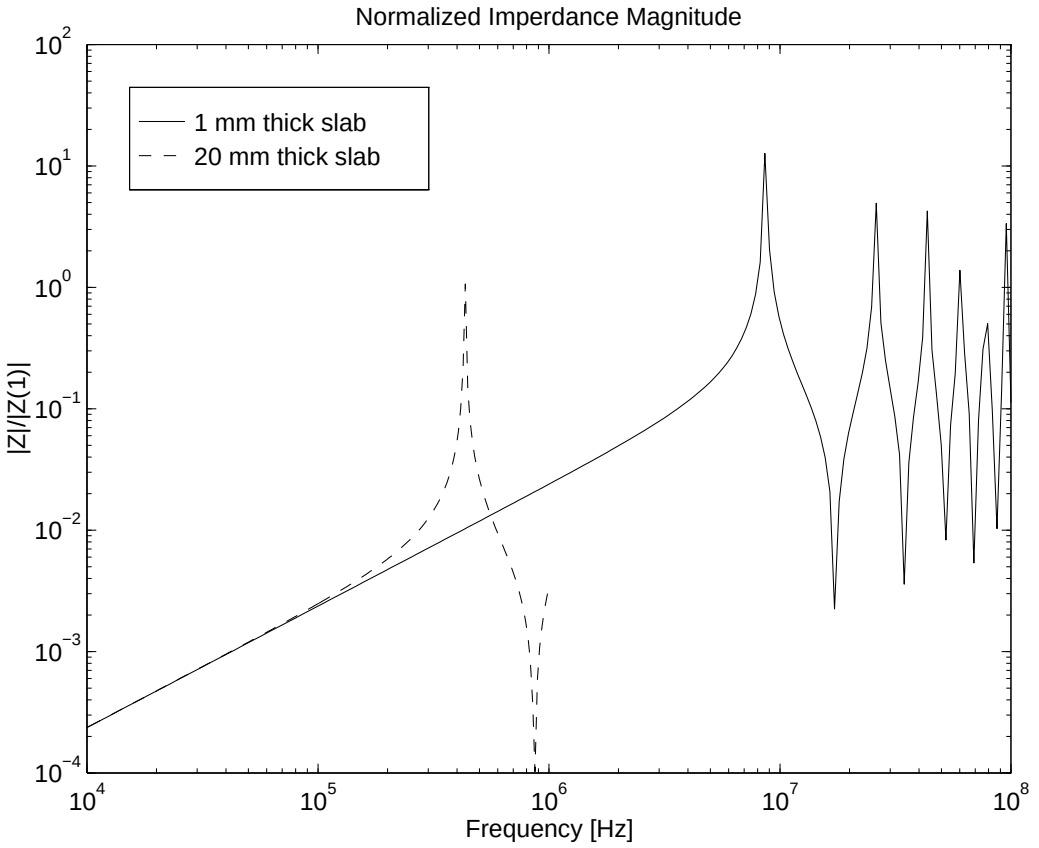

Figure 4.11: Impedance spectrum of two lossless geometries with $\underline{\mu} = 3000 - j0$, $\sigma = 0$, $\epsilon = 100,000$. The resonant point for each geometry occurs at the first minimum of the impedance response.

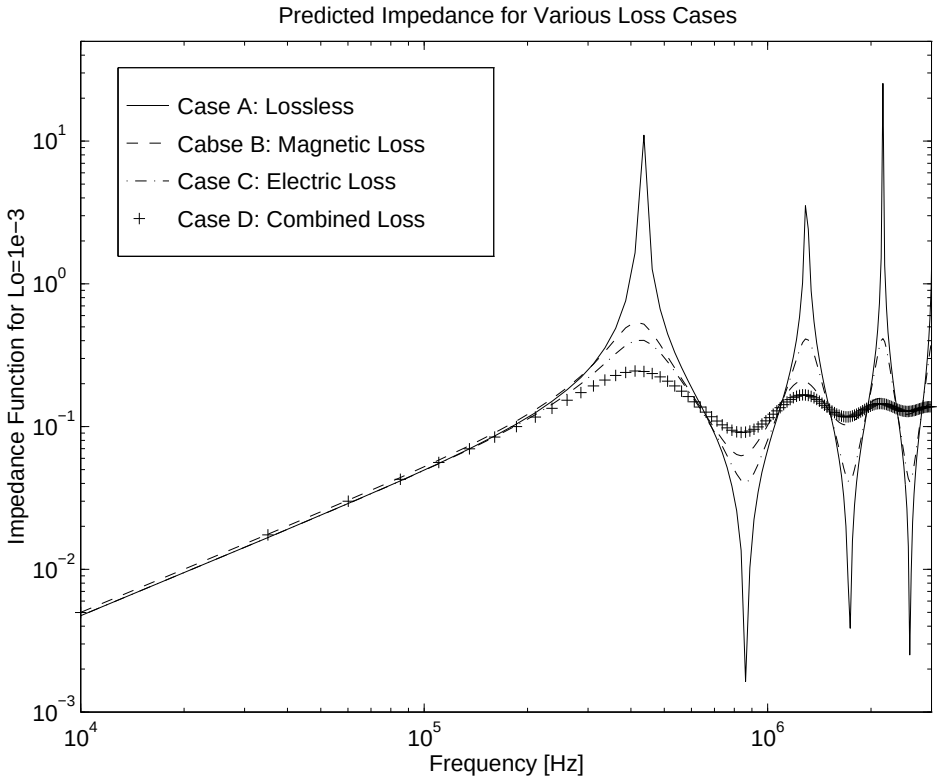

Figure 4.12: Magnitude of the impedance of a 20 mm thick infinite slab of ferrite with four different combinations of loss characteristics.

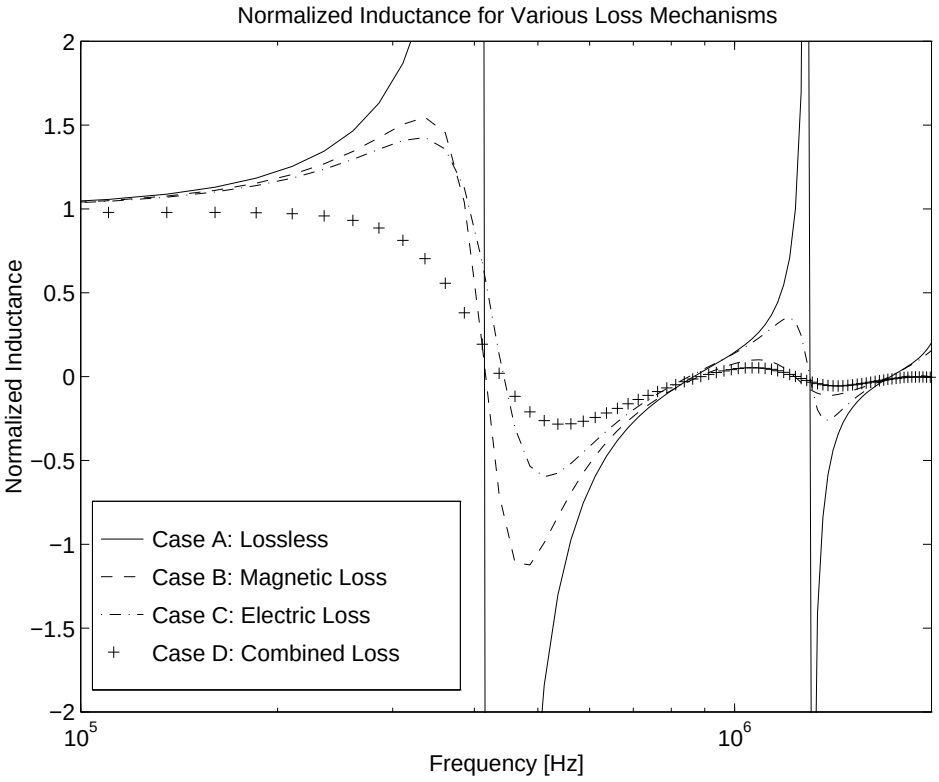

Figure 4.13: Normalized inductance in a 20 mm thick slab of ferrite as a function of frequency with four different combinations of loss characteristics.

The final figure in this section, Figure 4.14, shows a set of impedance plots for a fixed frequency with various sample thicknesses. Here the impedance normalized to the thickness of the slab is presented for the same four loss combinations presented in the previous plots. In addition, Figure 4.14 includes curves for a baseline material and a non-dielectric material. The baseline case models a purely magnetic material where $\underline{\mu_r} = 3000, \epsilon_r$ and $\sigma = 0$; the non-dielectric case models a core with only eddy current losses where the magnetic losses are zero and the dielectric constant is that of free space. These two limiting cases are included to illustrate the assumptions employed in standard design equations.

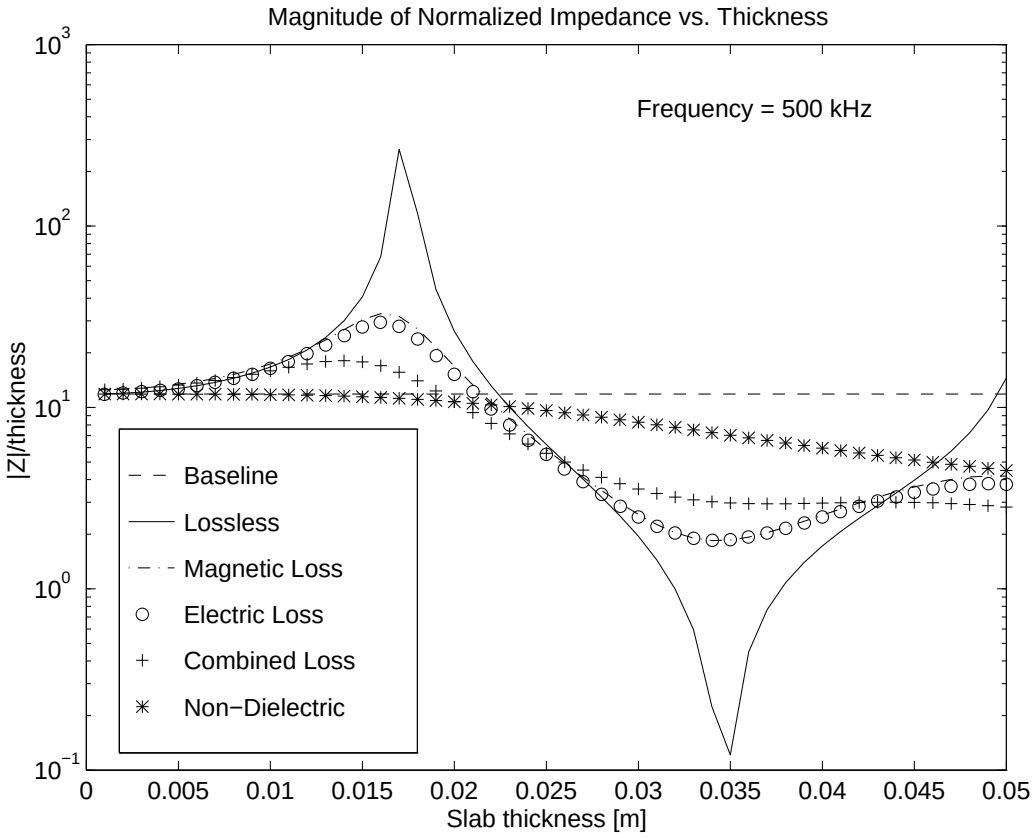

Figure 4.14: Normalized inductance in a 20 mm thick slab of ferrite as a function of frequency with four different combinations of loss characteristics.

Chapter 5

Numerical Modeling of Ferrite Core Structures

5.1 Finite Element Analysis Tools

The analytic solution presented in Chapter 4 shows one possible method—and the only method significantly represented in the literature—of modeling the dimensional effects in ferrite cores. The impedance predicted by this simplified one-dimensional model and the measured characteristics presented in Chapter 3 show an encouraging similarity, at least in general shape and character. However, there are significant limits to the use of such analytical models since they become unwieldy for complex shapes. This chapter introduces numerical field solutions and shows how they can be used to compute the impedance and loss performance of a wide variety of core geometries. This sets the groundwork for a detailed examination in Chapter 6 of the particular geometry of the inductively–coupled charger introduced in Chapter 1

The finite element analysis (FEA) technique is a useful numerical method for analyzing the field and loss distribution in transformer and inductor cores. Ideally, a complete FEA solver—or any other numerical solver such as a boundary element numerical solver—should be capable of:

- addressing the nonlinear ferrite material characteristics,
- performing coupled electromagnetic/thermal simulations,
- calculating a solution for anisotropic and inhomogeneous materials.

In addition, in order to study the problem of dimensional resonance the numerical solver should be able to solve the full wave equation including all of the loss and energy storage mechanisms and not simply a static or quasi-static approximation. In practice this means that the solvers must accommodate complex permeability and either complex permittivity or a combination of real permittivity and real conductivity.

5.1.1 Description of Commercial FEA Codes

This thesis utilizes a commercial FEA solver (Maxwell from Ansoft Corporation) to model the physical processes that take place in ferrite–cored devices. This commercial code uses a linear solver that represents the hysteresis losses in the core through the use of a complex permeability[1]. As discussed in Section 3.2.1, the complex permeability model represents the true B-H hysteresis loop as an ellipse. This is clearly not rigorous, but it has shown to be a rather acceptable approximation for core loss estimation below saturation flux density levels[129]. We use the simple-media relations here since they form the basis of the main FEA tools available for use in modeling the various cores of interest. Before proceeding, however, we note the likely difficulties related to using such a simplified approach.

5.1.2 Limits of the FEA Solvers

The most troublesome aspect of the simple-medium field solution is the assumption of homogeneity in the core. Since the flux density is a strong function of the magnetic field and since the H field in the core is non-uniformly distributed throughout the core, we know that the flux density is similarly non-uniform. In fact, since the permeability itself is a function of the flux density, the material is both inhomogeneous and nonlinear. This is true—although not usually problematic [125]—even in simple core structures such as toroids and small E cores.

If we consider for a moment the example of a toroidal core with rectangular cross section operating near saturation we can see how the nonlinearity and inhomogeneity of the core interact. Since the H field in the toroid falls off with the radius, the maximum field intensity is on the inner surface of the core. As the excitation current increases, the applied field increases, and eventually the innermost section of the toroid saturates. This forces the entire flux to flow in the remaining unsaturated portions of the core. In this partially saturated case the permeability in the saturated region is essentially that of air while the

[1]Nonlinear solvers that can model core saturation in the absence of hysteresis are also available in the commercial codes, but these are not used here.

rest of the core is essentially unsaturated ferrite. The material is therefore inhomogeneous as a result of its nonlinear nature.

While this is an extreme case, the same phenomenon occurs in all cores to some extent; if we can accommodate this effect in some way in the simulation of the core then we should be able to improve on the applicability of the results to actual devices. In the least, we need always to check that the results of the FEA simulation do not violate the assumption that the flux density is everywhere well below saturation.

5.2 Examination of Dimensional Effects Using Linear FEA

The foregoing discussion establishes the fundamental theory behind the simulation of ferrite cores using a linear field model as well as the limitations of such an approach. The main advantage of this tool over the use of analytical solutions such as those presented in Chapter 4 is its capability of solving arbitrary geometry problems with non-ideal boundary conditions. In this chapter, we use available commercial tools to examine a set of ferrite cores of various geometries. The goal here is to establish in some detail the fields that exist within these cores as dimensional effects become significant.

Specifically, we wish to illustrate the differences between eddy current effects and dimensional resonance effects in the core; through the use of the numerical solver we can examine the flux and loss distributions within the cores for various combinations of material characteristics. The approach in this Chapter mirrors that in Chapter 4: the frequency and amplitude dependent measured characteristics of the B2 and MN80 ferrite materials are used for modeling an actual ferrite and the influence of the various loss mechanisms is evaluated by using different combinations of representative constant-value material characteristics. The core shapes examined below include several ideal geometries as well as a large toroidal core and a multi-piece structure made up of several large blocks of core material; these geometries are two-dimensional representations of the cores used in section 3.6.

5.2.1 Infinite Slab Model

There are several simple structures that have been examined in the literature and for which closed-form analytic solutions exist. It is instructive to start the numerical simulation

process with just such models in order to establish the validity of the numerical solution to the problem and to build a foundation upon which we can make comparisons when we consider more complex structures.

Model Description

The simplest geometry that we consider is the same infinitely long slab of ferrite that is modeled analytically in Chapter 4. The geometry of this structure is repeated here in Figure 5.1 as it is modeled in the 2D FEA solver. This structure is the idealization of the case where a number of current carrying conductors are wound around a plate of ferrite such that the magnetic field has only a y component and the electric field has only an z component. In this case, the assumption is made that the plate is so much longer in both the y and z directions than in the x direction that the end effects in z and y can be neglected. These are exactly the assumptions made in the analytical solutions examined in Chapter 4.

Setting the Boundary Conditions of the Problem For convenience, we repeat here Equations (4.10) and (4.11), the closed form solutions for the variation in the $\underline{E}_z(x)$ and $\underline{H}_y(x)$ fields in the x direction based on the assumptions listed above[2]:

$$\underline{H}_y(x) = \underline{H}_{y_o} \frac{\cos(\underline{k}x)}{\cos(\underline{k}d/2)}$$

$$\underline{E}_z(x) = \underline{E}_{z_o} \frac{\cos(\underline{k}x)}{\cos(\underline{k}d/2)}$$

In these equations, the electrical losses in the material are included as an ϵ'' term within the complex wave number k. This loss term includes the dielectric losses and the losses due to the DC conductivity. Since the FEA solver accommodates only a real component of dielectric constant, we use the electric power loss equations in terms of an effective AC conductivity given by (3.41) repeated here:

$$\begin{aligned} \langle P_{d_e} \rangle &= \frac{1}{2} \int_V \left(\sigma_{eff} \frac{|\underline{J}_c|^2}{\sigma_{eff}^2} \right) dV \\ &= \frac{1}{2} \int_V \left(\frac{|\underline{J}_c|^2}{\sigma_{eff}} \right) dV \end{aligned}$$

[2]In these equations the coordinate system is changed to agree with that used in the Maxwell solver. The x coordinate remains the same, but since the solver represents the x-y cross-section of the model the H field is y-directed and the E field is z-directed.

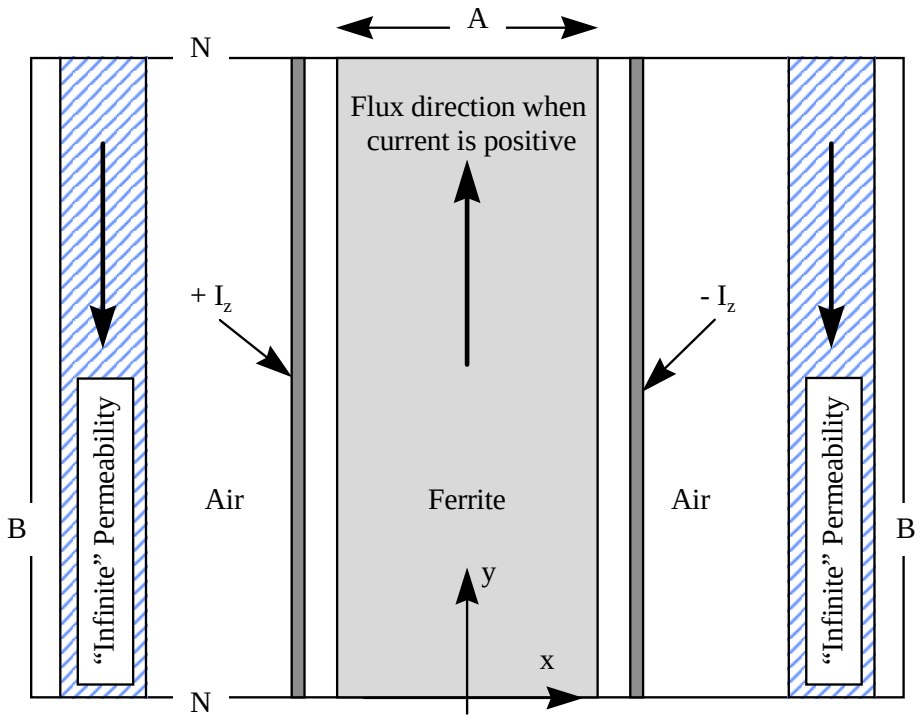

Figure 5.1: An infinite slab model of a section of a ferrite core. The line A-A′ is the line along which the field distributions are plotted in the results section.

The above equations are functions of the thickness of the slab, d, as well as the complex wave number, $\underline{k}$. As illustrated in (4.1), $\underline{k}$ is a function of the material characteristics as well as the excitation frequency. This means that we can examine the dimensional effects in a core based on the solution in (4.10) and (4.11) by varying either the core size, the frequency of excitation or any of the material characteristics. In the following sections—as in Section 4.3—we examine both the constant thickness case where the material constants vary with the excitation frequency as well as the constant frequency case where the material characteristics are constant and the core geometry is allowed to change.

Description of Simulation Cases

In simulating the infinite slab geometry, we utilize various combinations of the complex permeability, $\underline{\mu}$, real dielectric constant, ϵ, and the ac conductivity, σ_{eff}. Table 5.1 lists the material values used in the simulations and designates five different simulation test cases, Case A through Case E. Case A is the lossless case and Cases B, C and D each represent the presence of one particular loss mechanism in isolation, and Case E represents the full loss model:

Case A: Lossless Assumes an ideal magnetic core with a purely real permeability and permittivity and no loss mechanisms.

Case B: Magnetic Loss Includes hysteresis loss by including a complex permeability but sets the conductivity to zero.

Case C: Eddy Current Loss Models conduction losses consisting of both eddy-current losses and dielectric losses but with a dielectric constant of free space. This models the pure skin-effect problem in the absence of dielectric effects. The permeability is modeled by its complex value.

Case D: Electric Loss Includes ferrite ac conductivity as in Case C but also includes the high dielectric constant of ferrite.

Case E: Full Loss Case combines all of the loss mechanisms in one model. For this case, all of the material values as listed in Table 5.1 are used.

Table 5.2 lists the values of $\underline{\mu}$, ϵ', and σ_{eff} used in the simulation process. These data are derived from measurement of B2 cores with a flux excitation of 10 mT.

Table 5.1: Material values used for the various frequencies of the FEA simulations

Case	Loss Mechanism	μ	ϵ	σ [S/m]
A	None	Real	ϵ_r	0
B	Magnetic	Complex	ϵ_r	0
C	Eddy Current	Complex	ϵ_o	σ
D	Electric	Real	ϵ_r	σ
E	Combined	Complex	ϵ_o	σ

Table 5.2: Material Data Used for Simulation of B2 Material Cores at 10 mT

Frequency	μ_r'	μ_r''	ϵ_r	σ_{eff}
10 k	2000	10	202000	0.1725
100 k	1833	126	130000	0.349
200 k	1802	146	116000	0.483
300 k	1822	196	109000	0.599
400 k	1845	270	105000	0.705
500 k	1863	362	101000	0.807
600 k	1864	475	99100	0.906
700 k	1842	596	97400	1.01
1000 k	1664	905	93000	1.32

Field Plots for the 1D Cases

Figure 5.2 shows the lines of flux in the infinite slab model at 10 kHz and 1 MHz. The distribution in the high frequency case shows that the reversal of flux direction which is characteristic of the resonant condition in the core. The variation of the field distribution with frequency is illustrated in Figure 5.3 where the real part of the magnetic field and the flux density along line A-A′ shown in Figure 5.1. The real part of the field is plotted since it is the excitation source and since it is uniform and in-phase with the excitation current when the core dimension is not a significant issue. It is important to remember in examining these plots that the values of the field or flux density are time harmonic and therefore the instantaneous values of the fields are quite different from the magnitudes. The plots in Figure 5.3 show the H field in the 20 mm thick slab at selected frequencies with the core modeled as in Case E of Table 5.1. This figure shows the shielding of the core as expected based on the analytic model presented in Chapter 4. Figure 5.4 shows the field distribution within the core for the various loss mechanisms. Here we see that Case C which neglects the dielectric nature of the core—as is common practice—results in a field that is much more uniform than that of the full material model of Case E. Figure 5.4 also includes a curve showing the analytic solution calculated using (4.10) is plotted along with

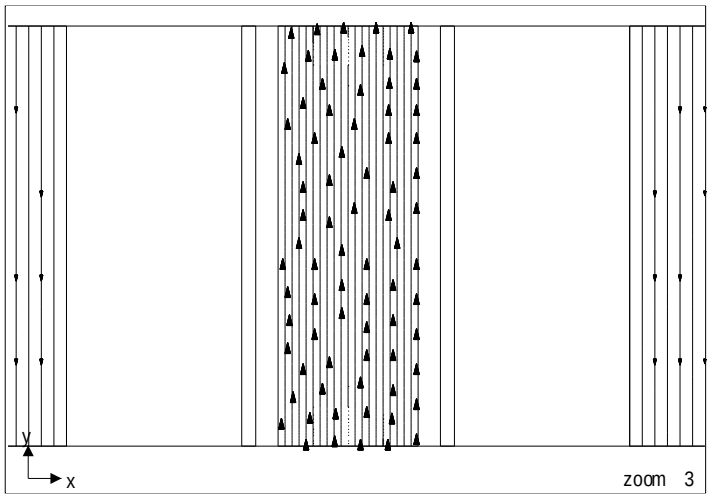

(a)

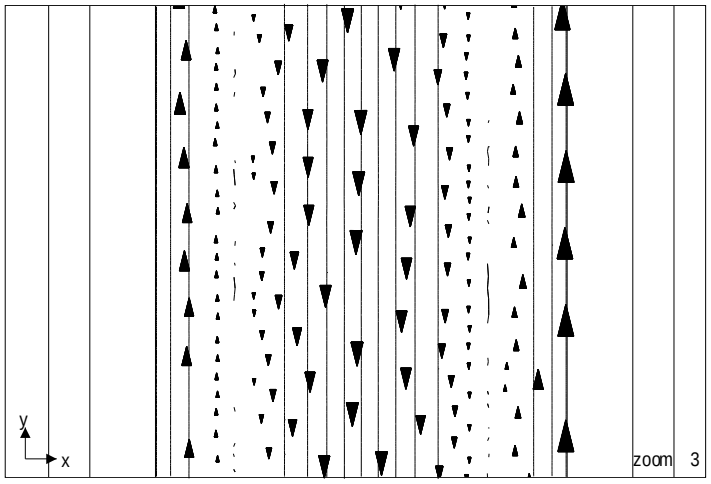

(b)

Figure 5.2: FEA simulation of field distribution in the infinite slab at low and high frequencies. (a)10 kHz and (b)1000 kHz

the simulated result for the full model of Case E.

While the field plots presented above are instructive in the way they illustrate the impact of various material characteristics on the field in the core, we are usually concerned more with how the device performs as a circuit element than we are about the actual fields. To that end, it is more useful to plot the simulation results in terms of losses, energy storage and equivalent inductance and resistance.

In order to model a particular device—rather than just a generic lossy ferrite—we now utilize the measured material data reported in Chapter 3. Figure 5.5(a) shows the various loss components and the total loss for the slab as a function of frequency; Figure 5.5(b) show similar plots for the electric and magnetic energy storage. The effective series resistance, R_s, and series inductance, L_s, per square meter of the 20 mm thick slab is are plotted in Figure 5.6.

5.2.2 Toroidal Core Structures

The solutions presented above for the infinite slab are computed using a 2D FEA solver, but because of the problem geometry the field distributions vary only in one dimension. That is, the boundary conditions and excitation sources eliminate one degree of freedom. The infinite slab model assumes that the curvature of toroidal core is negligible, and this assumption is generally valid for large radius cores with outer diameter to inner diameter ratios close to one. For many typical cores, however, the field in the core—even at low frequencies—varies considerably for different radial positions within the core.

Annular Ring with Axial Current

The natural next step in the modeling process is to include the radial dependence present in the toroidal structure; the core model shown in Figure 5.7 models a toroidal core of rectangular cross section as one-half of an annular ring with the field excitation provided by perfect conductors inside and outside the surfaces of the core. In order to maintain symmetry, we make the current sources full annular rings as well which forces all fields to be purely circumferential. Such a model still has only one degree of freedom since the fields can vary only as a function of the radius, r. What this model adds, however, is the ability to model the non-uniform field excitation and to examine how this radial variation changes as a function of frequency and material characteristics.

One significant drawback of using the 2D solver to simulate the short toroid is that the

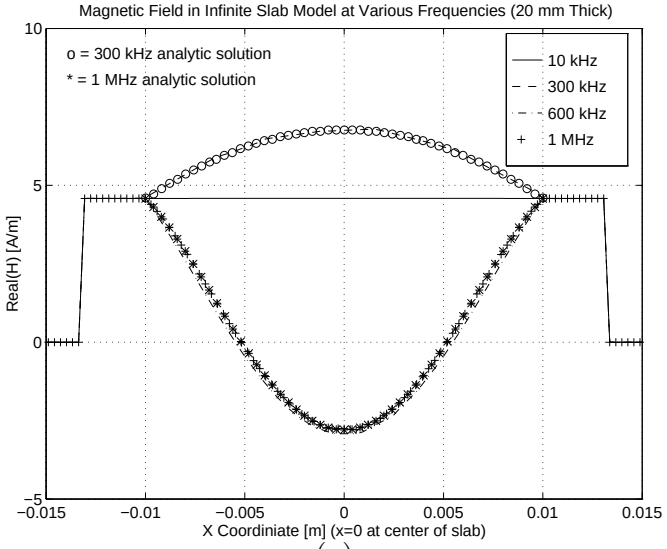

(a)

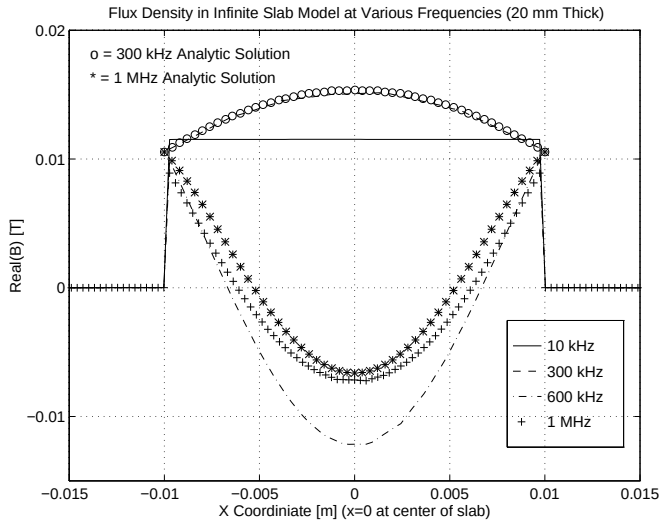

(b)

Figure 5.3: FEA simulation of field distribution at various frequencies in the infinite slab model for total loss case (Case E). The analytic solution from Chapter 4 is included for the 300 kHz and 1 MHz cases. (a) Real part of magnetic field (b) real part of flux density.

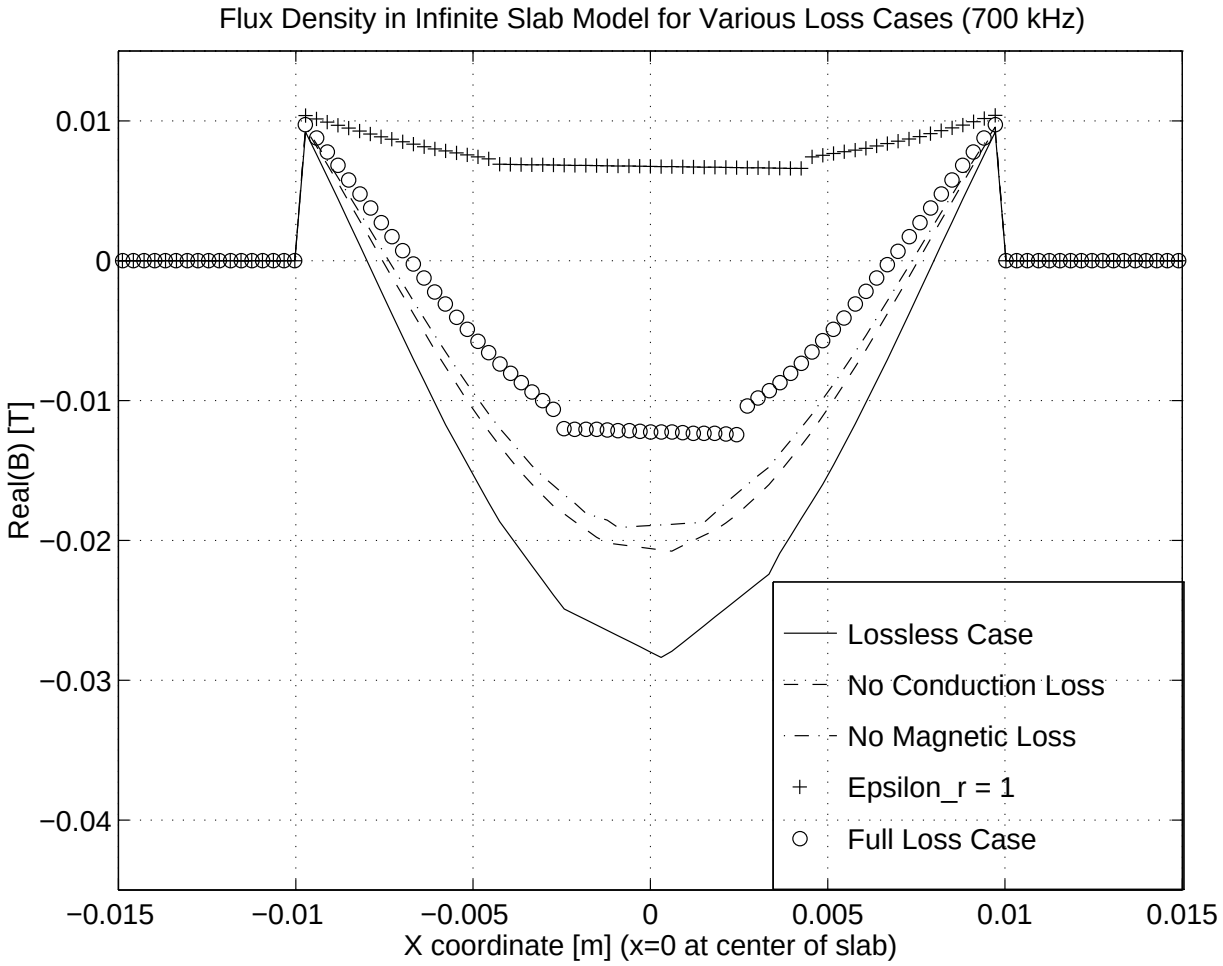

Figure 5.4: FEA simulation of field distribution in the infinite slab model for the various cases listed in Table 5.1 at 700 kHz. The poor data resolution in the center of the slab is a result of poor meshing of the problem in that region.

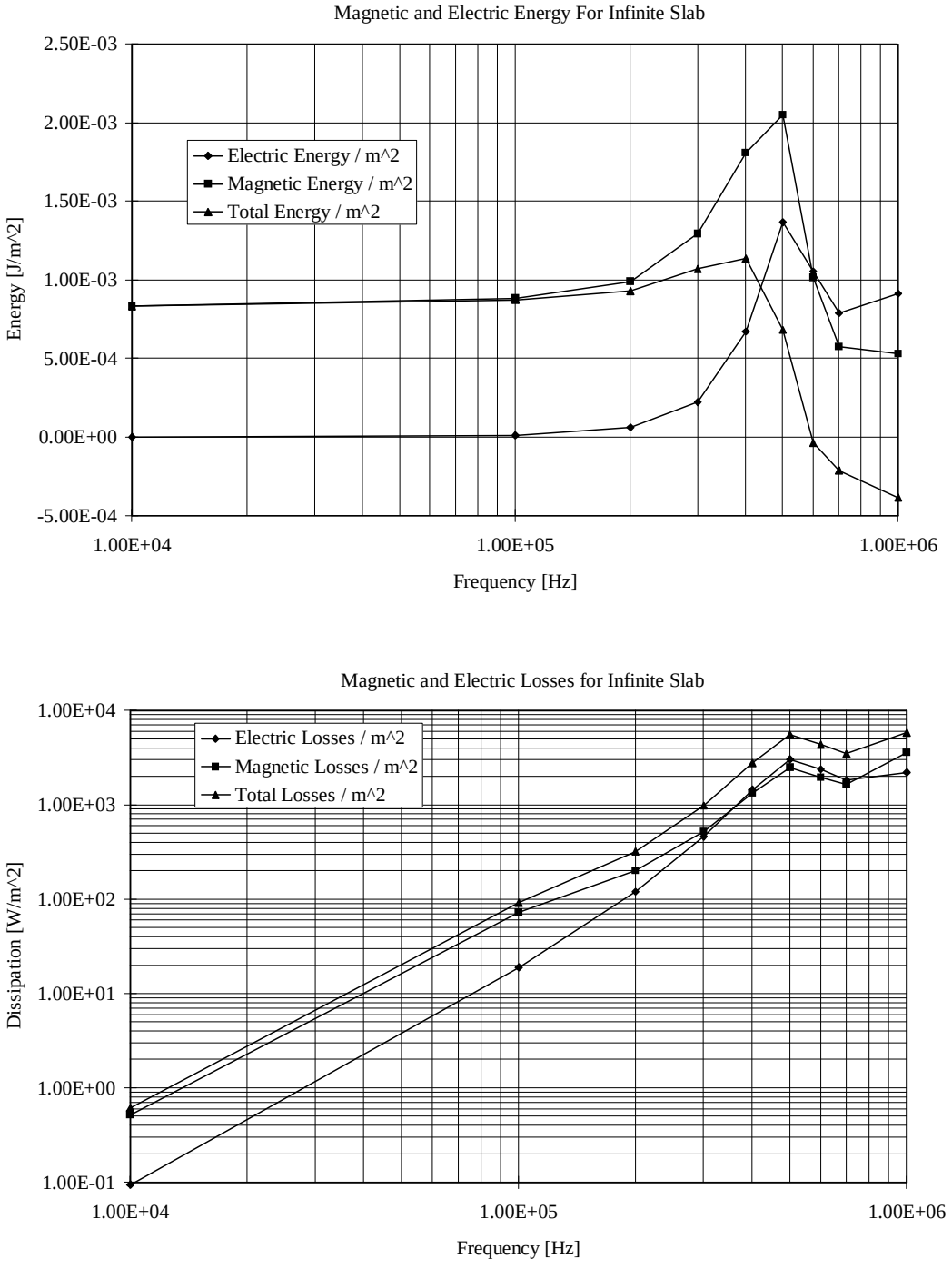

Figure 5.5: Losses and energy storage per square meter vs. frequency in the infinite slab model.

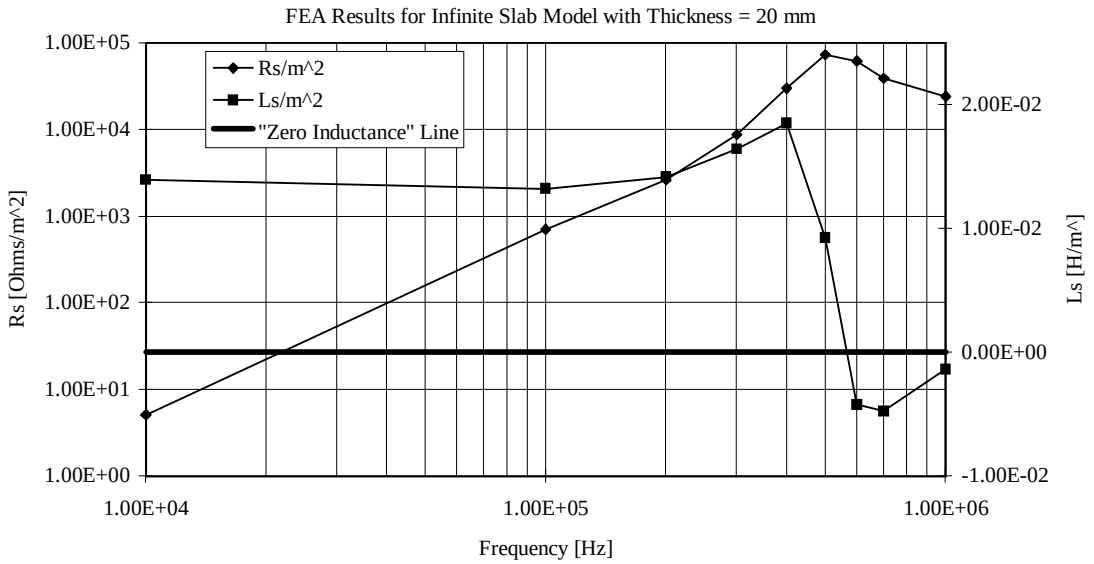

Figure 5.6: Series resistance and inductance per square meter for the infinite slab FEA model for the full loss case (Case E).

boundary conditions that should exist on the surfaces of the core are not independently controllable. Since the geometry is assumed infinite in the z direction, it is possible to establish a net axial current in the model that does not exist in the actual device. This is demonstrated here in terms of two different models for the toroid that both use the geometry of Figure 5.7: the first solution does not include the infinite permeability path and does not specify any constraint on the axial current that can flow in the core; the second solution sets the net current that can flow in the core to zero and includes the infinite permeability paths. These two models differ in the boundary fields that they establish on the interior and exterior regions of the core. The original problem does not constrain these values while the modified solution sets the interior and exterior fields to zero. The same set of simulations are run for the annular geometry problems as for the infinite slab; the results are presented in Figures 5.8–5.14.

Figure 5.8 shows the field distribution at one megahertz in the upper right quadrant of the core for the unconstrained or original simulation condition. It shows the flux reversal that occurs within the core as seen in the infinite slab. However, Figure 5.8 also shows a rapid attenuation of the flux density from the inner edge of the core to the outer edge. Plots of the H-field and B-field along a line cutting through the core cross-section show that the boundary values of the excitation field vary with the frequency for this unconstrained model. Figures 5.9 and 5.10 show the variations in the field distribution for the full loss case with varying frequency and the various loss cases at 700 kHz respectively.

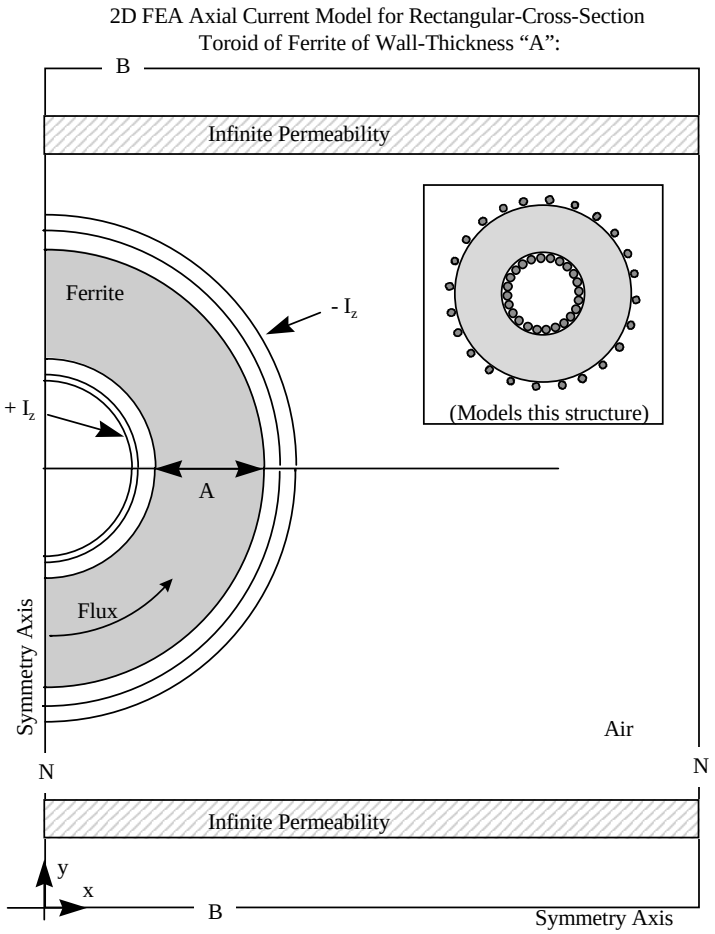

Excitations:
Currents in the positive and negative z directions are used inside and outside the core

Boundary Conditions:
Normal (N) : Flux is normal to the boundary (No tangential H field)
Balloon (B) : Boundary is as if model extends to infinity. (Open Boundary)

Figure 5.7: Annular representation of a toroidal core. The windings are modeled as perfect conductors inside and outside the surfaces of the annulus. This model is equivalent to a coaxial line with ferrite between the conducting inner and outer conductors. The Infinite Permeability objects provide a flux return path "at infinity" as in the infinite slab case.

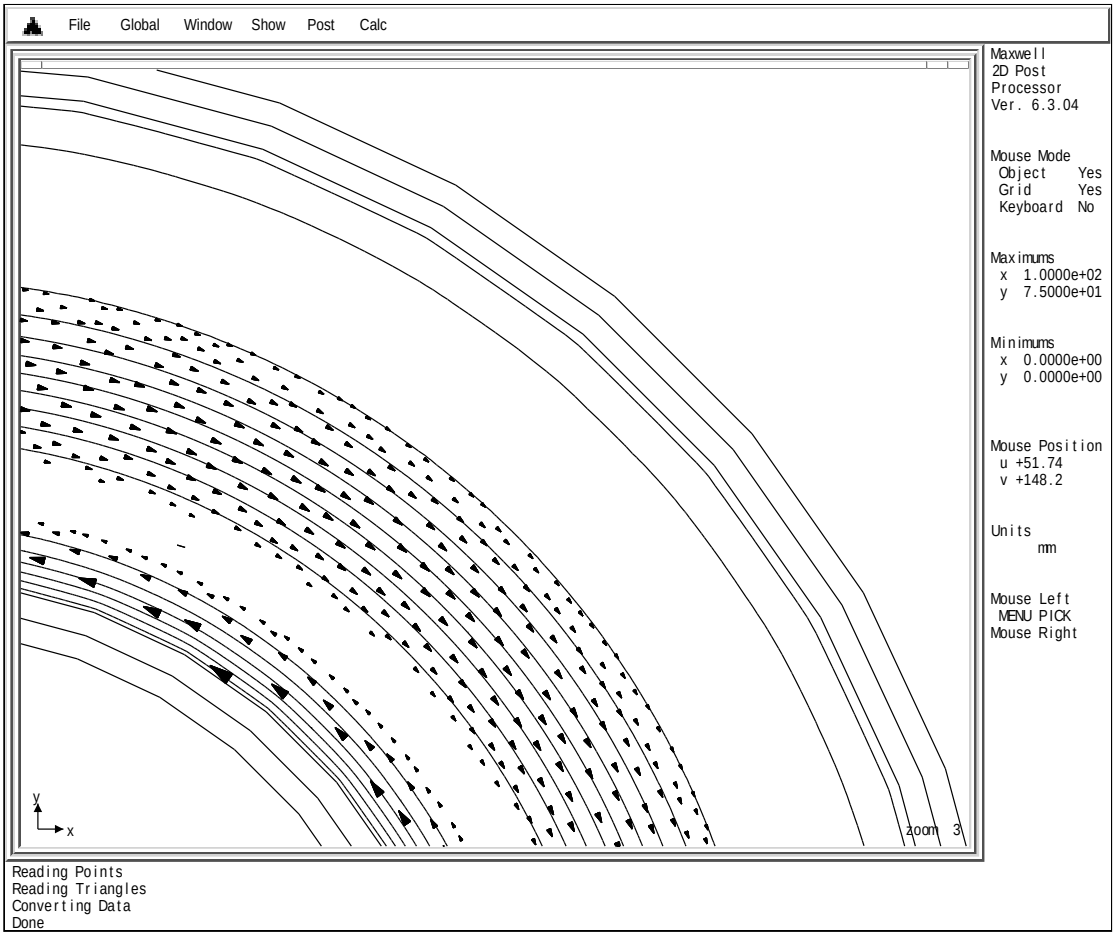

Figure 5.8: FEA simulation of field distribution in the annular toroid model at 1MHz.

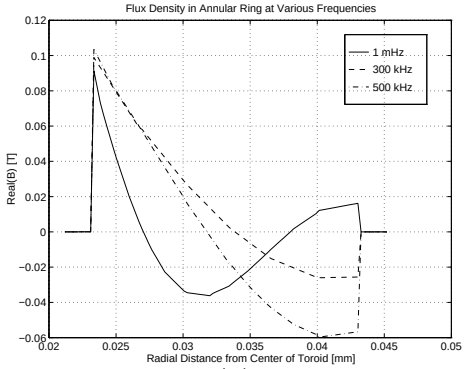

(a)

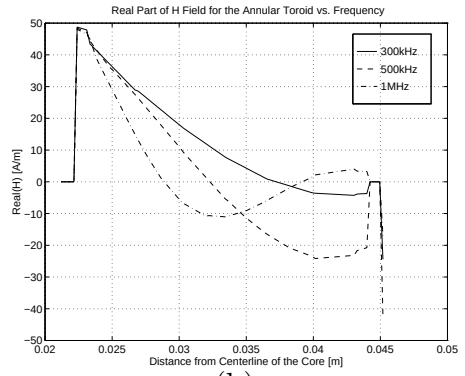

(b)

Figure 5.9: Field distribution in the original annular toroid model at various frequencies for the full loss model.(a) Real part of the magnetic field, (b) Real part of the flux density.

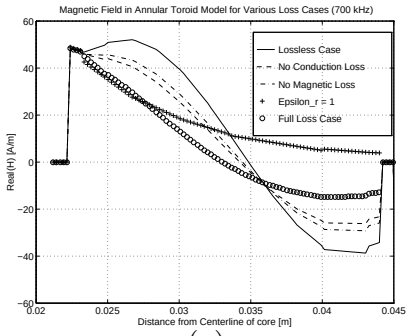

(a)

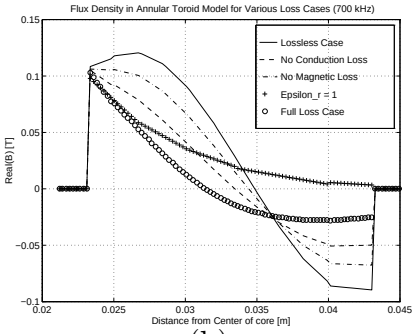

(b)

Figure 5.10: FEA simulation of field distribution in the original annular toroid model at 700 kHz for the various cases listed in Table 5.1. (a) Real part of the magnetic field, (b) Real part of the flux density.

If the annular model is now simulated with the constraint on the net current in the core and the external flux return "shorts" in place, the field distribution results are significantly different. Figure 5.11 shows that the flux distribution at one megahertz is now much less attenuated than in the unconstrained case. Figures 5.12 shows that the boundary H-field values are now essentially independent of the excitation frequency which is as expected for the actual device. Figure 5.13 shows the frequency variation in the energy storage and power dissipation of the constrained solution. The effect that the changes in boundary conditions have on the total resistance and inductance predicted by the simulation are illustrated in Figure 5.14 which shows the results for both the initial solution and the "modified annulus" solution.

The simulation results for the annular toroid model show a lower bandwidth for the unconstrained model whereas the constrained solution is quite similar to the results for the infinite slab model. The variation in the bandwidth of the various models in due in large part by the change in the boundary conditions of the exciting magnetic field that exists on the surface of the core. This dependence on boundary conditions is examined is addressed in a different way in the axial-field model of the following section.

Rectangular Cross Section with Axial H Field

As stated above, the 2D annular ring model is still in essence a 1D model since the fields are constrained to be circumferential. In order to have a true 2D field variation we need to either break the symmetry of the problem or remove the assumption of infinite length in one dimension or the other. One simple way to do this is to examine the field distribution on a plane orthogonal to the plane of the annular ring considered above, i.e. an x-y plane that cuts through one half of the core as illustrated in Figure 5.15. On this plane the current is assumed to have no z component and the H field is purely normal to the surface of the plane. We designate this case as the "2D-Axial" model. This model—unlike the 20 mm thick geometries of the previous section—has the actual geometry of the B2 #5 Core as listed in Table 3.4. Specifically, the wall thickness is 17.97 mm and the core height is 26.05 mm.

The boundary conditions on the core for the 2D-axial case are:

$$\underline{H}_{left} = \frac{N\underline{I}}{2\pi x_1} \tag{5.1}$$

$$\underline{H}_{right} = \frac{N\underline{I}}{2\pi x_2} \tag{5.2}$$

$$\underline{H}_{var} = \frac{N\underline{I}}{2\pi x} \tag{5.3}$$

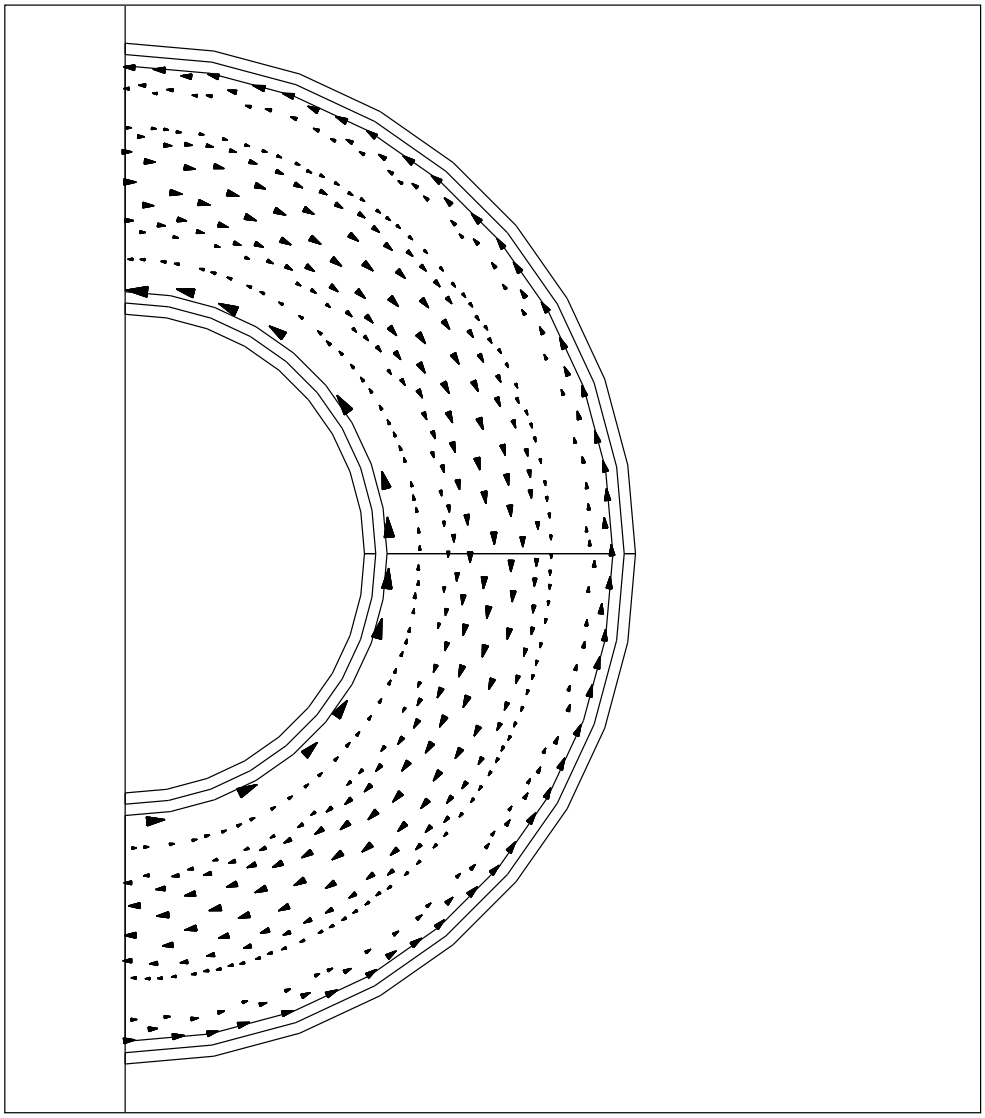

Figure 5.11: FEA simulation of field distribution in the annular toroid model at 1MHz.

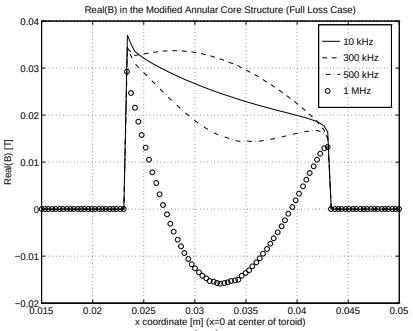

(a)

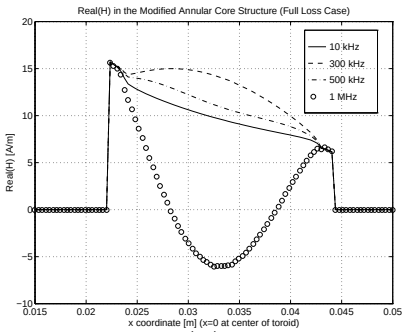

(b)

Figure 5.12: Field distribution in the constrained annular toroid model at various frequencies for the full loss model.(a) Real part of the magnetic field, (b) Real part of the flux density.

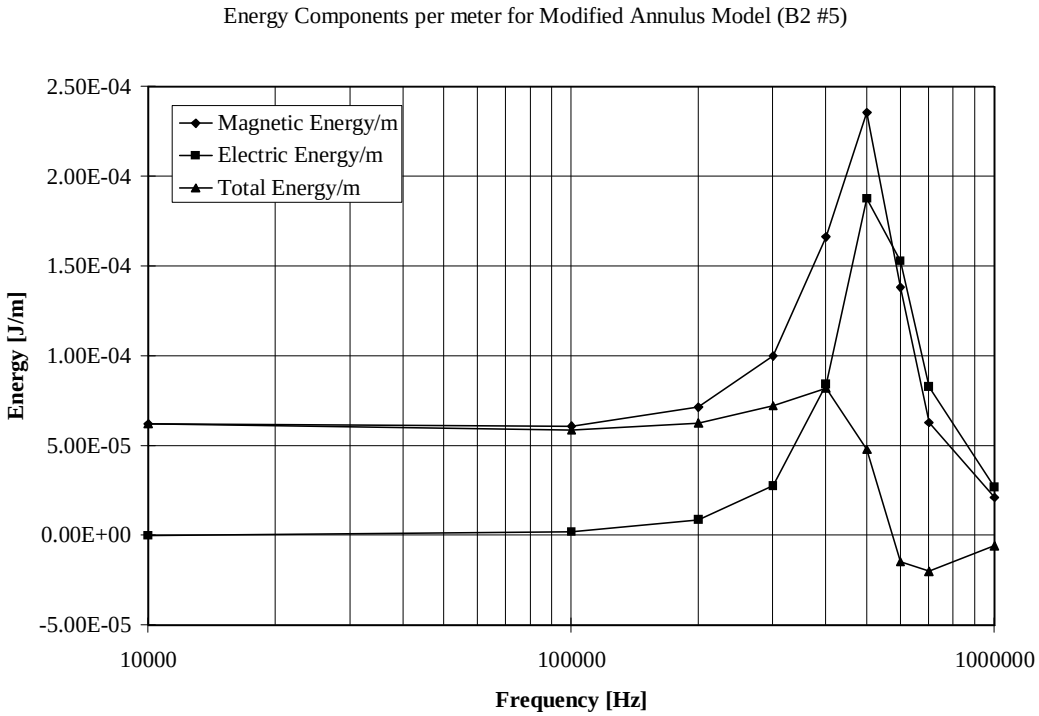

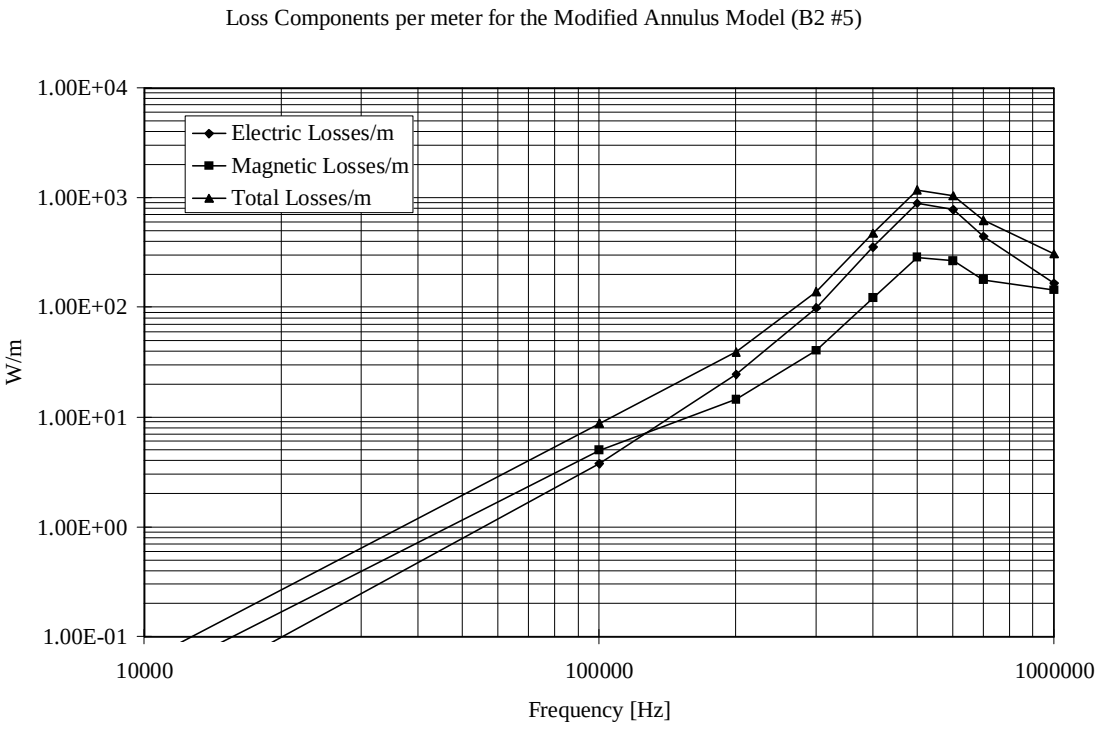

Figure 5.13: Losses and energy storage per meter vs. frequency in the annular toroid model.

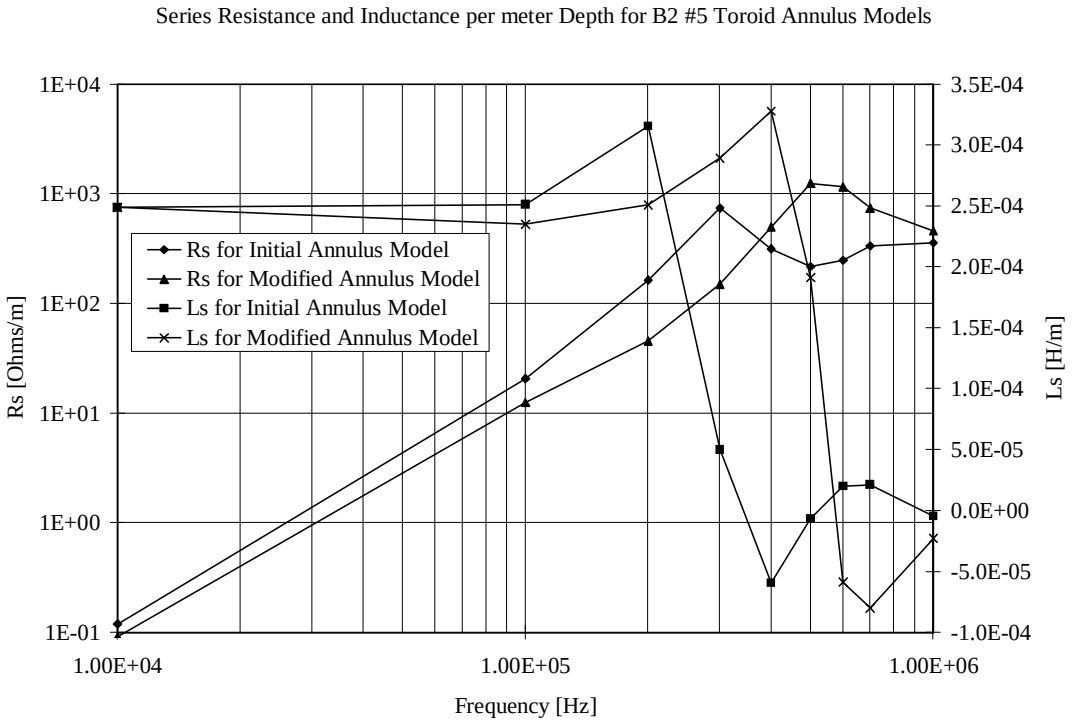

Figure 5.14: Series resistance and inductance per meter for the annular toroid FEA model for the material values listed in Table 5.2.

2D FEA Axial H-Field Model for Rectangular-Cross-Section
Toroid of Ferrite of Wall-Thickness "A"

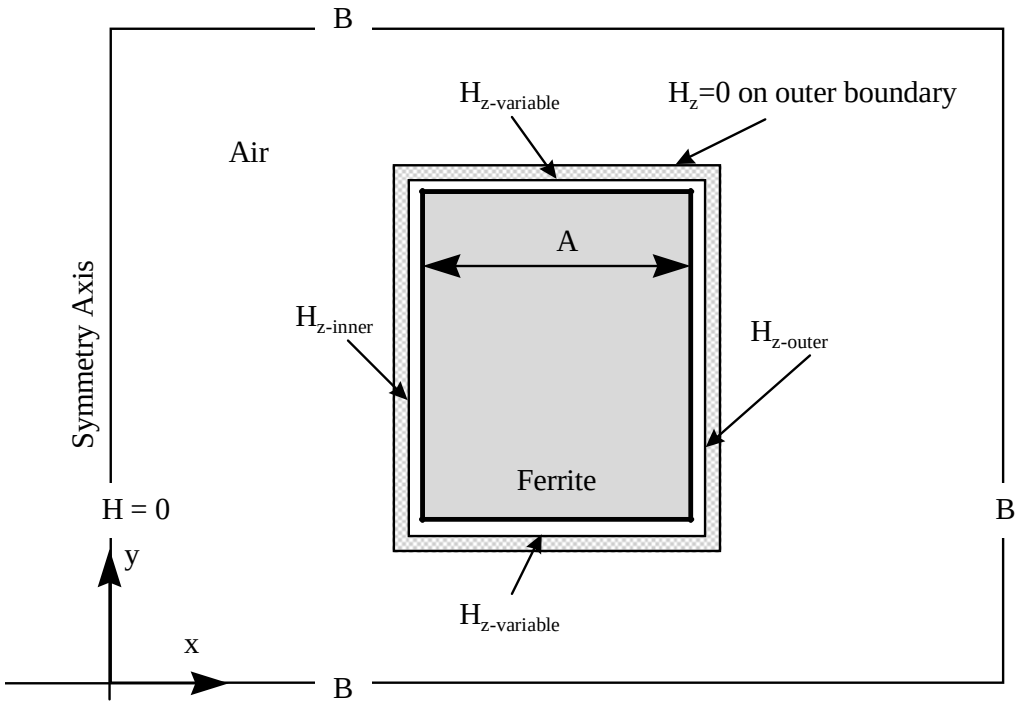

Excitations:

$H_{z\text{-inner}} = (N \underline{I}) / (2\pi X_1)$ where X_1 is the inner radius of the core

$H_{z\text{-inner}} = (N \underline{I}) / (2\pi X_2)$ where X_2 is the outer radius of the core

$H_{z\text{-variable}} = H_{z\text{-inner}} (X_1 / x)$ -- this models the radial dependence of the H-field

Boundary Conditions:

H = 0 : z-Directed H field (H_z) is zero on the boundary (Symmetry axis)

Balloon (B) : Boundary is as if model extends to infinity. (Open Boundary)

Figure 5.15: Geometry of a 2D axial-field model. The core geometry of this model is normal to the plane of the main core flux. The fields are plotted along the line A-A′.

where $N\underline{I}$ is the total ampere turns on the core, x_1 is the inner core radius and x_2 is the outer core radius. The boundary condition given by (5.3) models the $1/r$ variation in H-field[3].

The field solution for this case assumes that the geometry extends infinitely without variation in the direction normal to the x–y cross section. The boundaries of the problem space are set as shown in the figure: $H_z(0) = 0$, and the outer boundaries of the problem set as "open" boundaries. Under these conditions the model is similar to a rectangular waveguide that is completely filled with ferrite and can in fact be characterized in terms of the modal solutions that are characteristic of the physical dimensions of the device. A closed–form solution for this structure, however, is quite cumbersome due to the variable boundary conditions that exist on the core. In addition, it is worth noting that this structure no longer satisfies the assumptions made in [97] since no single dimension is significantly larger than the others.

The results for the the FEA simulations of the 2D-Axial model under the test conditions of Table 5.1 are presented in Figures 5.17 through 5.20. The line plots in Figures 5.17–5.18 are now plotted along the horizontal line $A - A'$ indicated in Figure 5.15. In this case, however, it is more instructive to look at a two-dimensional field plot such as that shown in Figure 5.16. Here we see that the flux is non-uniform in both the x and y directions. For all of the low frequency cases as well as the "ideal" core, the flux distribution is simply the $1/r$ distribution expected from the standard approximations. For the lossy cores and the highly dielectric core the simulation shows significant changes in the flux distribution to the point where there is no net linking flux such as is the case illustrated by Figure 5.16.

Comparison With Measurement

All of the preceding three models—the infinite-slab, the annular-toroid and the axial-field—can be used to compute the effective impedance of practical devices by converting the infinite dimension used in the models to the actual dimensions of a given structure. Figure 5.21 shows how the calculated impedance magnitude and phase of the B2 #5 Core compare to values measured in the laboratory. The simulated impedances all show the characteristic rolloff of inductance with frequency as the core dimensions become significant with the various models predicting different values for this frequency. The infinite-slab model and the modified annular-toroid model both predict a relatively low-frequency impedance

[3]The choice of geometry available in the field solver for this case is a rectangular x–y plane, and therefore the boundary conditions are given in terms of the actual problem geometry rather than in terms of the radius, r, of the core.

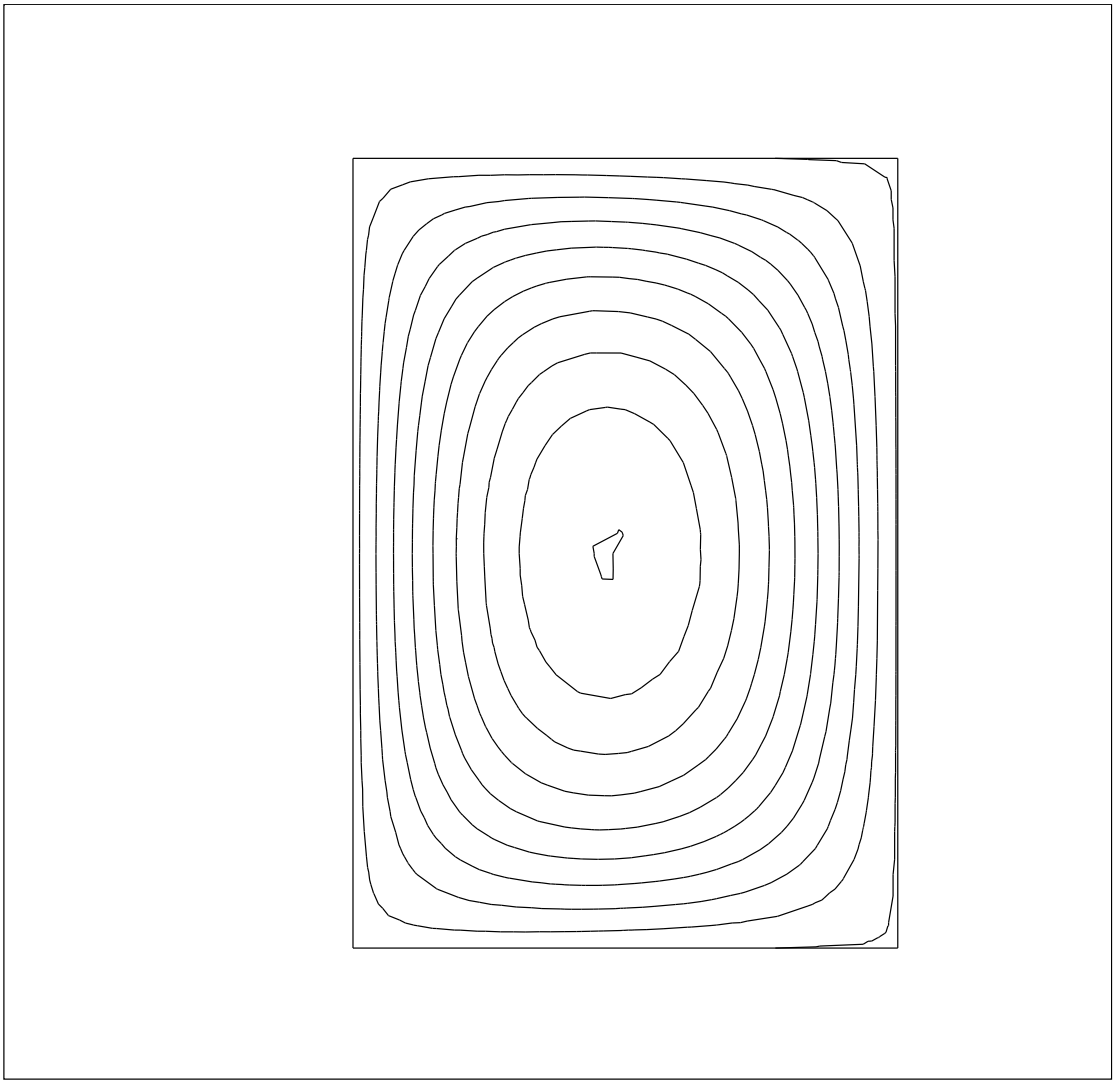

Figure 5.16: Field distribution in the axial field model of the toroid at 700 kHz.

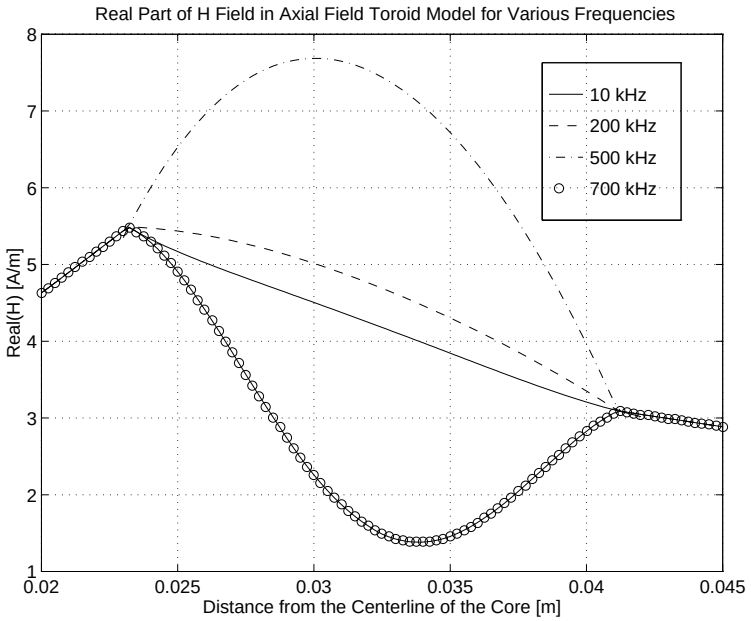

(a)

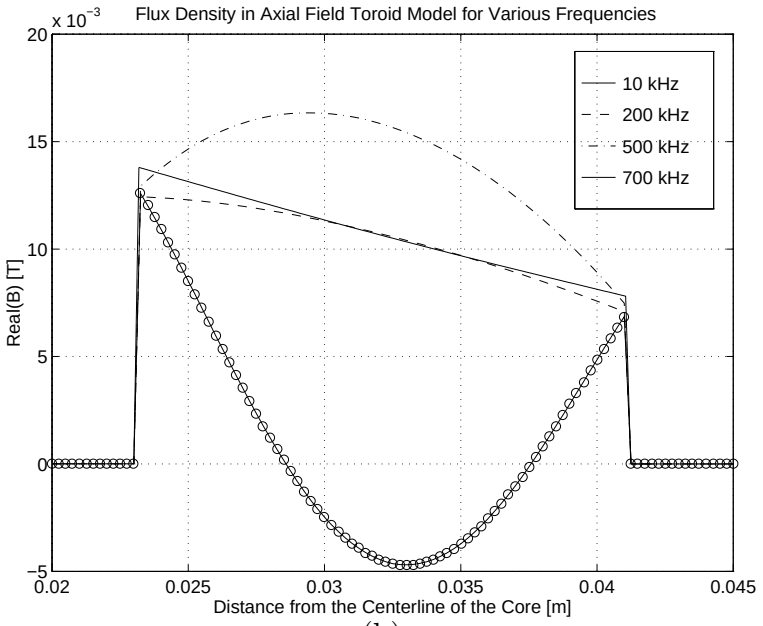

(b)

Figure 5.17: Field distribution in the axial field model at various frequencies for the full loss model.(a) Real part of the magnetic field, (b) Real part of the flux density.

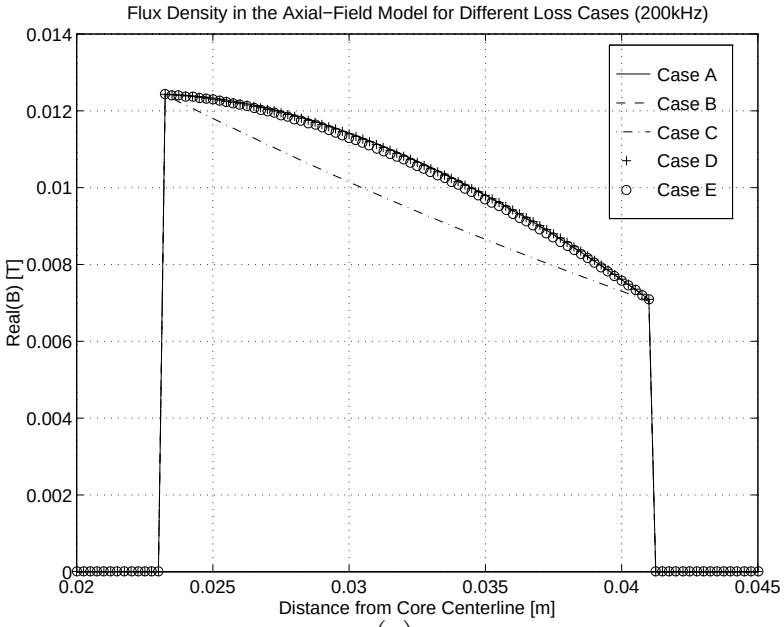

(a)

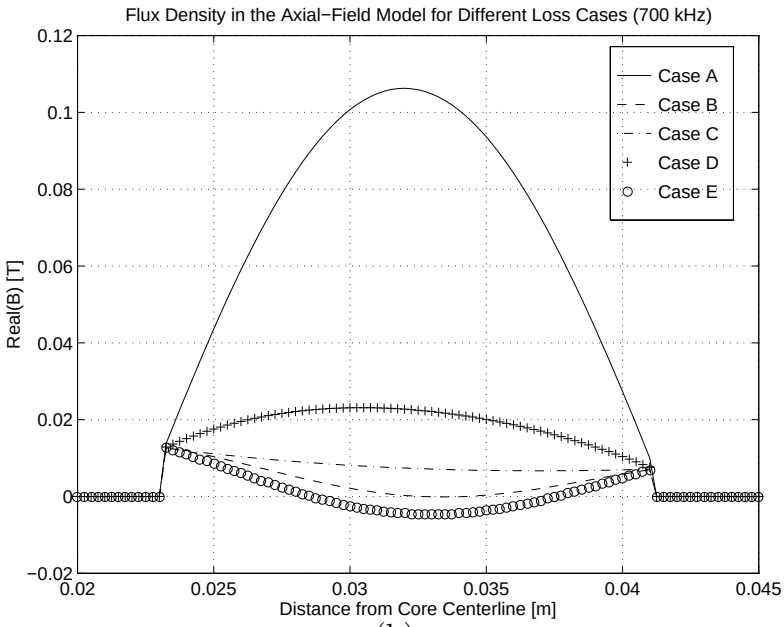

(b)

Figure 5.18: Field distribution in the axial field model for the various cases listed in Table 5.1. (a) Real part of the flux density at 200 kHz, (b) Real part of the flux density at 700 kHz.

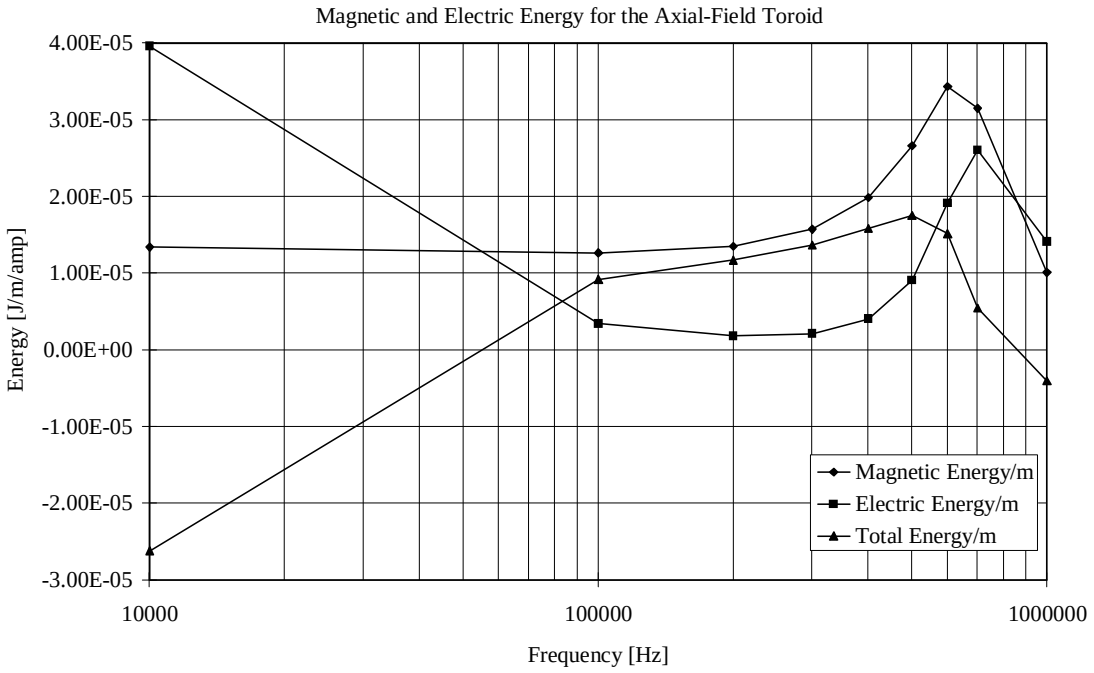

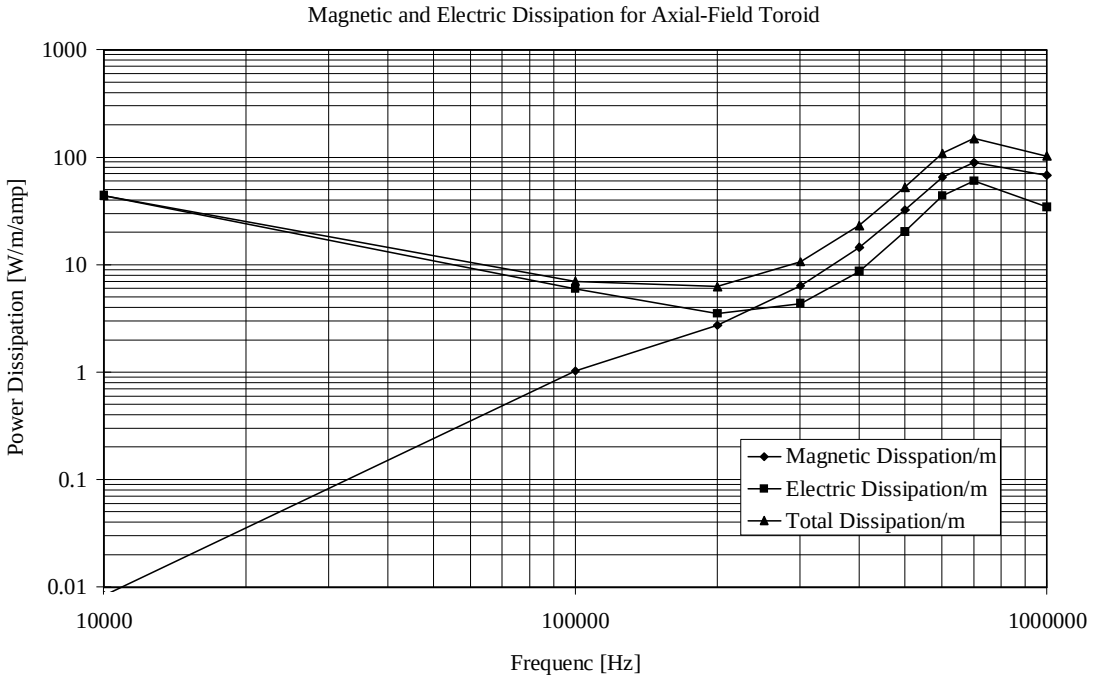

Figure 5.19: Losses and energy storage per meter vs. frequency in the axial field model.

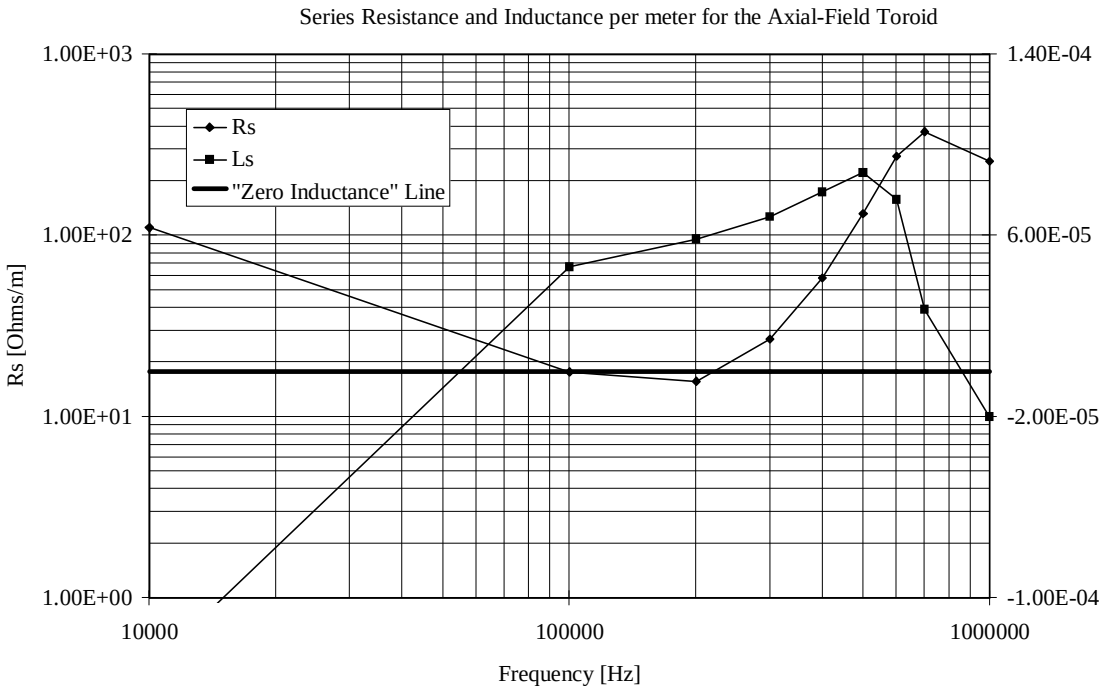

Figure 5.20: Series resistance and inductance per meter for the axial field FEA model for the material values listed in Table 5.2.

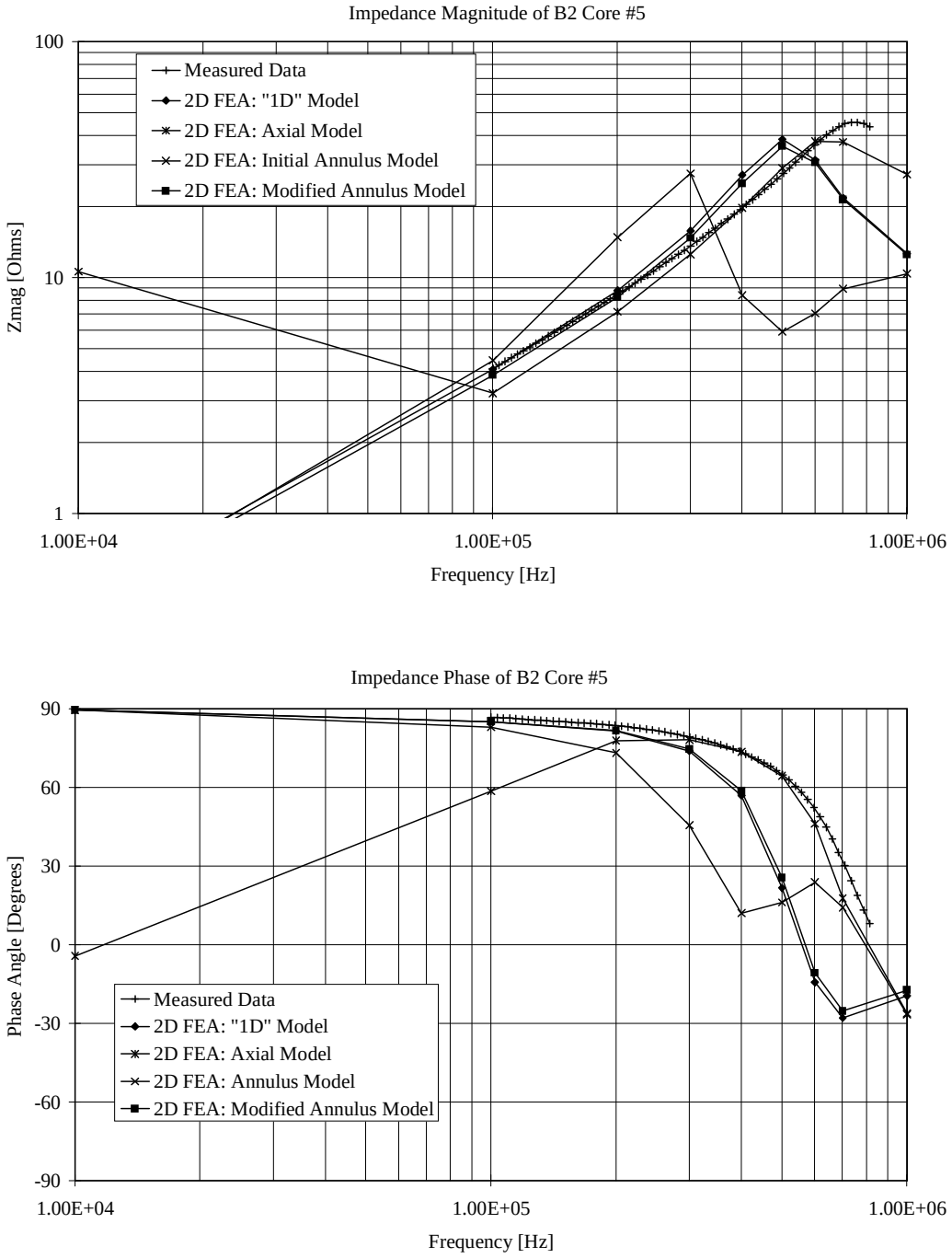

Figure 5.21: Comparison between the simulated and measured impedance magnitude and phase for the B2 #5 core.

rolloff, while the axial-field model matches the measured results rather closely at high frequencies; the initial solution for the unconstrained annular model gives a significantly lower bandwidth as discussed above. The low frequency results for the 2D-Axial case show significant problems and poor agreement with the other models. This anomalous result appears to result from a problem in the axial-field version of the Maxwell software package; the loss density appears to increase as $1/\omega$. This problem is currently being investigated by the manufacturer to determine the exact problem with the routine. Aside from the low-frequency problems with the axial-field model, the results in Figure 5.21 show fair agreement between the relatively simple field model and the actual measured impedance values.

5.2.3 Non-Toroidal Core Models

The core models discussed to this point are meant to introduce the principle results of the modeling process. The results of these models of the toroidal core illustrate not only the breakdown of losses in a given core but also the usefulness of relatively simple numerical modeling for use in examining the performance of magnetic devices built using complex core materials. To this point the shape of the core has been a simple toroid that is distinguished only in its relatively large size when compared to typical cores used in high-frequency converters. The results of Section 5.2.2 help confirm the existence of dimensional effects in the core and present a useful way to separate the losses caused by these effects into those associated with dimensional resonance and those caused by the more widely understood eddy-current phenomenon. Finally, the agreement between the modeled and measured inductance and core resistance values confirm the impact that dimensional effects of both types have on overall inductor performance. In the next section we extend this analysis to several cores with more complicated structures.

Block-Material Cores

The toroidal core analyzed in the previous section is simple enough that it is possible to write closed-form analytic solutions for several of the examples. In such simple cases the use of numerical techniques such as FEA may seem unnecessary. In such cases where analytic solutions can be written, it is often more advantageous and insightful to use closed-form solutions such as those presented in Chapter 4 directly.

The situation is different for more complicated geometries where closed-form solutions are either not possible or overly complex. In such cases, numerical solutions are the primary

analysis tool available. This section introduces two additional core geometries which exhibit dimensional resonance and eddy-current effects.

Figure 3.20 of Section 3.6.1 shows the geometry of two different cores made up of several separate blocks of ferrite. The blocks that make up Core #9 and Core #10 have dimensions of 2"x3"x4" and 0.75"x1.5"x3" respectively. As illustrated in the Section 5.2.2 as well as in Chapter 4, the cross-sectional dimensions of these cores are such that they are subject to dimensional losses in the frequency range of several hundred kilohertz. There are two main goals of this section:

1. To demonstrate that the FEA models adequately predict the measured performance of inductors built on such cores
2. To examine the effect of air gaps between the core blocks on the measured and modeled device performance

Block cores without air gaps The simulation of these block core devices is carried out in much the same way as it is for the toroidal and infinite-slab structures. In the 2D simulation these cores are assumed to extend infinitely in the plane normal to their cross-section and therefore any 3D effects not considered by this assumption are lost.

Figure 5.23 shows the simulated inductance and core loss characteristics for block cores of three different cross-sectional sizes based on the model in Figure 5.2.3. These results show the same general shape of the impedance as shown in the analytical model of the infinite slab as well as the FEA models of the simple toroidal core geometry. Figure 5.24 shows the field distributions in the block core corresponding to B2 Core #10 for excitation frequencies of 10 kHz and 500 kHz. The low frequency distribution is uniform—as expected—while the field at 500 kHz shows several pockets of circulating flux with a linking flux along the innermost portions of the core blocks.

Block cores with air gaps One of the main suggestions proposed in the literature for dealing with dimensional resonance problems in large cores is to insert an air gap somewhere in the core [97, 2]. The argument for using an air gap to reduce the effects of dimensional resonance is that the air gap lowers the effective permeability and therefore shifts the resonance to a higher frequency. In this section, the 0.75 inch block core examined above is simulated with air gaps of 20 and 200 mils (≈ 0.5 and ≈ 5 mm) inserted at the intersecting points of all of the blocks. Figure 5.26 shows the field distribution in the block core with and without air gaps for high-frequencies excitation.

Example: Simulation of Block Core

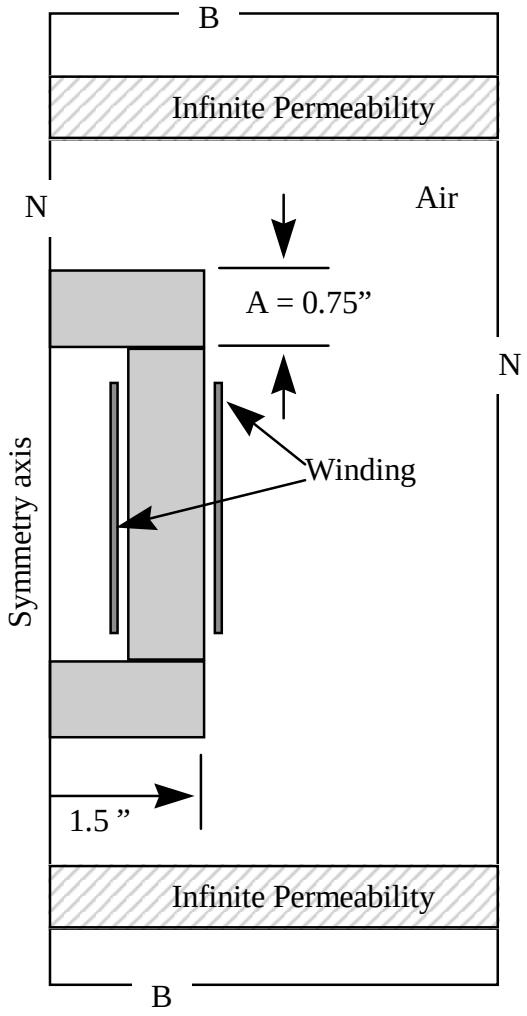

FEA Model for Block Core #10

- Ferrite-block core (#10) from measurement study
- Simulated using FEA for a fixed frequency and set of material constants

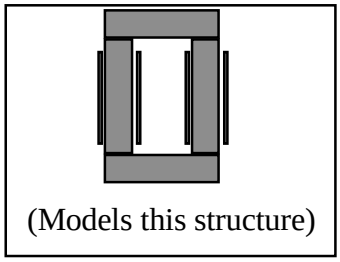

Figure 5.22: FEA model of the block core structures. The infinite permeability objects are provided for use in the modified simulation process discussed below.

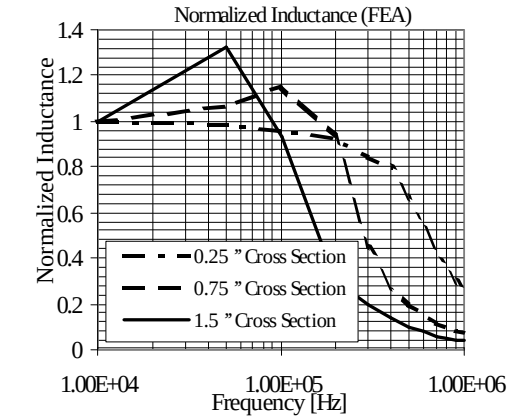

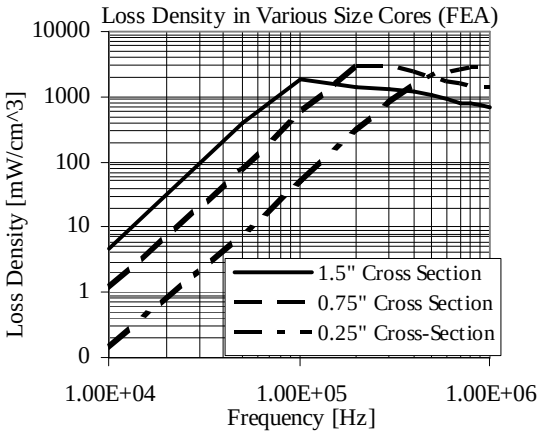

Figure 5.23: Normalized inductance and core loss density for block cores of various sizes as a function of frequency.

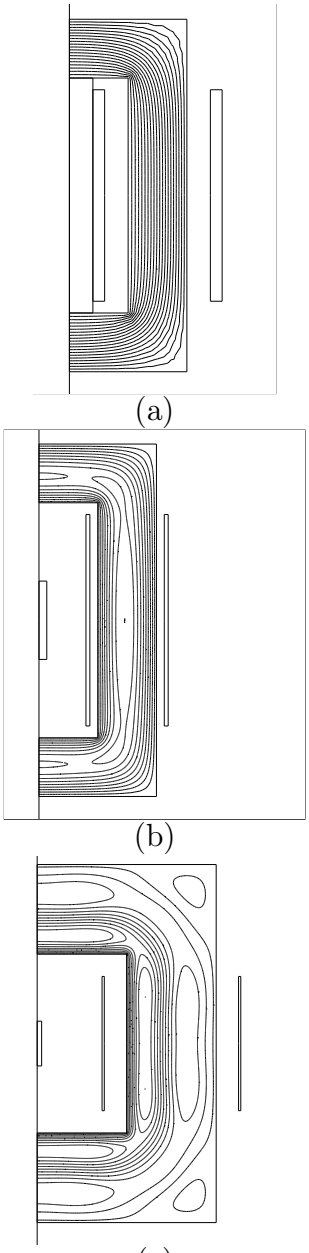

Figure 5.24: Field distribution in ungapped block cores of various thicknesses at 500 kHz. (a) 0.25 inch thickness, (b) 0.75 inch thick, (c) two inches thick.

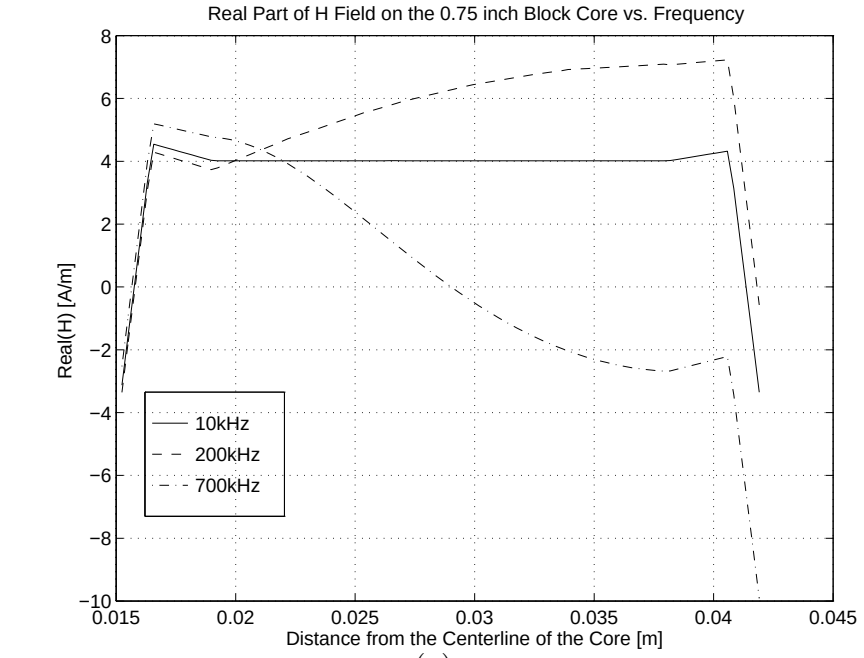

(a)

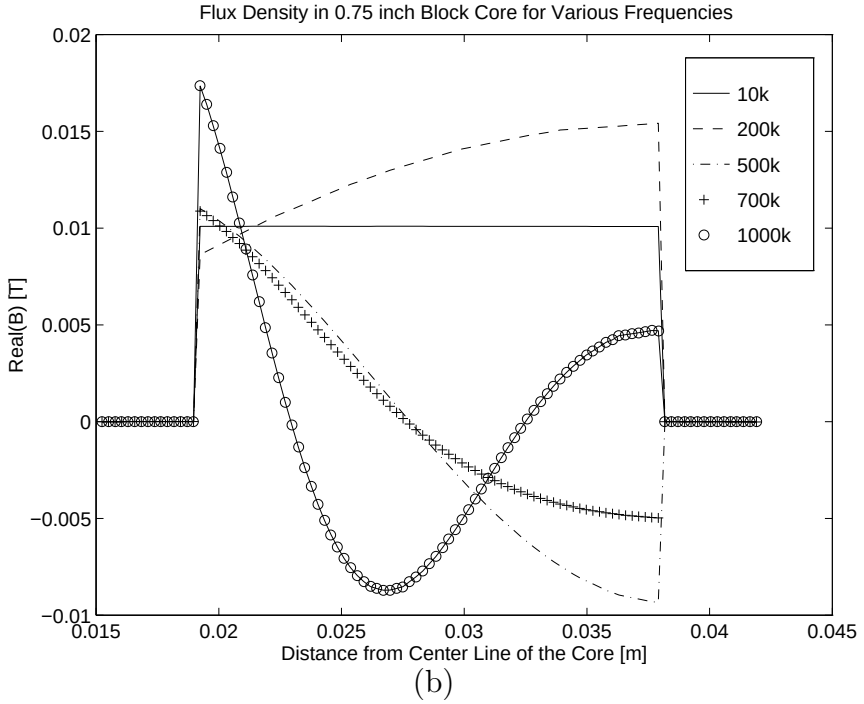

(b)

Figure 5.25: Field distribution in the 0.75 inch thick block core at various frequencies for the full loss model.(a) Real part of the magnetic field, (b) Real part of the flux density.

The simulation shows that both the gapped and ungapped cores have highly non-uniform flux distributions and that the presence of the gap does not in itself eliminate the dimensional resonance problem within the ferrite. What the gap does do, however, is help to spread the flux more evenly throughout the core, and this redistribution of flux helps to reduce the net effect of the dimensional resonance. In particular, we note that in the gapped structures the high flux density along the innermost surface of the ungapped core is distributed more evenly across the air gap of the gapped cores. This redistribution at the gap leads to a redistribution throughout the core. Since the losses in the core are a strong function of the flux density, this leveling of flux helps reduce the overall losses in the structure.

Boundary Conditions in the Block Core Geometries Since the block core simulations are performed with the same 2D field modeling techniques used in modeling the annular toroid model, the difficulties with the correct establishment of boundary conditions is present in these models as well. Figure 5.2.3 shows two infinite permeability blocks that are included in order to provide for some control over the external field values. Since the problem geometry of the block cores is not symmetrical, it is not as simple to determine the correct external field values as it is in the toroidal core case. However, in order to improve the simulation results presented above—which show a significant variation as demonstrated by the plots in Figure 5.25—it is possible to constrain the solution in order to reduce the net current that is induced in the model.

In the block core devices, however there are several difficulties in constraining the solution. First of all, the intention of forcing the net current that flows in the blocks to be zero is to better reflect the 3D nature of the structure. However, there are certainly currents induced in the blocks at high frequencies and they flow so as to oppose the changing flux density. In the geometry used here that means that the induced eddy current flow in the positive and negative z direction to enclose the flux lines. By restricting the net current to be zero we improve the situation somewhat, but this technique is more of a manipulation of the solver than a complete solution to the problem.

Figure 5.27 shows that when the block core with a cross section of 0.75 inches (Core #10) is simulated in this fashion the results are in much closer agreement with the measured impedance values than when the problem is left unconstrained. The frequency at which the impedance peaks is slightly higher for the measured core and this is in agreement with the comparison between the infinite slab models and the annulus model of the toroid. An additional issue that tend to increase the resonance frequency of the measured device is the unavoidable presence of small air gaps between the blocks. These gaps tend to limit the flux redistribution and thereby increase the resonance point as illustrated above.

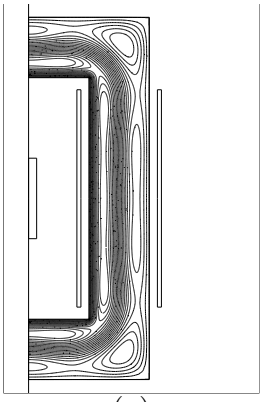

(a)

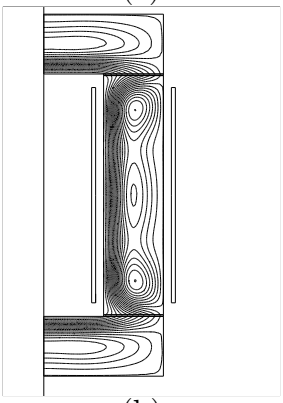

(b)

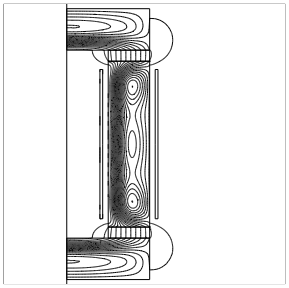

(c)

Figure 5.26: Field distribution in 0.75 inch thick block cores (a) ungapped core at 700 kHz, (b) core with a total gap of 80 mils at 800 kHz, (b) core with a total gap of 800 mils at 800 kHz.

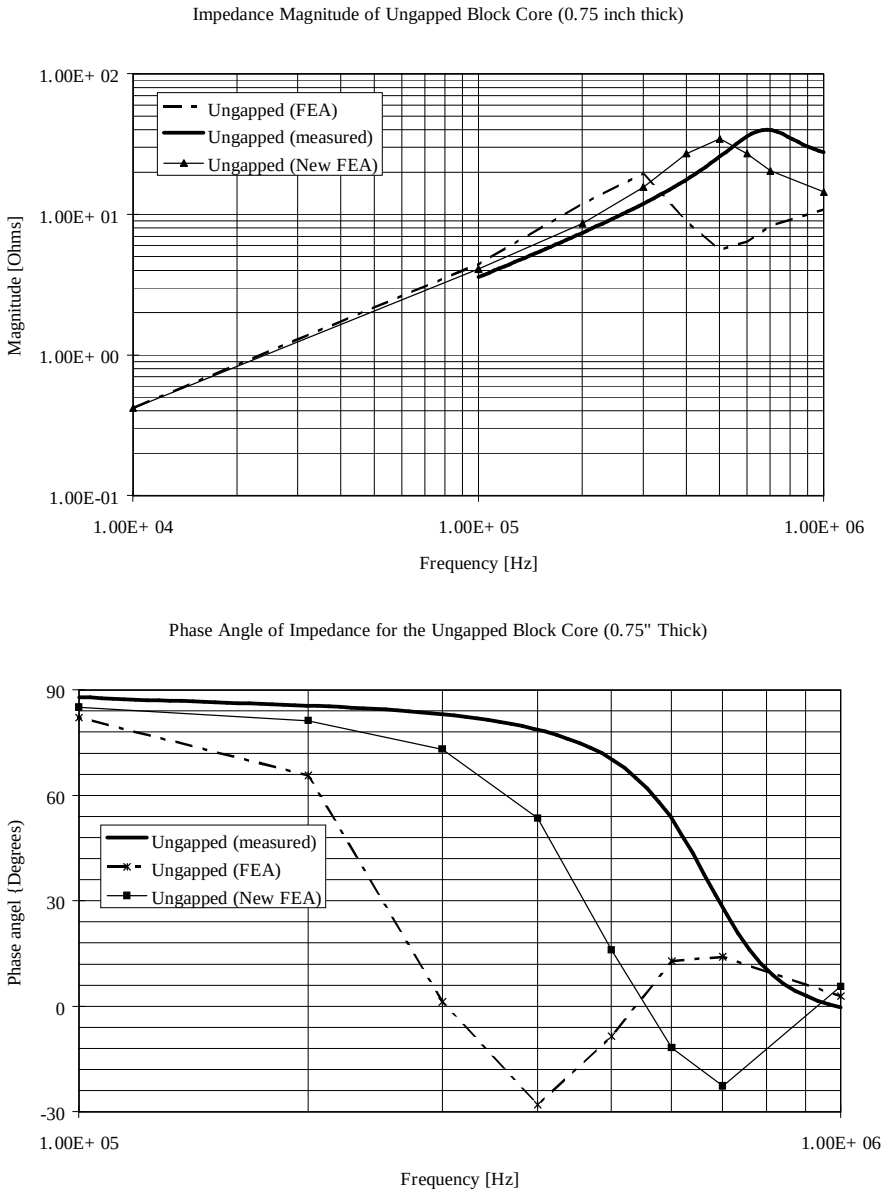

Figure 5.27: Simulated and measured impedance of the 0.75 inch thick block core (Core #10). The simulated curves result from an unconstrained and constrained simulation respectively.

Chapter 6

Application Example: The Inductive Coupling Transformer

6.1 Device Description

As introduced in Chapter 1, one motivating problem for the modeling effort presented in this thesis is the inductive charger proposed for charging electrical vehicles. The E-core type structure used for this charger is shown in Figure 1.4; it has several unique features:

1. a large diameter circular center post on each of the top and bottom parts of the core structure
2. a centerpost gap ferrite piece that is placed between the circular center-post sections of the top and bottom core pieces
3. a relatively large air gap between the annular centerpost-gap ferrite material and the top and bottom core pieces

This chapter uses the methods and analysis detailed in the studies of the toroidal and block cores in Chapter 5 to examine the performance of the core used for the current generation of the inductive charging circuit. Of particular interest are the dimensional effects present in the central post of the core and the "disk" that forms part of the center post. The inductive charger core is interesting from the dimensional effects perspective mainly because of the large diameter of the center post geometry. The results of the simulations presented to this point indicate that both high eddy current effects and high dimensional resonance effects

are possible in the puck. In addition, the walls of the core are approximately the same thickness as the toroidal core and block core structures considered above, and therefore similar frequency variations in performance can be expected in these sections of the core.

6.2 Modeling of Circular Disk

The disk in the center of the core is the object with the most likely dimensional impact on the overall performance of the core and we begin by examining the distribution of flux in this part of the device. From the cylindrical symmetry of the centerpost it is possible to pursue an analytical solution to this flux distribution if the H field on the surface of the material is known. In this case however it is more useful to take advantage of the numerical tools that we have and to use them for an evaluation of the structure under several different excitation and material conditions. In all of the following, the puck is modeled as an infinitely long cylinder and the boundary conditions on the cylinder are set exactly as was done for the axial-field model of the toroid in Chapter 5.

6.2.1 Solid Disk Design

Figure 1.4 shows the 3D representation of the E-core with the portion of the core that is modeled. From a static or low frequency 3D solution for this structure we can determine the values of the H field that exist on the boundaries of the circular disk for a given current excitation. As mentioned in relation to previous simulations, the material characteristics used in the simulation are those for a particular flux density. Since the solver assumes the material in linear and homogeneous, the boundary conditions can be normalized and the results for a unity H field are used to show the frequency response of the cylinder. The losses in the winding are neglected in any calculation of the overall loss in order to focus on the losses in the core material; this restriction can be removed for a particular design to calculate the losses in the winding which must be included in actual device performance.

The field plots in the introduction of this thesis show the overall shape of the flux density within a cylinder for a variety of excitation frequencies and material characteristics. The 2D axial field model of the cylinder is shown in Figure 6.1; this structure is simulated using the 2D axial-field solver for the same set of material and frequency conditions used for the previous simulations. Figure 6.2 shows how the magnetic field varies within the cylinder at 400 kHz for simulations where the material is modeled using either the full loss model, the lossless model or a non-dielectric core model. Figure 6.3 shows the variation of the flux

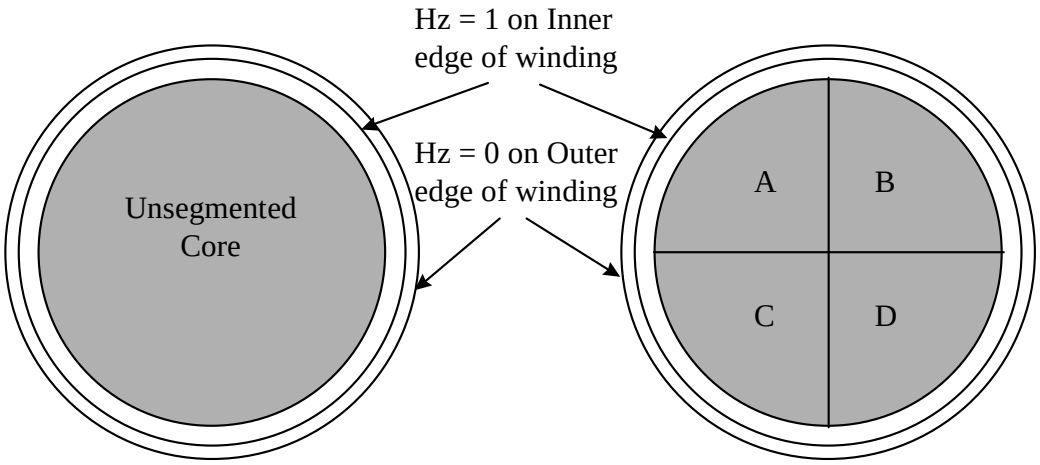

Figure 6.1: Cylindrical center post geometry modeled for axial-field simulation. The core diameter is 50 mm. The axial H–field is set to give a flux density of 10 mT at low frequencies.

density as a function of frequency for the full loss model. Figure 6.5 shows the resistance and inductance per meter for the cylinder as a function of frequency.

6.2.2 Segmented Disk Design

One alternative design for the cylindrical disk that has been proposed to help reduce the dimensional effects is to cut the disk into several separate parts and insert dielectric spacers between the various pieces. The argument for this design is to break up the paths of the eddy currents and thereby improve the overall response of the device. The FEA model for this segmented design is exactly the same as for the unsegmented case with the exception that 0.25 mm thick spacers with a dielectric constant of 3.4 (similar to teflon or other insulators) are inserted between the four quarters. The excitation field and the core material characteristics remain the same. Figure 6.4 shows that while the lamination of the puck does not reduce the high frequency effects completely, the segmented puck design has a much more uniform flux distribution than the unsegmented puck design. The resistance and inductance that each design represents per meter of depth are plotted in Figure 6.5 vs frequency. These results show that the piecepart disk shows improvement over the unsegmented disk since the frequency at which the geometrical effect in the core become significant is increased.

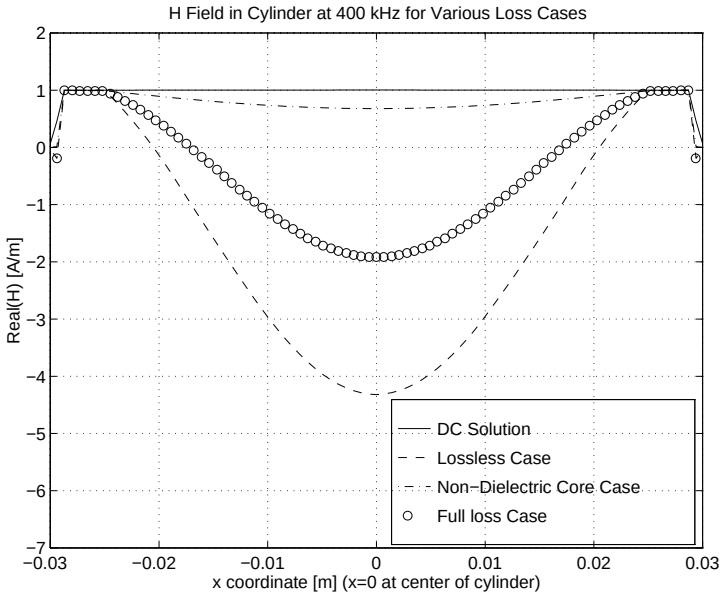

Figure 6.2: Magnetic field at 400 kHz in the ferrite cylinder for various loss cases.

6.3 Simulation of Core with and Without Centerleg Gap

While the use of a segmented center puck may prove useful in some cases, the added cost of such an approach makes it unattractive. The next level of simulation is to simulate the entire charger core structure with the disk in place in order to understand the larger picture of whether the complete charger core suffers the dimensional effect demonstrated in the cylindrical model. Figure 6.6 shows the 2D cross-section used to model the complete core. The key features of this model are:

1. it is modeled as an x-y structure which means it is assumed to extend infinitely in the z direction
2. the excitation is provided by the planar winding primary layer modeled as a perfect conductor with a known current
3. the total current in the puck is set to zero
4. the total current in *each side* of the top portion of the core is set to zero
5. the air gap between the puck and the core is either 0.5 mm (1 mm total gap) or zero and is changed by adjusting the thickness of the puck

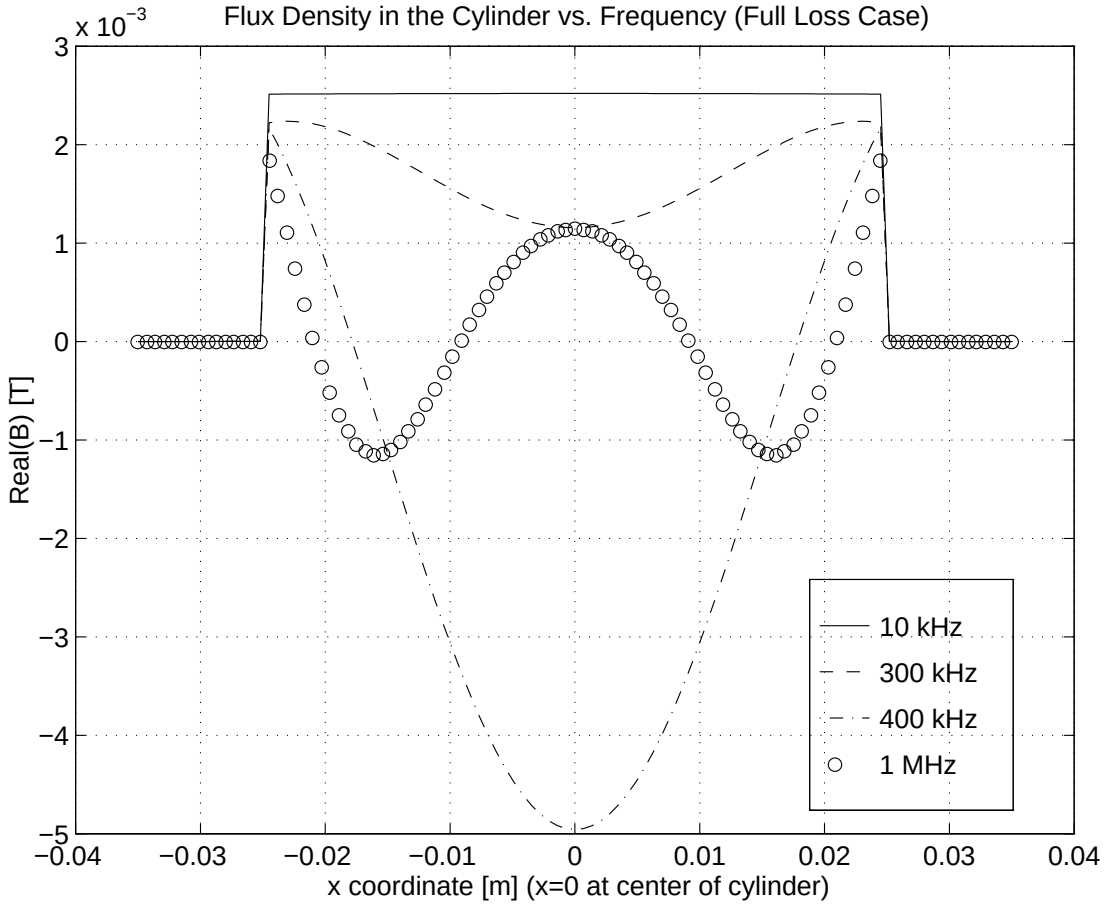

Figure 6.3: Flux density as a function of frequency in the cylinder for the full loss case.

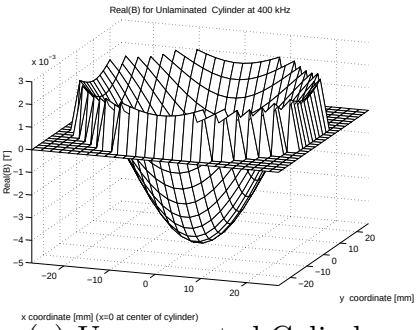

(a) Unsegmented Cylinder

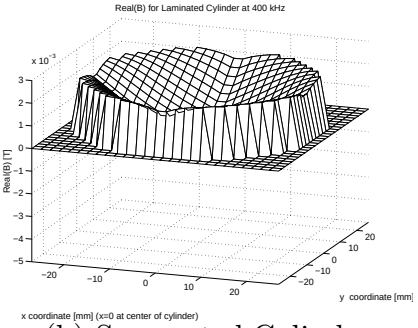

(b) Segmented Cylinder

Figure 6.4: Flux density in the (a) unsegmented and (b) segmented puck designs at 400 kHz. The segmentation of the puck reduces the overall variation in flux density.

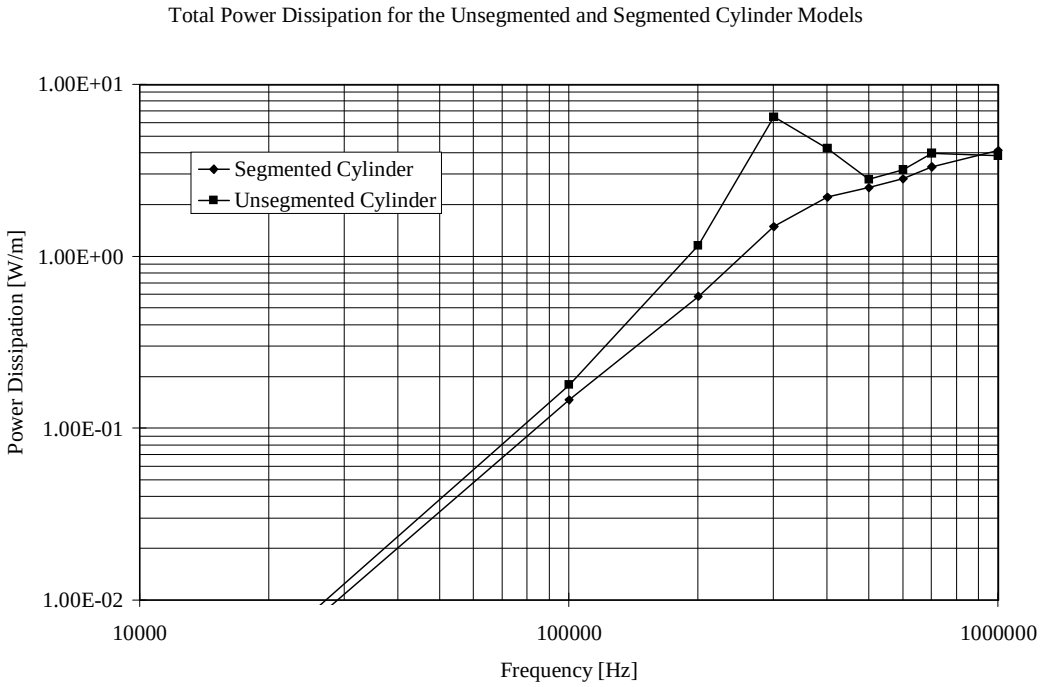

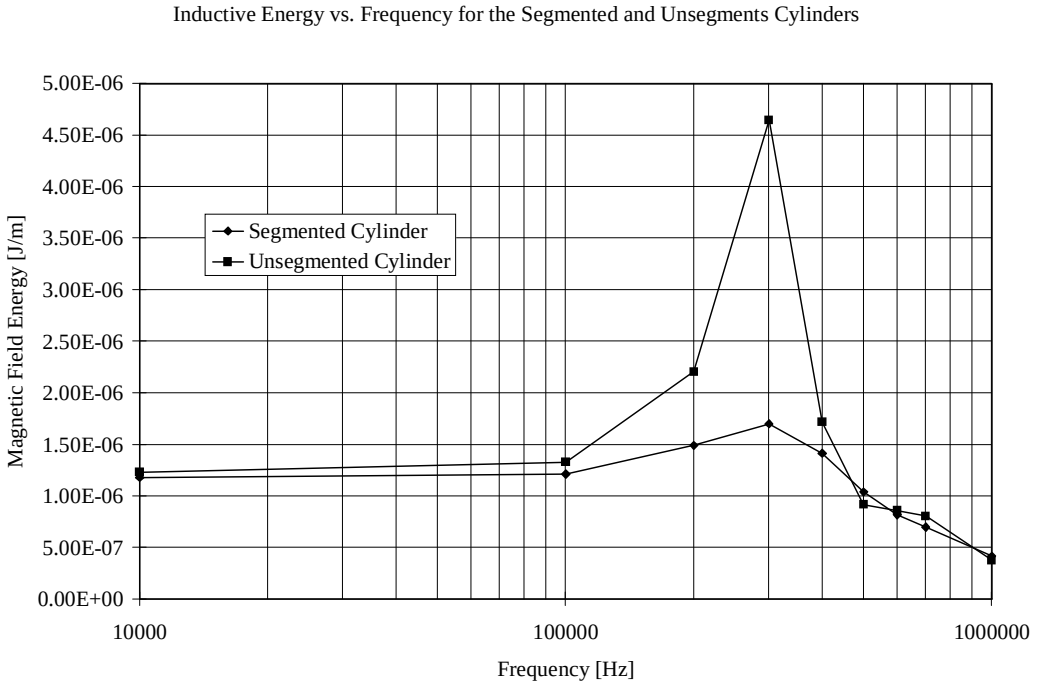

Figure 6.5: Total loss and magnetic energy per meter in the 2D cylindrical model for segmented and unsegmented designs (full loss case).

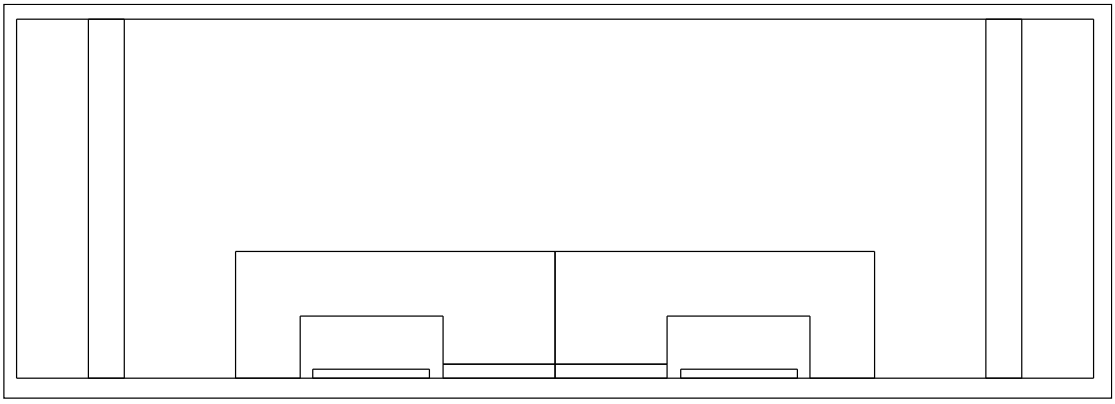

Figure 6.6: 2D FEA geometry for the charger transformer. The puck in the center leg is set to have no net induced current in the z direction. The left and right sides of the core are set separately to have no net current. The vertical bars on the edges of the model provide an infinite permeability path as in the infinite slab model.

Figure 6.7 shows the field plots of the core structure with and without an air gap at 700 kHz and 400 kHz respectively. The core with the air gap shows much more uniform flux distribution than does the core without the air gap. The differences in the device impedance magnitude and phase—shown in Figure 6.8—also show a significant difference. Other than the the obvious shift in magnitude due to the lower magnetizing inductance of the gapped core, the frequency at which the impedance phase angle moves significantly away from 90 degrees is much lower for the ungapped core. Figure 6.8 also includes a curve of the measured magnitude and phase of one sample of the charger core that has a center leg gap. There is significant disagreement between the measured and simulated curves, but the shift in the phase of the impedance has a similar quality in each.

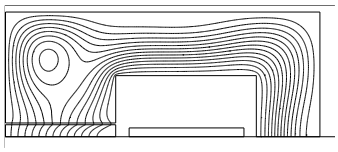

(a) Gapped centerleg structure at 700 kHz

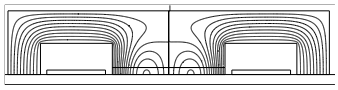

(b) Ungapped centerleg structure at 400 kHz

Figure 6.7: Flux distributions in the charger core for the gapped and ungapped cases at 700kHz and 400 kHz respectively.

6.4 Discussion of Results

There are several aspects of the 2D-FEA simulation as well as the measurement procedures that remain unresolved and that deserve additional research. First, as mentioned in the

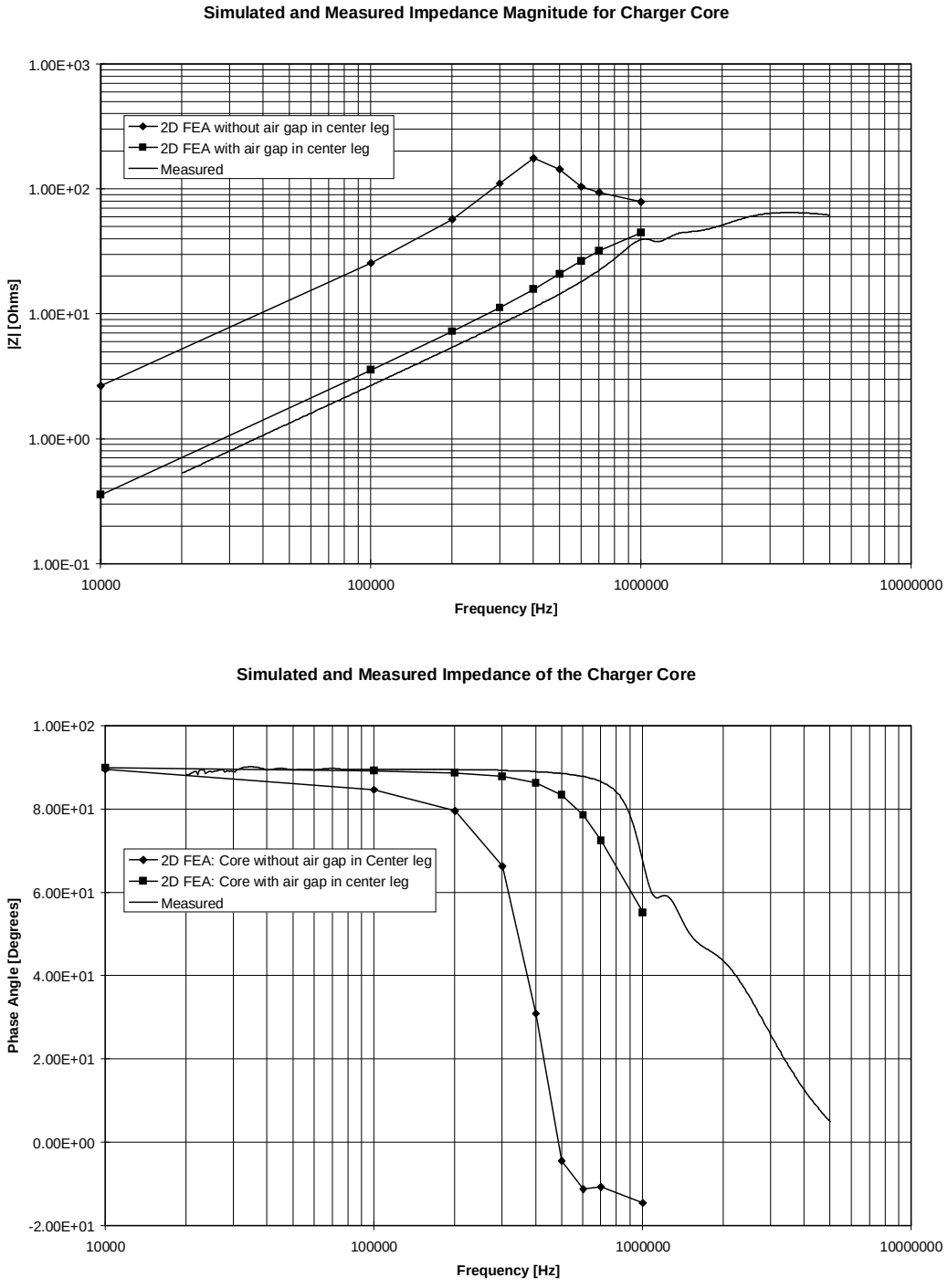

Figure 6.8: Impedance magnitude and phase for the 2D-FEA models of the charger core with and without an air gap in the center leg. the measured response of a sample device is also plotted.

previous chapter, the simulation procedure for truly three-dimensional structures using the available two-dimensional tools is fundamentally flawed. Since the displacement and conduction currents that are induced in the core flow normal to the model dimension, there is no way to accurately account for the depth of the core in the 2D model. The best that can be done is to enforce that the net current in a given region be set to zero. Since this does not restrict the current flow within that region in the same way that an actual geometry does, then it is not clear how well this method models reality. In addition, the charger core has both a circular center section that has cylindrical symmetry and an outer C-C structure that has rectangular symmetry. That means that any solution in r-z coordinates overestimates the losses in the top, bottom and outer legs of the core while a solution in x-y coordinates neglects the circumferential currents that are induced in the center leg.

The alternatives here are not presently very attractive for routine use by most designers. The available full-field solutions for three-dimensional problems have proven to be unwieldy, although improvements in this situation can be expected as the simulation software matures. At a basic level, however, the improvement in modeling structures such as those examined here may require a reformulation of the underlying field solution if the difficulties related to the setting of reasonable boundary conditions is not resolved in the full-wave 3D-solvers currently available or planned for release. Some possibilities in this area are the use of functional solutions in place of weighted residuals since the functional approach provides a more direct relationship between the fields and the numerical solution and represents a direct application of Maxwell's equations to the given equation. Another option is to simulate different sections of a given geometry separately and then combine the results of several simulations to give an approximate result for the entire structure. In such a case, the rectangular legs of the core may be simulated using an axial field solver to account for the field variations present in both the width and depth dimensions while the effects of gaps within the magnetic path are simulated in an axial current solver. This is clearly not the preferred solution—which in all cases would be a full three-dimensional model of the device—but the combination of several 2D simulations may provide more insight than a reliance on a single simulation that is unrepresentative of the true problem geometry.

Chapter 7

Conclusions

7.1 Summary

This dissertation has examined ways in which the size of a MnZn ferrite core changes the overall performance of the magnetic device of which it is a part. The goal of this work is to introduce the pertinent issues and examine practical modeling and analysis methods that can help predict these effects for any core shape. The early sections of the document explain the fundamental physical processes and show that for a semiconducting material like ferrite the overall response in a circuit results from a combination of electromagnetic effects. These include eddy currents induced in the core by time-varying flux as well as dimensional resonances that occur as the core cross-sectional dimensions approach the wavelength in the ferrite. The particular nature of MnZn ferrites has been highlighted since these materials are popular in the range of several hundred kilohertz and it is in this range of frequencies where electromagnetic resonance can be a significant problem for cores that are not unreasonably large.

In order for any modeling efforts to produce useful results, it is critical to have access to reliable, complete and accurate material characteristic data. This is true whether the modeling is based on analytical expressions such as described in Chapter 4 or on numerical models such as those in Chapters 5 and 6. Consequently, a significant portion of this dissertation deals with both the acquisition of measurement data and the use of this data in field modeling tools. This material characterization effort presented in Chapter 3, while useful in the analysis and simulation presented in later chapters, is quite general and can be applied to a variety of materials. The need to develop such a measurement scheme, furthermore, reflects the fact that the currently available sources of material information do not provide

adequate detail of the type needed for analytical or numerical modeling efforts. The combination of specially designed thin toroidal cores for use in magnetic characteristic testing and thin plates of ferrite with suitable electrodes for electrical characterization provides a relatively simple step-by-step procedure for acquiring the required material information. While the magnetic data acquisition described in Chapter 3 is performed with a particular set of computer-aided test equipment, the testing is essentially impedance testing and can therefore be performed with any set of impedance test equipment that can supply adequate voltage drive. Similarly, the extraction of complex dielectric constant information requires only a simple R–C admittance test.

Once material data is known, it can be used in either analytical or numerical solutions to give the response of the particular device geometry to known excitation fields. Chapter 4 presents the infinite slab field solution and from it derives expressions for the normalized impedance of a core based only on a single cross-sectional dimension. While this particular problem solution has limited use in more general device modeling, the results of the closed-form solution does provide a relatively simple method for gaining insight into the performance of various core materials under different excitation frequencies. Chapter 4 illustrates that the electromagnetic resonances in the ferrite cause a "transmission-line" effect in the device impedance and that the this effect is determined by the size of the core cross-section. In addition, both the magnetic losses and the eddy current losses in the core act to damp the swings in impedance and this results in an essentially resistive device above the initial resonance frequency.

Chapters 5 shows how a commercial finite element analysis tool can be used to model a variety of devices—both simple one-dimensional structures and more complicated gapped structures. This analysis provides one method for examining the field distribution in real-world designs. Through such field modeling it is possible to examine exactly which physical process dominates the overall response of the device. Such tools provide a way to visualize the effects that changes in material constant and/or core shape have on device performance and in general provide a way to predict the device performance prior to construction.

Several modeling issues are raised in Chapter 5, however, that present significant obstacles to the more widespread use of such tools. In particular, since the two-dimensional solvers assume an infinite depth of the structure, it is possible to set up fields that are not physically realistic. This is illustrated in the discussion by the variation of the boundary H-fields on a toroidal structure due to the presence of a net current in the core material itself. Chapter 5 presents some alternative solution set-ups that provide somewhat better results through the use of additional source excitations and artificial flux paths that provide for boundary conditions closer to those expected in the actual device. These alternate strategies do in fact improve the agreement of the 2D-FEA simulation and the measured values, but this is at best a manipulation of the software to provide a better match to known results. In the

future this issue needs to be addressed through improved FEA tools that would provide either true 3D modeling or would provide better control of the excitation fields—both the magnetic field and the electric field.

Even given the implementation problems of using a 2D-FEA solver to model a truly three-dimensional geometry, the comparison of simulated device performance to the measured performance provides encouragement for further development of these tools. The results for the toroidal and block cores of Chapter 5 show fair agreement with the measurements performed in the lab on similar structures. The analysis of gapped structures demonstrates that while an air gap in the structure makes the increased losses due to non-uniform flux distribution within the core less noticeable, it does not provide for the complete elimination of dimensional effects in the core. Specifically, the presence of an air gap forces the flux to distribute more evenly, and this leveling of the flux density results in a higher effective bandwidth for the device. However, as was noted in Chapter 5, the field distribution plots illustrate that the shift of resonance effects to higher frequencies is a complex function of the gap location and device geometry; it is not simply a result of the air gap lowering the effective permeability of the device and therefore increasing wavelength as has been stated in the literature. Within the blocks of ferrite themselves there is no inherent benefit of the discrete air gaps at the boundaries since the wavelength of the material itself is unaffected by the presence of such gaps.

Chapter 6 presents a 2D-FEA analysis of the inductive charger core introduced as a motivating example of the increasing usage of large ferrite structures. The large cross sectional dimension of the disk or "puck" in the charger's primary paddle presents the most concern for dimensional effects. However, the dimensional effects in the center of the core are mitigated by the relatively large air gap in its center leg. The analysis of the structure shows that without this air gap the inductive bandwidth of the device would be significantly reduced. The charger performance, therefore, may change considerably if this air gap varies as the paddle is repeatedly inserted and removed through the charger's life or if different charger core designs are implemented that minimize this air gap for other design reasons (such as the resulting reduction of charger magnetizing current). In the laboratory, the charger cores tested show a impedance phase rotation of up to 45 degrees at one megahertz. While this change in the device impedance is not as dramatic as the sharp loss of inductance demonstrated for the large toroidal and block cores, such an increase in the resistive component of the magnetizing impedance can still significantly impact the overall efficiency of the device.

7.2 Future Research

This work has focused on the demonstration and characterization of phenomena that occur in ferrites and that have received only generally vague mention over the years. The primary goal was to understand the effects and the interplay of eddy currents and dimensional resonance in ferrite structures. A secondary goal was to show that provided adequate material information is available as input, even relatively simple numerical solvers can provide reasonable prediction of device performance. One of the most fruitful areas of additional research is in the improvement of the numerical simulation process through both improved solver algorithms and improved data flow between the measurement and simulation environments. Specifically, these efforts would be greatly aided by the availability of stable and usable numerical routines that handle full three-dimensional models of material with complex material characteristics and that provide rapid simulation of a variety of design alternatives. While much of this work will depend on the commercial software developers, the user community for such tools can play a key role in helping to develop the functionality required.

Since all of the work presented here is based on linear field solutions, one obvious area for extension of this work is to simulate similar structures with non-linear solvers. The linear material assumption is usually a good one for many standard high-frequency designs where the flux density is low and the excitation frequency and voltage are relatively fixed. These assumptions, however, are being routinely tested by new applications such as power factor correction circuits where the input inductor is subjected to both line frequency and high frequency excitation and where the high-frequency excitation varies in both frequency and amplitude. The loss in the core of such a device is usually modeled based solely on sinusoidal loss measurement data published by the manufacturer as typical of that material. Research into ways of solving this general excitation problem have generally been limited to smaller devices where geometrical effects are neglected.

The "brass ring" of magnetics design and analysis, however, is often described as a tool that is more intimately connected with the rest of the circuit simulation process. Such a design tool would be able to take the electrical specifications—voltages and currents—from the circuit simulation and design the appropriate magnetic device automatically. This goal of a single design algorithm that applies to all structures is achievable at this point only through the oversimplification of the actual problem through the use of standard design equations. If the physical processes examined in this thesis are ever to be included into routine design equations, then the first thing that is needed is full material characterization of all commercial ferrite materials. This could be greatly aided by the establishment of a standard toroidal core size and thin plate geometry that all manufacturers could produce routinely for testing purposes.

Bibliography

[1] R. Severns, E. Yeow, G. Woody, J. Hall, and J. Hayes, "An ultra-compact transformer for a 100 W to 120 kW inductive coupler for electric vehicle battery charging", in *Applied Power Electronics Conference Conference Record*. IEEE, 1996, pp. 32–38.

[2] E.C. Snelling, *Soft Ferrites*, Butterworths, London, 1988.

[3] A.F. Goldberg, J.G. Kassakian, and M.F. Schlecht, "Issues related to 1-10 MHz transformer design", in *Power Electronics Specialists Conference (No.87CH2459-6)*. IEEE, 1987, pp. 379–86, IEEE; New York, NY, USA.

[4] Van Alan Niemela, *Analysis and Modeling of Leakage Inductance and AC Winding Resistance in High-Frequency Multiple-Winding Transformers*, PhD thesis, Duke University, 1992.

[5] E. Roess, "Adaptability of soft ferrite materials, cores and accessories to the needs of modern technology", in *Magnetic Materials Attract Business: Seminar Proceedings (ERA Report 87-0285)*. 1988, pp. 5.2/1–11, ERA Technol; Leatherhead, UK.

[6] Klaus Biedermann, "E ferrite cores for 10 W to 10 kW", *Siemens Components*, vol. 23, no. 2, pp. 60–4, 1988.

[7] G. Herzer and H. R. Hilzinger, "Recent developments in soft magnetic materials", *Physica Scripta*, vol. T24, pp. 22–8, 1988.

[8] A.F. Goldberg, "High field properties of Nickel-Zinc ferrites at 1-10 MHz", in *Applied Power Electronics Conference Record*. IEEE, 1988, pp. 311–18.

[9] P.M. Gradzski, *Core Loss Characterization and Design Optimization of High- Frequency Power Ferrite Devices in Power Electronics Applications*, PhD thesis, Virginia Polytechnic Institute and State University, 1992.

[10] Y. Saito, S. Hayano, and Y. Sakaki, "A parameter representing eddy current loss of soft magnetic materials and its consecutive equation", *Journal of Applied Physics*, vol. 64, no. 10, pp. 5684–5686, 1988.

[11] W. E. Babcock, "A simplified methods of determining high freequency characteristics of magnetic core materials", in *Proceedings of Powercon 10*, 1983, pp. F3–1–17.

[12] V.J. Thottuvelil, T.G. Wilson, and H.A. Owen, Jr., "High-frequency measurement techniques for magnetic cores", in *16th Annual IEEE Power Electronics Specialists Conference (Cat. No. 85CH2117-0)*. IEEE; ESA, 1985, pp. 412–25, IEEE; New York, NY, USA.

[13] V.J. Thottuvelil, T.G. Wilson, and H.A. Owen, Jr., "High-frequency measurement techniques for magnetic cores", *IEEE Transactions on Power Electronics*, vol. 5, no. 1, pp. 41–53, 1990.

[14] O. Inoue, N. Matsutani, and K. Kugimiya, "Low loss Mn-Zn ferrites: Frequency dependence of minimum power loss temperature", *IEEE Transactions on Magnetics*, vol. 29, no. 6, pp. 3532–4, 1993.

[15] W. A. Roshen, R. L. Steigerwald, R. Charles, W. Earls, G. Claydon, and C. F. Saj, "High efficiency high density MHz magnetic components for a low profile converter", in *Applied Power Electronics Conference*. IEEE, 1992, pp. 674–683.

[16] J. T. S. Irvine and A. R. West, "AC electrical and magnetic measurements of a NiZn ferrite", in *5th International Conference on Ferrites (ICF-5)*, 1989, pp. 221–225.

[17] Ju Zhang, Glenn R. Skutt, and Fred C. Lee, "Some practical issues related to core loss measurement using impedance analyzer", in *Applied Power Electronics Conference*. IEEE, 1995, pp. 547–554.

[18] B. Carsten, "Why the magnetics designer should measure core loss; with a survey of loss measurement techniques and a low cost, high accuracy alternative", in *Proceedings High Frequency Power Conversion '95*. 1995, pp. 103–119, Intertec Int; Ventura, CA, USA.

[19] R. F. Soohoo, *Theory and Application of Ferrites*, Prentice-Hall, 1960.

[20] A. R. von Hippel, *Dielectric Materials and Applications*, Wiley, 1954.

[21] International Electrotechnical Commission (IEC), *Cores for inductors and transformers for telecommunications: Part 1—Measuring Methods*, 2nd edition, IEC 367–1, 1982.

[22] MMPA, *Magnetic Materials Producers Association Ferrite Users Guide*, 1992.

[23] Philips, Inc., *Soft Ferrites Catalog*, no. 9398 184 01011, 1996.

[24] TDK, Inc., *TDK Ferrite Cores for power Supply and EMI/RFI Filter*, 1990.

[25] Magnetics Division of Spang & Company, *Ferrite Cores*, FC-601-5C, 1995.

[26] Siemens Components, *Ferrites and Accessories*, no. B5-P6115-X-X-7600, 1990/91.

[27] Thompson-CSF, Inc, *Soft Ferrties*, 1993.

[28] T. Matsuoka, T. Sato, and Y. Sakaki, "Dimension dependence of power losses in polycrystalline Mn-Zn ferrite cores", *Electronics and Communications in Japan, Part 2 (Electronics)*, vol. 72, no. 6, pp. 51–6, 1989.

[29] J.J. Thompson, *Notes on Recent Researches in electricity and Magnetism*, Clarendon Press, Oxford, England, 1893.

[30] P.L. Dowell, "Effects of eddy current in transformer windings", *Proc. of IEE*, vol. 113, no. 8, pp. 1387–1394, 1964.

[31] Perry M.P, "Multiple layer series connected winding design for minimum losses", *IEEE Trans. Power Apparatus Sys.*, vol. 98, no. 1, pp. 116–123, 1979.

[32] B. Carsten, "Design considerations for high frequency magnetics", in *Proceedings of High Frequency Power Conversion 1994*. 1994, pp. 459–501, Intertec Int; Ventura, CA, USA.

[33] S. Ticknor, "Magnetic core calculations-a basic program", *R.F. Design*, vol. 9, no. 8, pp. 58–9, 1986.

[34] J. Jongsma, "High-frequency ferrite power transformer and choke design", Tech. Rep., Philips Components and Materials Technical Publication, 1986.

[35] J.P. Vandelac and P. Ziogas, "A novel approach for minimizing high frequency transformer copper loss", *IEEE Transactions on Power electronics*, vol. 3, no. 3, pp. 266–276, 1988.

[36] V.A. Niemela, G.R. Skutt, A.M. Urling, Y.N. Chang, T.G. Wilson, H.A. Owen, Jr., and R.C. Wong, "Calculating the short-circuit impedances of a multiwinding transformer from its geometry", in *Power Electronics Speciaalists Conference Record*. IEEE, 1989, vol. 2, pp. 607–17.

[37] A.W. Lotfi, *The Electrodynamics of High Frequency Magnetics in Power Electronics*, PhD thesis, Virginia Polytechnic Institute and Statue University, 1993.

[38] E. Laveuve, J.P. Keradec, and G. Meunier, "Influence of induced currents in conductors on leakage and losses in a transformer", *Electric Machines and Power Systems*, vol. 19, no. 1, pp. 55–68, 1991.

[39] Rudy Severns, "Additional losses in high frequency magnetics due to non-ideal field distributions", in *Applied Power Electronics Conference*. IEEE, 1992, pp. 333–338.

[40] Z. Azzouz, A. Foggia, L. Pierrat, and G. Meunier, "3d finite element computation of the high frequency parameters of power transformer windings", *IEEE Transactions on Magnetics*, vol. 29, no. 2, pp. 1407–10, 1993.

[41] Glenn R. Skutt, Fred C. Lee, Ray Ridley, and Dale Nicol, "Leakage inductance and termination effects in a high-power planar magnetic structure", in *Applied Power Electronics Conference Record*. 1994, pp. 295–301, IEEE.

[42] A. Basak, Chi-Hang Yu, and G. Lloyd, "Efficient transformer design by computing core loss using a novel approach", *IEEE Transactions on Magnetics*, vol. 30, no. 5, 1994.

[43] Rakesh K. Dhawan, Patrick Davis, and Ashraf W. Lotfi, "High frequency loss evaluation in high frequency multi-winding power transformers", in *Applied Power Electronics Conference*. 1995, pp. 354–60, IEEE.

[44] Ning Dai, A. W. Lotfi, G. R. Skutt, W. Tabisz, and F. C. Lee, "A comparative study of high-frequency, low-profile planar transformer technologies", in *Applied Power Electronics Conference Record*. 1994, pp. 226–32, IEEE.

[45] L.M. Bosley, "Data sheets provide clues for optimizing selection of SMPS ferrite core material", *Powerconversion & Intelligent Motion*, vol. 19, no. 7, pp. 13–15, 1993.

[46] E. Otsuki, S.Y. Otsuka, K. Shoji, and T. Sato, "Microstructure and physical properties of Mn-Zn ferrites for high-frequency power supplies", *Journal of Applied Physics*, vol. 69, no. 8, pp. 5942–5944, 1991.

[47] C. Guillaud, "The properties of manganese-zinc ferrites and the physical processes governing them", *Proceedings of the IEE*, vol. Suppl. 5, pp. 165–178, 1957.

[48] C.G. Koops, "On the dispersion of resistivity and dielectric constant of some semiconductors at audio frequencies", *Physical Review*, vol. 83, no. 1, pp. 121–124, 1951.

[49] D. Polder, "Ferrite materials", *Proceedings of the IEE*, vol. 97(Part II), pp. 246–256, 1950.

[50] Lord Rayleigh, "Notes on electricity and magnetism III: On the behaviour of iron and steel under the operation of feeble magnetic forces", *Phil. Mag.*, vol. 23, pp. 225, 1887.

[51] Weiss, ", *Éclairage Électrique*, vol. 8, pp. 436, 1896.

[52] M. Wien, "Ueber die magnetisirung durch wechselstrom", *Ann. Phy. Chem.*, vol. 66, no. 13, pp. 859–953, 1898.

[53] G. A. Kelsall, "Permeameter for alternating current measurements at small magnetizing forces", *J. Opt. Soc. Am. Rev. Sci. Instr.*, vol. 8, no. 2, pp. 329–38, 1924.

[54] Bady, "Measurement of losses of magnetic materials at high inductions at frequencies up to 100 megacycles", *Journal of Applied Physics*, vol. 29, no. 3, pp. 393–4, 1958.

[55] P. P. Lombardini, R. F. Schwartz, and R. J. Doviak, "Measurement of the properties of various ferrites used in magnetically tuned resonant circuits in the 2.5–45 mc/sec region", *Journal of Applied Physics*, vol. 29, no. 3, pp. 395–6, 1958.

[56] H. E. Bussey, "Measurement of RF properties of materials: A survey", *Proceedings of the IEEE*, vol. 55, no. 6, pp. 1046–53, 1967.

[57] V. Cagan and M. Guyot, "Fast and convenient technique for broadband measurements of the complex initial per meability of ferrimagnets", *IEEE Transactions on Magnetics*, vol. MAG-20, no. 5, pp. 1732–4, 1984.

[58] R. H. Goldfarb and H. E. Bussey, "Method for measuring complex permeability", *Review of Scientific Instrumentation*, vol. 58, no. 4, pp. 624–627, 1987.

[59] A. Fessant, J Gieraltowski, J Loaëc, and H. Le Gall, "Strip-line method for measuring the complex permeability of magnetic materials", *Journal of Magnetic Materials*, vol. 83, pp. 557–8, 1990.

[60] James Baker-Jarvis, Michael D. Janezic, John H. Grosvenor, Jr., and Richard G. Geyer, "Transmission/reflection and short-circuit line methods for measuring permittivity and permeability", Tech. Rep. 1355-R, NIST, 1993.

[61] ASTM, *Standard Test Method for Complex Dielectric Constant of Nonmetallic Magnetic Materials at Microwave Frequencies*, Std. A 893–86,1991.

[62] A.C. Lynch, H.D. Griffiths, S. Appleton, A.L. Cullen, A. Khosrowbeygi, and R. Benjamin, "Free-wave measurement of permeability and permittivity of ferrites at millimetre-wave frequencies", *IEE Proc.-Sci. Meas. Technolol.*, vol. 142, no. 2, pp. 169–175, 1995.

[63] J. Tamsky, "A cathode-ray B-H tracer", *Electrical Engineering*, vol. 66, pp. 678–680, 1947.

[64] B. Christensen, "Radio frequency B-H tracer and power measurement of ferrites", *AIEE Conference on Magnetic Materials*, vol. T-78, pp. 361–364, 1955.

[65] T. Katane, T. Yamguchi, T. Ito, T. Sato, and Y. Sakaki, "A high-frequency iron loss measuring system", *IEEE Transactions on Magnetics*, vol. MAG-20, no. 5, pp. 1729–31, 1984.

[66] T. Mochizuki, I. Sasaki, and K. Murakawa, "A high-frequency core loss automatic measuring system", *IEEE Transactions on Magnetics*, vol. MAG-22, no. 5, pp. 668–70, 1986.

[67] T. Sato and Y. Sakaki, "Mechanism generating power losses in MHz band in polycrystalline Mn-Zn ferrite cores used for switching power supplies", *Electronics and Communications in Japan, Part 2 (Electronics)*, vol. 72, no. 6, pp. 42–50, 1989.

[68] H. W. Lord, "Dynamic hysteresis loop measuring equipment", *AIEE Transactions Part 1: Communications Electronics*, vol. 71, pp. 269–272, 1952.

[69] M. Kido, "B-H analyzer measures high-frequency magnetic characteristics", *JEE (Journal of Electronic Engineering)*, vol. 29, no. 310, pp. 52–6, 1992.

[70] Y. Sakaki, T. Matsuoka, and M. Yamaguchi, "Effect of dimensions on power losses in Mn-Zn ferrite cores", *IEEE Translation Journal on Magnetics in Japan*, vol. TJMJ-1, no. 9, pp. 1082–4, 1985.

[71] Y. Sakaki, M. Yoshida, and T. Sato, "Formula for dynamic power loss in ferrite cores taking into account displacement current", *IEEE Transactions on Magnetics*, vol. 29, no. 6, pp. 3517–19, 1993.

[72] D.C. Jiles and D.L. Atherton, "Theory of ferromagnetic hysteresis", *Journal of Magnetism and Magnetic Materials*, vol. 61, no. 1-2, pp. 48–60, 1986.

[73] Mark C. Williams, "A CAD model of nonlinear ferromagnetics for circuit simulation", Master's thesis, University of South Florida, 1994.

[74] M.C. Williams, R.S. Vogelsong, and K.S. Kundert, "Simulation and modeling of nonlinear magnetics", in *1995 IEEE Symposium on Circuits and Systems (Cat. No.95CH35771)*. 1995, vol. 1, pp. 736–9, IEEE; New York, NY, USA.

[75] K.H. Carpenter and S. Warren, "A wide bandwidth, dynamic hysteresis model for magnetization in soft ferrites", *IEEE Transactions on Magnetics*, vol. 28, no. 5, pp. 2037–41, 1992.

[76] D.C. Jiles, "Frequency dependence of hysteresis curves in 'non-conducting' magnetic materials", *IEEE Transactions on Magnetics*, vol. 29, no. 6, pp. 3490–2, 1993.

[77] D.C. Jiles, "Frequency dependence of hysteresis curves in conducting magnetic materials", *Journal of Applied Physics*, vol. 76, no. 10, pp. 5849–55, 1994.

[78] S.A. Amelin, A.A. Novikov, K.N. Stroyev, and N.N. Stroyev, "Modification of Jiles's and Atherton's model for taking account of frequency properties of magnetic materials", *Elektrichestvo*, , no. 11, pp. 60–3, 1995.

[79] J.H. Baranowski, "Modification of the model Jiles-Atherton (ferromagnetic hysteresis)", *Kwartalnik Elektroniki i Telekomunikacji*, vol. 40, no. 1, pp. 1–20, 1994.

[80] D.A. Philips, L.R. Dupre, and J.A. Melkebeek, "Comparison of Jiles and Preisach hysteresis models in magnetodynamics", *IEEE Transactions on Magnetics*, vol. 31, no. 6, pp. 3551–3, 1995.

[81] N. Schmidt and H. Guldner, "A simple method to determine dynamic hysteresis loops of soft magnetic materials", *IEEE Transactions on Magnetics*, vol. 32, no. 2, pp. 489–96, 1996.

[82] M.D. Takach and Peter O. Lauritzen, "Survey of magnetic core materials", in *Applied Power Electronics Conference*. IEEE, 1995, pp. 560–566.

[83] W. Roshen, "Ferrite core loss for power magnetic components design", *IEEE Transactions on Magnetics*, vol. 27, no. 6, pp. 4407–15, 1991.

[84] K.H. Al-Shara, R.S. Habib, and N.M. Aziz, "An approach to the formulation of high frequency ferrite hysteresis loss", *Journal of Electronics & Computers Research*, vol. 1, no. 2, pp. 35–45, 1987.

[85] Kader Hmood Augla, *Losses in High Frequency Power Inductors and Transformers*, PhD thesis, University of Bath, England, 1985.

[86] J. Hess, "Simple, speedy, systematic: calculating losses in ferrite cores", *Siemens Components (English Edition)*, vol. 28, no. 4, pp. 22–4, 1993.

[87] T. Fujiwara and R. Tahara, "Expression of high frequency-losses in Mn-Zn ferrite", *IEEE Translation Journal on Magnetics in Japan*, vol. 8, no. 11, pp. 795–800, 1993.

[88] S.A. Mulder, "Fit formulae for power loss in ferrites and their use in transformer design", in *Official Proceedings of the Twentysixth International Power Conversion Conference*. 1993, pp. 345–59, ZM Commun.; Nurnberg, Germany.

[89] J.K. Bowman, R.F. Cascio, M.P. Sayani, and T.G. Wilson, "A calorimetric method for measurement of total loss in a power transformer", in *Power Electronics Specialists Conference (Cat. No.91CH3008-0)*. IEEE, 1991, pp. 633–40, New York, NY, USA.

[90] Jiří Lammeraner and Miloš Štafl, *Eddy Currents*, CRC Press, 1967, English Translation edited by G.A Toombs, Originally published in Czechoslovakia in 1964.

[91] R. L. Stoll, *The analysis of eddy currents*, Clarendon, Oxford, 1974.

[92] J.Simkin, "Eddy current modeling in three dimensions", *IEEE Transactions on Magnetics*, vol. 22, no. 5, pp. 609–613, 1986.

[93] Seiichi Yamada, Etsuo Otsuki, and Tsutomu Otsuka, "AC resistivity of Mn-Zn ferrites", in *Intelec Conference Record*. 1991, pp. 703–708, IEEE.

[94] Hsiu-Fung Cheng, "Modeling of electrical response for semiconducting ferrite", *Journal of Applied Physics*, vol. 55, no. 6, pp. 1831–7, 1984.

[95] M.J. Tung, W.C. Chang, C.S. Liu, T.Y. Liu, C.J. Chen, and T.Y. Tseng, "Study of loss mechanisms of Mn-Zn ferrites in the frequency from 1 MHz to 10 MHz", *IEEE Transactions on Magnetics*, vol. 29, no. 6, pp. 3526–8, 1993.

[96] Jay Northrup Damask, "Characterization of commercial manganese-zinc ferromagnetic materials", Master's thesis, Massachusetts Institute of Technology, 1990.

[97] F.G. Brockman, P.H. Dowling, and W.G. Steneck, "Dimensional effects resulting from a high dielectric constant found in a ferromagnetic ferrite", *Physical Review*, vol. 77, no. 1, pp. 85–93, 1950, Incomplete Reference: need page numbers.

[98] W.M. Chen, P.D. Evans, and W.J.B. Heffernan, "Inductor design concepts for high frequency applications", *Proceedings of the EPE*, vol. 4, pp. 119–124, 1991.

[99] Glenn R. Skutt and Fred C. Lee, "Use of visualization tools for examining flux distributions is magnetic structures", in *Applied Power Electronics Conference Record*. IEEE, 1995, pp. 567–73.

[100] Y. Marechal, J.L. Coulomb, G. Meunier, and G. Touzot, "Use of the diffuse element method for electromagnetic field computation", *IEEE Transactions on Magnetics*, vol. 29, no. 2, pp. 1475–8, 1993.

[101] J. Hess, "Measurement and calculation techniques for power losses of ferrites from kHz to MHz range", in *Official Proceedings of the Twentysixth International Power Conversion Conference*. 1993, pp. 327–44, ZM Commun; Nurnberg, Germany.

[102] A. Ben Ahmed, J. Lucidarme, and P.F. Desesquelles, "Semi-numerical method for the design of machines with permanent magnets and centralized coils", *Journal de Physique III (Applied Physics, Materials Science, Fluids, Plasma and Instrumentation),(France)*, vol. 5, no. 6, pp. 703–25, 1995.

[103] R. Asensi, R. Prieto, J. A. Cobos, O. García, and J. Uceda, "A cad tool for magnetic components modeling", in *Applied Power Electronics Conference Record*. 1996, pp. 427–33, IEEE.

[104] A. Ben Ahmed, J. Ahmed, and G. Guy, "Computing ferrite core losses at high frequency by finite elements method including temperature influence", *IEEE Transactions on Magnetics*, vol. 30, no. 5, 1994.

[105] M. Jarnieux and G. Meunier, "FEM modelling of the magnetic, thermal, electrical and mechanical transient phenomena in linear induction launchers", in *9th Conference on the Computation of Electromagnetic Fields (COMPUMAG '93)*, 1994, pp. 3312–15.

[106] H. Fukunaga, H. Abe, Y. Ohta, and H. Kakehashi, "Evaluation of magnetization models for simultaneous analysis of flux and temperature distributions in ferrite cores", *Journal of Magnetism and Magnetic Materials*, vol. 133, no. 1-3, pp. 516–19, 1994.

[107] G. Meunier, J.C. Sabonnadiere, and J.L. Coulomb, "The finite element post-processor of FLUX3D (field computation package)", *IEEE Transactions on Magnetics*, vol. 27, no. 5, pp. 3786–91, 1991.

[108] B.T. Chia, J.L. Coulomb, and J.C. Verite, "Impact of solid modelers on electromagnetic device design", *Journal of Applied Physics*, vol. 67, no. 9, pp. 5800–2, 1990.

[109] B.T. Chia, J.L. Coulomb, J.C. Sabonnadiere, J.C. Verite, and A. Nicolas, "A unified database for data exchange in electromagnetic field computation", *IEEE Transactions on Magnetics*, vol. 26, no. 2, pp. 811–14, 1990.

[110] H. Yamashita, T. Johkoh, and E. Nakamae, "Interactive visualization of interaction between magnetic flux density and eddy currents in a 3D steady state field", *IEEE Transactions on Magnetics*, vol. 28, no. 2, pp. 1778–81, 1992.

[111] L.J. Rosenblum, "Research issues in scientific visualization", *IEEE Computer Graphics and Applications*, vol. 14, no. 2, pp. 61–3, 1994.

[112] V. Cingoski and H. Yamashita, "An improved method for magnetic flux density visualization using three-dimensional edge finite element method", *Journal of Applied Physics*, vol. 75, no. 10, pp. 6042–4, 1994.

[113] Hoon Jung, Sun-Ki Hong, and Jong-Soo Won, "Finite element analysis of magnetic fields with hysteresis characteristics", *Transactions of the Korean Institute of Electrical Engineers*, vol. 38, no. 12, pp. 1033–40, 1989.

[114] J.M. Dedulle, G. Meunier, L. Pierrat, and J.C. Sabonnadiere, "Homogenization for nonlinear problems applied to the modelling of transformers", in *Modelling and Control of Electrical Machines: New Trends. Proceedings of the Third International Symposium*, J. Le Doeuff, R.and Robert, Ed., pp. 59–64. North-Holland; Amsterdam, Netherlands, 1991.

[115] J. R. Garcia, J. M. Burdio, A. Martinez, and J. Sancho, "A method for calculating the workpiece power dissipation in induction heating processes", in *Applied Power Electronics Conference Record*. 1994, pp. 302–7, IEEE.

[116] Jia-Tzer Hsu, *CAD Models and Formulations for Electro-Magneto-Thermal Simulation of Power Semiconductor and Magnetic Devices*, PhD thesis, University of Florida, 1995.

[117] E. Logcais, J.-P. Yonnet, J.-L. Coulomb, G. Meunier, and S. Gitosusastro, "Comparison between 3D, 2D finite element methods and analytical calculations for electromagnetic problems", *IEEE Transactions on Magnetics*, vol. 24, no. 1, pp. 66–9, 1988.

[118] J.F. Janak, "Dynamics of diffusion-damped domain wall motion", *Journal of Applied Physics*, vol. 34, no. 4, pp. 1119–1120, 1963.

[119] D. Park, "Magnetic rotation in a polycrystaline ferrite", *Phys. Rev.*, vol. 97, no. 1, pp. 60–66, 1955.

[120] Constantine A. Balanis, *Advanced Engineering Electromagnetics*, John Wiley & Sons, 1989.

[121] S. Ramo, J. R. Whinnery, and T. Van Duzer, *Fields and Waves in Communication Electronics*, Wiley, 2nd edition, 1984.

[122] Charles A. Holt, *Introduction to Electromagnetic Fields and Waves*, John Wiley & Sons, 1963.

[123] W. H. Hayt, *Engineering Electromagnetics*, McGraw-Hill, New York, fifth edition, 1989.

[124] J. D. Kraus, *Electromagnetics*, McGraw-Hill, 3rd edition, 1984.

[125] Ping Han, "Characterization of MnZn ferrite materials and finite element method for MnZn ferrite core loss calculations", Master's thesis, Virginia Polytechnic Institute and State University, 1995.

[126] International Electrotechnical Commission (IEC), *Calculation of the effective parameters of magnetic piece parts*, IEC 205, 1966.

[127] Hewlett-Packard, *HP 16451B Dielectric Test Fixture Operation and Service Manual*, 1994.

[128] Frederick Emmons Terman, *Radio Engineering*, McGraw-Hill, 1947.

[129] Ping Han, Glenn R. Skutt, and Fred C. Lee, "Finite element method for ferrite coreloss calculation", in *Applied Power Electronics Conference Record*. IEEE, 1995, pp. 348–353.

Vita

Glenn R. Skutt

The author was born in Radford, Virginia on January 2, 1963. He attended Virginia Tech for his undergraduate studies during which time he worked as a cooperative education student at the NASA Johnson Space Center in Houston, Texas. He received his Bachelor of Science degree in Electrical Engineering from Virginia Tech in June of 1986. Upon completion of his undergraduate studies, he began graduate work at Duke University. He completed his Master of Science degree in Electrical Engineering at Duke in June of 1988 in the area of power electronics with a particular focus on magnetics design issues for high-frequency transformers. From 1988 until 1992 he was employed as a senior engineer for Digital Equipment Corporation in Northboro, Massachusetts where he was engaged in magnetic component design and development for high-density DC-DC converters. He returned to Virginia Tech from the fall of 1992 until the fall of 1996 during which time he worked as a graduate research assistant in the Virginia Power Electronics Center (VPEC). His research interests at VPEC included the computer-aided analysis of magnetic structures, scientific visualization techniques for use in the analysis of magnetic device performance and the effects of core geometry on the performance of transformers and inductors.